

**Optimal Covariance Control on Singular Manifolds with
Application to Aerospace Mission Design**

by

Casey R. Heidrich

B.S., University of California Davis, 2013

M.S., Georgia Institute of Technology, 2015

A thesis submitted to the
Faculty of the Graduate School of the
University of Colorado in partial fulfillment
of the requirements for the degree of
Doctor of Philosophy

Ann and H.J. Smead Department of Aerospace Engineering Sciences

2021

Committee Members:

Dr. Marcus J. Holzinger, Chair

Dr. Robert D. Braun, Co-Chair

Dr. Hanspeter Schaub

Dr. Jay McMahon

Dr. Soumyo Dutta

Dr. Michael Grant

Heidrich, Casey R. (Ph.D., Aerospace Engineering Sciences)

Optimal Covariance Control on Singular Manifolds with Application to Aerospace Mission Design

Thesis directed by Dr. Marcus J. Holzinger

Atmospheric trajectory design and entry guidance are highly enabling technologies for hypersonic entry flight missions. Current methodologies are often rooted in certainty equivalence, wherein optimization is performed on best-estimates of variable or uncertain quantities. The aerospace sciences in general may benefit from improvements to optimal motion planning under uncertainty. Further, solution methodologies should focus on scalability and practicality, without relying on implicit root-solving or a priori knowledge of the solution structure. This work leverages principles of indirect methods in optimal control theory to develop accurate, reliable solution strategies that transform complex, multi-phase constrained problems into single-phase unconstrained problems. New developments in regularization methods are shown to greatly simplify construction of the Hamiltonian boundary value problem without sacrificing solution accuracy. Advances in constraint regularization using generalized sigmoid functions and differential system extension allow application of the new method to a wide range of engineering problems. Classes of ill-posed singular control problems are also studied with aerospace applications. An indeterminate problem structure is shown to produce infinite-order singular arcs which the standard convexity conditions fail to resolve. A relaxation method is developed to produce a nominal trajectory minimizing statistical variation of the state error covariance about a singular terminal state manifold. These principles are then applied to numerical predictor-corrector entry guidance algorithms. A consider uncertainty analysis is shown to maximize probabilistic likelihoods of achieving downrange targeted states from anticipated measurement conditioning effects. Reformulation of the entry guidance problem for *risk-adverse* performance may improve confidence in challenging aeroassist maneuvers such as aerocapture. Impacts of this work on mission design are demonstrated through rapid solution of complex entry flight problems with uncertainty in system states and parameters.

Acknowledgements

I owe an overwhelming amount of appreciation to the many people and organizations that have supported my research over the years. Any omission is purely a result of the limited space on this page I am given in which to express this gratitude. First, I owe an enormous thank you to my graduate advisors, Bobby Braun and Marcus Holzinger. Both of you provided substantial mentorship and advice throughout my student career, and I am deeply grateful for the extensive time and resources you put forth in furtherance of my degree. Thank you for your continued support and patience. I would also like to acknowledge Michael Grant and Michael Sparapany, both of whom provided significant guidance during my two-year internship at Sandia National Labs. I gained a substantial amount of knowledge from you both, and I always felt welcome to ask for help when I (often) needed it. I also thank Dr. Hanspeter Schaub for exemplary mentorship during my time as a Teaching Assistant for his Spacecraft Formation Flying graduate course. Thank you to my NASA advisors, Soumyo Dutta and Brandon Smith, for providing excellent industry perspective and personal guidance. I also gratefully acknowledge generous support received through a NASA Space Technology Research Fellowship (NNX17AG09H) and a U.S. Department of Education GAANN fellowship at the University of Colorado Boulder (P200A180014).

Most importantly, thank you to my family and friends. To my parents, Gary and Dina, and my brother, Dane, thank you for your encouragement no matter the outcome of my degree. To my fiancé, Brie, I owe too much to ever express in words, but I am forever grateful for your unwavering support. To those not mentioned here – you know who you are!

Contents

Chapter

1	Introduction	1
1.1	Motivation	1
1.2	Background	2
1.2.1	Aerocapture Conceptual Design	2
1.2.2	Entry Guidance and Uncertainty Quantification	5
1.2.3	Optimal Control Theory and Applications	7
1.3	Relation to Existing Work	9
1.4	Scope of Thesis	11
1.5	Publications	15
2	Generalized Regularization of Constrained Optimal Control Problems	17
2.1	Regularization and Path Constraint Smoothing Techniques	17
2.2	Indirect Optimization Variational Approach	19
2.3	Generalization of Bang-bang Optimal Control Regularization	23
2.3.1	Regularization Using Control Sigmoid Functions	27
2.3.2	Accommodating Arbitrary Control Bounds	34
2.3.3	Example: Van der Pol Oscillator	36
2.3.4	Example: Sounding Rocket	39
2.4	Extension to General Hamiltonian Structures	44

2.4.1	Nonlinear Control Terms	45
2.4.2	Path Constraint Regularization	46
2.4.3	Example: Time-Energy Optimal Control	49
2.5	Application to Aerospace Systems	52
2.5.1	3-DOF Hypersonic Problem	52
2.5.2	Keep-out Zone	59
2.6	Summary	62
3	Relaxation of Infinite-Order Singular Arcs by Auxiliary Covariance Minimization	64
3.1	Optimal Control Uniqueness and Well-Posedness	64
3.2	The Minimum Principle	68
3.2.1	Pontryagin Minimum Principle	68
3.2.2	Singular Arcs: Existence and Order	70
3.3	A Convexity Condition for Infinite-Order Singular Arcs	72
3.3.1	End-time Fixed	73
3.3.2	Example: 1-D Integrator	77
3.3.3	End-time Free with State Constraint	80
3.4	Relaxation by Auxiliary Covariance Minimization	81
3.4.1	Uncertainty Quantification	82
3.4.2	Expectation Cost Objective	86
3.4.3	Auxiliary Problem Definition	87
3.4.4	Example: Uncertain Van der Pol Oscillator	90
3.5	Numerical Solution Strategy for Complex Systems	95
3.6	Aerospace Mission Design Applications	96
3.6.1	Relative Orbit Formation Flying	97
3.6.2	Planetary Aerocapture	110
3.7	Summary	124

4	Optimal Information Filtering for Planetary Aerocapture	125
4.1	Entry Guidance Perspective	125
4.2	Observer-based Trajectory Design and Guidance	127
4.2.1	Robust Optimization of Dynamic Systems	127
4.2.2	Covariance Approximation of the Distributional Cost Measure	129
4.2.3	Discrete-time Extended Consider Kalman Filtering	132
4.2.4	Parametric Control Solution	136
4.3	Application to Aerocapture	137
4.3.1	Process and Measurement Models	137
4.3.2	Optimal Control Objectives	139
4.3.3	Consider Parameter Uncertainty Models	141
4.3.4	Bang-bang Parametric Control	144
4.4	Results	147
4.4.1	Mars Aerocapture Mission	147
4.4.2	Numerical Results and Discussion	148
4.5	Summary	158
5	Conclusions and Future Work	159
	Bibliography	163
	Appendix	
A	Relating UTM and GCRM Control Laws	178
B	Singular Controls and Differential Extension	181
C	Proof of Proposition 2	183

D Linearized Dynamics and Measurement Models	186
E Traditional Atmospheric Estimation	188
F Acknowledgements for Chapter 2	189

Tables

Table

1.1	Overview of thesis contributions and existing literature.	14
2.1	Normalized regularization functions and error-control terms for $ u \leq 1$	30
2.2	Parameters used in the sounding rocket example.	42
2.3	Path constraint regularization functions.	48
2.4	Initial and final state constraints for hypersonic Earth reentry scenario.	56
2.5	Constants for hypersonic Earth reentry scenario.	56
2.6	Parameters used in the keep-out zone constraint.	60
3.1	State constraints and problem parameters for CW relative motion example.	102
3.2	Auxiliary states and problem parameters for relative motion example.	105
3.3	State constraints and problem parameters for Mars aerocapture example.	114
3.4	Auxiliary states and problem parameters for Mars aerocapture example.	118
4.1	Initial state and parameter uncertainties for Mars aerocapture mission.	148
4.2	Monte Carlo simulation statistics for ECKF and unfiltered cases.	157

Figures

Figure

1.1	Traditional TCW conceptual design for a Neptune aerocapture mission.	4
1.2	Aerocapture entry guidance prediction problem.	6
1.3	Flowchart of thesis contributions.	13
2.1	Illustration of solution arcs relative to constraint surface $c(x_1, x_2, x_3) = 0$	20
2.2	Illustration of orthogonality in geometric and functional spaces.	24
2.3	Arctangent regularization function derivatives	29
2.4	Control and error-control regularizing functions.	31
2.5	Convergence of smoothed optimal control Hamiltonian over regularization.	32
2.6	Structure of UTM optimal control law.	35
2.7	Structure of GCRM optimal control law.	35
2.8	Minimum-time Van der Pol solution with GCRM arctangent regularization.	39
2.9	Solution to sounding rocket example using GCRM error function.	43
2.10	Optimal control cost over regularization parameter for sounding rocket example.	44
2.11	Arctangent path constraint penalty function.	49
2.12	Solution to time-energy example using hyperbolic tangent regularization.	52
2.13	Lift-to-drag ratio and drag polar for generic hypersonic reentry vehicle.	54
2.14	Converged trajectory of the 3-DOF hypersonic reentry problem.	58
2.15	Bank rate regularization for 3-DOF hypersonic reentry problem.	59

2.16	Ground track of the hypersonic 3-DOF example with keep-out zone.	61
2.17	Performance comparison with keep-out zone constraint.	62
3.1	Conceptual illustration of finite- and infinite-order arc reachability.	78
3.2	Symmetry of infinite-order arc solutions in 1-D integrator example.	80
3.3	Conceptual illustration of auxiliary problem.	82
3.4	Infinite-order singular arc solutions of Van der Pol example.	92
3.5	Auxiliary minimum solution of Van der Pol example.	94
3.6	Phase portrait and error covariance propagation for Van der Pol example.	94
3.7	Numerical continuation homotopy over boundary condition parameters.	95
3.8	Relative orbital motion geometry in rotating Hill frame.	98
3.9	Infinite-order singular solution arcs in the CW relation motion example.	103
3.10	Infinite-order singular solution arcs in the CW relation motion example.	106
3.11	Propagated position and velocity errors for relative motion example.	108
3.12	Terminal state error covariances projected onto zero-drift target manifold.	108
3.13	Propagated unforced radial and along-track relative motion for 5 chief orbits.	109
3.14	Illustration of aerocapture maneuver with single-burn ΔV	111
3.15	Continuation interval over final radius r_f in aerocapture example.	115
3.16	Illustrative subset of infinite-order singular arcs in aerocapture example.	116
3.17	Phase-space portrait of infinite-order singular arcs in aerocapture example.	117
3.18	Auxiliary minimum solution of aerocapture example.	119
3.19	Propagated error covariance $2\text{-}\sigma$ bounds for auxiliary solution to aerocapture example.	120
3.20	Propagated uncertainty $2\text{-}\sigma$ error ellipses for auxiliary solution to aerocapture example.	120
3.21	Aerocapture conceptual design tradespace for singular solutions.	122
3.22	Aerocapture conceptual design tradespace for auxiliary minimum solution.	123
4.1	Illustrative sensitivity of final covariance with equivalent optimality of mean states. .	132
4.2	Exit interface orbital parameters for select aerocapture mission concepts.	140

4.3	Density perturbation models from MarsGRAM dispersion data.	145
4.4	GRAM atmospheric density variations as a function of altitude.	145
4.5	Representative bang-bang bank angle control profile with single switch time.	146
4.6	Nominal Mars aerocapture trajectory ($\sigma_d = 90$ deg).	150
4.7	ECKF estimation error residuals ($\sigma_d = 90$ deg).	151
4.8	ECKF $2\text{-}\sigma$ exit state estimate uncertainty as a function of bank angle switch.	152
4.9	Robust cost trade as a function of bank angle switch parameter.	153
4.10	Optimal switch time for robust cost minimum.	153
4.11	Time history of bank angle input for chosen σ_d cases.	154
4.12	Terminal state error distribution at atmospheric exit interface.	155
4.13	Apoapsis targeting for selected bank angle switch values.	156
4.14	Comparison of ΔV performance for selected bank angle switch values.	157

Chapter 1

Introduction

1.1 Motivation

Conceptual design of hypersonic entry systems is a critical decision-making process for any spacecraft destined to pierce the atmosphere of a planet at orbital velocities. Atmospheric entry is highly enabling for a wide degree of science and exploration missions otherwise intractable with propulsive orbit insertion [1]. Unfortunately, due to the often unpredictable nature of hypersonic flight, these missions are subject to considerable uncertainty in the achievable accuracy and reliability of such maneuvers. A considerable effort has been put forth in the literature regarding the development of online entry guidance algorithms [2–22] designed to continuously re-target down-range flight conditions. The vast majority of entry guidance work has been developed under the guise of certainty equivalence [23], wherein uncertain states and parameters are substituted for their best estimate. This has the effect of greatly reducing the parameter space in optimization, but in turn degrades the accuracy of predicted future states with imprecise system knowledge. Further, due to poor dimensional scaling of Monte Carlo simulation methods, uncertainty quantification (UQ) is generally undertaken asynchronously to trajectory and guidance design. This general approach has led conceptual trade studies to produce over-designed vehicles with considerable risk posture, as opposed to leveraging flight-proven heritage entry systems. Coupled with significant research and development investment timescales required for flagship missions, many high-priority scientific destinations in the solar system remain unexplored to-date. Improving the reliability of hypersonic entry flight systems will directly impact planetary exploration and discovery for the

forseeable future.

The general consensus in the atmospheric flight mechanics community is that the effect of uncertainty can be mitigated by flying entry guidance in closed-loop. This belief is by no means unfounded. Successful missions at Mars demonstrated guided entry accuracy on the order of 10 km [24, 25]. However, whereas existing approaches may be sufficient for present needs, future missions may require landed accuracy on the order of meters. Other highly enabling aeroassist concepts such as aerocapture remain unproven as a result of disagreement in the research and engineering community regarding their likelihood of success.

The notion of uncertainty-robust trajectory design may provide a significant path of improvement moving forward. Incorporating models of underlying uncertainty into trajectory optimization and guidance can greatly improve dispersed performance. Furthermore, because the system must continuously reacquire its current state from in-situ measurement information, the nominal trajectory can be designed to enhance estimation and control. These benefits come at the cost of increased complexity in the underlying optimization statement and numerical solution. We are thus motivated to study tractable, reliable solution methodologies that enhance hypersonic entry performance under uncertainty. In this work, we are largely concerned with planetary aerocapture, though the results extend to many other classes of aeroassist missions, including aerobraking and direct entry.

1.2 Background

1.2.1 Aerocapture Conceptual Design

The future of space exploration calls for advanced technology to accommodate increasingly large payloads at scientifically interesting destinations in the solar system. Aerocapture is an aeroassist maneuver to generate considerable attention in the literature [26–29]. The objective in aerocapture is the dissipation of kinetic energy to capture a space vehicle from an unbounded approach trajectory into a bounded science observation orbit. Following the atmospheric pass,

errors in the capture orbit must be corrected using a series of small propulsive maneuvers. The velocity-loss achieved by the atmospheric pass can be significant depending on the destination and hyperbolic excess velocity. When compared to fully-propulsive orbit insertion, the maneuver may provide a 40–80% increase in delivered mass to orbit [27]. Aerocapture is frequently identified as a highly enabling technology for planetary exploration. Many mission scenarios are prohibitive or intractable without aerocapture, including Earth aeroassist for human return from Mars, circular orbits about Jupiter and Saturn, exploration of the ice giants, and orbit insertion at Titan [1].

A common tool in aerocapture mission feasibility assessment is theoretical corridor width (TCW) [30]. TCW defines the range of entry flight-path angles permitting a successful capture trajectory using the available control authority of the vehicle. Entry flight-path angles too steep will shed excess energy and undershoot the target orbit (potentially resulting in direct entry). Similarly, too-shallow entry flight-path angles will provide insufficient velocity loss, risking an overshoot trajectory and possibly unbounded exit orbit. Aerocapture conceptual design relies on TCW to determine the necessary aerodynamic lift-to-drag ratio (L/D) a vehicle must produce during atmospheric flight. As a result, the configuration design landscape can vary widely. Earth aerocapture concepts, such as Lunar or Mars return of high-mass payloads, can leverage significant improvements in Earth approach navigation demonstrated by the Stardust and Genesis sample return missions [31,32]. A conservative TCW of 0.4 deg for Earth entry velocities of 11–14 km/s has been shown to facilitate moderate L/D of 0.1–0.3 [33]. Robotic payloads subject to less stringent deceleration limits may reduce L/D requirements even further. Moderate L/D is also sufficient for aerocapture with Mars [34] entry velocities of 4–6 km/s and Venus [35] entry velocities above 11 km/s. Aeroshells producing low to moderate lift, indicative of Apollo-era and Mars Viking blunt-body designs, have a history of successful atmospheric entry [36]. Entry systems based on flight-proven heritage technology are significantly more appealing from a cost and risk perspective, enabling rapid performance evaluation and design based on existing data.

A stark contrast exists for conceptual design of aerocapture missions to relatively unexplored systems, such as the ice giants, due to numerous sources of uncertainty. Interplanetary transit tra-

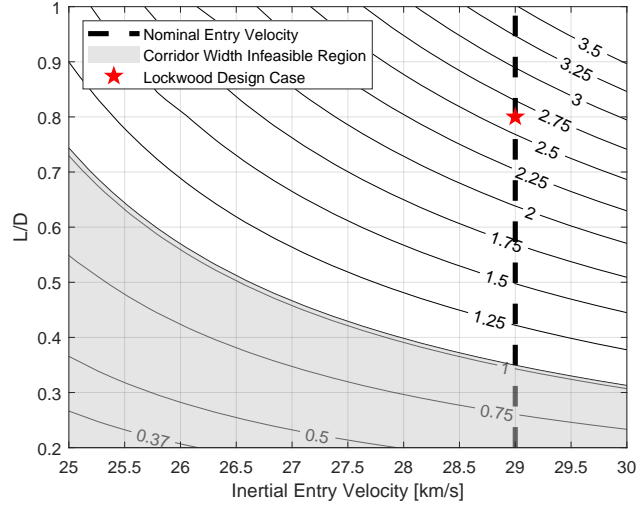


Figure 1.1: Traditional TCW conceptual design for a Neptune aerocapture mission (Heidrich *et al.* [37]).

jectories to Neptune, for example, utilize a Venus-Jupiter combined flyby to balance transit time and delivery performance [38]. A lack of orbital assets at these destinations degrades entry interface approach navigation accuracy, increasing entry flight-path angle dispersions. Knowledge regarding the atmosphere and gravity field of Neptune relies partly on data collected by the Voyager 2 flyby in 1989 [39]. In addition, overshoot risks are evident at missions to the ice giants, where the exit velocity is close to escape velocity [40]. A trade study on Neptune aerocapture by Lockwood [41] indicates an L/D of 0.6–0.8 needed for entry velocities in the 28–30 km/s range to accommodate expected dispersions in delivery flight-path angle and atmospheric guidance reliability. This conceptual design trade is illustrated in Fig. 1.1 for a nominal entry velocity of 29 km/s. Although entry interface delivery uncertainties could permit moderate-lift vehicles, a large margin in L/D is included for atmospheric uncertainty and entry guidance performance. A more recent study on ice giants exploration [42] concludes similar findings for both Uranus and Neptune, noting that recent advancements in TPS materials may alleviate peak heat rate limitations of previous studies.

As a result of historically high L/D requirements, these missions cannot leverage the proven flight history of heritage blunt-body entry systems. Instead, aerocapture at these destinations would

require development of lifting-body vehicles with low technology readiness levels (TRL), ostensibly spanning a significant design and testing campaign. These factors limit the viability of attempting aerocapture at the ice giants, especially for first-time flights carrying high-value payloads.

1.2.2 Entry Guidance and Uncertainty Quantification

TCW is useful as a first-order tool for evaluating aerocapture mission feasibility. However, TCW alone is not an indicator of satisfactory atmospheric flight performance. The overall performance of an aerocapture maneuver is highly sensitive to system parameters spanning a range of engineering disciplines. These parameters may rely on incomplete data or lack Earth-based testing capabilities. Most aerocapture conceptual design studies have entailed entry guidance to maintain an acceptable flight envelope. A general illustration of the entry guidance problem for aerocapture is shown in Fig. 1.2. These strategies typically share a common goal (the precise dissipation of kinetic energy through aerodynamic force vectoring), though each particular implementation varies widely.

Hypersonic entry guidance of low-lifting vehicles dates back to the Apollo missions designed for human return from Lunar orbit [43]. Fixed-trim bank-to-steer guidance strategies have been flown or planned on many direct entry missions. Guidance strategies for aerocapture have largely been adapted from direct entry algorithms, building on experience from flight-proven data and research. The analytical predictor-corrector (APC) method was proposed for Mars Sample Return (MSR) and Mars aerocapture [44–46]. Another explicit guidance method uses matched asymptotic solutions to target apogee [47]. Other analytical aerocapture guidance developments include the terminal point controller (TPC) [40, 48] and the hybrid predictor-corrector aerocapture scheme (HYPAS) [49–51]. A guidance comparison campaign [52] found the TPC to be more robust than other existing analytical methods. More recent advancements in aerocapture NPC strategies [53, 54] have demonstrated increased orbit insertion accuracy through numerical integration of the nonlinear entry dynamics.

The purpose of entry guidance is to recompute a reference flight profile and control after en-

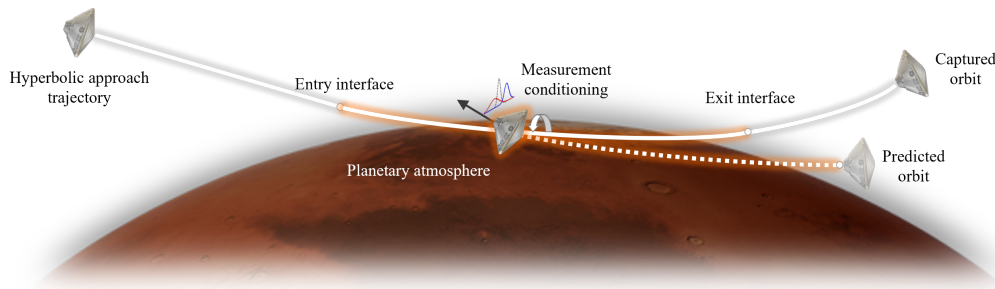


Figure 1.2: Aerocapture entry guidance prediction problem.

countering perturbations in flight. UQ is frequently performed to assess the dispersed performance of a guidance algorithm, where simulated trajectories are tested with variable vehicle performance parameters and environment conditions. Halder [55] gives a comprehensive overview of UQ methods in hypersonic entry flight. In dispersion analysis, the guidance routine is isolated from “truth” models and operates its internal prediction logic on nominal states and parameters. The goal of UQ is to determine the effect of input and model uncertainties on response metrics of interest. Sources of uncertainty are often classified as *aleatory* or *epistemic* [56]. The former refers to irreducible uncertainty, in which quantities are variable by nature. The latter refers to reducible uncertainty resulting from a lack of knowledge due to sparse data or subjective probabilistic descriptions [57]. For the hypersonic entry problem, atmospheric density is partly epistemic due to a lack of understanding of the underlying mechanisms of spatial atmospheric density variations. Parameters describing the dynamics of an entry vehicle (mass, aerodynamic coefficients, drag area, etc.) may introduce both aleatory and epistemic uncertainty based on available data and the designer’s knowledge of each subsystem [58]. Algorithmic errors may also be introduced by the internal guidance routine [52].

The most common UQ technique for atmospheric entry is the Monte Carlo (MC) framework [33, 59, 60]. MC methods simulate a large number of runs with dispersed initial conditions and system parameters randomly sampled from known probability distributions. A single run is considered valid if its output is bounded to within a desired interval satisfying trajectory con-

straints. Uncertainty is estimated by statistical inference of the output time histories of each run. These methods have the benefit of straightforward implementation and provide a basis for physical reasoning. However, MC methods have several downfalls, most notably poor numerical scaling and no statistically consistent method to quantify the evolution of uncertainty [61]. Even with a large number of runs, there are no guarantees with MC methods to capture every possible realization of the initial uncertainty distribution. Due to these challenges, MC dispersions are historically applied “outside the loop.” That is, the nominal control and corresponding trajectory are generated assuming perfect knowledge of the system state and models. This feature is a commonality of most existing atmospheric trajectory generation and guidance techniques. Even if current UQ approaches are sufficiently accurate to quantify output interval dispersions, existing entry guidance methodologies are limited to incorporating uncertainty models outside of the trajectory and guidance design process.

1.2.3 Optimal Control Theory and Applications

Optimal control is a broad topic encompassing many practical science and engineering problems. Outside of its common use in aerospace fields, optimal control theory has seen extensive application including environmental sustainability [62], financial asset allocation [63], biological models [64], and epidemiology of emerging and reemerging infectious diseases [65, 66], among others. Information on the optimal behavior of these systems has broad societal impacts, driving a continuing need in the research community to improve and innovate reliable, tractable solution methodologies. Outside of simple, well-behaved systems, iterative numerical methods are required to solve an optimal control problem (OCP). Solution strategies are often broadly classified as *direct* or *indirect* methods. Direct methods typically discretize the solution domain over a set collocation nodes [67]. In contrast, indirect methods enforce necessary conditions of optimality through variational equations [68]. Each approach presents unique opportunities and challenges for the particular application.

Direct methods transform an OCP into a large-scale parameter optimization problem solved

by nonlinear programming (NLP). State-of-the-art software packages such as GPOPS-II [69] and SNOPT [70] have made direct methods highly accessible, owing to their popularity. Direct methods enjoy many benefits, including reduced sensitivity to initial guess, large domain of attraction, and ease of implementation in highly-constrained problems [71, 72]. Direct methods are approximate by design, relying on implicit numerical integration of the state equations between nodes. This approximate nature enables solutions to complex problems without a close initial guess [73]. However, these benefits come at the cost of solution precision and computational complexity with increasing nodes. Direct methods may also suffer from control “jitter” in sensitive problems due to discretization errors or improper spacing of collocation nodes [74, 75]. Applications requiring rapid or high precision solutions, such as real-time trajectory optimization and machine learning training algorithms [76, 77], may not benefit from direct methods.

Indirect methods, in contrast, enforce necessary conditions of optimality through the Euler-Lagrange variational equations [68, 78]. A Hamiltonian boundary value problem (HBVP) is constructed from adjoint equations for the costates, with boundary conditions defined at the terminus of the trajectory. Indirect methods give exact solutions and can require less computational overhead [79]. Rapid convergence is usually possible with modern BVP solvers given a close initial guess. Indirect formulations also present unique opportunities for data compression and parallel computing using multiple shooting [80], making them useful for real-time applications. As with their direct method counterparts, indirect methods have some setbacks. Indirect methods are notoriously sensitive with a much smaller domain of attraction. The less-intuitive nature of costates makes it difficult to produce a feasible initial guess, though some methodologies exist [81]. Underlying assumptions from calculus of variations assume process equations are continuously smooth and differentiable, limiting their usefulness on data-driven applications. Adjoint equations must also be constructed through symbolic manipulation to derive conditions for optimality. This process has become more automated with indirect software packages [82]. Further advancements in numerical continuation strategies [83–85] and reduction methods [86] have improved outlooks on indirect methods and driven continued use within the engineering community.

Indirect methods in particular have been shown to greatly enhance hypersonic trajectory optimization and conceptual design [87–90]. A wide range of design points can be iterated over by varying problem parameters and trajectory constraints through symbolic manipulation and numerical continuation techniques. This has been shown to enable rapid trade study development for vehicle design. Furthermore, optimal control theory has served as the basis for entry guidance algorithms [21, 91, 92], underpinning its importance in online path planning. Improvements to indirect methods may also enhance direct methods by virtue of the covector mapping theorem (CMT) [73, 93]. Continuing developments in the rapid construction and numerical solution of optimal control problems serves to benefit a wide class of engineering applications.

1.3 Relation to Existing Work

In the traditional indirect approach, constrained solution arcs must be treated separately and stitched together through solution of a multi-point boundary value problem (MPBVP). This problem structure is often not known prior to numerical solution, particularly in complex multi-stage problems. In response, a number of regularization strategies [94–99] have been developed to overcome these challenges. Generally speaking, regularization involves substituting constrained quantities with smoothing functions, as well as augmenting error-control terms to increase solution precision. The methods operate over a numerical continuation interval on small regularization parameters, such that the original problem structure is retained.

Regularization methodologies have demonstrated considerable promise by eliminating the need for a priori knowledge of constrained solution arcs. However, current approaches vary widely in their application and are often problem-specific. For example, logarithmic barrier functions are studied for a class of control-affine systems with bang-bang control structures in Ref. [94]. The piecewise-defined control law must distinguish between bang-bang and singular arcs. A topological smoothing technique for a single-input minimum-time problem is developed in Ref. [95]. The resulting problem is regular, but requires numerical root-solving to determine the optimal control policy. More recent approaches utilize geometric sine-cosine orthogonality using trigonometric

regularization [97, 99]. Trigonometric smoothing can resolve bang-bang and singular arcs in a uniform fashion. However, the resulting control law is expressed in terms of non-surjective functions, requiring point-wise application of the Minimum Principle [100] to identify the optimal control. Limitations of existing approaches may not scale well in complex, high-dimensional problems.

A common feature in optimal control is a singular solution structure. Singular arcs result from solution segments in which the control imparts no change on the Hamiltonian, leading to an indeterminate control structure. In many problems, singular arcs are well-posed and can be resolved through additional convexity conditions on the Hamiltonian [101, 102]. However, an interesting feature occurs when the singular arc presents with infinite order [103]. In this case, the control form is degenerate, as no further information on the optimal policy can be obtained by successive differentiation of the switching function. This behavior is strongly linked to uniqueness and posedness of the underlying optimization problem [104]. Though infinite-order singular arcs may seem like a rare exception, they are sometimes observed in relevant aerospace applications [105–107]. Limited existing work [108, 109] is available on the numerical solution of these problems. Moreover, existing approaches rely on direct or hybrid direct-indirect solution. These problems would benefit from improvements to indirect methodologies on infinite-order singular arcs.

Current approaches to the entry guidance problem are strongly rooted in certainty equivalence. Nonetheless, some existing work has begun to reexamine this assumption. Aleatory-epistemic uncertainty reduction has been attempted for hypersonic entry flight using hybrid coevolutionary algorithms [58]. The method is applied to design of aerocapture trajectories characterized by uncertainties in atmospheric density, vehicle shape and aerodynamic coefficients using evidence theory. Reference [110] proposes a blended control predictor-corrector algorithm to confront dispersions in entry states and atmospheric conditions. Another study applies desensitized optimal control (DOC) to the entry trajectory optimization problem using direct collocation methods [60]. DOC attempts to reduce the sensitivity of terminal states with respect to perturbations along the trajectory by minimizing individual entries of the sensitivity matrix. Covariance steering methods have been applied to the powered descent problem in Ref. [111], where a control input is generated to steer

an initial state covariance to its desired final distribution. Navigation-enhanced entry trajectory optimization [112, 113] has been shown to reduce terminal state errors due to sensitivities in initial conditions and parameters. Linear covariance analysis [114] and closed-loop steering laws [115, 116] have been applied to atmospheric entry problems to desensitize closed-loop entry guidance with stochastic processes. Moving forward, it is important for the research community to continue developing methods for robust trajectory design in order to enable a broader class of aeroassist missions to unexplored destinations in the solar system.

1.4 Scope of Thesis

This work develops methodologies for reducing uncertainty in aeroassist problems using accurate and reliable solution methodologies. The statement of this thesis can be summarized as follows:

A class of problems in optimal control theory exhibit indeterminate solution structures that can be resolved by projection of statistical error covariances onto singular terminal manifolds. This work develops tractable solution methodologies for such problems with relevance to aerospace mission design and entry guidance under uncertainty.

This statement is supported by the following contributions. Together, these contributions are expected to enhance atmospheric flight problems with uncertainty, as well as improve outlooks in the research and engineering community regarding the efficacy and reliability of challenging aeroassist maneuvers, such as aerocapture. Figure 1.3 illustrates the relationship between each of these contributions. The relation to existing work is summarized in Table 1.1.

Contribution 1) Generalized indirect optimal control constraint regularization. Constraints in optimal control problems introduce challenges with traditional indirect methods. Bang-bang/singular solutions with discontinuous or indefinite control laws add further difficulty in numerical solutions. Recent efforts in control regularization strategies have sought to overcome these limitations. Regularization generates a smoothed constraint transformation of a multi-phase Hamiltonian boundary value problem to a single-phase unconstrained problem. This work develops

a new approach to regularization using orthogonal error-control saturation functions. The method is developed for problems in bang-bang/singular form. The method is then applied to problems of general Hamiltonian structure using system extension and differential control. Applications in state constraint regularization are discussed. A key feature of the new approach is to eliminate ambiguity of the control law derived from the first-order necessary conditions of optimality. Results show desirable stability and convergence in numerical continuation. The method is applied to classical problems in optimal control, as well as problems of interest in aerospace mission design.

Contribution 2) Auxiliary Covariance Minimization for Ill-posed Singular Control Problems. Singular arcs are a common feature in optimal control problems when the standard necessary conditions fail to reveal a candidate control. In some cases, a singular arc can be proven to be non-optimal and discarded. In other cases, the solution can be resolved through additional convexity conditions on the Hamiltonian. A less common, but nonetheless interesting, scenario occurs when the singular arc appears with infinite order. This situation becomes apparent when the problem definition lacks sufficient information to identify a unique solution. In this work, we consider conditions under which singular optimal control problems may exhibit indeterminate behavior due to insufficiency of the cost objective and boundary conditions. The resulting problem is shown to be singular, but in a degenerate sense in which the necessary conditions yield no new information. A relaxation approach is developed to repose the problem with augmented covariance dynamics. Under moderate assumptions on the problem structure, the method permits finite-order arcs and produces a well-posed problem. The approach has relevance to engineering systems, which are almost always subject to some level of uncertainty in initial states or parameters. Examples are provided based on classical problems in optimal control, as well as applications to aerospace mission design.

Contribution 3) Optimal Information Filtering and NPC Guidance Allocation for Planetary Aerocapture. Entry flight is a critical mission phase of planetary aeroassist problems. During atmospheric flight, aleatory-epistemic uncertainty and environmental factors reduce the accuracy of predicted future states for precision targeting. This problem has been approached

historically with closed-loop guidance rooted in certainty equivalence. This property separates estimation and control problems, allowing each to be considered independently. In other concept studies, an observer model is neglected altogether in favor of assuming perfect state knowledge. However, a flight system will inevitably have imprecise state information and variability in its underlying dynamics and measurement models. Systemic uncertainty is a fundamental limitation of existing entry guidance approaches. This work seeks to overcome these challenges by posing aerocapture as a robust optimization problem. The cost objective of the maneuver is reformulated to account for uncertainty in atmospheric structure, vehicle performance parameters, and state estimation accuracy using an observer-based consider filter. An expected value performance cost is developed from anticipated measurement conditioning effects. A rapid solution methodology is illustrated using explicit integration strategies with a parametrized control structure. Results for a Mars aerocapture concept study show improvement in the post-capture orbit accuracy with low computational overhead.

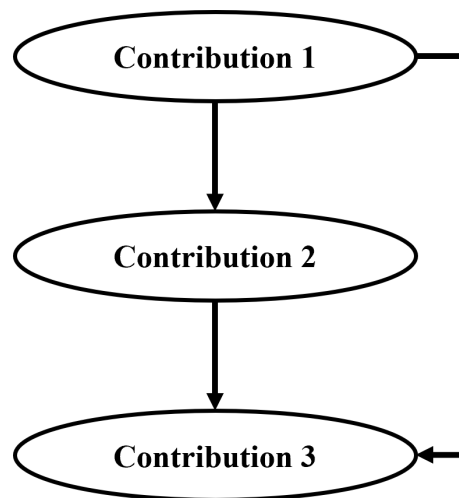


Figure 1.3: Flowchart of thesis contributions.

Table 1.1: Overview of thesis contributions and existing literature.

	Contribution 1	Contribution 2	Contribution 3	
Relation to existing literature	Bertrand and Epenoy [94], Silva and Trélat [95]	Topological and logarithmic barrier continuation smoothing		
	Mall <i>et al.</i> [97, 99], Taheri and Junkins [117]	Trigonometric and hyperbolic bang-off-bang control		
	Powers [103], Fraser-Andrews [118]		Definition of intrinsic and local singular arc order	
	Bortins <i>et al.</i> [105], Seywald and Kumar [106], Harris [107]		Computational verification of infinite-order singular arcs	
	Zimmer <i>et al.</i> [119], Oguri and McMahon [120], Jenson and Scheeres [121], Nolan <i>et al.</i> [112]		Multiobjective covariance optimization using indirect methods	
	Lu <i>et al.</i> [20, 91], Webb <i>et al.</i> [122], Deshmukh <i>et al.</i> [123]		Deterministic optimal control theory applied to entry guidance	
	Li and Peng [60], Xu and Cui [124], Cui <i>et al.</i> [125], Makkapati <i>et al.</i> [113]		Desensitized entry trajectory optimization using direct collocation	
	Shaviv and Oshman [126, 127], Jianwei <i>et al.</i> [128], Dutta <i>et al.</i> [129, 130]		Atmospheric entry state estimation and trajectory reconstruction	
	This work	Chapter 2 J2, C1, C2	Analytic control regularization with functional orthogonality	
		Chapter 3 J3, C5		Infinite-order singular arc existence and relaxation
Chapter 4 J1, C3, C6			Estimation-enhanced NPC guidance allocation	

1.5 Publications

For reference, journals, conferences, and other publications are listed chronologically within each category (most recent first).

Journals

- J1** Heidrich, C. R., Holzinger, M. J., and Braun, R. D., “Optimal Information Filtering for Robust Aerocapture Trajectory Generation and Guidance,” *Journal of Spacecraft and Rockets*, 2021. (In press)
- J2** Heidrich, C. R., Sparapany, M. J., and Grant, M. J., “Generalized Regularization of Constrained Optimal Control Problems,” *Journal of Spacecraft and Rockets*, 2021. (Under revision)
- J3** Heidrich, C. R., and Holzinger, M. J., “Relaxation of Infinite-Order Singular Arcs by Auxiliary Covariance Minimization,” *Journal of Guidance, Control, and Dynamics*, 2021. (Planned submission)

Conferences

- C1** Heidrich, C. R., and Grant, M. J., “Indirect 6-DOF Hypersonic Entry Trajectory Optimization,” *AAS Guidance, Navigation and Control Conference*, Breckenridge CO, February 2022. (Extended abstract)
- C2** Heidrich, C. R., Sparapany, M. J., and Grant, M. J., “Investigation of Control Regularization Functions in Bang-Bang/Singular Optimal Control Problems,” *AIAA SciTech Forum and Exposition*, Virtual Event, January 2021.
- C3** Heidrich, C. R., and Holzinger, M. J., “Robust Optimal Trajectory Design and Guidance for Planetary Aerocapture,” *AAS/AIAA Astrodynamics Specialist Conference*, Virtual Event, August 2020.

- C4** Heidrich, C. R., Roelke, E., Albert, S. W., and Braun, R. D., “Comparative Study of Lift and Drag Modulation Control Strategies for Aerocapture,” *AAS Guidance, Navigation and Control Conference*, Breckenridge CO, January 2020.
- C5** Heidrich, C. R., and Braun, R. D., “Aerocapture Trajectory Design in Uncertain Entry Environments,” *AIAA SciTech Forum and Exposition*, Orlando FL, January 2020.
- C6** Heidrich, C. R., Dutta, S., and Braun, R. D., “Modern Aerocapture Guidance to Enable Reduced-Lift Vehicles at Neptune,” *AAS/AIAA Space Flight Mechanics Meeting*, Kaanapali HI, January 2019.
- C7** Heidrich, C. R., and Braun, R. D., “Ballistic Reentry of Lifting Capsules at Earth Using Bank Rate Modulation,” *AIAA Space Forum and Exposition*, Orlando FL, September 2017.

Other publications

- Heidrich, C. R., and Braun, R. D., “An Accessory Minimization Problem for Robust Numerical Predictor-Corrector Aerocapture Guidance,” *Poster session presented at IPPW-16*, Oxford UK, July 2019.
- Heidrich, C. R., and Dutta, S., “Reduced Lift-to-drag Vehicle Concepts for Neptune Aerocapture,” *Poster session presented at IPPW-15*, Boulder CO, June 2018.
- Heidrich, C. R., Smith, B. P., and Braun, R. D., “Technology Overview and Assessment for Small-Scale EDL Systems,” *Poster session presented at IPPW-13*, Laurel MD, June 2016.
- Heidrich, C. R., and Braun, R. D., “Technologies to Enable Low Mass EDL for Mars Exploration Payloads,” (Master’s Special Topics), Georgia Institute of Technology, Atlanta GA, December 2015.

Chapter 2

Generalized Regularization of Constrained Optimal Control Problems

2.1 Regularization and Path Constraint Smoothing Techniques

Constraints in trajectory optimization problems are an important representation of system performance and solution feasibility. The constraints may be expressed as pure state, control, or mixed state-control bounds. Constrained problems introduce challenges in constructing and solving the associated Hamiltonian BVP. A conceptual illustration of constrained trajectory arcs is given in Fig. 2.1. Using traditional indirect methods, prior knowledge of the number and ordering of multiple constrained solution arcs is required [78]. The entry and exit behavior must also be specified using the Weierstrass-Erdmann corner conditions [131], adding further complexity. Outside of simple problems that provide analytical insight, predicting the constraint structure and order may not be feasible. Further, over numerical continuation on boundary condition parameters, the structure of active and inactive constraints may change dynamically. Solution of complex OCP constraints represents a significant challenge under the traditional indirect approach.

A common feature of some control-constrained OCPs is a bang-bang/singular control law. This is frequently the case when control terms appear linearly in the optimal control Hamiltonian. Pontryagin's Minimum Principle (PMP) [132] may provide a solution based on point-wise minimization of the Hamiltonian. These solutions rely on a *switching function*, where changes in sign indicate the instantaneous switching of the control on its upper or lower bound. Further difficulties are possible when the switching function is zero over a finite time interval, leading to a singular control. PMP is not well-suited to solving problems of this type, requiring further analysis such

as the generalized Legendre-Clebsch conditions [133]. Without prior knowledge of the appearance and order of singular arcs in each control dimension, constructing and solving the representative multi-point boundary value problem (MPBVP) may prove difficult or infeasible. These challenges increase rapidly for complex, high-dimensional systems.

A number of methods have been developed over the years in response to limitations of indirect methods in constrained applications. The focus of these methods is to transform the constrained OCP to an unconstrained problem using a process termed *regularization*. Regularization reduces the original multi-phase Hamiltonian BVP to a single-phase unconstrained problem by replacing constraints with appropriate smoothing and error-control terms. For example, early studies [134, 135] include an energy perturbation term as a quadratic function of the control to the integral cost. The modified, non-singular problem is repeatedly solved as the error term is gradually reduced to zero. Another study [95] develops a control smoothing method for a single-input control-affine system applied to the minimum-time problem. Control smoothing functions have been applied to constrained control problems [117, 136, 137] to inherently bound quantities in an unconstrained manner. A further improvement is the Epsilon-Trig method [97, 138] for regularization of control constraints using trigonometric functions. This method reduces the number of required error parameters and simplifies the construction and solution process of the augmented problem. A recent effort is the Unified Trigonometrization Method (UTM) [99], which ties together many useful constraint techniques using trigonometric smoothing terms. The UTM can handle affine and mixed state-control constraints and resolve singular arcs. The UTM produces multiple control options resulting from necessary conditions, requiring further analysis such as PMP to disambiguate the control law.

A drawback of indirect methods is the highly problem-specific knowledge needed to construct the necessary conditions and transform the OCP to its associated Hamiltonian BVP. This is particularly important in constrained problems where the structure and ordering of constraint arcs cannot be predicted prior to solution. Moreover, the solution structure may change during numerical solution as constrained arcs become active (or inactive) over a continuation interval. While

recent constraint regularization methods have shown promise, there remain opportunities for improvement. A notable limitation of current methods is ambiguous or implicit nonlinear control laws, requiring solution using collocation or numerically-expensive root finding operations.

This chapter presents a generalized method for regularization of constrained OCPs using orthogonal error-control saturation functions. A limitation of current strategies is overcome by resolving ambiguity in the optimal control law, requiring less effort in constructing and solving the Hamiltonian BVP. The benefits of this work include 1) flexibility in control regularization function choices in a generalized approach, 2) introduction of positive-definite integral error terms ensuring OCP convergence, 3) disambiguation of the optimal control law enabling algebraic substitution, and 4) application to a broad class of OCPs using system extension and generalized path constraint regularization.

The outline of this chapter is summarized as follows.¹ Section 2.2 gives an overview of the OCP form and theory of indirect methods in optimization. Section 2.3 develops the novel regularization method and derives necessary conditions for optimality. Results are shown for classical problems in optimal control with known solutions for comparison. Section 2.4 extends the method to problems of general form using system extension. Section 2.5 illustrates the method for aerospace systems. Section 2.6 summarizes findings for the chapter.

2.2 Indirect Optimization Variational Approach

A brief overview of indirect methods is presented as a theoretical basis for the remainder of this work. See Bryson [68] and Stengel [78] for a complete description. An OCP is a functional minimization problem to optimize a time-varying input $u^*(t)$ producing an optimal state history $\mathbf{x}^*(t)$. The optimal control objective Eq. (2.1a) is presented in *Bolza* form including integral and terminal cost terms. The solution must be consistent with the system dynamics Eq. (2.1b) and initial conditions Eq. (2.1c). The problem may also have constraints on the terminal state Eq. (2.1d), as well as path inequality constraints Eq. (2.1e). For brevity, we assume a single scalar

¹ Please see Appendix F for an acknowledgement regarding this chapter.

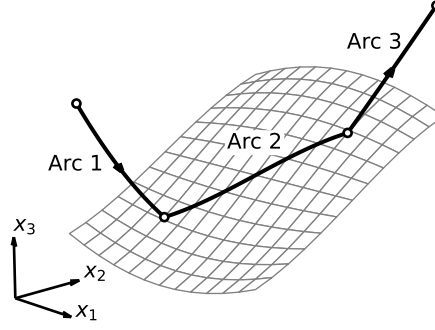


Figure 2.1: Illustration of solution arcs relative to constraint surface $c(x_1, x_2, x_3) = 0$.

control; however, all expressions can be extended to multiple control variables without loss of generality. Notation for time-dependency is omitted unless explicitly required.

$$\min_u J = \phi(\mathbf{x}(t_f), t_f) + \int_{t_0}^{t_f} L(\mathbf{x}, u, t) dt \quad (2.1a)$$

$$\text{Subject to: } \dot{\mathbf{x}} - \mathbf{f}(\mathbf{x}, u, t) = 0 \quad (2.1b)$$

$$\mathbf{x}(t_0) = \mathbf{x}_0 \quad (2.1c)$$

$$\boldsymbol{\psi}(\mathbf{x}(t_f), t_f) = 0 \quad (2.1d)$$

$$\mathbf{c}(\mathbf{x}, u, t) \leq 0 \quad (2.1e)$$

Indirect methods leverage the classical calculus of variations approach by appending the dynamics to the cost objective with a costate vector $\boldsymbol{\lambda}(t)$. Each costate corresponds to one state equation and can be interpreted as a time-varying Lagrange multiplier enforcing the system dynamics constraint in Eq. (2.1b). It is convenient to define the *Hamiltonian* of the system

$$H = \boldsymbol{\lambda}^T \mathbf{f}(\mathbf{x}, u, t) + L(\mathbf{x}, u, t) \quad (2.2)$$

The first-order necessary conditions of optimality transform an OCP to a well-defined Hamiltonian BVP through adjoint equations on the costates. On trajectory arcs where the constraint

Eq. (2.1e) is inactive, the following conditions hold

$$\dot{\boldsymbol{\lambda}} = - \left(\frac{\partial H}{\partial \boldsymbol{x}} \right)^{\text{T}} \quad (2.3a)$$

$$\dot{\boldsymbol{x}} = \left(\frac{\partial H}{\partial \boldsymbol{\lambda}} \right)^{\text{T}} \quad (2.3b)$$

$$\frac{\partial H}{\partial u} = 0 \quad (2.3c)$$

$$\boldsymbol{\lambda}(t_f) = \left(\frac{\partial \Phi}{\partial \boldsymbol{x}} \right)^{\text{T}}_{t=t_f} \quad (2.3d)$$

where we define the augmented terminal function as

$$\Phi(\boldsymbol{x}(t_f), t_f) = \phi(\boldsymbol{x}(t_f), t_f) + \boldsymbol{\nu}^{\text{T}} \boldsymbol{\psi}(\boldsymbol{x}(t_f), t_f) \quad (2.4)$$

The parameter vector $\boldsymbol{\nu}$ is a set of Lagrange multipliers adjoined to the cost in order to satisfy terminal constraints Eq. (2.1d). These parameters are appended to the BVP solver as additional unknowns. On trajectories where the final time is unspecified, the endpoint is determined implicitly by the *transversality condition*

$$\left(H + \frac{\partial \Phi}{\partial t} \right)_{t=t_f} = 0 \quad (2.5)$$

Equations (2.3a–2.3d) give a well-defined two-point BVP. Boundary conditions are specified on the states at the initial time t_0 , whereas boundary conditions on the costates are defined at the final time t_f . Thus, the primary challenge is determining the unknown initial costates $\boldsymbol{\lambda}(t_0)$ and Lagrange multipliers $\boldsymbol{\nu}$. The necessary condition for u is found from Eq. (2.3c). In the case where u can be solved for explicitly, the optimal control law is eliminated from the Hamiltonian BVP through direct substitution. However, in cases where multiple solutions for u exist, further analysis is required to identify the optimal control.

We note that the classical approach using calculus of variations assumes continuity and smoothness. These equations are valid for admissible controls on interior solution arcs. However, in cases where the necessary conditions fail to reveal an optimal control, Pontryagin’s Minimum Principle (PMP) may yield a solution based on the bounds of the control [132]. PMP can be useful to disambiguate non-unique control laws resulting from multiple roots of Eq. (2.3c). This principle

states that the optimal control u^* at any point minimizes the Hamiltonian compared to any other control u on the same trajectory.

$$H(\mathbf{x}^*, \boldsymbol{\lambda}^*, u^*, t) \leq H(\mathbf{x}^*, \boldsymbol{\lambda}^*, u, t) \quad (2.6)$$

A problem arises when the necessary condition for u in Eq. (2.3c) gives no new information on the optimal control law. This is commonly the case when control terms appear linearly in the Hamiltonian. Suppose the Hamiltonian has the structure

$$H = H_0(\mathbf{x}, \boldsymbol{\lambda}, t) + H_1(\mathbf{x}, \boldsymbol{\lambda}, t)u \quad (2.7)$$

where H_0 and H_1 terms depend only on states and costates. Taking the necessary condition Eq. (2.3c) eliminates u and provides no new information on the optimal control, since

$$\frac{\partial H}{\partial u} = H_1 \quad (2.8)$$

In the case where the control is bounded $|u| \leq 1$, PMP yields a solution commonly known as bang-bang/singular form.

$$u^* = \begin{cases} -1 & \text{if } H_1 > 0, \\ +1 & \text{if } H_1 < 0, \\ \text{indeterminate} & \text{if } H_1 = 0 \end{cases} \quad (2.9)$$

The first two cases of Eq. (2.9) represent a bang-bang solution with instantaneous switching of the control on its boundary due to changes in the sign of H_1 . The last case in Eq. (2.9) refers a singular control solution. PMP is not well-suited to solving problems of this type, as the control imparts no effect on the optimal control Hamiltonian (and therefore cost).

For a candidate singular control, an optimal singular arc may exist over time interval $t \in [t_1, t_2]$, $t_1 \neq t_2$ based on the vanishing of a switching function defined as

$$H_u = \frac{\partial H}{\partial u} = 0 \quad (2.10)$$

A time derivative of Eq. (2.10) can be taken as

$$\frac{d}{dt}H_u = \frac{\partial H_u}{\partial t} + \frac{\partial H_u}{\partial \mathbf{x}}\dot{\mathbf{x}} + \frac{\partial H_u}{\partial \boldsymbol{\lambda}}\dot{\boldsymbol{\lambda}} + \frac{\partial H_u}{\partial u}\dot{u} \quad (2.11)$$

where the last term vanishes. In some problems, when Eq. (2.10) holds the singular arc can be resolved from the Legendre-Clebsch generalized convexity condition [133]. Here, successive time derivatives of Eq. (2.3c) are taken and set equal to zero until the control appears explicitly

$$\frac{d^{2q}}{dt^{2q}} \left(\frac{\partial H}{\partial u} \right) = 0 \quad (2.12)$$

where the integer q is referred to as the *order* of the singular arc. The convexity condition on the singular arc is

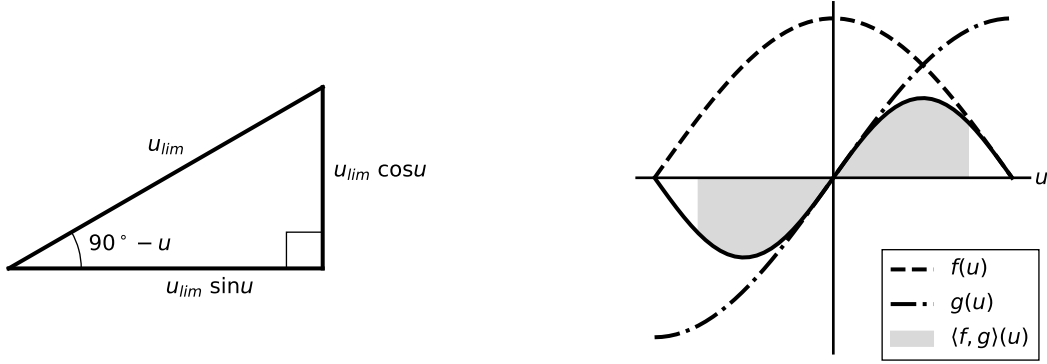
$$(-1)^q \frac{\partial}{\partial u} \left[\frac{d^{2q}}{dt^{2q}} \left(\frac{\partial H}{\partial u} \right) \right] \geq 0 \quad (2.13)$$

If conditions Eq. (2.12) and Eq. (2.13) hold simultaneously over a finite time interval $t \in [t_1, t_2]$, then the singular arc is optimal. Clearly, derivation of the singular control requires significant algebraic manipulation. For complex systems, this process can be cumbersome and may not immediately yield an optimal control law if the singular arc is of higher order.

The preceding discussion of traditional indirect methods serves to illustrate the challenges accompanying constraints in OCPs. Outside of simple intuitive problems, constructing the Hamiltonian BVP and identifying active constraint arcs may be infeasible or require significant trial-and-error. The benefit of regularization is to forgo this burdensome procedure through approximation. At the cost of a minor reduction in solution precision, this allows for a large-scale constrained OCP to be easily constructed and solved using numerical methods. Although the method does not introduce new opportunities for parallelization, solution of the regular problem is easier to construct and solve in serial computing paradigms.

2.3 Generalization of Bang-bang Optimal Control Regularization

A general, flexible approach is proposed for regularization OCP with bang-bang/singular form. This method, termed the generalized control regularization method (GCRM), allows for choice in regularizing functions while ensuring convergence through successive solutions of an auxiliary problem. The method replaces bounded control quantities with smoothing functions and augments a small error-control penalty term to the integral cost. Mall and Grant [97] find that



(a) Geometric orthogonality (reproduced from [138])

(b) Functional orthogonality

Figure 2.2: Illustration of orthogonality in geometric and functional spaces.

geometric orthogonality of sine and cosine terms produces smoothing behavior by avoiding instantaneous switching between bang arcs. This idea can be extended to *functional* orthogonality, where the integral product of the control and error-control terms produces optimal smoothing. This property couples the regularization terms in order to minimize the projected error due to approximation. These concepts are illustrated in Fig. 2.2. Existing methods use integral error terms to provide numerical stability. In this work, however, we carefully construct terms to also provide desirable analytics of the regularized OCP. As opposed to existing methods, the optimal control law is uniquely determined, enabling direct algebraic substitution into the Hamiltonian BVP to eliminate the control variable.

To begin, consider the simplest case of Eq. (2.2) with a single scalar control u appearing linearly. Without loss of generality, we assume the control magnitude is bounded to unity; we restrict our current case to a scalar unit control for simplicity and clarity of notation. We also consider the problem with no active path state constraints Eq. (2.1e). The Hamiltonian for this system takes the form in Eq. (2.14), where dependency of H_0 and H_1 on states and costates is implied.

$$H = H_0 + H_1 u, \quad |u| \leq 1 \quad (2.14)$$

The GCRM replaces all bounded control terms by a smooth, continuously differentiable function \tilde{u} . In addition, an integral error term \tilde{L} is appended to the running cost. A small parameter $\epsilon > 0$ is introduced as the regularization parameter. The desired behavior of ϵ is to converge to the optimal solution of Eq. (2.1a) with $\{\mathbf{x}, \tilde{u}\} \rightarrow \{\mathbf{x}^*, u^*\}$ in the limit as $\epsilon \rightarrow 0$. The regularized OCP is summarized as

$$\min_u \quad \tilde{J} = \phi(\mathbf{x}(t_f), t_f) + \int_{t_0}^{t_f} L(\mathbf{x}, \tilde{u}(u, \epsilon), t) + \tilde{L}(u, \epsilon) dt \quad (2.15a)$$

$$\text{Subject to: } \dot{\mathbf{x}} - \mathbf{f}(\mathbf{x}, \tilde{u}(u, \epsilon), t) = 0 \quad (2.15b)$$

$$\mathbf{x}(t_0) = \mathbf{x}_0 \quad (2.15c)$$

$$\psi(\mathbf{x}(t_f), t_f) = 0 \quad (2.15d)$$

with $\tilde{u} : \mathbb{R} \times \mathbb{R}_{>0} \rightarrow (-1, 1)$ and $\tilde{L} : \mathbb{R} \times \mathbb{R}_{>0} \rightarrow [0, \infty)$ providing regularization over the control variable u . We assume the terminal cost and boundary conditions do not depend on the control.

The regularized Hamiltonian \tilde{H} is expressed as

$$\tilde{H} = H_0 + H_1 \tilde{u} + \tilde{L} \quad (2.16)$$

We now establish a relationship between the regularizing functions \tilde{u} and \tilde{L} . First, note that in order to provide the required bounding behavior on the effective control, we require $|\tilde{u}| \leq 1$. Application of the necessary condition Eq. (2.3c) to Eq. (2.16) yields

$$\frac{\partial \tilde{H}}{\partial u} = H_1 \frac{\partial \tilde{u}}{\partial u} + \frac{\partial \tilde{L}}{\partial u} = 0 \quad (2.17)$$

A key component of the GCRM is the construction of the integral error term to provide useful properties of the resulting optimal control law. Suppose \tilde{L} is defined relative to the control regularization function \tilde{u} as

$$\tilde{L}(u, \epsilon) = \int_0^u \xi \left[\frac{\partial \tilde{u}(\xi, \epsilon)}{\partial \xi} \right] d\xi \quad (2.18)$$

where ξ is a placeholder variable of integration. Using integration by parts gives a simpler expression

$$\tilde{L} = u\tilde{u} - \int \tilde{u} du + C_0 \quad (2.19)$$

where C_0 is an integration constant. This integration constant will be found later by enforcing the constraint

$$\tilde{L}(0, \epsilon) = 0 \quad (2.20)$$

which must hold for any $\epsilon > 0$. In tandem with the following restrictions on \tilde{u} , this definition ensures \tilde{L} will always introduce a positive-definite running cost. This behavior plays an important role in convergence behavior of the auxiliary problem. Substituting Eq. (2.18) into the necessary condition Eq. (2.17) gives

$$\frac{\partial \tilde{H}}{\partial u} = (H_1 + u) \frac{\partial \tilde{u}}{\partial u} = 0 \quad (2.21)$$

We enforce the additional requirement that \tilde{u} be strictly increasing over u such that $\partial \tilde{u} / \partial u > 0$. As a result, the trailing term in Eq. (2.21) is always positive. This resolves the necessary condition for u with the remarkably simple optimal control law

$$u^* = -H_1(\mathbf{x}^*, \boldsymbol{\lambda}^*, t) \quad (2.22)$$

Orthogonality of the control and error-control terms has been shown to produce optimal smoothing by minimizing the projection of errors due to regularization [95,97]. This property is expressed in functional form by the integral product

$$\langle \tilde{u}, \tilde{L} \rangle = \int_{-c}^c \tilde{u} \tilde{L} du = 0 \quad (2.23)$$

where c is an arbitrary constant. Orthogonality is ensured through proper choice of regularization function pairs in the following section.

For perspective, it is helpful to compare the control law Eq. (2.22) to the optimal control established by PMP in Eq. (2.9). Point-wise application of PMP produces three possible branches depending on the sign of the switching function H_1 . In contrast, the GCRM approach reduces the number of branches to one. Thus, the primary feature of the modified error-control approach is to smoothly approximate the signum operator on bang arcs. The on-off behavior of bang-bang solution arcs can introduce errors in variable step size numerical integrators, which is alleviated in the auxiliary problem. No distinction need be made for singular arcs. The method is capable

of resolving singular arcs through selection of an appropriate control regularization function \tilde{u} and corresponding error-control term \tilde{L} giving the unique control law in Eq. (2.22).

Before proceeding, it is helpful to outline the assumptions required of the new approach. First, the system must be cast in bang-bang/singular form for the control law in Eq. (2.22) to apply. This requires affine control in Eq. (2.1b), although the dynamics may remain nonlinear in the system states. The integral cost term in Eq. (2.1a), if present, must also contain control terms appearing linearly. Second, the admissible control must be bounded within a compact set. We restrict our case to constant upper and lower control bounds, though other approaches may enable state-dependent bounds [139]. Finally, as presented, the regularization method is designed for a scalar, single-input system. However, the method is easily generalizable to multiple-input systems. Application with multiple control variables is demonstrated in the examples to follow.

2.3.1 Regularization Using Control Sigmoid Functions

A candidate control \tilde{u} must be developed in order to apply the regularization procedure. The previously stated requirements are 1) \tilde{u} be bounded to unity and 2) \tilde{u} be a strictly increasing function. These together point towards generalized *sigmoid* functions, which are smooth approximations of the signum operator. The following example illustrates the regularization procedure for the arctangent function.

To begin, define the control mapping

$$\tilde{u} = \arctan\left(\frac{u}{\epsilon}\right) \frac{2}{\pi} \quad (2.24)$$

where a scaling factor $2/\pi$ is introduced such that $\tilde{u} \in (-1, 1)$. The regularization parameter ϵ is included in a manner ensuring u and ϵ remain dimensionally consistent, which can be important in BVP solvers performing distance and time scale normalization. Using Eq. (2.19), the error term

\tilde{L} corresponding to the arctangent regularization function is

$$\begin{aligned}
\tilde{L} &= u\tilde{u} - \int \tilde{u} du + C_0 \\
&= u \arctan\left(\frac{u}{\epsilon}\right) \frac{2}{\pi} - \frac{2}{\pi} \int \arctan\left(\frac{u}{\epsilon}\right) du + C_0 \\
&= u \arctan\left(\frac{u}{\epsilon}\right) \frac{2}{\pi} - \frac{2}{\pi} \left(-\frac{1}{2}\epsilon \log(\epsilon^2 + u^2) + u \arctan\left(\frac{u}{\epsilon}\right) \right) + C_0 \\
&= \epsilon \log(\epsilon^2 + u^2) \frac{1}{\pi} + C_0
\end{aligned} \tag{2.25}$$

The integration constant is found from Eq. (2.20) as

$$C_0 = -\epsilon \log(\epsilon^2) \frac{1}{\pi} \tag{2.26}$$

giving the arctangent regularization error-control term

$$\tilde{L} = \epsilon \log\left(1 + \frac{u^2}{\epsilon^2}\right) \frac{1}{\pi} \tag{2.27}$$

The Hamiltonian of the smoothed problem then has the form

$$\tilde{H} = H_0 + H_1 \arctan\left(\frac{u}{\epsilon}\right) \frac{2}{\pi} + \epsilon \log\left(1 + \frac{u^2}{\epsilon^2}\right) \frac{1}{\pi} \tag{2.28}$$

The optimal control law can be verified by substituting Eq. (2.28) into Eq. (2.17).

$$\frac{\partial \tilde{H}}{\partial u} = \frac{2}{\pi} \frac{\epsilon}{u^2 + \epsilon^2} (H_1 + u) = 0 \tag{2.29}$$

It is easy to verify the following limit behavior of the leading term in Eq. (2.29)

$$\lim_{u \rightarrow 0} \left(\frac{\epsilon}{u^2 + \epsilon^2} \right) = \frac{1}{\epsilon}, \quad \lim_{\epsilon \rightarrow 0} \left(\frac{\epsilon}{u^2 + \epsilon^2} \right) = 0 \tag{2.30}$$

Therefore, the leading term non-zero for $u \in \mathbb{R}$ given $\epsilon > 0$. Note that u is now an unconstrained quantity in optimization and is no longer restricted to $|u| \leq 1$. The regularization parameter ϵ can become arbitrarily small, but not precisely zero as this will produce an indeterminate case when $u = 0$. Given these properties, the leading terms in Eq. (2.3) can be dropped, verifying the optimal control law of Eq. (2.22). The arctangent regularization function slope is illustrated in Fig. 2.3 for a range of values of the regularization parameter ϵ . As ϵ approaches small values, the slope of

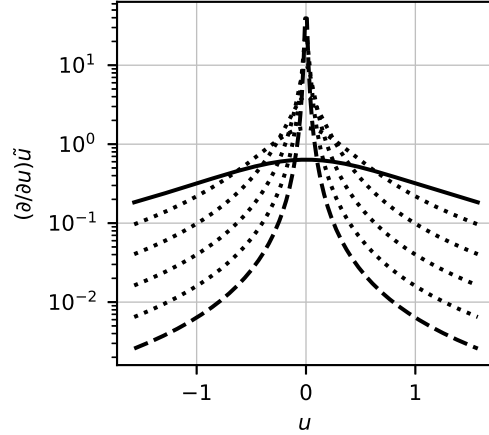


Figure 2.3: Arctangent regularization function derivatives for $\epsilon = 1$ (solid line) to $\epsilon = 0.01$ (dashed line).

the regularization function sees a sharp peak at $u = 0$. This behavior reflects an approximation of bang-bang switch points. However, because the function is smooth and continuous, this switch behavior is continuously differentiable, making it more amenable to variable step size numerical integrators. We note that H_1 is no longer a switching function because the auxiliary problem is regular. However, the solution behavior of H_1 in the regularized problem will reflect that of the true switching function as $\epsilon \rightarrow 0$. This convergence behavior is verified in the following sections.

The formulation of the GCRM leaves flexibility in choice of sigmoid functions. Using a process similar to the arctangent function, control and error-control terms for several sigmoid functions are developed in Table 2.1. Each control smoothing term is scaled to provide unit bounds on \tilde{u} . An associated error-control term \tilde{L} is derived based on definitions in Eq. (2.19) and Eq. (2.20). For problems with Hamiltonian structure in Eq. (2.14), these function pairs will always produce a unique control law Eq. (2.22) when substituted into the necessary conditions in Eq. (2.3c). Optimization can then be performed over the control variable u in an unconstrained manner, since the response is inherently bounded. This smoothing effect enforces the upper and lower bounds in bang-bang problems. The regularization parameter ϵ provides numerical stability during solution of the auxiliary problem. The solution procedure typically begins with larger values of $\epsilon \geq 1$. Suc-

Table 2.1: Normalized regularization functions and error-control terms for $|u| \leq 1$.

Method	Regularization function	Error-control term
Arctangent	$\arctan\left(\frac{u}{\epsilon}\right) \frac{2}{\pi}$	$\epsilon \log\left(1 + \frac{u^2}{\epsilon^2}\right) \frac{1}{\pi}$
Error function	$\operatorname{erf}\left(\frac{u}{\epsilon}\right)$	$\epsilon \left(1 - \exp\left(-\frac{u^2}{\epsilon^2}\right)\right) \frac{1}{\sqrt{\pi}}$
Hyperbolic tangent	$\tanh\left(\frac{u}{\epsilon}\right)$	$u \tanh\left(\frac{u}{\epsilon}\right) - \epsilon \log\left(\cosh\left(\frac{u}{\epsilon}\right)\right)$
Logistic	$2\left(1 + \exp\left(-\frac{u}{\epsilon}\right)\right)^{-1} - 1$	$-2\epsilon \log\left(\frac{1}{2}\left(1 + \exp\left(-\frac{u}{\epsilon}\right)\right)\right)$ $+ 2u \left(\left(1 + \exp\left(-\frac{u}{\epsilon}\right)\right)^{-1} - 1\right)$
Algebraic	$\left(\frac{u}{\epsilon}\right) \left(1 + \left(\frac{u^2}{\epsilon^2}\right)\right)^{-\frac{1}{2}}$	$\epsilon \left(1 - \left(1 + \left(\frac{u^2}{\epsilon^2}\right)\right)^{-\frac{1}{2}}\right)$
Einstein function	$1 - 2 \frac{1 + \left(\frac{u}{\epsilon} - 1\right) \exp\left(\frac{u}{\epsilon}\right)}{\left(\exp\left(\frac{u}{\epsilon}\right) - 1\right)^2}$	$2\epsilon \left(1 - \left(\frac{u}{\epsilon}\right)^2 \frac{\exp\left(\frac{u}{\epsilon}\right)}{\left(\exp\left(\frac{u}{\epsilon}\right) - 1\right)^2}\right)$

cessive solutions are then obtained using a numerical continuation procedure with decreasing values of ϵ , where the previous solution is used as an initial guess for the current BVP solver iteration.

The shape of each control and error-control function pair in Table 2.1 is illustrated in Fig. 2.4. Trends are plotted versus the control variable u over a range of ϵ values. The smoothing effect in \tilde{u} is apparent beginning at an ϵ of 1. The functions remain upper and lower bounded to unity, but require larger absolute values of u to approach these bounds. This amplifies the smoothing effect in the OCP mapping, which has the benefit of reducing sensitivity to errors in the initial solution guess. Once a solution to this initial Hamiltonian BVP is found, reducing the ϵ parameter forces the \tilde{u} response closer to the signum function. This emulates the on-off behavior of bang-bang controls for relatively small changes in u . Trends in the \tilde{L} response also illustrate positive-definiteness of the error-control terms. This avoids adding a non-zero path cost penalty, which would otherwise impose an artificial time-minimization objective that may not be present in the original OCP.

Each function pair in Table 2.1 satisfies the orthogonality condition in Eq. (2.23), ensuring convergence to the original OCP as ϵ approaches zero. This property is illustrated by comparing the smoothed Hamiltonian to its expected output prior to regularization. We consider the case $H = 0$ and therefore $H_0 = -H_1$ in Eq. (2.14). The smoothed Hamiltonian is then computed over a range of ϵ values. Figure 2.5 shows the convergence qualities of each regularization function in Table 2.1. It is immediately clear that each function trends uniformly to the expected Hamiltonian

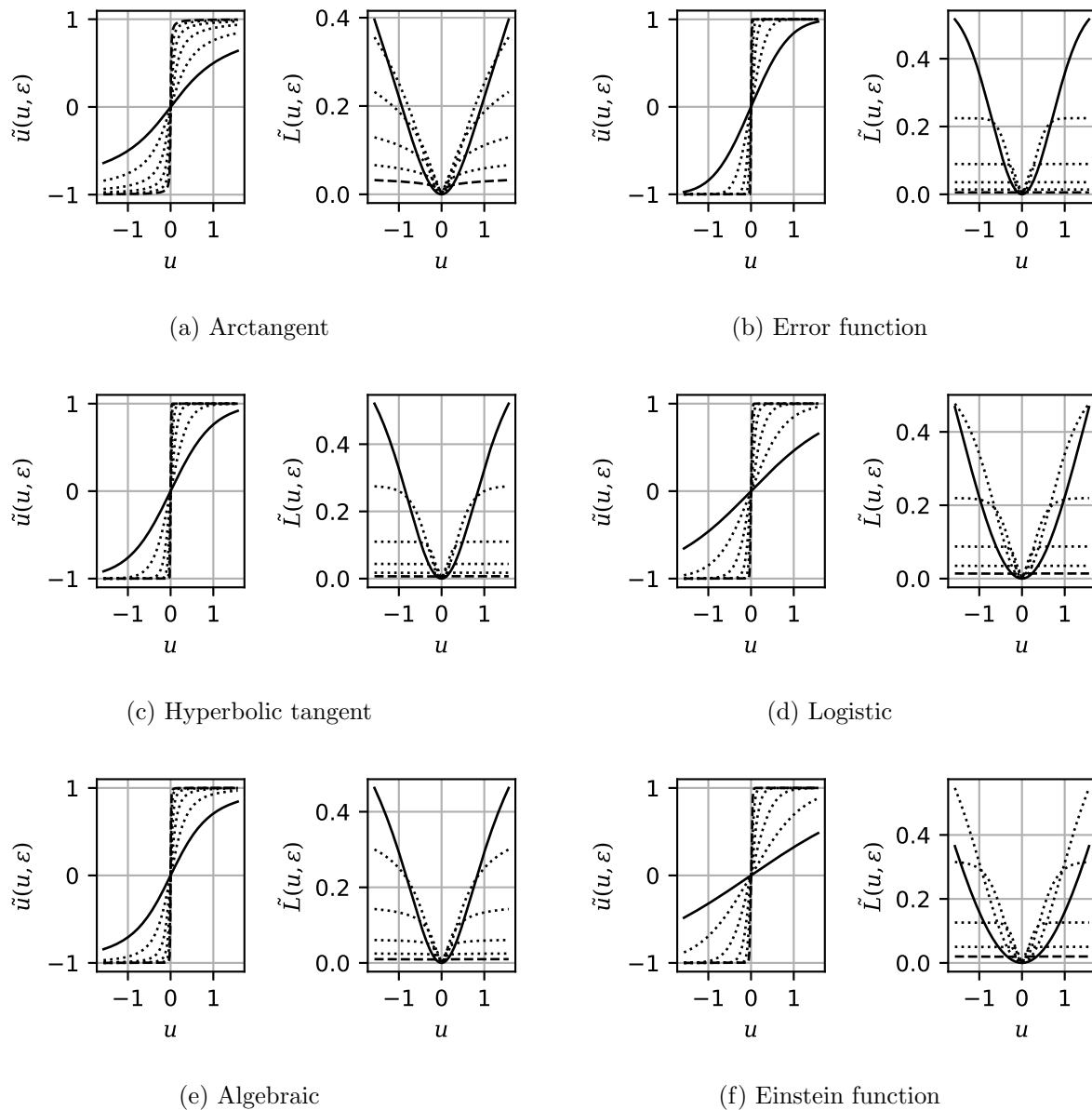


Figure 2.4: Control and error-control regularizing functions for $\epsilon = 1$ (solid line) to $\epsilon = 0.01$ (dashed line).

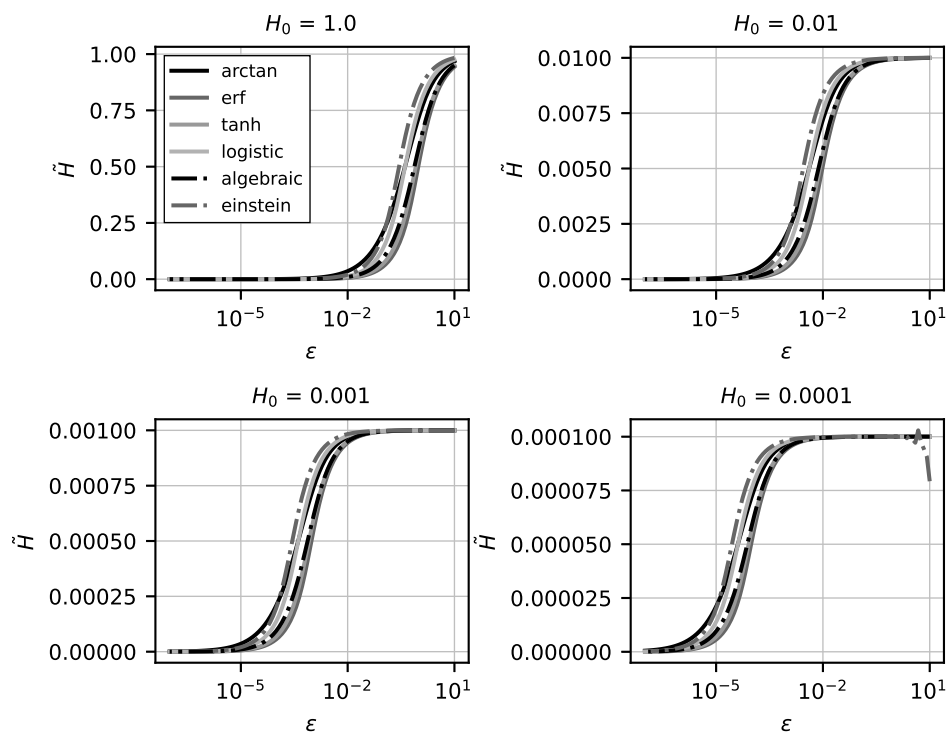


Figure 2.5: Convergence of smoothed optimal control Hamiltonian over regularization.

value of zero for decreasing values of the regularization parameter. The Hamiltonian is monotonic in its convergence with respect to ϵ , though it is interesting to note that the rate of convergence differs for each basis function. For example, the arctangent function rapidly attenuates smoothing errors at higher ϵ values, but for $\epsilon \leq 10^{-1}$ the arctangent shows the slowest rate of convergence. The hyperbolic tangent appears to provide the lowest approximation errors in comparison, but this may come at the cost of smaller step size requirements over the continuation interval for ϵ . The Einstein function shows numerical instability for decreasing values of H_1 . This behavior is attributed to the fact that the regularization function in Table 2.1 produces 0/0 behavior in the limit as $u \rightarrow 0$. This limit exists in theory, but poses numerical anomalies that should be avoided in optimization. Thus, each function introduces differing numerical behavior that may prove advantageous or disadvantageous depending on the problem complexity.

The benefits of the new approach are apparent when compared to existing work. Previous optimal control regularization studies have proposed smoothing functions resulting in ambiguous or implicit control laws [94,99,136]. This adds an additional layer of complexity, as further analysis is required to construct the Hamiltonian BVP. With multiple roots of Eq. (2.3c), PMP may be able to distinguish the optimal control. However, multiple control variables require point-wise evaluation of PMP along the trajectory for each permutation of potential control solutions. For example, the UTM [99] produces two control laws for each variable appearing linearly in the Hamiltonian, necessitating application of PMP at each time step for updated values of the adjoint system variables. See Fig. 2.6. This adds numerical overhead and eliminates the analytical form of the control law. Similarly, if a control law is defined implicitly, a numerical root-finding algorithm must be employed at each time step to determine the control, which can be numerically burdensome. If multiple roots for u exist, optimality and convergence may not always be guaranteed. In contrast, the GCRM control law is always unique, allowing for direct algebraic substitution into the Hamiltonian BVP to eliminate the control variables. See Fig. 2.7. This effectively transforms the control-constrained problem to an unconstrained problem, allowing direct elimination of all control variables. Appendix A gives a further comparison between the UTM and GCRM control laws. OCPs involving

multiple control variables in bang-bang/singular form may benefit greatly from disambiguation of the optimal control law using the GCRM.

2.3.2 Accommodating Arbitrary Control Bounds

Many practical problems impose asymmetric upper and lower bounds on the control, whereas the preceding developments assume a control bound of unity. There is no loss of generality in this assumption, as bounds on u can be absorbed into H_0 and H_1 terms in the Hamiltonian Eq. (2.14). However, it is helpful to provide a form of the \tilde{u} and \tilde{L} functions that can directly accommodate arbitrary control bounds without performing further analysis into the Hamiltonian structure. This can be accomplished by defining scaling and offset constants in the control [99]. To this end, we modify the control mapping function as follows. Define the scaled control mapping \tilde{u}' as

$$\tilde{u}' = c_1 \tilde{u} + c_0 \quad (2.31)$$

where c_0 and c_1 are constants defined relative to the upper and lower bounds on the control. For the case when $u \in [u_{\min}, u_{\max}]$, these constants are computed as

$$c_0 = \frac{(u_{\max} + u_{\min})}{2}, \quad c_1 = \frac{(u_{\max} - u_{\min})}{2} \quad (2.32)$$

A further step is also taken due to the definition of \tilde{L} in Eq. (2.18). Since the scaling constant c_1 directly multiplies the control, it must also appear in the error-control term to maintain dimensional consistency. The scaled error-control term \tilde{L}' is simply

$$\tilde{L}' = c_1 \tilde{L} \quad (2.33)$$

The scaled problem can be related to the unscaled problem as

$$\begin{aligned} \tilde{H}' &= H_0 + H_1 \tilde{u}' + \tilde{L}' \\ &= H_0 + H_1 (c_1 \tilde{u} + c_0) + c_1 \tilde{L} \\ &= H_0 + H_1 c_0 + (\tilde{H} - H_0) c_1 \end{aligned} \quad (2.34)$$

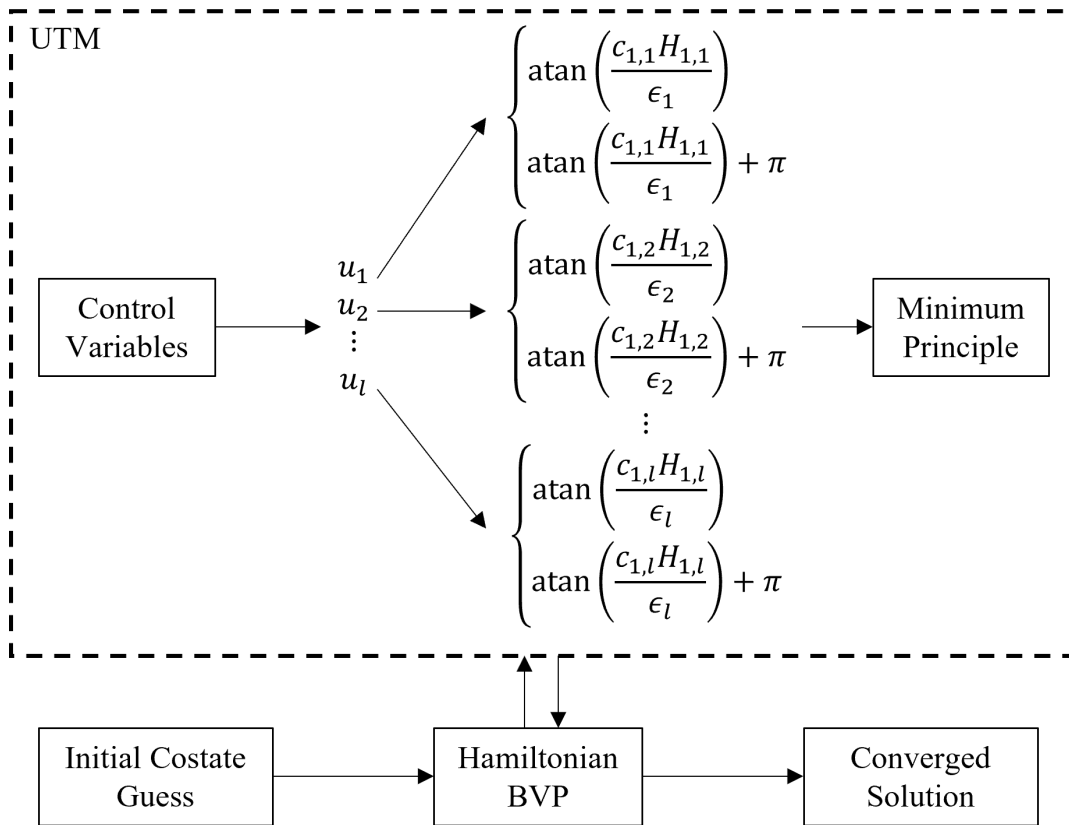


Figure 2.6: Structure of UTM optimal control law.

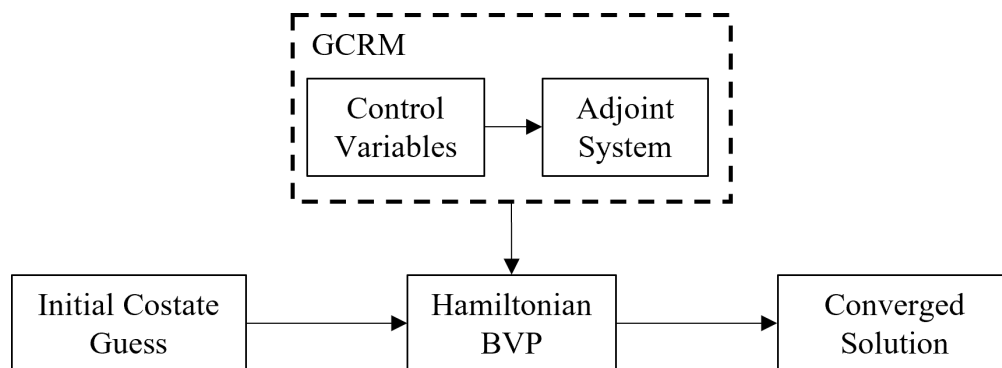


Figure 2.7: Structure of GCRM optimal control law.

where \tilde{H} is the unscaled regularized Hamiltonian. It is easy to see that when $u_{\max} = -u_{\min} = 1$, $c_0 = 0$ and $c_1 = 1$, giving $\tilde{H}' = \tilde{H}$.

The scaling constants enable application of GCRM to problems with arbitrary upper and lower control bounds. The scaled expressions also allow direct substitution into existing problems without consulting the Hamiltonian structure. One final point is made regarding the units of the regularization parameter ϵ . Noting the definition of the scaling constants in Eq. (2.32) and the error-control terms in Table 2.1, the units of ϵ can be inferred as units of the path cost L divided by units of the control bound c_1 . BVP solvers performing distance and time scale normalization should use these units for ϵ to ensure proper dimensional scaling.

Given the regularization function pairs in Table 2.1, application of the GCRM to problems in bang-bang/singular form is straightforward. This can be achieved through substitution of control terms with a chosen control smoothing function and error-control penalty term. The resulting control law can then be substituted to produce a well-defined Hamiltonian BVP as a function of states and costates only. The following examples serve to illustrate the procedure on simple problems. These problems are chosen to allow for analysis using traditional methods prior to numerical solution using control regularization.

2.3.3 Example: Van der Pol Oscillator

A well-known classical problem in optimal control is the Van der Pol Oscillator. Several variants of this problem have been studied in the literature, including minimum-time (James [140], Maurer [141]) and minimum damping (Vossen [142]) objectives. The former has been proven to contain no singular arcs, whereas the latter is known to have bang-singular form.

The GCRM is first applied to the minimum-time Van der Pol to illustrate the regularization procedure for a bang-bang problem. Prior numerical studies of this problem [143] give insight on

the optimal solution structure. Consider the following objective and state equations.

$$J = t_f, \quad t_f \text{ free} \quad (2.35)$$

$$\dot{x}_1 = x_2, \quad \dot{x}_2 = -x_1 + x_2(1 - x_1^2) + u \quad (2.36)$$

with initial conditions $x_1(0) = x_2(0) = 1$. The stop conditions are enforced by a terminal state constraint of the form

$$x_1(t_f)^2 + x_2(t_f)^2 = r^2, \quad r = 0.2 \quad (2.37)$$

The control is bounded to $|u| \leq 1$. The Hamiltonian for this problem is constructed as

$$H = \lambda_1 x_2 + \lambda_2 (-x_1 + x_2(1 - x_1^2) + u) \quad (2.38)$$

The costate dynamics are derived from Eq. (2.3a) as

$$\dot{\lambda}_1 = -\frac{\partial H}{\partial x_1} = \lambda_2(1 + 2x_1x_2) \quad (2.39a)$$

$$\dot{\lambda}_2 = -\frac{\partial H}{\partial x_2} = -\lambda_1 - \lambda_2(1 - x_1^2) \quad (2.39b)$$

The terminal state constraint Eq. (2.37) is adjoined with a Lagrange multiplier ν_f . The augmented terminal function is

$$\Phi(\mathbf{x}(t_f), t_f) = t_f + \nu_f (x_1(t_f)^2 + x_2(t_f)^2 - r^2) \quad (2.40)$$

leading to boundary conditions on the costates of $\lambda_1(t_f) = 2\nu_f x_1(t_f)$ and $\lambda_2(t_f) = 2\nu_f x_2(t_f)$.

Applying the necessary condition for u gives

$$\frac{\partial H}{\partial u} = \lambda_2 \quad (2.41)$$

Since the control u appears linearly in the Hamiltonian Eq. (2.38), the solution is expected to have bang-bang/singular form.

It is easy to show by contradiction that a singular arc is not optimal in this problem. Suppose a singular arc exists over some time interval $t \in [t_1, t_2]$ with $t_2 > t_1$. Then $\lambda_2 = \dot{\lambda}_2 = 0$ on this interval. Substituting into Eq. (2.39b) gives $\lambda_1 = 0$. The Hamiltonian on the singular arc is then $H = 0$. Since H does not depend explicitly on time, we also have $\dot{H} = 0$. However, the

transversality conditions Eq. (2.5) with Eq. (2.40) indicate that $H(t_f) = -1$. This contradicts the original assumption that an optimal singular arcs exists. Therefore the solution has the bang-bang structure in Eq. (2.42).

$$u^* = \begin{cases} -1 & \text{if } \lambda_2 > 0 \\ +1 & \text{if } \lambda_2 < 0 \end{cases} \quad (2.42)$$

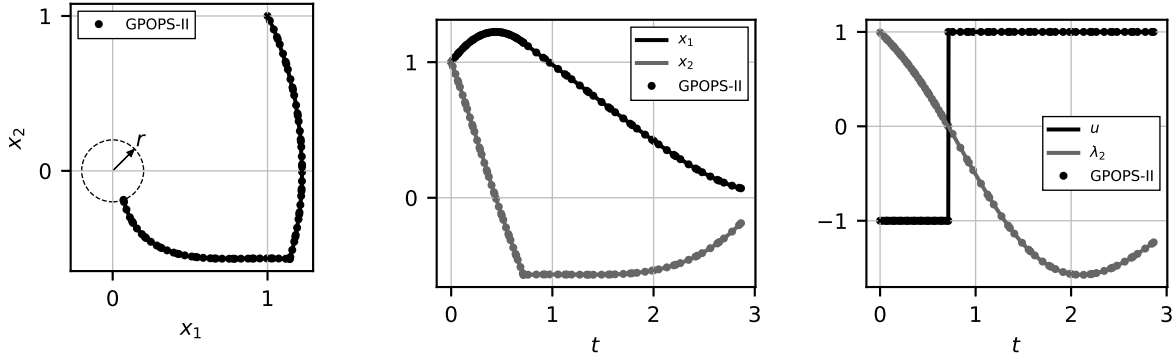
Even for simple problems such as the Van der Pol oscillator, traditional indirect methods require significant analysis to understand the solution form. This analysis may differ based on the specific problem structure. Moreover, the number and order of bang arcs may not be known prior to numerical solution. In contrast, the GCRM solves the problem in a much simpler manner. The arctangent regularization method is applied to the time-optimal Van der Pol problem as follows. Control terms u are replaced by the smoothing function Eq. (2.24) and the error control term Eq. (2.27) is augmented to the running cost. The regularized problem is summarized as

$$J = t_f + \int_0^{t_f} \epsilon \log \left(1 + \frac{u^2}{\epsilon^2} \right) \frac{1}{\pi} dt, \quad t_f \text{ free} \quad (2.43)$$

$$\dot{x}_1 = x_2, \quad \dot{x}_2 = -x_1 + x_2 (1 - x_1^2) + \arctan \left(\frac{u}{\epsilon} \right) \frac{2}{\pi} \quad (2.44)$$

with the preceding initial conditions and terminal state constraint. The scaled arctangent operation implicitly bounds the control response to unit values, allowing optimization for u to be performed in an unconstrained manner. The integral path cost ensures numerical stability while producing the unique optimal control law $u^* = -\lambda_2$.

To solve the regularized problem, a numerical continuation procedure is performed on ϵ , starting at a value of 10 and ending on a value of 10^{-6} . A bisection method is used over the continuation interval with equally spaced points on a logarithmic scale. Figure 2.8 shows results for the minimum-time Van der Pol problem using the arctangent regularization method. Figure 2.8a shows a phase portrait of x_1 and x_2 along with a depiction of the radially bounded terminal state constraint Eq. (2.37). The state response in Fig. 2.8b sees a sharp bend corresponding to the bang arc switching from -1 to 1. This bend remains continuous over ϵ due to the regularization smoothing effect. Figure 2.8c shows the control and switching function time history. A single switch



(a) Phase space and terminal constraint

(b) State history

(c) Control and switching function

Figure 2.8: Minimum-time Van der Pol solution with GCRM arctangent regularization.

is determined to take place at 0.7139 seconds with a final time of 2.8641 seconds. Numerical studies by Maurer [143] for the time-optimal Van der Pol problem confirm these values, as well as the overall solution structure consisting of two bang arcs. The GCRM approximates the expected bang-bang control well, with a rapid transition between the upper and lower bounds on u . This behavior is important in order to correctly solve for bang arcs without degrading the overall predicted cost due to approximation.

The GCRM provides a straightforward solution methodology by slight modification of the problem structure. The solution is obtained without ambiguity in the control law, and application of PMP is not required. The current example serves to illustrate the application of GCRM to problems in bang-bang form. The following example concerns problems involving singular arcs, which require additional analysis using traditional methods.

2.3.4 Example: Sounding Rocket

A common case of the Hamiltonian structure in Eq. (2.14) is a singular arc. This occurs when the switching function is zero over a finite time interval, and the control imparts no effect on the Hamiltonian. The GCRM can easily solve such problems through regularization of the singular control. Consider the sounding rocket problem [144] consisting of vertical flight through a uniform

density field. The objective is to determine the thrust u to maximize the final altitude $z(t_f)$ subject to the differential equation

$$\frac{d^2z}{dt^2} + k \left(\frac{dz}{dt} \right)^2 + g = u \quad (2.45)$$

with $z(0) = 0$. The control thrust is limited to $0 \leq u \leq B$. The endpoint is defined implicitly by the isoperimetric constraint

$$\int_0^{t_f} u dt = b \quad (2.46)$$

which can be interpreted as an energy (or fuel) constraint on the total impulse. The system is cast into OCP form Eq. (2.1a) by augmenting an auxiliary state x_3 to track the integrated control effort in Eq. (2.46). The problem is summarized as

$$J = -x_1(t_f), \quad t_f \text{ free} \quad (2.47)$$

$$\dot{x}_1 = x_2, \quad \dot{x}_2 = -kx_2^2 - g + u, \quad \dot{x}_3 = u \quad (2.48)$$

with the required boundary conditions $x_1(0) = x_2(0) = x_3(0) = 0$ and $x_3(t_f) = b$. The augmented terminal function Eq. (2.4) can be written as

$$\Phi(\mathbf{x}(t_f), t_f) = -x_1(t_f) + \nu_f(x_3(t_f) - b) \quad (2.49)$$

where incorporation of the terminal state constraint with Lagrange multiplier ν_f ensures exact satisfaction of the energy constraint in Eq. (2.46).

We first consider a solution to this problem using the traditional indirect methods approach. The Hamiltonian for this system is constructed as

$$H = \lambda_1 x_2 + \lambda_2 (-kx_2^2 - g + u) + \lambda_3 u \quad (2.50)$$

The costate rates are derived from Eq. (2.3a) as

$$\dot{\lambda}_1 = -\frac{\partial H}{\partial x_1} = 0 \quad (2.51a)$$

$$\dot{\lambda}_2 = -\frac{\partial H}{\partial x_2} = -\lambda_1 + 2k\lambda_2 x_2 \quad (2.51b)$$

$$\dot{\lambda}_3 = -\frac{\partial H}{\partial x_3} = 0 \quad (2.51c)$$

with corresponding boundary conditions $\lambda_1(t_f) = -1$, $\lambda_2(t_f) = 0$, and $\lambda_3(t_f) = \nu_f$ from Eq. (2.3d) and Eq. (2.49). Given the costate rates in Eq. (2.51a) and Eq. (2.51c), the boundary conditions imply constant values $\lambda_1 = -1$ and $\lambda_3 = \nu_f$. Application of the necessary condition for u gives

$$\frac{\partial H}{\partial u} = \lambda_2 + \lambda_3 = 0 \quad (2.52)$$

Since u is eliminated from this expression, the problem is bang-bang/singular. This example does allow for singular arcs, which can be shown using the generalized convexity condition Eq. (2.13).

Define the shorthand notation $H_u := \partial H / \partial u$. Taking the time derivative of Eq. (2.52) gives

$$\begin{aligned} \frac{d}{dt}(H_u) &= \dot{\lambda}_2 + \dot{\lambda}_3 \\ &= -\lambda_1 + 2k\lambda_2 x_2 = 0 \end{aligned} \quad (2.53)$$

Together with the expression for λ_1 this implies

$$\lambda_2 = -\frac{1}{2kx_2} \quad (2.54)$$

Taking a second time derivative of Eq. (2.52) gives

$$\frac{d^2}{dt^2}(H_u) = 2k\lambda_2(-kx_2^2 - g + u) = 0 \quad (2.55)$$

where we leverage the fact that $\dot{\lambda}_1 = 0$ and $\dot{\lambda}_2 = 0$ on the singular arc. Equation (2.55) gives the singular control law

$$u^* = kx_2^2 + g \quad (2.56)$$

When considered in the context of the x_2 dynamics, this implies $\dot{x}_2 = 0$. Thus, the singular arc is a constant-velocity manifold that balances the control thrust with drag and gravity terms. The Legendre-Clebsch generalized convexity condition Eq. (2.13) is

$$(-1) \frac{\partial}{\partial u} \left[\frac{d^2}{dt^2}(H_u) \right] = -2k\lambda_2 = \frac{1}{x_2} \geq 0 \quad (2.57)$$

which must hold since $x_2 > 0$. One further insight can be made by noting that, on the singular arc, the Hamiltonian Eq. (2.50) with control law Eq. (2.56) is

$$H = -x_2 + \lambda_3(g + kx_2^2) = 0 \quad (2.58)$$

which, in tandem with Eq. (2.52) and Eq. (2.54), gives a value for the velocity on the singular arc of $x_2 = \sqrt{g/k}$. Substituting into Eq. (2.56) results in a simplified expression $u^* = 2g$ for the optimal singular control.

The approach using traditional indirect methods shows that, although solutions exist on singular arcs, the requisite analysis can become cumbersome. The sounding rocket example has a singular arc with order $q = 1$, but other problems may require further successive time derivatives of H_u to resolve the control. This process may be intractable with large-scale, complex optimization problems with multiple state and control variables. In comparison, the GCRM can resolve the bang-bang/singular arcs in the sounding rocket problem with relative ease. The error function regularization method is implemented using the \tilde{u} and \tilde{L} definitions in Table 2.1. Since the control bounds are asymmetric, we use the scaling constants $c_0 = c_1 = B/2$ in Eq. (2.32). The regularized problem is summarized as

$$J = -x_1(t_f) + \int_0^{t_f} \epsilon \frac{B}{2} \left(1 - \exp\left(\frac{u^2}{\epsilon^2}\right) \right) \frac{1}{\sqrt{\pi}} dt, \quad t_f \text{ free} \quad (2.59)$$

$$\dot{x}_1 = x_2, \quad \dot{x}_2 = -kx_2^2 - g + \frac{B}{2} \left(\operatorname{erf}\left(\frac{u}{\epsilon}\right) + 1 \right), \quad \dot{x}_3 = \frac{B}{2} \left(\operatorname{erf}\left(\frac{u}{\epsilon}\right) + 1 \right) \quad (2.60)$$

where optimization is performed over the control variable u . The previous initial conditions and terminal state constraint remain in effect. Forming the regularized optimal control Hamiltonian and applying the necessary condition Eq. (2.3c) gives $u^* = -\lambda_2 - \lambda_3$. Note that this control law is globally valid and no distinction need be made over bang-bang versus singular arcs.

Table 2.2: Parameters used in the sounding rocket example.

Parameter	g	k	b	B
Value	9.81 m/s ²	0.002 m ⁻¹	350 m/s	4g

Constants used in this problem are given in Table 2.2. These parameters are chosen to illustrate the solution form and are not necessarily representative of any physical system. A two-step numerical continuation procedure is performed. First, the value for b is set to 10 m/s, and a continuation step is performed to reach its final value of 350 m/s. Since the b parameter dictates

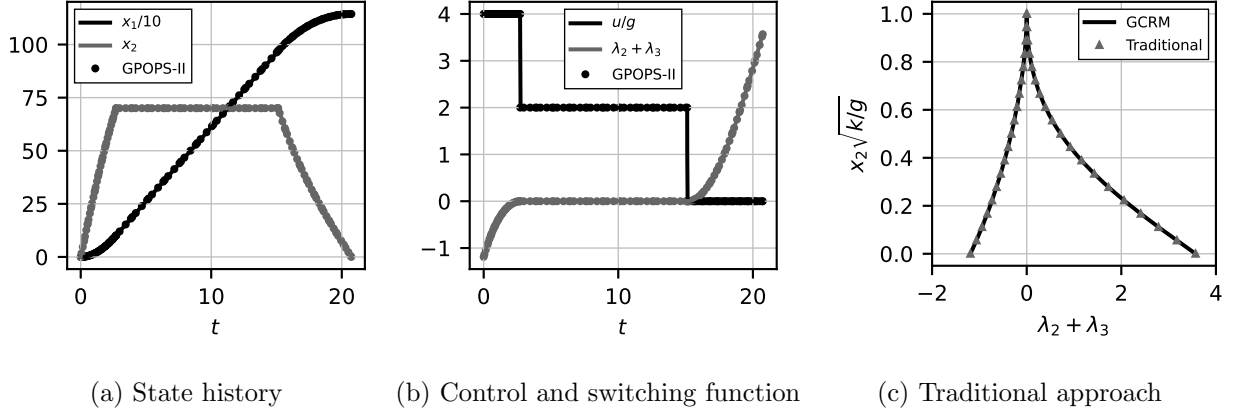


Figure 2.9: Solution to sounding rocket example using GCRM error function.

the stop conditions of the problem in Eq. (2.46), smaller values correspond to shorter trajectories, allowing for convergence to an initial feasible solution from a rough initial costate guess. The second continuation step is performed on the regularization parameter ϵ , starting with a value of 10^0 and ending at 10^{-7} . The computed cost of the final converged trajectory is -1143.84 m. This cost corresponds to the negative of the maximum altitude achieved. The control solution structure is bang-singular-bang, with computed switch times t_1 of 2.726 and t_2 of 15.114 seconds.

Figure 2.9 illustrates the state and control histories. The x_1 coordinate is divided by a factor of 10 for plotting purposes. Figure 2.9a shows the state histories. The singular arc is evident at a velocity of $x_2 = \sqrt{g/k}$. The auxiliary state x_3 is excluded from these plots, but it is found by inspection that the boundary condition $x_3(t_f) = b$ is exactly met. The altitude ramps up linearly over the singular arc, which is expected because the velocity remains constant. Figure 2.9b shows the control and switching function defined by Eq. (2.52). The bang arcs are well-approximated by the regularization procedure, as well as the singular arc which verifies the singular control law $u^* = 2g$. A further relationship can be found between x_2 and the switching function $\lambda_2 + \lambda_3$ by noting $H = 0$ and using the control law from PMP. Using this result, a comparison of the regularized problem to traditional methods is given in Fig. 2.9c. The expected trend is closely followed by the GCRM, indicating that the regularization procedure maintains conditions for optimality in the

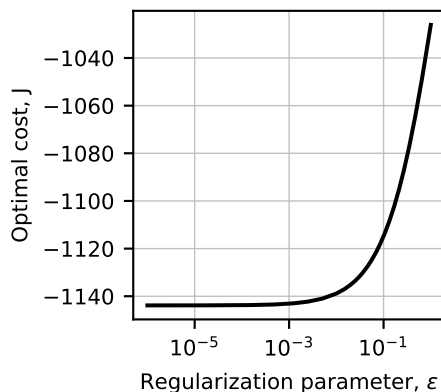


Figure 2.10: Optimal control cost over regularization parameter for sounding rocket example.

original OCP. Finally, convergence of the regularized OCP over ϵ is shown in Fig. 2.10. The cost is initially higher due to the smoothing effect of the regularizing functions. As the value of ϵ decreases, the cost approaches a constant value asymptotically. Values of ϵ below 10^{-6} are not found to decrease the computed cost significantly.

The overall solution structure and accuracy of the regularized problem when compared to the traditional approach are reliable indicators that an optimal solution is reached. This is confirmed through comparison to analytical results obtained using traditional methods, as well as the direct optimization software GPOPS-II [69]. Note that with the GCRM, no prior knowledge regarding the number and ordering of solution arcs is required, nor is a derivation for the analytical form of the singular control. The present example serves to validate performance on singular arcs. In next section, we extend the method to more complex OCP structures representing a broader class of problems.

2.4 Extension to General Hamiltonian Structures

The preceding developments assume that an OCP has the Hamiltonian form in Eq. (2.14) with control terms appearing linearly. Many interesting problems do not adhere to this structure, in which case the GCRM will not yield the unique control law Eq. (2.22). However, an OCP can be transformed into bang-bang/singular form through a process termed system extension and

differential control (SEDC). This method maps nonlinear control terms as additional states in the system, allowing for application of the GCRM functions through auxiliary control variables. An additional consideration is made for state path constraints, which are required to enforce bounds on the control variable following system extension.

2.4.1 Nonlinear Control Terms

Consider problem $\text{OCP}(u)$ with general Hamiltonian structure

$$H^{(u)} = h(\mathbf{x}, \boldsymbol{\lambda}, u, t) \quad (2.61)$$

where the superscript (u) emphasizes that optimization is performed over the control u . Control terms appearing in transcendental or nonlinear form may result in an ambiguous control structure for u from Eq. (2.3c). The objective of SEDC is to remove this ambiguity through integration of the differential rate for u , while simultaneously satisfying optimality conditions. A similar strategy exists for index reduction of semi-explicit differential-algebraic equations (DAE) [145, 146]. Index reduction casts a DAE into an ordinary differential equation (ODE) by: 1) appending an algebraic constraint to the system boundary, and 2) integrating its differential with respect to auxiliary variables. For example, Antony and Grant [80] use this method to solve implicit expressions for u in Eq. (2.3c) by integrating an expression for \dot{u} subject to initial conditions $(\partial H / \partial u)_{t=t_0} = 0$. However, the method still requires a numerical root-finding algorithm to solve Eq. (2.3c) on the boundary. If multiple roots for u exist, the BVP solver may converge to a suboptimal solution. In contrast, SEDC ensures optimality for u without solving Eq. (2.3c) directly. Other system extension approaches have been proposed in Refs. [112, 136, 137, 147], though the approaches are often problem-specific.

The process is summarized as follows. Suppose the OCP Hamiltonian has terms with u appearing in nonlinear form Eq. (2.61). Solution of $\partial H / \partial u = 0$ may prove difficult in this case. Instead, the control variable u is augmented to the system as an additional state, and a new control

v is defined as its differential rate. The extended problem OCP(v) is written as

$$\min_v J = \phi(\mathbf{x}(t_f), t_f) + \int_{t_0}^{t_f} L(\mathbf{x}, u, t) dt \quad (2.62a)$$

$$\text{Subject to: } \dot{\mathbf{x}} - \mathbf{f}(\mathbf{x}, u, t) = 0 \quad (2.62b)$$

$$\dot{u} = v \quad (2.62c)$$

$$u(t_0), u(t_f) \text{ free} \quad (2.62d)$$

With the extended system, optimization is performed over the new control variable v . The Hamiltonian is affine in v , enabling application of the GCRM. Unlike the approach in Ref. [80], we need not append the necessary condition for u to the boundary. The GCRM is instead able to resolve necessary conditions for v and therefore u as an additional state

One further observation is made regarding solution of Eq. (2.62a) following SEDC. After transformation to bang-bang/singular form, solution segments on bang arcs are dictated by the upper and lower bounds on v . Such bounds may not exist in the original problem Eq. (2.61), giving a suboptimal solution. We show in Appendix B that this control solution must be totally singular. This behavior can be avoided after regularization by setting arbitrarily large bounds on v , such that bang arcs are never reached. However, a more practical approach lies in the fact that many engineering systems have bounds on control actuator *rates*. In this case, it remains useful to set $v \in [v_{\min}, v_{\max}]$ based on system requirements. In addition, the free condition in Eq. (2.62d) could instead enforce an initial or final state constraint on u . Thus, SEDC enables solutions to OCPs with general Hamiltonian structure while modeling more realistic control actuation with physics-based systems.

2.4.2 Path Constraint Regularization

Path constraints add additional complications using traditional indirect methods. Along constrained arcs, the optimal control law is determined by the constraint function and its derivatives along the active arc, instead of the unconstrained necessary condition on u . In addition, the entry and exit transition of states and costates along constrained arcs must be carefully designed. A full

discussion of traditional methods with path constraints is outside of the scope of this work. Instead, we provide a brief summary for context. Suppose a scalar inequality constraint $c(\mathbf{x}, u, t) \leq 0$ is to be enforced. Traditional methods append the active constraint to the Hamiltonian with a Lagrange multiplier μ as

$$H = \boldsymbol{\lambda}^T \mathbf{f}(\mathbf{x}, u, t) + L(\mathbf{x}, u, t) + \mu c(\mathbf{x}, u, t) \quad (2.63)$$

When the constraint is active, the Lagrange multiplier takes on an effective value μ_{eff} , such that

$$\mu = \begin{cases} 0 & \text{if } c(\mathbf{x}, u, t) < 0 \\ \mu_{\text{eff}} & \text{if } c(\mathbf{x}, u, t) = 0 \end{cases} \quad (2.64)$$

The Hamiltonian incorporates this additional (possibly time varying) factor, therefore introducing piecewise-defined conditions of optimality dependent on whether the constraint is active. Adjoined constraints effectively split the problem into multiple solution arcs. Each arc must be stitched together in order to provide a complete solution, adding further challenges in constructing and solving the Hamiltonian BVP.

The SEDC approach enables application of the GCRM to a broad class of problems. Through a minor alteration of the OCP structure, the problem is cast into bang-bang/singular form in terms of the auxiliary control variable v . Bounds on u are neglected because regularization is not applied to the original control. However, because u is a state in the extended system, bounding behavior on u can be recovered using standard inequality constraint regularization techniques. These constraints are enforced through interior penalty functions augmented to the integral cost. For example, previous studies have utilized trigonometric [99, 148] and logistic [149] smoothing functions for state constraint regularization. The approach is extended using the GCRM functions in Table 2.1 as follows.

Consider a scalar inequality constraint in Eq. (2.1e) of the form $c(\mathbf{x}, t) \in [a_i, b_i]$, where a_i and b_i are the upper and lower constraint bounds, respectively. This expression can be normalized [148] as

$$c'(\mathbf{x}, t) = \frac{2}{b_i - a_i} c(\mathbf{x}, t) - \frac{b_i + a_i}{b_i - a_i} \quad (2.65)$$

Table 2.3: Path constraint regularization functions.

Method	Path constraint penalty, ζ
Arctangent	$\epsilon \tan^2(\pi c'/2)$
Error function ^a	$\epsilon \operatorname{erfinv}^2(c')$
Hyperbolic tangent	$\epsilon \operatorname{atanh}^2(c')$
Logistic	$\epsilon \log^2((1+c')/(1-c'))$
Algebraic	$\epsilon c'^2/(1-c'^2)$
Einstein function	undefined ^b

^a erfinv is the inverse error function.

^bThis inverse does not exist.

with $c'(\mathbf{x}, t) \in [-1, 1]$. We seek to penalize values of the constraint near the prescribed bounds. A penalty function $\zeta : (-1, 1) \times \mathbb{R}_{>0} \rightarrow [0, \infty)$ is augmented to the integral cost, such that the resulting OCP objective is

$$J = \phi(\mathbf{x}(t_f), t_f) + \int_{t_0}^{t_f} L(\mathbf{x}, u, t) + \zeta(c'(\mathbf{x}, t), \epsilon) dt \quad (2.66)$$

Due to the normalization of c' , an appropriate penalty function can be constructed from each of the control regularization functions in Table 2.1 as

$$\zeta(c'(\mathbf{x}, t), \epsilon) = \frac{1}{\epsilon} [\tilde{u}^{-1}(c'(\mathbf{x}, t), \epsilon)]^2 \quad (2.67)$$

where \tilde{u}^{-1} is the inverse function (not the reciprocal) of each regularizing control term. This functional form was deduced by noting the bounding behavior of \tilde{u}^{-1} corresponds directly to the normalization of the path constraint Eq. (2.65). The square of the inverse is taken to ensure only positive values are augmented to integral cost. Finally, the division by ϵ ensures dimensional consistency with the Lagrangian. As a result, ϵ has the same units as L . Due to limit behavior of ζ , exact satisfaction of the constraint bound is infeasible as the interior penalty function approaches infinity. In practice, however, small values of ϵ will rapidly reduce the push-off factor of the interior penalty, facilitating a close numerical approximation of the constraint bounds.

Path constraint penalty terms are summarized for the sigmoid functions in Table 2.3. An inverse function is found for each case suitable for path constraint regularization, with the exception of the Einstein function. Figure 2.11 illustrates the trend of the penalty function corresponding

to the arctangent regularization method. For larger values of ϵ , the interior penalty has a large push-off factor, which increases the smoothing effect of the path constraint regularization. As the value of ϵ is decreased, the bounds are pulled closer to the desired limits of the normalized path constraint. Thus, the overall effect is to impose large penalties for any state configurations that approach the path constraint bounds. Note that no prior knowledge of the entry and exit points of the constraint are required. Instead, the mapping will transition seamlessly between constrained and unconstrained arcs through the integral penalty effect in ζ .

With SEDC and path constraint regularization, the GCRM can be applied to a wide range of OCP structures with minimal effort required of the designer. The additional state constraint penalty functions do not affect the necessary conditions for the control. Thus, the unique optimal control law Eq. (2.22) will hold following regularization for v . In the next subsection, we show an example of this procedure for a simple problem with bounded nonlinear control terms.

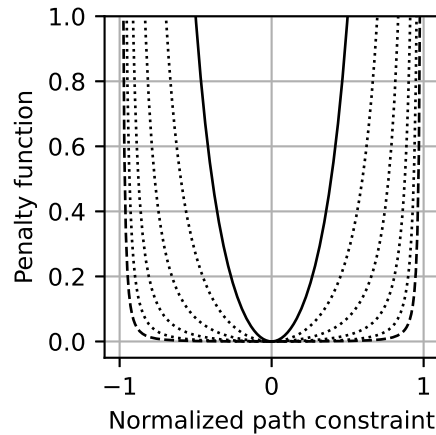


Figure 2.11: Arctangent path constraint penalty function for $\epsilon = 1$ (solid line) to $\epsilon = 0.001$ (dashed line).

2.4.3 Example: Time-Energy Optimal Control

Consider a time-energy minimization problem with the objective

$$J = \int_0^{t_f} 2 + u^2 dt, \quad t_f \text{ free} \quad (2.68)$$

and state equation

$$\dot{x} = -x + u \quad (2.69)$$

The initial and final state is constrained to $x(0) = 1.5$ and $x(t_f) = 0$. The control is bounded to $|u| \leq$

1. We first consider the traditional approach using indirect methods. Forming the Hamiltonian,

$$H = \lambda(-x + u) + 2 + u^2 \quad (2.70)$$

on unconstrained arcs when $|u| < 1$ the costate rate is

$$\dot{\lambda} = -\frac{\partial H}{\partial x} = \lambda \quad (2.71)$$

It is immediately apparent that the control u appears in Eq. (2.70) quadratically. The solution for u is obtained from Eq. (2.3c) as

$$\frac{\partial H}{\partial u} = \lambda + 2u = 0 \quad (2.72)$$

leading to the control law $u^* = -\lambda/2$ when $|\lambda| < 2$. Since there is no possibility of singular arcs in this problem, the solution on control constrained arcs can be determined by PMP. This leads to the following control structure.

$$u^* = \begin{cases} +1 & \text{if } \lambda < -2, \\ -\frac{1}{2}\lambda & \text{if } -2 \leq \lambda \leq 2, \\ -1 & \text{if } \lambda > 2 \end{cases} \quad (2.73)$$

While application of indirect methods leads to a relatively straightforward expression for u^* , it remains piecewise continuous and relies on knowledge of the switching function λ . Kirk [150] gives further details on the costate structure which are omitted here for brevity.

It is demonstrated that SEDC and path constraint methods can be applied to the time-energy problem to facilitate rapid solution. The control u is appended as a new system state, with a new auxiliary control variable v . In addition, a path constraint penalty function Eq. (2.67) is augmented to the integral cost to enforce bounds on u . The problem is then solved using the GCRM. Using

the hyperbolic tangent functions, the regularized problem structure becomes

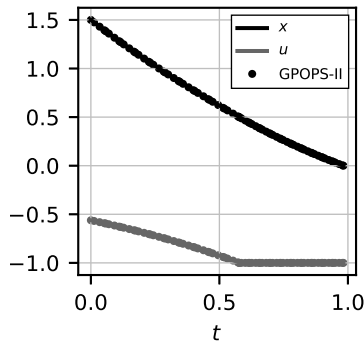
$$J = \int_0^{t_f} 2 + u^2 + v \tanh\left(\frac{v}{\epsilon_1}\right) - \epsilon_1 \log\left(\cosh\left(\frac{v}{\epsilon_1}\right)\right) + \epsilon_2 \operatorname{atanh}^2(u) dt, \quad t_f \text{ free} \quad (2.74)$$

$$\dot{x} = -x + u, \quad \dot{u} = \tanh\left(\frac{v}{\epsilon_1}\right) \quad (2.75)$$

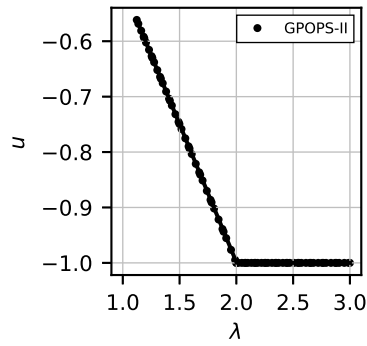
$$u(0), u(t_f) \text{ free} \quad (2.76)$$

with resulting control law $v^* = -\lambda_u$, where λ_u is a costate corresponding to the auxiliary state u . A distinction is made between ϵ_1 and ϵ_2 , which are used for control and path constraint regularization, respectively. In practice, both regularization parameters will attenuate to similarly small values. However, separating these parameters allows for tuning to improve numerical convergence, which may be important in more complex OCPs.

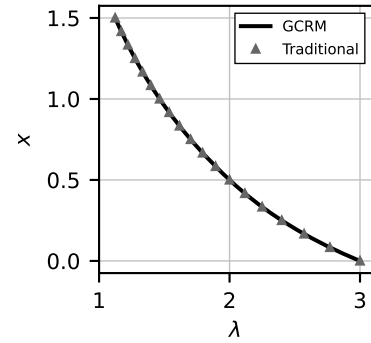
The time-energy problem is solved using a numerical continuation on ϵ_1 and ϵ_2 , starting at values of 10^0 and ending at 10^{-7} . Results are shown in Fig. 2.12. The control history starts in the unconstrained region with $|\lambda| < 2$, until a time of about 0.6 where the solution transitions to the control lower bound. The state history in Fig. 2.12a is also shown to coincide with the prescribed initial and final conditions. Note that the optimal solution is obtained without enforcing any boundary conditions on u . The optimal control law relationship in Eq. (2.73) is verified in Fig. 2.12b. The optimal cost is 2.7128 with final time of 0.9825, which match those reported in Ref. [150]. As with the preceding examples, it is possible to generate a relationship between the state and costate in the time-energy problem by noting $H = 0$ and applying the control law Eq. (2.73) given by PMP. Figure 2.12c shows a comparison of the GCRM results to traditional methods. We note that two distinct solution arcs are present for $\lambda > 2$ and $\lambda \leq 2$. In both the constrained and unconstrained regions, the numerical results obtained using GCRM closely follow those predicted by traditional indirect methods. These results indicate the SEDC and path constraint regularization approach is consistent with solutions to problems with nonlinear control terms in the Hamiltonian structure.



(a) State and control



(b) Control law



(c) Comparison to traditional approach

Figure 2.12: Solution to time-energy example using hyperbolic tangent regularization.

2.5 Application to Aerospace Systems

The benchmark examples illustrate the capability of the GCRM to solve simple problems. In the following section, a more difficult scenario involving optimal maneuvering of an atmospheric reentry vehicle is explored to validate the proposed method for engineering analysis.

2.5.1 3-DOF Hypersonic Problem

A practical and often useful problem in optimal control of aerospace systems is trajectory optimization of an atmospheric flight segment. Although the underlying system is more complex, this example shows how the GCRM may be applied with little difficulty to complex problems.

Equations of motion for unpowered flight, ignoring rotation effects of the Earth, are [151]

$$\dot{h} = V \sin \gamma \quad (2.77a)$$

$$\dot{\theta} = \frac{V \cos \gamma \cos \psi}{r \cos \phi} \quad (2.77b)$$

$$\dot{\phi} = \frac{V \cos \gamma \sin \psi}{r} \quad (2.77c)$$

$$\dot{V} = -D - g \sin \gamma \quad (2.77d)$$

$$\dot{\gamma} = \frac{1}{V} \left[L \cos \sigma + \left(\frac{V^2}{r} - g \right) \cos \gamma \right] \quad (2.77e)$$

$$\dot{\psi} = \frac{1}{V} \left[\frac{L \sin \sigma}{\cos \gamma} - \frac{V^2}{r} \cos \gamma \cos \psi \tan \phi \right] \quad (2.77f)$$

The state variables include geocentric altitude h , longitude θ , latitude ϕ , velocity magnitude V , velocity flight-path angle γ , and velocity heading angle ψ . Convention for flight-path angle is positive above the local horizontal. Heading angle is defined zero for a heading due East. The bank angle σ is defined zero for a lift-up orientation in the local vertical plane, and positive producing a left turn. We make the assumption for a spherical planet such that $r = r_e + h$ where r_e is the radius of the Earth. An inverse-square gravity law $g = \mu/r^2$ is assumed with the standard Earth gravitational coefficient μ . The L and D terms represent the lift and drag acceleration, respectively, given by

$$L = \frac{1}{2} \rho V^2 \frac{C_L A_{\text{ref}}}{m}, \quad D = \frac{1}{2} \rho V^2 \frac{C_D A_{\text{ref}}}{m} \quad (2.78)$$

where m is the vehicle mass, ρ is the local atmospheric density, C_L and C_D are the lift and drag coefficients, respectively, and A_{ref} is the aerodynamic reference area. The atmospheric density is assumed to follow an exponential model $\rho = \rho_0 \exp(-h/S)$, where ρ_0 is the reference density and S is the atmospheric scale height. The lift and drag coefficients are prescribed functions of angle-of-attack α . An aerodynamic model is adapted from [152] for a lifting-body hypersonic glide vehicle with peak lift-to-drag ratio of 1.5. A sufficiently accurate approximation of the lift and drag

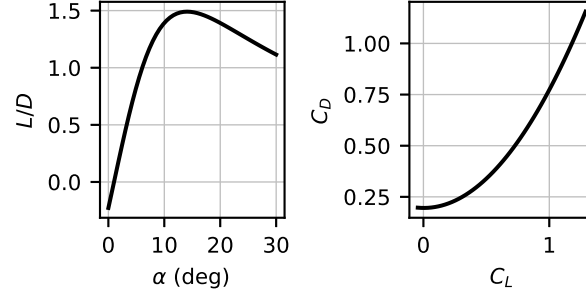


Figure 2.13: Lift-to-drag ratio and drag polar for generic hypersonic reentry vehicle.

coefficient curves is

$$C_L = 2.5457\alpha - 0.0448 \quad (2.79)$$

$$C_D = 3.7677\alpha^2 - 0.1427\alpha + 0.1971 \quad (2.80)$$

with α in radians. The lift-to-drag performance and drag polar for this simple aerodynamic model are illustrated in Fig. 2.13. It is also of use to consider the sensed acceleration during reentry η , which is dictated by lift and drag acceleration terms.

$$\eta = \sqrt{L^2 + D^2} \quad (2.81)$$

In some cases it may be necessary to constrain the maximum acceleration experienced during reentry; in this example, however, it is defined merely for informative and plotting purposes.

A reasonable objective is to minimize the integrated control effort in angle-of-attack, stated as

$$J = \int_{t_0}^{t_f} \alpha^2 dt, \quad t_f \text{ free} \quad (2.82)$$

The endpoint is determined by terminal state constraints on the altitude, longitude, and latitude as

$$h(t_f) = 0, \quad \theta(t_f) = \theta_f, \quad \phi(t_f) = \phi_f \quad (2.83)$$

The first control variable is angle-of-attack $u_1 = \alpha$, which appears in the equations of motion through C_L and C_D . We note that the bank angle σ appears in trigonometric form in Eq. (2.77a),

introducing ambiguity in the resulting control law when traditional methods are applied. We implement the SEDC approach by appending σ as an additional state in the system with state equation

$$\dot{\sigma} = u_2 \quad (2.84)$$

We choose a maximum value of the bank rate such that $|u_2| \leq \dot{\sigma}_{\max}$. Incorporating bank angle as an auxiliary state has benefits from an engineering modeling perspective. The bank performance is limited by control actuation flaps or thrusters with finite time delay between commanded and actual bank angle. This model allows an additional degree of freedom in modeling such dynamics. The hypersonic problem structure is summarized in Table 2.4 with initial and final state constraints. Other constants used in this problem are defined in Table 2.5.

The traditional approach begins with formulating the Hamiltonian of the system

$$\begin{aligned} H = & \lambda_h V \sin \gamma + \lambda_\theta \frac{V \cos \gamma \cos \psi}{r \cos \phi} + \lambda_\phi \frac{V \cos \gamma \sin \psi}{r} + \lambda_V (-D - g \sin \gamma) \\ & + \lambda_\gamma \frac{1}{V} \left[L \cos \sigma + \left(\frac{V^2}{r} - g \right) \cos \gamma \right] + \lambda_\psi \frac{1}{V} \left[\frac{L \sin \sigma}{\cos \gamma} - \frac{V^2}{r} \cos \gamma \cos \psi \tan \phi \right] + \lambda_\sigma u_2 + \alpha^2 \end{aligned} \quad (2.85)$$

Although the state equations are nonlinear with respect to angle-of-attack in the lift and drag coefficient curves Eq. (2.79), a unique expression for u_1^* results from Eq. (2.3c) as

$$u_1^* = A_{\text{ref}} \rho_0 V \frac{25457 \left(\lambda_\gamma \cos \sigma + \lambda_\psi \frac{\sin \sigma}{\cos \gamma} \right) + 1427 \lambda_V V}{75354 A_{\text{ref}} \lambda_V \rho_0 V^2 - 40000 m \exp \left(\frac{h}{H} \right)} \quad (2.86)$$

A unique control law for angle-of-attack is possible because α terms appear quadratically in the Hamiltonian and no bounds are enforced. Due to drag penalties at higher angles-of-attack evident in Fig. 2.13, there is an inherent limiting effect on the angle of attack in order to minimize velocity-loss. Moreover, the objective Eq. (2.82) will also limit the angle-of-attack to reduce the integrated control effort. The second control variable u_2 appears linearly in Eq. (2.85), leading to the bang-

Table 2.4: Initial and final state constraints for hypersonic Earth reentry scenario.

State	h	θ	ϕ	V	γ	ψ	σ	t
Initial	40 km	0 deg	0 deg	2 km/s	-15 deg	0 deg	0 deg	0 s
Final	0 km	2 deg	0.5 deg	Free	Free	Free	Free	Free

bang/singular control law

$$u_2^* = \begin{cases} -\dot{\sigma}_{\max} & \text{if } \lambda_\sigma > 0, \\ +\dot{\sigma}_{\max} & \text{if } \lambda_\sigma < 0, \\ \text{indeterminate} & \text{if } \lambda_\sigma = 0 \end{cases} \quad (2.87)$$

Due to the highly nonlinear nature of the hypersonic entry problem, it is prohibitive to ascertain an analytical expression for the switching function for u_2 across all solution arcs. This underscores the utility of regularization in difficult problems.

Table 2.5: Constants for hypersonic Earth reentry scenario.

Parameter	Value
Gravity Parameter, μ	$3.986 \times 10^{14} \text{ m}^3/\text{s}^2$
Reference Density, ρ_0	$1.2 \text{ kg}/\text{m}^3$
Scale Height, S	7500 km
Vehicle Mass, m	340.19 kg
Earth Radius, r_e	6378 km
Reference Area, A_{ref}	0.29186 m^2
Max Bank Rate, $\dot{\sigma}_{\max}$	10 deg/s

The arctangent regularization method is applied to resolve the control form for u_2 . Introducing the error-control and penalty terms from Table 2.1 with small parameter ϵ , the control law is verified using Eq. (2.17) as $u_2^* = -\lambda_\sigma$. The numerical continuation methodology used in this problem is more involved than the previous examples. As demonstrated by Ref. [99], a multi-step continuation procedure can be used to solve more challenging OCPs starting from rough initial costates. The continuation begins with a flight-path angle of -88 degrees, indicative of near-vertical flight straight towards the planet surface. The simulation is run for 0.5 seconds to allow an initial trajectory to converge. Then a continuation step is performed to bring the final altitude down to

0 km. Next, continuation to a final downrange angle of 0.01 degrees is performed to start moving the trajectory towards its forward target. The third continuation step pushes the initial flight-path angle and final longitude to meet the prescribed constraints in Table 2.4. The next step pushes the final latitude to 0.5 degrees satisfy cross-range requirements. Finally, a continuation step is performed on the error parameter ϵ , starting from an initial value of 10^1 to a final value 10^{-5} . Lower values of ϵ are not found to affect the cost further. Dimensional consistency in the BVP solver is enforced with units for ϵ in seconds.

Results for the hypersonic reentry example are shown in Fig. 2.14. These results correspond to the final converged trajectory following the continuation procedure. The first plot shows the trajectory of the vehicle in altitude-velocity coordinates. The initial flight-path angle of -15 degrees puts the vehicle on a relatively steep initial descent, which is reflected by a rapid decline in altitude in the initial segment of the trajectory. Figure 2.14 also shows the angle-of-attack time history. In order to meet downrange requirements, the vehicle must initially ramp up angle-of-attack to generate sufficient aerodynamic lift. This in turn increases aerodynamic drag, resulting in a spike of 4.2 g's sensed acceleration at about 30 seconds. Once the trajectory bottoms out, the flight-path angle rises briefly above the local horizontal providing a loft in the trajectory. The effect of this loft maneuver is to conserve kinetic energy compared with a more direct entry path towards the terminal downrange and altitude. Conserving kinetic energy allows for higher velocities later in the trajectory to produce lift at lower angles-of-attack, reducing the overall integrated control effort. Although in this problem the angle-of-attack is controlled with no rate constraints, the time response of α is sufficiently slow as to neglect such constraints.

Figure 2.15 also shows the bank angle rate time history. The initial arc of the solution for u_2 is constrained by the upper-bound $\dot{\sigma}_{\max}$ of 10 deg/s. This constraint is reflected in the bank angle response as it ramps up linearly in time. Upon exiting the initial bang arc, the remaining trajectory is a singular arc no longer constrained by the control magnitude bound. A lower maximum bank angle rate could potentially introduce additional constrained solution arcs. The chosen value of $\dot{\sigma}_{\max}$ will determine the overall solution structure. One obvious benefit of the regularization procedure

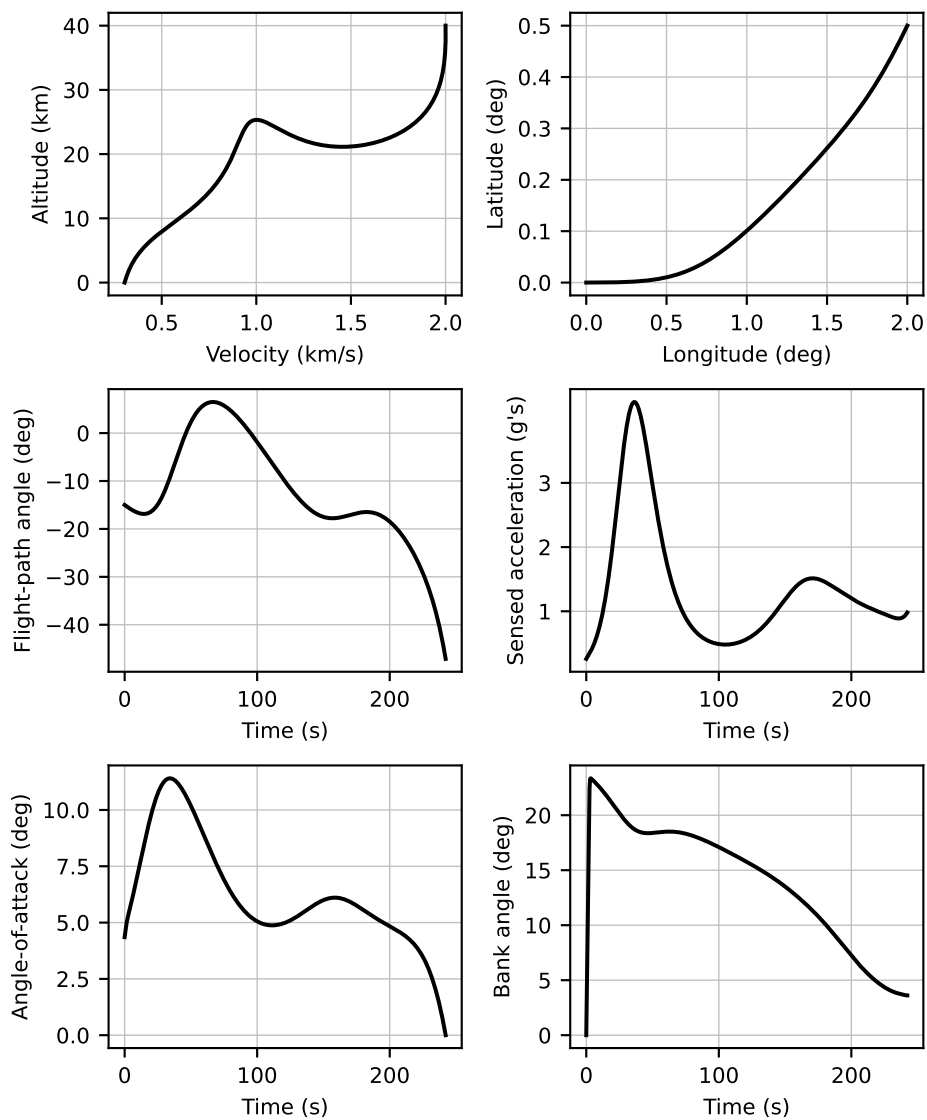


Figure 2.14: Converged trajectory of the 3-DOF hypersonic reentry problem.

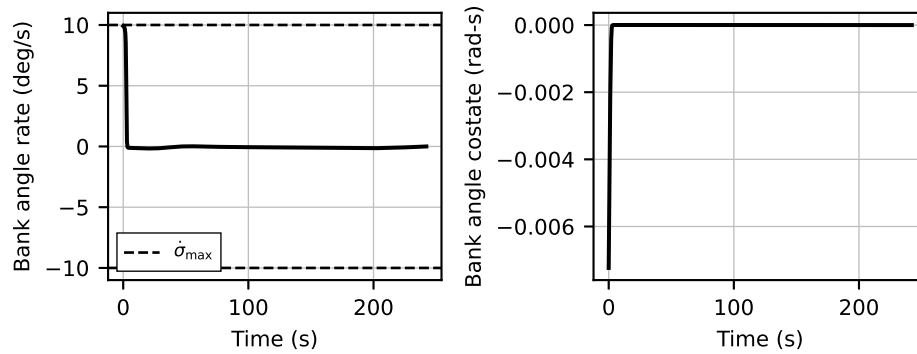


Figure 2.15: Bank rate regularization for 3-DOF hypersonic reentry problem.

is to eliminate any required insight or knowledge of these constrained arcs prior to attempting numerical solution.

The bank angle rate control incorporates a pseudo-attitude degree of freedom by modeling the rigid-body response delay of a realistic flight system. For real-time applications, the vehicle will likely have a known initial bank angle based on current state information. The optimal trajectory must then account for the bank angle time response through bang arcs in the bank angle rate. Previous studies directly controlling bank angle neglect this behavior, because no boundary conditions are present on the control variables. Any initial bank angle configuration could be studied pending a feasible solution exists. A boundary condition could also be imposed on the final bank angle, limiting the available cross-range control in the final segment of the trajectory as the bank angle is forced to its required value.

2.5.2 Keep-out Zone

Path constraints are a common requirement in optimization of aerospace systems. For the hypersonic 3-DOF entry problem, examples include limits on the maximum sensed acceleration, aero-thermal heating, or dynamic pressure. These constraints must be enforced over the full trajectory, and will generally become active and inactive across various trajectory segments. To illustrate the preceding path constraint regularization procedure, a keep-out zone in longitude-latitude co-

Table 2.6: Parameters used in the keep-out zone constraint.

Parameter	θ_c	ϕ_c	R_{\min}	R_{\max}
Value	1 deg	0.25 deg	0.35 deg	25 deg ^a

^aArbitrary upper bound

ordinates is considered that the vehicle must circumnavigate. Situations such as extreme weather events or contested airspace may impose constraints of this form.

A radial bound is imposed for a circular keep-out zone defined as

$$R_{\min}^2 \leq (\theta - \theta_c)^2 + (\phi - \phi_c)^2 \leq R_{\max}^2 \quad (2.88)$$

where R_{\min} and R_{\max} are the lower and upper bounds, respectively, and θ_c and ϕ_c are the centroid coordinates. Using the scaling constants in Eq. (2.65), the constraint is normalized as

$$-1 \leq \frac{2}{R_{\max}^2 - R_{\min}^2} ((\theta - \theta_c)^2 + (\phi - \phi_c)^2) - \frac{R_{\max}^2 + R_{\min}^2}{R_{\max}^2 - R_{\min}^2} \leq 1 \quad (2.89)$$

In practice, only the lower bound R_{\min} is required to enforce the keep-out constraint. A large arbitrary value can be chosen for the upper bound to prevent interference during optimization, though the value should not be chosen too large as to introduce numerical ill-conditioning. Parameters for the keep-out zone constraint are summarized in Table 2.6.

The keep-out constraint Eq. (2.88) is implemented using the arctangent method in Table 2.3. Results are shown in Fig. 2.16 for the unconstrained and constrained scenarios. With the constraint inactive, the trajectory traverses the keep-out zone in order to reach terminal cross-range while conserving energy. In comparison, with the constraint active, the vehicle must use a portion of its initial kinetic energy to perform a bank maneuver outside the keep-out zone. The net effect of this maneuver is apparent in comparing the altitude-velocity profile of each trajectory (see Fig. 2.17a). With the constraint active, the trajectory has a less pronounced loft, increasing the velocity-loss early in the trajectory. As a result, the integrated angle-of-attack in Fig. 2.17b increases order to meet downrange and cross-range requirements while enforcing the keep-out zone constraint. In general, active path constraints are expected to reduce the achieved cost. In this case, the integral

angle-of-attack cost is increased from 3.319 to 13.748 $\text{rad}^2\text{-s}$ with the path constraint active. The final time is also higher, with the constrained case terminating at 313.6 seconds versus 242.2 seconds for the unconstrained case. The extra time is necessary as the vehicle must fly a greater total range to avoid the keep-out zone. Using the GCRM, these operational limitations can be easily augmented to an OCP structure and solved using numerical continuation.

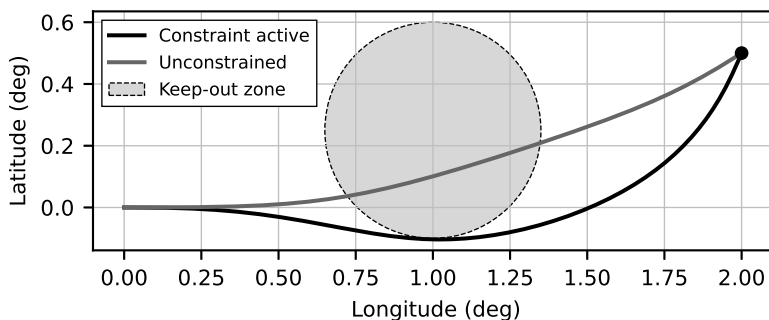


Figure 2.16: Ground track of the hypersonic 3-DOF example with keep-out zone.

The hypersonic reentry example illustrates the utility of the control regularization procedure proposed in this work. Traditional methods in bang-bang/singular control problems require a priori knowledge regarding the solution structure and number of constrained arcs to solve an OCP. In addition, traditional methods result in a multi-phase Hamiltonian BVP with corner conditions on the costates between constrained arcs. Control regularization strategies in general avoid these issues by reducing the problem to a single-stage unconstrained approximation of the true OCP. The GCRM functions provide a further benefit over existing methods by simplifying the form of the control law while maintaining desirable numerical convergence behavior. In addition, because of the positive-definite form of the error-control penalty function, the smoothed problem retains its overall structure without imposing an artificial time-minimization objective at larger values of ϵ . These methods enable rapid solution of complex, multi-phase OCPs with minimal effort required of the designer to implement and solve challenging problems.

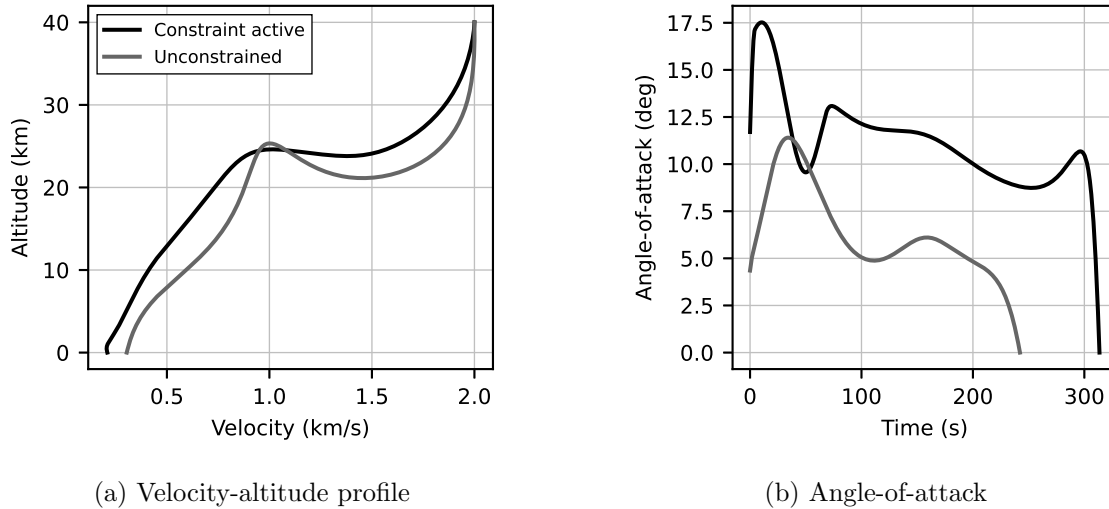


Figure 2.17: Performance comparison with keep-out zone constraint.

2.6 Summary

Regularization of OCPs with bang-bang/singular solution structures provides many benefits over traditional methods. The overall number of trajectory arcs and boundary conditions are greatly reduced in the smoothed approximation, with only minor degradation of the overall solution accuracy. No previous knowledge regarding the solution structure and number of constrained arcs is required. In addition, derivation of the analytical control law in singular control problems, typically an involved and cumbersome symbolic process, is no longer needed in the regularized problem. This research improves upon existing methods by modifying the control regularization and associated error-control terms to provide more desirable characteristics of the smoothed OCP. The primary benefit of the new method is the elimination of any ambiguity in the optimal control law. This eliminates the need for point-wise application of the Minimum Principle to identify an optimal control. The solution maintains its fully-analytical characteristics, with many benefits from an implementation and programming perspective. Classes of regularization functions are developed from generalized sigmoid functions with varying numerical convergence behavior, allowing flexibility in the construction of the constrained OCP. The approach is extended to problems with arbitrary

Hamiltonian structure using system extension and differential control. Results for benchmark problems from the literature with known solution structures validate the accuracy of the new method. A more involved problem regarding hypersonic reentry trajectory optimization illustrates applicability to practical problems in aerospace engineering.

Chapter 3

Relaxation of Infinite-Order Singular Arcs by Auxiliary Covariance Minimization

3.1 Optimal Control Uniqueness and Well-Posedness

Underlying many tools of practice in engineering optimization are assumptions for regularity and well-posedness. One must assume that there exists an admissible control driving the state from initial conditions to the required terminal set (with final time possibly specified). This can be interpreted as a controllability requirement of the system. Unfortunately, few existence results in optimal control are available for application to nonlinear problems [153]. In general, an optimization statement is considered well-posed in the sense of Hadamard [154] if its solution depends continuously on the variable parameters of problem. Under certain regularity conditions, well-posedness implies existence and uniqueness of an optimal control [155]. Problems that are not well-posed in this manner are considered ill-posed. Solution of the indirect formulation frequently depends on necessary conditions for optimality, meaning well-posedness may not be guaranteed even if a local minimum is found. This poses particular challenges for ambiguous or indefinite solution forms, requiring further analysis to reveal the optimal control, if it exists. Thus, we are motivated to consider cases in which an ill-posed problem may introduce itself under practical considerations. Furthermore, these problems would benefit from methodologies to repose the Hamiltonian system to a form admitting unique solvability and regularity conditions.

As discussed in Chapter 2, a common attribute in optimal control of Newtonian systems is a bang-bang/singular solution structure. This is often the case when control terms appear linearly

in the Hamiltonian. Bang-bang solutions are characterized by piecewise controls residing on the boundary of the admissible set, with discontinuities occurring at discrete switch points. If the Minimum Principle fails to reveal the optimal control over some solution arc, the control structure is singular [78, 156]. A singular arc produces no variation in the Hamiltonian for a change in the control, requiring further analysis to resolve the singularity. The classical Legendre-Clebsch (or Kelley) theorem [102] imposes an additional convexity condition on the Hamiltonian, which is often sufficient to determine the optimal control law over a singular arc. This condition can be interpreted as solving for the control that remains on the singular arc. Goh's necessary condition [101] is a stronger statement to minimize a so-called *accessory minimum problem* to regulate the second variation of the cost along the minimizing arc. These conditions can involve significant symbolic manipulation and may not always yield an optimal control.

This work primarily concerns indeterminacy due to non-uniqueness of the optimal control policy. That is, a solution can be found minimizing the objective compatible with all boundary conditions and constraints, but the solution is not unique. For example, the Lasalle bang-bang principle for linear systems [157] states that, for any point reachable with admissible controls, the same point can be reached with bang-bang controls, meaning the bang-bang control is not always unique. This property has also been extended to classes of nonlinear systems [158]. Upon application of traditional indirect methods to such problems, the result may at first appear contradictory. Ross [159] posits a seemingly trivial variant of the single integrator system, for which traditional indirect methods yield no solution. In their example, application of the Pontryagin Minimum Principle leads to the (false) conclusion that no extremal solution exists. However, further analysis reveals an “infinite family of globally optimal solutions” consisting of an uncountable set of globally minimizing state-control pairs. The result is an argument in favor of direct methods; due to their inherently approximate nature, direct methods are guaranteed to find at least one solution, whereas the indirect approach finds none. Another result is given by Powers [104] linking uniqueness of the optimal control to singular arc order. We put forth a rather compelling quote from on the relationship between arc order and indeterminacy as follows.

Infinite-order singular optimal controls [...] occur when the optimal control for the original problem is nonunique. Recall [...] that nonuniqueness problems were also associated with the order of the problem and the arcs. Intuitively, these properties indicate that there exists a strong connection between singular problem and arc order and uniqueness of optimal controls. [104]

Uniqueness of singular controls is also developed by Serovaiskii [160], showing that the Kelley condition becomes a strict equality (i.e., $0 = 0$) for the indeterminate case. Although the solutions satisfy the Minimum Principle and convexity conditions, they do so trivially.

The concept of infinite-order singularity has persisted in the mathematical community for some time [161]. However, its relevance to engineering fields is less widespread. This is in part due to the fact that authors tend to choose well-posed problems for study. Nonetheless, relevant applications exist. For example, Seywald and Kumar [106] study singular arcs in the minimum-time spacecraft reorientation problem. The arcs may appear as finite or infinite order, noting in the latter case that any numerical value for the control is arbitrary so long as the control bounds and final position constraints are satisfied. The well-known catalyst mixing problem [162,163] admits infinite-order singular arcs through cyclic derivatives of the switching function. Similar characteristics have been found in the target guarding problem [107], with application to missile guidance and other types of pursuer-evader scenarios. Infinite-order arcs for the time-invariant linear-quadratic problem [105] exhibit the useful property that singular arcs arise from cost functionals of exact differentials. Application of traditional indirect methods to these types of problems may lead to erroneous conclusions, warranting further study.

The objectives of this chapter are two-fold. First, we aim to better categorize situations in which infinite-order singular arcs arise in engineering problems. It turns out these singularities are not a mathematical oddity, but an indication that a Hamiltonian BVP is ill-posed. We show that convexity of the Mayer cost objective, coupled with certain reachability conditions on the system dynamics, leads to the indeterminate case. The arcs are shown to be totally singular, spanning the entire trajectory. The second objective of this work is to demonstrate a novel relaxation method for infinite-order singular arcs via an auxiliary covariance minimization problem. The augmented

problem considers first-order uncertainty propagated about a nominal (or mean) state. Covariance optimization is a broad topic with application to uncertain asteroid transfers [120, 121], powered descent guidance [164, 165], and planetary aerocapture [113, 166], among others. Prior studies often rely on sequential convexification or direct methods in solution, which preclude some of the analytical intuition provided by indirect methods. The utility of covariance optimization as a relaxation method for infinite-order singular arcs is not well-studied. As most engineering systems are subject to some small level of uncertainty in states or parameters, the approach has relevance to a wide array of practical problems.

Although the field of indirect methods is well-developed, there is no uniform solution procedure, necessitating various approaches based on the given problem structure. This problem is further challenging for ill-posed problems wherein the traditional necessary conditions fail to reveal a solution. In this chapter, we present a novel method for identifying and resolving such problems. The contributions of this work can be enumerated follows: 1) existence conditions for singular arcs with infinite local order, 2) identification of singular manifolds with convex Mayer objectives producing infinite-order arcs, 3) development of a covariance-augmented relaxation method on singular arcs, and 4) application to aerospace mission design by improving trajectory optimization under uncertainty.

The outline of this chapter is summarized as follows. Section 3.2 gives relevant theory on indirect methods and the minimum principle, as well as notions of order in singular control. Section 3.3 develops conditions for a control-affine nonlinear system to exhibit infinite-order singular arcs. Section 3.4 proposes a relaxation method based on a first-order model of uncertain system dynamics. Section 3.5 details the numerical solution strategy of the auxiliary problem. Section 3.6 demonstrates application of the relaxation method to classical examples in optimal control theory, as well as a practical aerospace mission design problem. Finally, Sec. 3.7 concludes the chapter.

3.2 The Minimum Principle

We begin with a formulation of the indirect problem for general nonlinear systems. The approach will be applied to a class of OCPs exhibiting indeterminate behavior in the following sections. Consider the system in Eq. (3.1) with state vector $\mathbf{x} \in \mathbb{R}^n$, scalar control input $u \in \mathbb{R}$, and dynamics $f : \mathbb{R}^n \times U \times [t_0, t_f] \rightarrow \mathbb{R}^n$.

$$\dot{\mathbf{x}} = f(\mathbf{x}, u, t), \quad \mathbf{x}(t_0) = \mathbf{x}_0 \quad (3.1)$$

Notation for time dependency is omitted except where required. A general OCP is stated as

$$\text{Problem 1} \left\{ \begin{array}{l} \min_u \quad J = \phi(\mathbf{x}(t_f), t_f) + \int_{t_0}^{t_f} L(\mathbf{x}, u, t) dt \\ \text{s.t.} \quad \mathbf{x}(t_0) = \mathbf{x}_0 \\ \quad \quad u \in U \\ \quad \quad \psi(\mathbf{x}(t_f), t_f) = 0 \end{array} \right. \quad (3.2)$$

where the admissible controls $U \subset \mathbb{R}$ are a closed and bounded (i.e., compact) set, and all functions are assumed smooth and continuously differentiable. The problem is to minimize an integral (or Lagrange) cost $L : \mathbb{R}^n \times U \times [t_0, t_f] \rightarrow \mathbb{R}$ and terminal (or Mayer) cost $\phi : \mathbb{R}^n \times t_f \rightarrow \mathbb{R}$, subject to initial conditions and terminal state constraint $\psi : \mathbb{R}^n \times t_f \rightarrow \mathbb{R}^m$. The controls are assumed to be piecewise continuous in U .

3.2.1 Pontryagin Minimum Principle

A useful result for identifying optimal solution candidates of Problem 1 is given by the celebrated Minimum Principle. This theorem is summarized as follows.

Theorem 1 (Minimum Principle). *Let (\mathbf{x}^*, u^*) be an optimal state-control trajectory of Problem 1. Define the Hamiltonian function $H : \mathbb{R}^n \times \mathbb{R}^n \times U \times [t_0, t_f] \rightarrow \mathbb{R}$ with costate vector $\boldsymbol{\lambda}^* \in \mathbb{R}^n$ and multiplier $\lambda_0 \in \mathbb{R}$ as follows*

$$H(\mathbf{x}^*, \boldsymbol{\lambda}^*, u^*, t) = \boldsymbol{\lambda}^{*\top} f(\mathbf{x}^*, u^*, t) + \lambda_0 L(\mathbf{x}^*, u^*, t) \quad (3.3)$$

If there exists a nontrivial vector

$$(\boldsymbol{\lambda}^{*\top}(t_f), \lambda_0) \neq \mathbf{0} \in \mathbb{R}^{n+1} \quad (3.4)$$

then the following conditions are satisfied

$$\dot{\mathbf{x}}^* = H_{\boldsymbol{\lambda}}(\mathbf{x}^*, \boldsymbol{\lambda}^*, u^*, t) \quad (3.5a)$$

$$\dot{\boldsymbol{\lambda}}^* = -H_{\mathbf{x}}(\mathbf{x}^*, \boldsymbol{\lambda}^*, u^*, t) \quad (3.5b)$$

$$\mathbf{x}^*(t_0) = \mathbf{x}_0 \quad (3.5c)$$

$$\boldsymbol{\lambda}^{*\top}(t_f) = \lambda_0 \phi_{\mathbf{x}}(\mathbf{x}^*(t_f), t_f) + \boldsymbol{\nu}^{\top} \psi_{\mathbf{x}}(\mathbf{x}^*(t_f), t_f) \quad (3.5d)$$

Furthermore, for all $t \in [t_0, t_f]$, the Hamiltonian has a global minimizer $u^* \in U$ such that

$$u^* = \arg \min_{q \in U} H(\mathbf{x}^*, \boldsymbol{\lambda}^*, q, t) \quad (3.6)$$

If the final time is free, then the so-called transversality condition must be satisfied

$$H(\mathbf{x}^*(t_f), \boldsymbol{\lambda}^*(t_f), u^*(t_f), t_f) = -\lambda_0 \phi_t(\mathbf{x}^*(t_f), t_f) - \boldsymbol{\nu} \psi_t(\mathbf{x}^*(t_f), t_f) \quad (3.7)$$

Proof. The proof to this theorem is well-known. See Pontryagin and Semenovitch [100]. \square

Theorem 1 defines a set of conditions for optimality of a candidate state-control trajectory pair. When the Minimum Principle is satisfied, the solution of Eq. (3.6) gives conditions for *global* optimality. Moreover, the Minimum Principle is a stronger statement than the traditional Euler-Lagrange variational equations, as the admissible solutions include piecewise-continuous on-off controls, better known as bang-bang solutions. Extremal trajectories of bang-bang form are dictated by the boundaries of the admissible control set U , with instantaneous changes occurring based on the sign of a switching function. A cautionary note on the Minimum Principle is that, as a necessary condition for optimality, there are no guarantees of existence or uniqueness for general problems. Cases in which multiple solutions exist may benefit from Eq. (3.6) to single out multiple possible controls by point-wise minimization of the Hamiltonian over u .

Equation (3.4) states conditions regarding the normality of a solution. The constant λ_0 appears proportionally to the terminal and running cost objectives. Cases where $\lambda_0 = 0$ are termed *abnormal*, meaning the cost is ignored altogether and solutions are fully described by the nature of the system dynamics and boundary conditions. These cases are uncommon, but nonetheless important in identifying redundant OCP objectives. Otherwise, with $\lambda_0 \neq 0$, the problem is termed *normal* (in the normal case, the abnormal multiplier is usually scaled to unity). The nontriviality condition of Eq. (3.4) states that the costate vector $\boldsymbol{\lambda}$ and abnormal multiplier λ_0 must not vanish identically. This situation can be useful to rule out candidate controls as a violation of the Minimum Principle. This holds even for solution arcs containing controls in the interior of the admissible set U . Note that, because the adjoint equation for $\boldsymbol{\lambda}$ is linear in the costates (see Eq. (3.5b)), if $\boldsymbol{\lambda}$ and λ_0 vanish at any time, they must vanish for all time. Thus, a violation of Eq. (3.4) at any time precludes optimality of the candidate control. Theorem 1 is a useful tool in identification of candidate optimal controls. However, in some cases these conditions may not be sufficient to reveal the optimal control. We discuss such cases in the following sections.

3.2.2 Singular Arcs: Existence and Order

Solution segments for which Theorem 1 fails to reveal an optimal control are referred to as singular arcs. Powers [103] notes that two distinct qualities can be ascertained about a singular arc: the *problem* (or intrinsic) order and the *arc* (or local) order. The former refers to the number of successive differentiations of Eq. (2.10) required for the control variable to reappear. The latter involves the number of differentiations (possibly greater than the problem order) for which the control law u^* can be solved on the singular arc without a leading coefficient of zero. The following definitions are intended to help clarify this distinction.

Definition 1 (Problem Order). Let Problem 1 contain at least one optimal singular arc. Let $2q$ be the first total derivative of Eq. (2.10) in which u appears explicitly as

$$\frac{d^{2q}}{dt^{2q}} H_u = a(\mathbf{x}^*, \boldsymbol{\lambda}^*, t) + b(\mathbf{x}^*, \boldsymbol{\lambda}^*, t)u \quad (3.8)$$

Then, Problem 1 is said to have problem order q . If u never appears in differentiation, the problem is said to be of infinite order.

It is well-known that u must first appear in an even time derivative of H_u [102]. The expressions for derivatives of H_u are valid along all extremal arcs [104]. Note that the problem order can be computed a priori as a property of the OCP structure (hence its designation as *intrinsic*). It is easy to show that the intrinsic order of problems with affine control in the Hamiltonian must have order $q \geq 1$, and the control appears linearly in $(d^{2q}/dt^{2q})H_u$. This useful result will be leveraged in the following sections.

Motivation for definition of arc order can be seen from the expression for u in Eq. (3.8). On the state and costate trajectory of any optimal singular arc, there exists a possibility for the leading coefficient $b(\mathbf{x}^*, \boldsymbol{\lambda}^*, t) = 0$, leading to indefiniteness of the control. Thus, the following definition is taken into consideration.

Definition 2 (Arc Order). For an optimal singular subarc of Problem 1 over time interval $t \in [t_1, t_2]$, $t_2 > t_1$ the arc order is the smallest integer $p \geq q$ for which

$$\frac{\partial}{\partial u} \left[\frac{d^{2p}}{dt^{2p}} H_u \right] \neq 0 \quad (3.9)$$

If no derivative exists satisfying Eq. (3.9), the arc is said to have infinite order with $p = \infty$.

It is easy to see that the arc order must be greater than or equal to the problem order, since u cannot appear before $2q$ derivatives of H_u . Lewis [104] also notes that, for arcs with local order greater than the problem order, the control may not appear linearly in $(d^{2p}/dt^{2p})H_u$. With Definitions 1 and 2 in mind, the following convexity condition for optimality of the singular arc is stated with respect to local order as follows.

Theorem 2 (Generalized Legendre-Clebsch Condition). *Let $(\mathbf{x}^*, \boldsymbol{\lambda}^*, u^*)$ be an extremal arc for control u with local order p over $t \in [t_1, t_2]$, $t_2 > t_1$. A necessary condition for optimality of the singular arc is*

$$(-1)^p \frac{\partial}{\partial u} \left[\frac{d^{2p}}{dt^{2p}} H_u \right] \geq 0 \quad (3.10)$$

for all $t \in [t_1, t_2]$.

Proof. The proof of this theorem is well-known. See Robbins [102]. □

This section introduces useful properties of the optimal control Hamiltonian and necessary conditions for optimality. While singular arcs may seem like an exception rather than a rule, these solutions are in fact quite common. Studying the optimal behavior of singular arcs can provide insight on many practical engineering problems. The notion of intrinsic and local order of singular arcs helps clarify the source of singular arcs, as well as potential avenues for solution.

3.3 A Convexity Condition for Infinite-Order Singular Arcs

This work concerns OCP structures in which the arc order tends to infinity. These scenarios can be linked to indeterminacy of the necessary conditions for optimality resulting from ill-posed OCP problem structures. Note that Theorem 1 relies implicitly on an assumption that an optimal solution exists and is well-posed. Because the Minimum Principle fails to reveal any control policy, applying the traditional indirect approach yields no new information on the optimal solution. Unfortunately, few if any results are available to guarantee uniqueness in general nonlinear problems. However, under some moderate assumptions, it can be shown that a rather broad class of practical problems exhibit this indeterminate behavior. We are motivated to examine the underlying sources of singularity, as well as potential avenues for resolving the problem structure to a more tractable form for solution.

Some simplifying assumptions about the problem structure are taken to aid in analysis. These assumptions are mild in nature, and lend well to many practical and useful problems in optimal control. Consider an autonomous nonlinear system with affine control

$$\dot{\mathbf{x}} = f(\mathbf{x}) + g(\mathbf{x})u, \quad \mathbf{x}(t_0) = \mathbf{x}_0 \tag{3.11}$$

General motion of Newtonian systems is well-described by systems of this form through its constants of motion [167,168]. If there exists a mapping of system states onto integrals of motion, a canonical

coordinate transformation of the form in Eq. (3.11) can be found. These integrals may not be immediately known for complex system dynamics. Fortunately, many practical problems exhibit such form without loss of generality.

Assumptions are also made regarding the form of applied constraints. Two classes of problems are considered covering a wide array of applications: end-time fixed, and end-time free with a partially constrained terminal state. Both cases have relevance in engineering applications. For simple problems, it may be immediately apparent when an OCP statement and its associated Hamiltonian BVP are not well-posed. However, for more complex systems, particularly with end-time free, this distinction may not be obvious. The following existence propositions help outline conditions under which infinite-order singular arcs may appear.

3.3.1 End-time Fixed

Consider the simplest form of Problem 1 with an unspecified terminal state and fixed end-time. The problem is stated in terms of the Mayer objective $\phi : \mathbb{R}^n \rightarrow \mathbb{R}$ with fixed end-time t_f .

$$\text{Problem 2} \left\{ \begin{array}{l} \min_u \quad J = \phi(\mathbf{x}(t_f)) \\ \text{s.t.} \quad \mathbf{x}(t_0) = \mathbf{x}_0 \\ \quad \quad u \in U \\ \quad \quad t_f \text{ fixed} \end{array} \right. \quad (3.12)$$

Because Lagrange and Mayer forms are interchangeable [131], the terminal cost objective is merely for notational convenience and warrants no loss of generality. Let the Mayer objective be defined such that a surface S can be constructed in \mathbb{R}^n containing the set of all points for which its gradient is zero.

$$S = \{\mathbf{x}_1 \in \mathbb{R}^n \mid \phi_{\mathbf{x}}(\mathbf{x}_1) = \mathbf{0} \in \mathbb{R}^n\} \quad (3.13)$$

The surface S describes the set of points over a subspace of \mathbb{R}^n such that the first-order necessary conditions for a minimum (or maximum) are met. The dimensionality of this subspace depends on the structure of the cost objective. If $k = 1$, the surface represents a regular point, whereas higher

dimensional k represents a hypersurface in \mathbb{R}^n .

Suppose the system permits feasible solutions terminating on S . This assumption requires a non-empty intersection with the fixed-time reachable set of the system. Though numerical computation of reachable sets is a rich field of study [169, 170], these methods are beyond the scope of this paper. Instead, it is reasonable to postulate that, if such a solution exists, it can be found through numerical solution of the Hamiltonian BVP. Under the preceding assumptions regarding the structure of Problem 2, the main result is summarized as follows.

Proposition 1. *Let $u^* \in U$ be an admissible control and let $\mathbf{x}^* \in \mathbb{R}^n$ be an optimal state trajectory solution of Problem 2 for $t \in [t_0, t_f]$ such that $\mathbf{x}^*(t_f) \in S$. Then $\phi_{\mathbf{x}}^*(t_f) = \mathbf{0} \in \mathbb{R}^n$ is sufficient for existence of a singular arc with local order $p \rightarrow \infty$.*

Proof. The proof begins by transforming the Mayer cost to its integral form.

$$J = \phi(\mathbf{x}(t_f)) = \phi(\mathbf{x}(t_0)) + \int_{t_0}^{t_f} \phi_{\mathbf{x}}(f + gu) dt \quad (3.14)$$

The leading term can be ignored because the initial state is fixed, and the integral cost is $L(\mathbf{x}, u) = \phi_{\mathbf{x}}(f + gu)$. The Hamiltonian for this system is formulated with abnormal multiplier λ_0 as

$$\begin{aligned} H &= \boldsymbol{\lambda}^T(f + gu) + \lambda_0 \phi_{\mathbf{x}}(f + gu) \\ &= (\boldsymbol{\lambda}^T + \lambda_0 \phi_{\mathbf{x}})(f + gu) \end{aligned} \quad (3.15)$$

For the existence of a candidate singular arc, the necessary condition for u requires

$$H_u = (\boldsymbol{\lambda}^T + \lambda_0 \phi_{\mathbf{x}})g = 0 \quad (3.16)$$

Taking the first time derivative gives

$$\begin{aligned} \frac{d}{dt} H_u &= (\dot{\boldsymbol{\lambda}}^T + \lambda_0 \phi_{\mathbf{x}\mathbf{x}} \dot{\mathbf{x}})g + \lambda_0 \phi_{\mathbf{x}} g_{\mathbf{x}} \dot{\mathbf{x}} \\ &= (-\lambda_0 \phi_{\mathbf{x}\mathbf{x}}(f + gu) - (\boldsymbol{\lambda}^T + \lambda_0 \phi_{\mathbf{x}})(f_{\mathbf{x}} + g_{\mathbf{x}}u) + \lambda_0 \phi_{\mathbf{x}\mathbf{x}} \dot{\mathbf{x}})g + \lambda_0 \phi_{\mathbf{x}} g_{\mathbf{x}} \dot{\mathbf{x}} \\ &= -(\boldsymbol{\lambda}^T + \lambda_0 \phi_{\mathbf{x}})(f_{\mathbf{x}} + g_{\mathbf{x}}u)g + \lambda_0 \phi_{\mathbf{x}} g_{\mathbf{x}}(f + gu) \\ &= (\boldsymbol{\lambda}^T + \lambda_0 \phi_{\mathbf{x}})(g_{\mathbf{x}}f - f_{\mathbf{x}}g) \end{aligned} \quad (3.17)$$

For convenience, define $\boldsymbol{\sigma}^T = \boldsymbol{\lambda}^T + \lambda_0 \phi_{\mathbf{x}}$. Equations Eq. (3.16) and Eq. (3.17) can be rewritten compactly as

$$H_u = \boldsymbol{\sigma}^T g = 0 \quad (3.18)$$

$$\frac{d}{dt} H_u = \boldsymbol{\sigma}^T [f, g] = 0 \quad (3.19)$$

where $[f, g] = (g_x f - f_x g)$ is the Lie bracket of f and g . Following the pattern established in References [171] and [118], higher-order derivatives of H_u can be summarized as

$$\begin{aligned} \frac{d^j}{dt^j} H_u &= \boldsymbol{\sigma}^T [f, [f, [\dots [f, g]]] \dots] \\ &= \boldsymbol{\sigma}^T [f, \text{ad}^{j-1}(f)g] \end{aligned} \quad (3.20)$$

for $j = 1, 2, \dots, p$ where $\text{ad}^j(f)g = [f, \text{ad}^{j-1}(f)g]$ and $\text{ad}^0(f)g = g$. Because $\boldsymbol{\sigma}$ appears linearly in H_u and all further derivatives, it is sufficient to show that if $\boldsymbol{\sigma} = \mathbf{0} \in \mathbb{R}^n$ then $H_u = 0$. Noting Eq. (3.5) and taking a total derivative

$$\begin{aligned} \dot{\boldsymbol{\sigma}}^T &= \dot{\boldsymbol{\lambda}}^T + \lambda_0 \dot{\phi}_{\mathbf{x}} \\ &= -\lambda_0 \phi_{\mathbf{x}\mathbf{x}}(f + gu) - (\boldsymbol{\lambda}^T + \lambda_0 \phi_{\mathbf{x}})(f_{\mathbf{x}} + g_{\mathbf{x}}u) + \lambda_0 \phi_{\mathbf{x}\mathbf{x}}(f + gu) \\ &= -\boldsymbol{\sigma}^T (f_{\mathbf{x}} + g_{\mathbf{x}}u) \end{aligned} \quad (3.21)$$

The terminal state is free, and the boundary conditions on the costates are $\boldsymbol{\lambda}(t_f) = \mathbf{0} \in \mathbb{R}^n$. Because $\phi_{\mathbf{x}}(t_f) = \mathbf{0} \in \mathbb{R}^n$, we have $\boldsymbol{\sigma}(t_f) = \mathbf{0} \in \mathbb{R}^n$ on the candidate singular arc. The dynamics of $\boldsymbol{\sigma}$ are a linear matrix differential equation, and therefore $\boldsymbol{\sigma}(t) = \mathbf{0} \in \mathbb{R}^n$ for $t \in [t_1, t_f]$. Thus, u will never reappear with a non-zero coefficient in $(d^j/dt^j)H_u$ for $j = 1, 2, \dots$, and Problem 2 has a candidate singular arc with local order $p \rightarrow \infty$. \square

We make some remarks regarding the utility of Proposition 1. First, the preceding results give a sufficient condition for existence of an infinite-order arc in Problem 2. That is, if a minimum of the Mayer objective is reachable in time $t = t_f$, then the local order is infinite. It is also important to clarify that, when Proposition 1 holds, it provides only a necessary condition for optimality by Theorem 1. Because the Minimum Principle remains valid on singular arcs, and the abnormal

multiplier $\lambda_0 \neq 0$, the solution is a potential minimum. However, as the traditional approach provides no new information on the singular arc through successive differentiation of the switching function, the solution is degenerate. The following Corollaries provide some useful consequences of Proposition 1.

Corollary 2.1. *A solution of Problem 2 with local order $p \rightarrow \infty$ is totally singular. That is, $H_u = 0$ for all $t \in [t_0, t_f]$.*

Proof. It is easy to see that the choice of t_1 over integration of σ in Eq. (3.21) is arbitrary. Thus, we conclude that on the singular arc, $H_u = 0$ for all $t \in [t_0, t_f]$. \square

Corollary 2.2. *Let Problem 2 have intrinsic order $q \rightarrow \infty$. Then $\phi_{\mathbf{x}}(t_f) = \mathbf{0} \in \mathbb{R}^n$ is necessary and sufficient for existence of a singular arc with local order $p \rightarrow \infty$.*

Proof. The proof for necessity is shown by contradiction. Suppose Problem 2 has a solution such that $\phi_{\mathbf{x}}(t_f) \neq \mathbf{0} \in \mathbb{R}^n$. Equation (3.5d) requires that $\lambda(t_f) = \mathbf{0} \in \mathbb{R}^n$. For $\sigma(t_f) = \lambda(t_f) + \lambda_0 \phi_{\mathbf{x}}(t_f) = \mathbf{0} \in \mathbb{R}^n$ to hold on the singular arc, $\lambda_0 = 0$. Thus, $(\lambda^T(t_f), \lambda_0) = \mathbf{0} \in \mathbb{R}^{n+1}$. This constitutes a violation of Theorem 1, contradicting the assumption that $\phi_{\mathbf{x}}(t_f) \neq \mathbf{0} \in \mathbb{R}^n$. \square

Proposition 1 is a logical finding for cases in which the Mayer objective has a minimum coinciding with the reachable set of the system. The infinite local order implies that the necessary conditions provide insufficient information to resolve the optimal control structure. The solution instead permits an infinite family of global minimizers satisfying the objective. Because of their exact nature, traditional indirect methods fail to reveal any solution. In addition, this non-uniqueness problem reduces Theorem 2 to a strict equality [160]. Thus, the necessary conditions hold in an absolute sense along the optimal singular arc, but the solutions lie within an uncountable set of optimal policies.

A conceptual illustration of local order is shown in Fig. 3.1. In Fig. 3.1a, for a reachable footprint of the system at time $t = t_f$, the order is finite if a minimum of the objective function lies outside this set. In this case, the costates are transverse to the objective function contours at

the edge of the reachable set. While uniqueness is still not guaranteed, singular arcs must appear with finite order (greater than or equal to the problem order). In contrast, Fig. 3.1b illustrates a solution for which the interior of the reachable set contains a minimum of the objective function. In this case, there is not enough information in the problem to identify any candidate control because all candidate solutions satisfy the objective. This path-indeterminacy is reflected in the null costate solution, and the singular arc remains unresolved. In contrast, if the reachable set of the system does not intersect the target set, the control form reverts to bang-bang/singular form, and Proposition 1 is ruled out. Although assumptions for reachability are difficult to prove analytically (outside of simple problems), trajectories can be verified in numerical solution of the Hamiltonian BVP. The following example is intended to clarify this behavior for a simple system.

3.3.2 Example: 1-D Integrator

The utility of Proposition 1 can be readily verified using an informative example. The seemingly trivial single integrator problem from Ref. [160] can yield an indeterminate solution structure. Consider the problem to minimize the objective

$$J = \int_0^1 xu \, dt \quad (3.22)$$

with state equation

$$\dot{x} = u \quad (3.23)$$

where the control is bounded to $|u| \leq 1$. The initial conditions are fixed to $x(0) = 0$, with the terminal state free. Applying Theorem 1 with abnormal multiplier λ_0 gives

$$H = \lambda u + \lambda_0 x u = (\lambda + \lambda_0 x)u \quad (3.24)$$

with costate dynamics

$$\dot{\lambda} = -\frac{\partial H}{\partial x} = -\lambda_0 u \quad (3.25)$$

and boundary conditions $\lambda(1) = 0$. Minimizing the Hamiltonian gives the bang-bang form

$$H_u = \lambda + \lambda_0 x \quad (3.26)$$

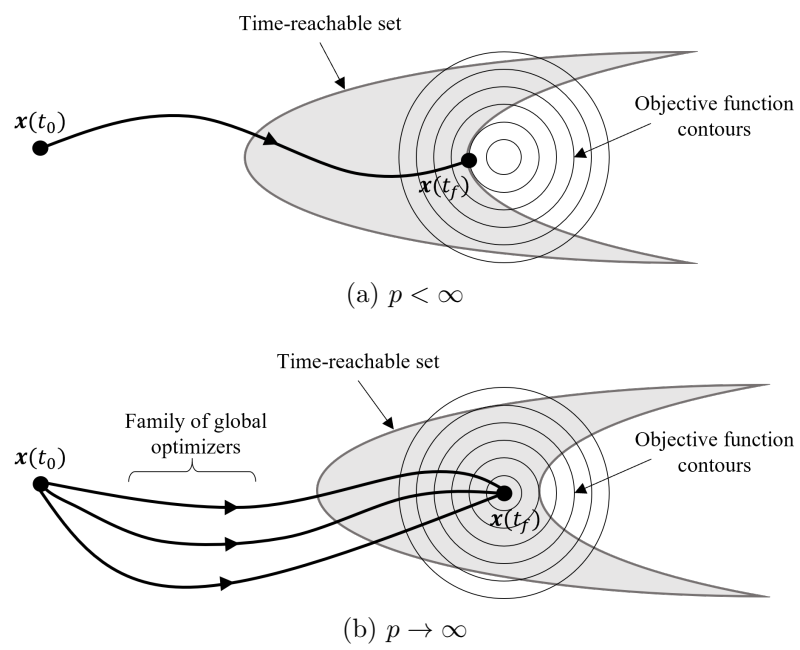


Figure 3.1: Conceptual illustration of finite- and infinite-order arc reachability.

On a singular arc,

$$\begin{aligned}\frac{d}{dt}H_u &= \dot{\lambda} + \lambda_0 \dot{x} \\ &= -\lambda_0 u + \lambda_0 u = 0\end{aligned}\tag{3.27}$$

Thus, we are presented with an indeterminate $0 = 0$ form, and the control variable will not appear in higher time derivatives of H_u . The problem then has intrinsic order $q \rightarrow \infty$. Any singular arcs, if they exist, will fail to reveal an optimal control policy under the standard necessary conditions.

Further insight on this problem can be gained by noting the cost objective can be recast into Mayer form as

$$\begin{aligned}J &= \int_0^1 xu \, dt = \int_0^1 x \dot{x} \, dt = \int_0^1 \frac{1}{2} \frac{d}{dt} (x)^2 \, dt = \frac{1}{2}x(1)^2 - \frac{1}{2}x(0)^2 \\ &\Rightarrow \phi(x(1)) = \frac{1}{2}x(1)^2\end{aligned}\tag{3.28}$$

where the initial cost penalty is dropped because $x(0) = 0$. Because the cost objective is stated in terms of an exact differential, the problem exhibits a quadratic form penalizing the terminal state $x(1)$. By Proposition 1 and Corollary 2.2, the singular arc exists if and only if $\phi_x = x(1) = 0$, which is satisfied for all control inputs u such that

$$x(1) = \int_0^1 u \, dt = 0\tag{3.29}$$

Further, these solutions are global minimizers because the objective Eq. (3.28) is convex. Equation (3.29) can be interpreted as a controllability requirement for existence of an infinite-order singular arc in the 1-D integrator. Clearly, this condition is satisfied for any optimal control history that integrates to zero for $t \in [0, 1]$. The control solution is non-unique, instead belonging to the family of global optimizers observed by Ross [159]. Figure 3.2 illustrates a subset of these minimizers for this example. Notable symmetry is present in the state and control phase histories. It is important to note that a solution of bang-bang form can still be found for this example, as pictured in Fig. 3.2c. However, because the control solution is non-unique, the necessary conditions do not dictate any one feasible control history.

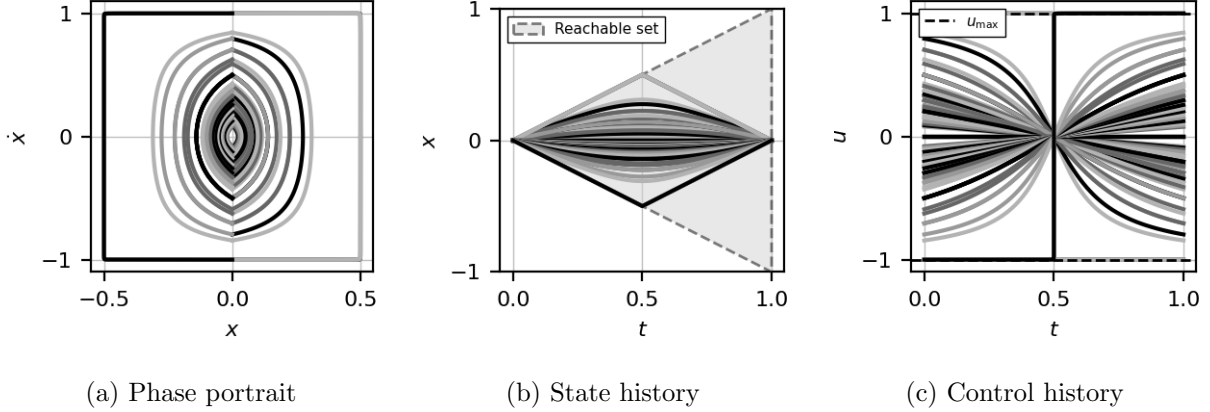


Figure 3.2: Symmetry of infinite-order arc solutions in 1-D integrator example.

3.3.3 End-time Free with State Constraint

The preceding results are developed for a fixed end-time with free terminal state. While this formulation covers a wide range of optimal control problems, it is often the case that the end-time is kept free in optimization. We next consider a class of problems in which the terminal state is partially constrained, and the end-time is determined implicitly by the transversality condition of Theorem 1. The terminal constraints must be satisfied exactly for any feasible solution. Let us assume that the terminal state constraints do not interfere with the optimal value of the objective. This assumption requires that any constraints permit terminal state configurations in the target set S . Let Θ represent a k -dimensional manifold in \mathbb{R}^n of state configurations in S compatible with all terminal constraints for $k \leq n$.

$$\Theta = \{\mathbf{x} \in S \mid \psi_1(\mathbf{x}) = \psi_2(\mathbf{x}) = \dots = \psi_m(\mathbf{x}) = 0\} \quad (3.30)$$

The end-time free optimization problem is stated as

$$\text{Problem 2'} \left\{ \begin{array}{l} \min_u \quad J = \phi(\mathbf{x}(t_f)) \\ \text{s.t.} \quad \mathbf{x}(t_0) = \mathbf{x}_0, \quad \mathbf{x}(t_f) \in \Theta \\ \quad \quad u \in U \\ \quad \quad t_f \text{ free} \end{array} \right. \quad (3.31)$$

The following extension of Proposition 1 gives existence conditions for singular arcs with infinite local order for the state-constrained end-time free problem.

Proposition 2. *Let $u^* \in U$ be an admissible control and let $\mathbf{x}^* \in \mathbb{R}^n$ be an optimal state trajectory solution of Problem 2' for $t \in [t_0, t_f]$ such that $\mathbf{x}^*(t_f) \in \Theta$. Then $\phi_{\mathbf{x}}^*(t_f) = \mathbf{0} \in \mathbb{R}^n$ is sufficient for existence of a singular arc with local order $p \rightarrow \infty$.*

Proof. See Appendix C. □

3.4 Relaxation by Auxiliary Covariance Minimization

The preceding section gives conditions for the existence of singular arcs with infinite order. This behavior is attributed to cases where the Mayer objective function and constraints are inadequate to fully define the optimal control. Although the solutions do not contradict the Minimum Principle, the indirect approach fails to reveal any optimal control. This indeterminacy introduces challenges in numerical optimization, as the optimal control law cannot be eliminated from the Hamiltonian BVP.

It is helpful to consider modifications to these problem structures that will eliminate infinite-order arcs. For example, an appropriate step could be the minimization of an objective implying terminal states outside the reachable set of the system. These modifications may include minimum time or control effort, in many cases uniquely defining the optimal control. However, a notable underlying factor in aerospace systems is the presence of systemic uncertainty. This uncertainty may be a result of inaccurate initial state knowledge or measurable uncertainty in parameters of the system. Traditional filtering and control strategies rely on certainty equivalence, which implies that estimation and control errors are orthogonal. These properties are well-known for linear systems. However, it is also the case that, for nonlinear system dynamics or measurement models, uncertainty propagation is greatly influenced by the mean trajectory [172]. This is sometimes referred to as the dual control problem [173], which seeks to develop control solutions robust to random inputs and disturbances. The path-dependent nature of uncertainty propagation for nonlinear systems

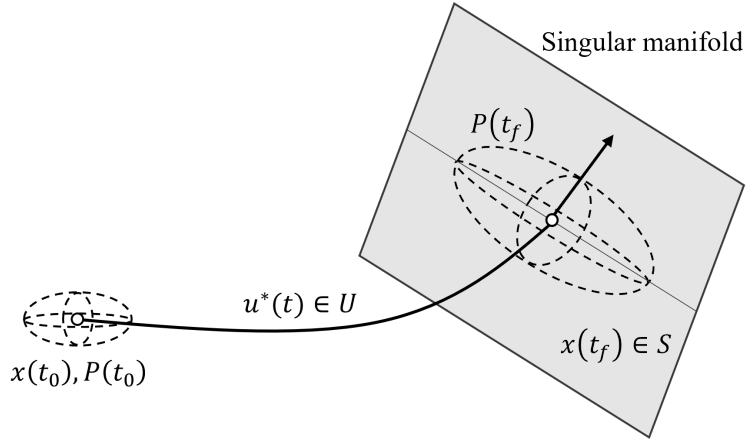


Figure 3.3: Conceptual illustration of auxiliary problem.

provides an outlet for resolving indeterminate problems.

In this section, we propose an auxiliary covariance minimization objective for relaxation of infinite-order singular arcs. A problem modification is developed to minimize the projection of a propagated Gaussian error distribution onto the Mayer objective. This problem is illustrated in Fig. 3.3. The method presents a practical strategy for mitigating uncertainty inherent to optimization of engineering systems. This uncertainty may be derived from historical or in-situ data. Alternatively, the approach can be interpreted as an artificial augmentation allowing for resolution of infinite-order singular arcs. The proposed method enables more robust solutions when compared to those developed from certainty equivalent objectives.

3.4.1 Uncertainty Quantification

Consider a scenario for Problem 1 wherein system states may not be known with absolute certainty. We seek to construct an appropriate system representation and objective capturing the effect of propagated uncertainty on output metrics of interest, largely following the procedure from Ref. [174]. Let \boldsymbol{x} represent a nominal or mean trajectory subject to the dynamics of Eq. (3.1). Furthermore, suppose the true state of the system $\boldsymbol{x}_t \in \mathbb{R}^n$ cannot be known with absolute certainty in optimization. A first-order Taylor series approximation of the truth state about the nominal

state and control is

$$\dot{\mathbf{x}}_t = f(\mathbf{x}, u, t) + \frac{\partial f(\mathbf{x}, u, t)}{\partial \mathbf{x}}(\mathbf{x}_t - \mathbf{x}) + \mathcal{O}(\|\mathbf{x}_t - \mathbf{x}\|^2) \quad (3.32)$$

Furthermore, let $\mathbf{w} \in \mathbb{R}^n$ represent an additive white Gaussian process in the uncertain system with noise intensity Q . For small deviations from the mean reference $\tilde{\mathbf{x}} = \mathbf{x}_t - \mathbf{x}$, the error dynamics are approximated to

$$\dot{\tilde{\mathbf{x}}}(t) = A(t)\tilde{\mathbf{x}}(t) + \mathbf{w}(t) \quad (3.33)$$

where $A(t)$ is the continuous-time approximation of the nonlinear dynamics sensitivities in Eq. (3.32).

A solution to Eq. (3.33) can be written as

$$\tilde{\mathbf{x}}(t_f) = \Phi(t_f, t_0)\tilde{\mathbf{x}}(t_0) + \int_{t_0}^{t_f} \Phi(t_f, \tau)\mathbf{w}(\tau) d\tau \quad (3.34)$$

where $\Phi(t_f, t_0)$ is a state transition matrix (STM) obeying the relations

$$\dot{\Phi}(t, t_0) = A(t)\Phi(t, t_0), \quad \Phi(t_0, t_0) = I_{n \times n} \quad (3.35)$$

Starting with the definition of the error covariance and assuming $\tilde{\mathbf{x}}$ and \mathbf{w} are uncorrelated gives

$$\begin{aligned} P(t_f) &= \mathbb{E}[\tilde{\mathbf{x}}(t_f)\tilde{\mathbf{x}}^T(t_f)] \\ &= \Phi(t_f, t_0)P(t_0)\Phi^T(t_f, t_0) + \int_{t_0}^{t_f} \Phi(t_f, \tau)Q(\tau)\Phi^T(t_f, \tau) d\tau \end{aligned} \quad (3.36)$$

with initial covariance

$$P(t_0) = \mathbb{E}[\tilde{\mathbf{x}}(t_0)\tilde{\mathbf{x}}^T(t_0)] \quad (3.37)$$

where Q represents the process noise intensity. Note that Eq. (3.36) fully defines the evolution of uncertainty at time t_f , relative to a first-order Taylor series approximation of the system dynamics.

The elements of STM could be augmented to the system state with matrix differential equation and initial conditions in Eq. (3.35), such as the approach in Ref. [121]. However, a more prudent approach lies in using symmetry of the error covariance matrix to reduce the number of terms that must be appended to the Hamiltonian BVP [112]. This behavior will be leveraged in the following sections.

It is often the case that a system contains constant parameters that influence the dynamics. Coupling between model parameters can introduce nonlinearity, even if the original system is linear. In this section, we illustrate how this property holds even though the parameters do not change with time. Further, the state error covariance and STM can be partitioned in such a way as to eliminate a subset of states and constraints. These quantities can instead be treated as constants in optimization. This decreases the complexity and dimensionality of the resulting Hamiltonian BVP, particularly when many parameters are present.

Consider the system dynamics

$$\dot{\mathbf{x}} = f(\mathbf{x}, \mathbf{p}, u, t), \quad \mathbf{x}(t_0) = \mathbf{x}_0 \quad (3.38)$$

where $\mathbf{p} \in \mathbb{R}^q$ is a set of constant parameters affecting the motion of the system. Consider deviations about a truth state \mathbf{x}_t as well as the true value of the parameters \mathbf{p}_t that are not known in optimization. In a similar manner as Eq. (3.33),

$$\dot{\mathbf{x}}_t \approx f(\mathbf{x}, \mathbf{p}, u, t) + \frac{\partial f(\mathbf{x}, \mathbf{p}, u, t)}{\partial \mathbf{x}}(\mathbf{x}_t - \mathbf{x}) + \frac{\partial f(\mathbf{x}, \mathbf{p}, u, t)}{\partial \mathbf{p}}(\mathbf{p}_t - \mathbf{p}) \quad (3.39)$$

which reduces to

$$\dot{\tilde{\mathbf{x}}}(t) = A(t)\tilde{\mathbf{x}}(t) + E(t)\tilde{\mathbf{p}}(t) + \mathbf{w}(t) \quad (3.40)$$

where $\tilde{\mathbf{p}} = \mathbf{p}_t - \mathbf{p}$ is the parameter error, and $A(t)$ and $E(t)$ are the state and parameter sensitivity matrices, respectively, from Eq. (3.38). A solution to Eq. (3.40) can be written as

$$\tilde{\mathbf{x}}(t_f) = \Phi(t_f, t_0)\tilde{\mathbf{x}}(t_0) + \Psi(t_f, t_0)\tilde{\mathbf{p}} + \int_{t_0}^{t_f} \Phi(t_f, \tau)\mathbf{w}(\tau) d\tau \quad (3.41)$$

where $\Psi(t_f, t_0)$ is the STM representing propagated effects of model parameter variations on $\tilde{\mathbf{x}}$.

Next, partition the state error covariance as

$$P = \begin{bmatrix} P_{xx} & P_{xp} \\ P_{px} & P_{pp} \end{bmatrix} \quad (3.42)$$

where

$$P_{xx} = E[\tilde{\mathbf{x}}\tilde{\mathbf{x}}^T], \quad P_{xp} = E[\tilde{\mathbf{x}}\tilde{\mathbf{p}}^T], \quad P_{pp} = E[\tilde{\mathbf{p}}\tilde{\mathbf{p}}^T] \quad (3.43)$$

We are interested in computing the terminal state error covariance for optimization. Assuming $\tilde{\mathbf{x}}$ and $\tilde{\mathbf{p}}$ are uncorrelated with process noise \mathbf{w} , the terminal state error covariance is expressed from Eq. (3.41) as

$$P_{xx}(t_f) = \Phi(t_f, t_0)P_{xx}(t_0)\Phi^T(t_f, t_0) + \Phi(t_f, t_0)P_{xp}(t_0)\Psi^T(t_f, t_0) + \Psi(t_f, t_0)P_{px}(t_0)\Phi^T(t_f, t_0) + \int_{t_0}^{t_f} \Phi(t_f, \tau)Q(\tau)\Phi^T(t_f, \tau) d\tau \quad (3.44)$$

In order to compute Eq. (3.44), we require the matrix differential equation governing the dynamics of each STM. Considering the homogenous dynamics of Eq. (3.41) at time t gives

$$\dot{\tilde{\mathbf{x}}}(t) = \dot{\Phi}(t, t_0)\tilde{\mathbf{x}}(t_0) + \dot{\Psi}(t, t_0)\tilde{\mathbf{p}} \quad (3.45)$$

Noting that Eq. (3.41) can be written at time t without process noise as

$$\begin{aligned} \dot{\tilde{\mathbf{x}}}(t) &= A(t)\tilde{\mathbf{x}} + E(t)\tilde{\mathbf{p}} \\ &= A(t)(\Phi(t, t_0)\tilde{\mathbf{x}}(t_0) + \Psi(t, t_0)\tilde{\mathbf{p}}) + E(t)\tilde{\mathbf{p}} \\ &= A(t)\Phi(t, t_0)\tilde{\mathbf{x}}(t_0) + (A(t)\Psi(t, t_0) + E(t))\tilde{\mathbf{p}} \end{aligned} \quad (3.46)$$

Comparing Eqs. (3.45) and (3.46), the dynamics of each STM are then known as

$$\dot{\Phi}(t, t_0) = A(t)\Phi(t, t_0), \quad \Phi(t_0, t_0) = I_{n \times n} \quad (3.47)$$

$$\dot{\Psi}(t, t_0) = A(t)\Psi(t, t_0) + E(t), \quad \Psi(t_0, t_0) = 0_{q \times q} \quad (3.48)$$

where initial conditions are inferred from Eq. (3.41).

The resulting subproblem is a deterministic representation of the stochastic differential equation in Eq. (3.32), with the STM integrated along the mean dynamics in Eq. (3.1). The nonlinearity of the system couples the nominal trajectory to its error covariance through the continuous time Jacobian matrices $A(t) \approx A(\mathbf{x}(t), \mathbf{p}(t), u(t))$ and $E(t) \approx E(\mathbf{x}(t), \mathbf{p}(t), u(t))$. Assuming additive white Gaussian process noise, the intensity matrix Q does not introduce any state-dependent effects in optimization. However, process noise is retained for consistency and numerical conditioning. Future work may consider path-dependent uncertainty propagation due to correlated state or control-dependent noise in the auxiliary problem.

3.4.2 Expectation Cost Objective

In order to introduce auxiliary error covariance states, we develop a Mayer objective function for the extended problem. The preceding section shows that a Mayer objective admits infinite-order singular arcs if a minimum is reachable subject to the system dynamics and constraints. Suppose the control objective seeks to minimize a set-point tracking or sum-squared deviation from a desired target set of terminal states. These functions are sometimes referred to as mean squared error (MSE) or signal-to-noise measures in robust optimization [175]. We seek to resolve the singular arc order by penalizing the projection of a propagated Gaussian uncertainty ellipse onto the deterministic terminal manifold.

Suppose the Mayer objective can be cast into the following form

$$J = \phi(\mathbf{x}(t_f)) = \sum_{i=1}^{\kappa} \frac{1}{2} \tilde{\phi}_i(\mathbf{x}(t_f))^2 \quad (3.49)$$

where $\tilde{\phi} : \mathbb{R}^n \rightarrow \mathbb{R}$ defines a loss or penalty function of state deviations with $\tilde{\phi}(\mathbf{x}^*(t_f)) = 0$. An expectation of Eq. (3.49) results in

$$\sum_{i=1}^{\kappa} \mathbb{E} \left\{ \frac{1}{2} \tilde{\phi}_i(\mathbf{x}(t_f))^2 \right\} = \sum_{i=1}^{\kappa} \text{tr}\{W_i(\mathbf{x}(t_f))P(t_f)\} \quad (3.50)$$

where $W_i \in \mathbb{R}^{n \times n}$ is a weighting matrix composed from the following outer product.

$$W_i = \begin{bmatrix} \tilde{\phi}_{x_1}^2 & \tilde{\phi}_{x_1} \tilde{\phi}_{x_2} & \cdots & \tilde{\phi}_{x_1} \tilde{\phi}_{x_n} \\ \tilde{\phi}_{x_2} \tilde{\phi}_{x_1} & \tilde{\phi}_{x_2}^2 & \cdots & \tilde{\phi}_{x_2} \tilde{\phi}_{x_n} \\ \vdots & \vdots & \ddots & \vdots \\ \tilde{\phi}_{x_n} \tilde{\phi}_{x_1} & \tilde{\phi}_{x_n} \tilde{\phi}_{x_2} & \cdots & \tilde{\phi}_{x_n}^2 \end{bmatrix}_i \quad (3.51)$$

As the matrix trace is a linear operator, the summation in Eq. (3.50) reduces the objective to

$$J = \text{tr}\{W(\mathbf{x}(t_f))P(t_f)\}, \quad W = \sum_{i=1}^{\kappa} W_i \quad (3.52)$$

By construction, W is a positive semidefinite matrix with $\text{rank}(W) \leq \kappa$. Equation (3.50) can be interpreted as penalizing a projection of the error covariance along the gradient of the penalty function, or the normal cone to the tangent cone of $\tilde{\phi}$ at $\mathbf{x}(t_f)$. If the penalty function is linear

in its arguments, then W is a constant matrix. However, if the penalty function is nonlinear, the weighting matrix W introduces state-dependent terminal excursions along the target set S for which the trace of the error covariance must be minimized. This introduces an additional degree of freedom in optimization.

3.4.3 Auxiliary Problem Definition

In this section, we present a novel method for relaxation of indeterminate control problems resulting from infinite-order singular arcs. The error covariance dynamics in Eq. (3.54) can be treated as an extended system with deterministic states, as stochastic perturbation terms have been removed. If nonlinear effects are present in the error covariance dynamics, the auxiliary problem can resolve the indeterminate control structure through minimization of the weighted covariance trace objective Eq. (3.52).

The error covariance solution in Eq. (3.36) introduces an additional n^2 states and initial constraints in optimization for elements of the STM. However, we will leverage the symmetry property of the error covariance matrix to reduce the dimensionality of the auxiliary problem. Taking a time derivative of Eq. (3.36) at time t and noting Eq. (3.35) gives

$$\begin{aligned} \dot{P}(t) = & \dot{\Phi}(t, t_0)P(t_0)\Phi^T(t, t_0) + \Phi(t, t_0)P(t_0)\dot{\Phi}^T(t, t_0) \\ & + \int_{t_0}^t \frac{\partial}{\partial t} \Phi(t, \tau)Q(\tau)\Phi^T(t, \tau) d\tau + \int_{t_0}^t \Phi(t, \tau)Q(\tau)\frac{\partial}{\partial t} \Phi^T(t, \tau) d\tau + \Phi(t, t)Q\Phi^T(t, t) \end{aligned} \quad (3.53)$$

Noting the STM dynamics in Eq. (3.35) and rearranging terms results in the well-known linear matrix differential equation for the error covariance dynamics

$$\dot{P}(t) = A(t)P(t) + P(t)A(t)^T + Q(t) \quad (3.54)$$

Similar expressions can be derived for the parameter-extended system in Eq. (3.44), which are omitted for brevity. We will utilize the partitioned system with uncertain parameters in the following section. The nominal state follows the dynamics in Eq. (3.11) and the error covariance dynamics

Eq. (3.54). Dropping notation for time dependency, the combined system is expressed as

$$\dot{\mathbf{x}} = f + gu \quad (3.55)$$

$$\dot{P} = (f_{\mathbf{x}} + g_{\mathbf{x}}u)P + P(f_{\mathbf{x}} + g_{\mathbf{x}}u)^{\text{T}} + Q \quad (3.56)$$

In the auxiliary problem the expectation cost Eq. (3.50) replaces the deterministic Mayer objective. The original objective is enforced by a terminal state constraint coinciding with target set S . The approach is applicable to both the end-time fixed and end-time free with partially-constrained terminal state. We consider the latter here but show examples for both cases. Given the preceding developments, the end-time free problem is summarized as follows.

$$\text{Problem 3} \left\{ \begin{array}{l} \min_u \quad J = \text{tr}\{W(\mathbf{x}(t_f))P(t_f)\} \\ \text{s.t.} \quad \mathbf{x}(t_0) = \mathbf{x}_0, \quad \mathbf{x}(t_f) \in \Theta \\ \\ P(t_0) = P_0 \\ \\ u \in U \\ \\ t_f \text{ free} \end{array} \right. \quad (3.57)$$

It is helpful to show that Problem 3 has a similar structure to Problem 2'. The auxiliary problem system is concatenated into nonlinear state-space form as

$$\begin{bmatrix} \dot{\mathbf{x}} \\ \text{vec}(\dot{P}) \end{bmatrix} = \begin{bmatrix} f \\ \text{vec}(f_{\mathbf{x}}P + Pf_{\mathbf{x}}^{\text{T}} + Q) \end{bmatrix} + \begin{bmatrix} g \\ \text{vec}(g_{\mathbf{x}}P + Pg_{\mathbf{x}}^{\text{T}}) \end{bmatrix} u \quad (3.58)$$

where $\text{vec}(\cdot)$ is the matrix vectorization operator. More compactly,

$$\dot{\mathbf{z}} = F(\mathbf{z}) + G(\mathbf{z})u, \quad \mathbf{z}(t_0) = \mathbf{z}_0 \quad (3.59)$$

where $\mathbf{z}^{\text{T}} = [\mathbf{x}^{\text{T}}, \text{vec}(P)^{\text{T}}] \in \mathbb{R}^l$ is an augmented state vector with initial conditions

$$\mathbf{z}(t_0)^{\text{T}} = [\mathbf{x}(t_0)^{\text{T}}, \text{vec}\{P(t_0)\}^{\text{T}}] \quad (3.60)$$

where $l = n(1 + n)$. The extended mappings are $F : \mathbb{R}^l \rightarrow \mathbb{R}^l$ and $G : \mathbb{R}^l \rightarrow \mathbb{R}^l$. The augmented problem is summarized as follows, where $O \in \mathbb{R}^{n^2}$ is the zero set corresponding to the dimensions

of $\text{vec}(P)$.

$$\text{Problem 3'} \left\{ \begin{array}{l} \min_u \quad J = \phi(\mathbf{z}(t_f)) \\ \text{s.t.} \quad \mathbf{z}(t_0) = \mathbf{z}_0, \quad \mathbf{z}(t_f) \in (\Theta \cup O) \\ \\ u \in U \\ \\ t_f \text{ free} \end{array} \right. \quad (3.61)$$

Because the control is affine in the system dynamics, and the initial state is fixed, Problem 3' and Problem 2' have equivalent forms.

We consider the indirect approach to the relaxed problem with augmented error covariance dynamics by adjoining the covariance dynamics to the Hamiltonian BVP [119,172]. In addition to the costates $\boldsymbol{\lambda}$, we require n^2 multipliers to adjoin the covariance states. Define a matrix $\Lambda \in \mathbb{R}^{n \times n}$ of multipliers corresponding to each entry of the matrix differential equation in Eq. (3.54).

$$\Lambda = \begin{bmatrix} \Lambda_1 & \cdots & \vdots \\ \Lambda_2 & \cdots & \Lambda_{n^2-1} \\ \vdots & \cdots & \Lambda_{n^2} \end{bmatrix} \quad (3.62)$$

The Hamiltonian for this system is constructed as

$$\begin{aligned} H &= \boldsymbol{\lambda}^\top \dot{\mathbf{x}} + \text{vec}(\Lambda)^\top \text{vec}(\dot{P}) \\ &= \boldsymbol{\lambda}^\top \dot{\mathbf{x}} + \text{tr}(\Lambda^\top \dot{P}) \\ &= \boldsymbol{\lambda}^\top (f + gu) + \text{tr}\{\Lambda^\top ((f_{\mathbf{x}}P + Pf_{\mathbf{x}}^\top + Q) + (g_{\mathbf{x}}P + Pg_{\mathbf{x}}^\top)u)\} \end{aligned} \quad (3.63)$$

where we use the property of the Frobenius inner-product that $\text{tr}(A^\top B) = \text{vec}(A)^\top \text{vec}(B)$ for real matrices A and B . The costate dynamics for Problem 3 can be written as

$$\dot{\boldsymbol{\lambda}}^\top = -\frac{\partial H}{\partial \mathbf{x}} = -\boldsymbol{\lambda}^\top (f_{\mathbf{x}} + g_{\mathbf{x}}u) - \frac{\partial}{\partial \mathbf{x}} \text{tr}\{\Lambda^\top ((f_{\mathbf{x}}P + Pf_{\mathbf{x}}^\top + Q) + (g_{\mathbf{x}}P + Pg_{\mathbf{x}}^\top)u)\} \quad (3.64a)$$

$$\dot{\Lambda} = -\frac{\partial H}{\partial P} = -(f_{\mathbf{x}}^\top \Lambda + \Lambda f_{\mathbf{x}}) - (g_{\mathbf{x}}^\top \Lambda + \Lambda g_{\mathbf{x}})u \quad (3.64b)$$

Because the control u appears linearly in the Hamiltonian, we expect the solution to have bang-bang singular form. The switching function for Problem 3 is

$$H_u = \boldsymbol{\lambda}^\top g + \text{tr}\{\Lambda^\top (g_{\mathbf{x}}P + Pg_{\mathbf{x}}^\top)\} \quad (3.65)$$

Next, consider the existence and order of singular arcs. Noting the objective in Eq. (3.50), the boundary conditions on the costates are

$$\boldsymbol{\lambda}(t_f) = \boldsymbol{\nu}^T \psi_{\mathbf{x}}(\mathbf{x}(t_f), t_f) \quad (3.66a)$$

$$\Lambda(t_f) = W \quad (3.66b)$$

By Proposition 1, $\phi_{\mathbf{z}} = \mathbf{0} \in \mathbb{R}^l$ is sufficient for existence of singular arcs with infinite order. For any weighting matrix $W \neq 0 \in \mathbb{R}^{n \times n}$, the boundary conditions for $\text{vec}(\Lambda(t_f)) \neq \mathbf{0} \in \mathbb{R}^{n^2}$ immediately rule out the sufficient condition. Thus, the relaxation method introduces an auxiliary problem to minimize the propagated state error covariance along the nominal trajectory, and the necessary conditions will reveal a candidate local minimum using the standard indirect approach.

3.4.4 Example: Uncertain Van der Pol Oscillator

We consider a variant of the example from Sec. 2.3.3 to demonstrate infinite-order singular arcs. The forced Van der Pol equation is

$$m\ddot{x} + 2c(x^2 - 1)\dot{x} + kx = u \quad (3.67)$$

where m , c , and k are real, positive parameters. For simplicity we set $m = k = 1$ and $c = 0.5$. The system is cast into first-order form with state vector $\mathbf{x} = [x_1, x_2]^T$ as

$$\dot{x}_1 = x_2 \quad (3.68a)$$

$$\dot{x}_2 = -(x_1^2 - 1)x_2 - x_1 + u \quad (3.68b)$$

The initial conditions are $x_1(0) = 1$ and $x_2(0) = 0$ with control bound $0 \leq u \leq 2$. The objective is to minimize the distance from the origin at fixed end-time $t_f = \pi$.

$$J = \frac{1}{2}x_1(t_f)^2 + \frac{1}{2}x_2(t_f)^2 \quad (3.69)$$

The traditional approach begins by forming the Hamiltonian

$$H = \lambda_1 x_2 + \lambda_2 (-(x_1^2 - 1)x_2 - x_1 + u) \quad (3.70)$$

The costate differential rates are

$$\dot{\lambda}_1 = \lambda_2(2x_1x_2 + 1) \quad (3.71a)$$

$$\dot{\lambda}_2 = -\lambda_1 + \lambda_2(x_1^2 - 1) \quad (3.71b)$$

with boundary conditions $\lambda_1(t_f) = x_1(t_f)$ and $\lambda_2(t_f) = x_2(t_f)$. On a candidate singular arc, the switching function defined by Eq. (2.10) is

$$H_u = \lambda_2 = 0 \quad (3.72)$$

Taking a first derivative gives

$$\frac{d}{dt}H_u = \dot{\lambda}_2 = -\lambda_1 + \lambda_2 2(x_1^2 - 1) = 0 \quad (3.73)$$

which in tandem with Eq. (3.72) implies $\lambda_1 = \lambda_2 = 0$ on the singular arc. Because the adjoint equations are linear in the costates, u will never reappear in differentiation with a non-zero coefficient. Therefore, the singular arc has intrinsic order $q \rightarrow \infty$. By Proposition 1, an optimal singular arcs exists if $\phi_{\mathbf{x}}(t_f) = (x_1(t_f), x_2(t_f)) = (0, 0)$. Intuitively, this condition suggests that any initial state from which the origin is reachable in fixed time t_f will produce the singular arc. If the end-time is varied such that the origin is not reachable, the solution will revert to bang-bang form. In our case, the problem permits singular arcs and $H_u = 0$ for all $t \in [0, \pi]$.

Results are generated for the Van der Pol example using the regularization strategy outlined in Sec. 3.5. Although traditional indirect methods do not yield a candidate control, the numerical shooting method is able to find a solution given a small non-zero guess for the initial costates. Figure 3.4 shows a phase portrait and control history for each solution found within the family of global minimizers. Each solution is consistent with the initial conditions and minimum of the sum-squared Mayer objective. Furthermore, the control solutions remain well within the upper and lower control bounds. While it is possible to find bang-bang trajectories satisfying the same objective, the existence of intermediate singular trajectories rules out the bang-bang solution as a globally unique control.

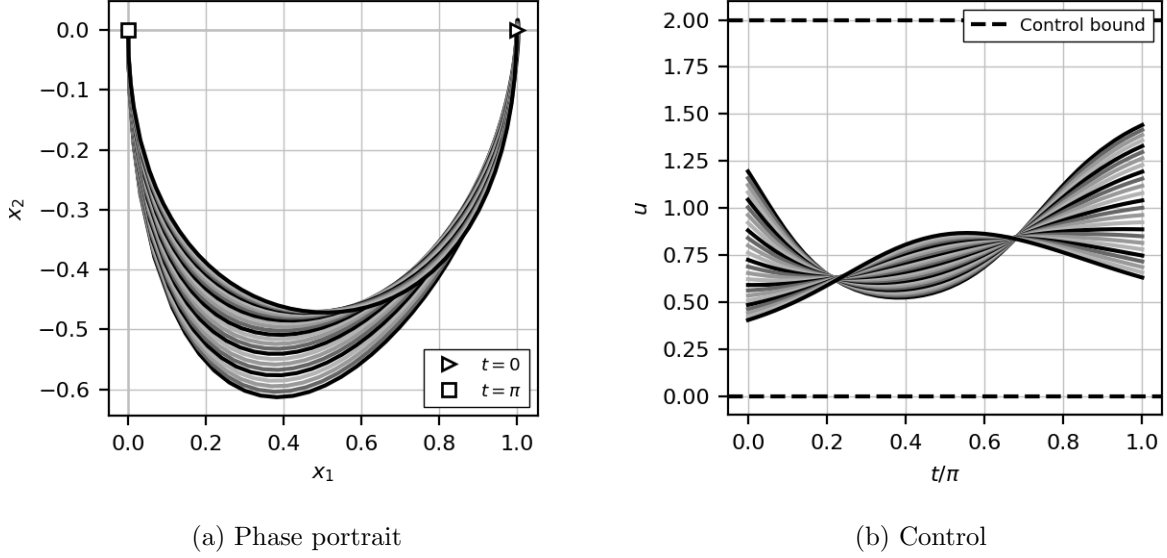


Figure 3.4: Infinite-order singular arc solutions of Van der Pol example.

The auxiliary covariance relaxation method is applied to the Van der Pol example as follows.

A state error covariance matrix P and sensitivity matrix A are constructed as

$$P = \begin{bmatrix} P_{11} & P_{12} \\ P_{12} & P_{22} \end{bmatrix}, \quad A = \begin{bmatrix} 0 & 1 \\ -2x_1x_2 - 1 & 1 - x_1^2 \end{bmatrix} \quad (3.74)$$

giving from Eq. (3.54) the state error covariance matrix dynamics

$$\dot{P}_{11} = 2P_{12} + Q_{11} \quad (3.75a)$$

$$\dot{P}_{12} = P_{11}(-2x_1x_2 - 1) + P_{12}(1 - x_1^2) + P_{22} + Q_{12} \quad (3.75b)$$

$$\dot{P}_{22} = 2P_{12}(-2x_1x_2 - 1) + 2P_{22}(1 - x_1^2) + Q_{22} \quad (3.75c)$$

The error covariance states are appended to the state equation with initial conditions $P_{11}(t_0) = 0.1^2$, $P_{12}(t_0) = 0$, and $P_{22}(t_0) = 0.05^2$. Process noise intensity terms are included for $Q_{11} = Q_{12} = 0$ and $Q_{22} = 0.01^2$. Referring to the expectation objective in Eq. (3.52), the weighting matrix is simply $W = I \in \mathbb{R}^{2 \times 2}$ leading to the auxiliary cost

$$J = \text{tr}\{P(t_f)\} = P_{11}(t_f) + P_{22}(t_f) \quad (3.76)$$

The terminal states are constrained to $x_1(t_f) = x_2(t_f) = 0$ ensuring the nominal state lies within the target set $S = \{0, 0\}$.

Results for the auxiliary Van der Pol problem are illustrated in Fig. 3.5. Two cases are plotted for comparison. The first is a sample trajectory from the infinite-order arc family that adheres to the boundary conditions and system dynamics. The second is the auxiliary minimization objective. In both cases, the error covariance terms are propagated forward with identical initial conditions for comparison. The control histories and switching functions are plotted in Figs. 3.5a and 3.5b, respectively. In the infinite-order case, the control remains well within the upper and lower bounds, and its corresponding switching function remains identically zero as expected. We emphasize that this solution is one of many possible global minimizers. In contrast, the auxiliary covariance objective produces a bang-bang control structure with a non-zero switching function for all time. This evidence supports the utility of the relaxation approach; with the auxiliary objective, the solution is uniquely determined. Furthermore, the covariance trace in Fig. 3.5c is considerably reduced from 0.10520 in the singular case to 0.05312 in the auxiliary problem. The net effect is about a 50% reduction in the expectation cost objective. It is interesting to note that, near time $t = \pi/4$, the covariance trace is actually larger in the auxiliary problem, meaning that the auxiliary cost is not necessarily lower at every point in time.

Figure 3.6 illustrates a phase portrait of both cases with the projected error covariance ellipse at equal time intervals of $\pi/10$. It is clear that the propagated error covariance matrix retains a lower trace in solution of the auxiliary problem compared to the indeterminate solutions. By application of indirect methods with regularization strategies, these solutions can be rapidly obtained for nonlinear systems. Although the Van der pol example is commonly seen as a theoretical problem, these results have implications for real-world systems for which optimal motion-planning can reduce systemic uncertainty.

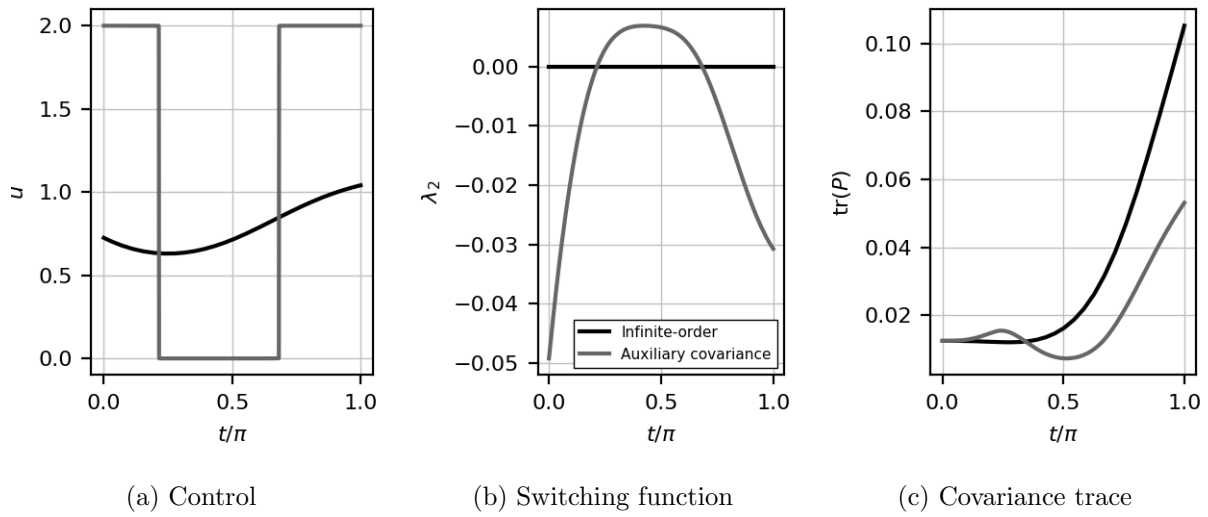


Figure 3.5: Auxiliary minimum solution of Van der Pol example.

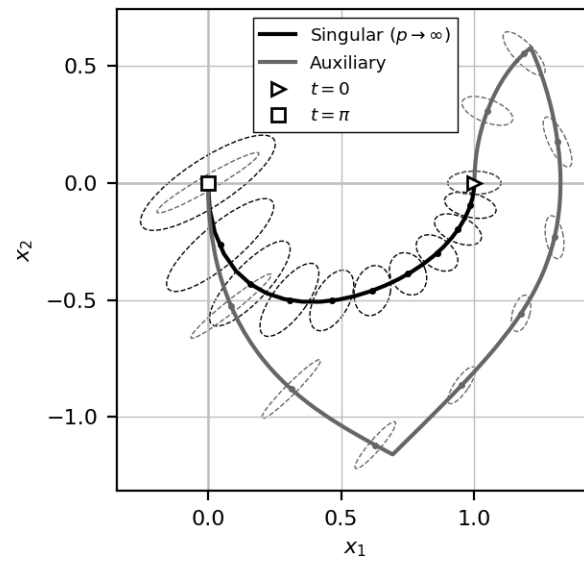


Figure 3.6: Phase portrait and error covariance propagation for Van der Pol example.

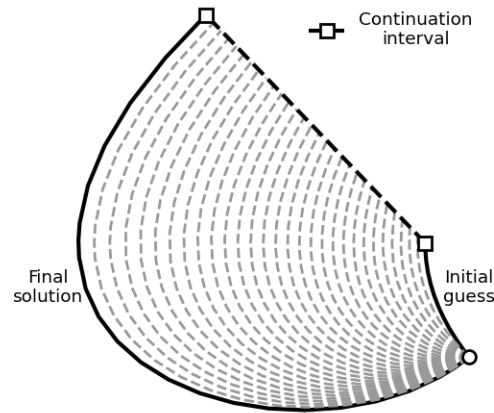


Figure 3.7: Numerical continuation homotopy over boundary condition parameters.

3.5 Numerical Solution Strategy for Complex Systems

The indeterminate problem presented in Propositions 1 and 2 introduces several difficulties in numerical solution. When constructing the indirect formulation, the switching function provides no new information on the optimal control policy. This in turn means the control variable u cannot be eliminated from the Hamiltonian BVP. Even in well-posed problems, solutions in bang-bang/singular form introduce challenges in optimization due to the discontinuous nature of the controls. These limitations can be overcome via the generalized regularization procedure of Chapter 2. The Hamiltonian is regular following this transformation, allowing for bounded quantities to be treated in optimization as unconstrained [99,176]. Regularization enables solution over bang-bang/singular problems without prior knowledge regarding the order and number of arcs. Regularization produces smooth, continuously differentiable functions that are compatible with variable step-size numerical integrators. Because the problem is regular, the infinite-order arcs can be resolved by inputting a non-zero initial costate guess to the BVP solver. The regularization method enables solutions that are otherwise unattainable under the traditional indirect approach, with only minor reduction in solution accuracy due to approximation.

A limitation of indirect methods is the small region of convergence in numerical solution

of the Hamiltonian BVP. Without a close initial trajectory, modern BVP solvers are unlikely to achieve convergence in complex problems. Though some methodologies exist for estimating initial costates [177, 178], these approaches are usually highly problem-specific. Homotopy continuation methods [83, 85, 179, 180] can greatly enhance convergence in complex problems by producing a series of neighboring BVPs. The method introduces a scalar continuation parameter over constants of the OCP process equations and boundary conditions. A short initial trajectory is used as a guess for neighboring solutions. Starting from an initial trajectory, the continuation step pushes the constants to desired values by solving each BVP with the prior solution as its initial guess. Figure 3.7 shows a conceptual illustration of a continuation interval for a simple problem. Numerical continuation methodologies can greatly enhance convergence in complex problems where a feasible initial guess is difficult to generate.

The auxiliary covariance minimization problem presented in Sec. 3.4 is solved by appending elements of the covariance dynamics as states in the Hamiltonian BVP. Because the error covariance matrix is symmetric, the full vectorization operator contains redundant information that contributes numerical overhead in optimization. Instead, the half-vectorization operator is used to extract the unique elements of P_{xx} and P_{xp} from Eq. (3.42) along with the corresponding initial conditions. Parameter uncertainties in P_{pp} are appended as constants in the BVP solver, reducing the dimensionality of the problem compared to appending the full error covariance matrix dynamics. Finally, through application of numerical continuation methods, solutions are obtained for complex engineering problems starting from a rough initial guess.

3.6 Aerospace Mission Design Applications

The auxiliary covariance minimization strategy provides an alternative approach when traditional indirect methods yield indeterminate solutions. Solution over the extended state-space produces well-posed solutions with finite singular arc order. In the following examples, we illustrate the method in practical aerospace engineering applications.

3.6.1 Relative Orbit Formation Flying

The relative motion of spacecraft has been extensively studied for on-orbit formation flying and station keeping [181, 182]. Optimal maneuvering in relative orbital motion is of high import, as small perturbations can increase station-keeping requirements over successive orbits. Spacecraft maneuvers are usually subject to strict fuel usage and thrust constraints, leading a number of studies to develop minimum-fuel impulsive transfer [183, 184] and relative orbit element control laws [185, 186]. Other studies have sought to perform optimal maneuvering for passively-safe satellite station-keeping and collision avoidance [187–190]. This represents a challenging task, particularly when observations can only be made with limited resources or time-frames. Periods of time in which the spacecraft must rely on elapsed state information pose adverse risk if the vehicle cannot adequately compensate for potential collisions.

In this example, a simple relative motion model with Gaussian uncertainty is studied. For a class of spacecraft maneuvers, the control structure can produce indeterminate singular arcs. The auxiliary relaxation method is applied to these cases to demonstrate its utility in spacecraft motion planning. Further, the method produces open-loop trajectories minimizing the effects of model and state uncertainty in the relative motion system.

To begin, the Tschauner-Hempel equations [191] describe the relative motion of a deputy (or follower) satellite with respect to a chief (or leader) satellite placed in an elliptical orbit. With some moderate assumptions, notably a circular chief orbit and small relative separation distances, the well-known Clohessy-Wiltshire (CW) [192] equations of motion result. Atmospheric drag terms may become important at lower atmospheric altitudes due to the integrated effect of perturbing forces. The CW equations can be modified to include quadratic drag terms [193] for an initially circular chief orbit, where it is assumed the chief and deputy have identical drag coefficients. The

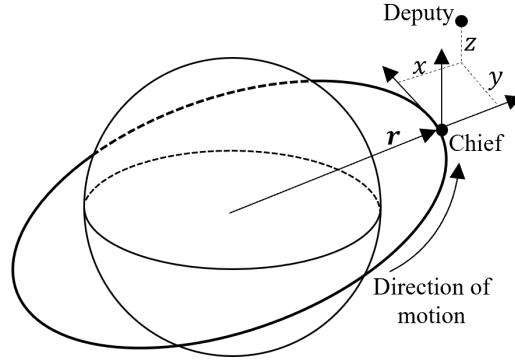


Figure 3.8: Relative orbital motion geometry in rotating Hill frame.

equations of motion are stated as

$$\ddot{x} - 2n\dot{y} - 3(1 + 4b^2)n^2x = u_1 \quad (3.77a)$$

$$\ddot{y} + 2n\dot{x} = u_2 \quad (3.77b)$$

$$\ddot{z} + n^2z = u_3 \quad (3.77c)$$

where n is the mean orbit rate defined as

$$n = \sqrt{\frac{\mu}{a^3}} \quad (3.78)$$

for a circular chief orbit with semi-major axis a and gravity parameter μ . The parameter b incorporates vehicle shape and aerodynamic properties contributing to aerodynamic drag. The relative motion states include the radial x , along-track y , and cross-track z components. See Figure 3.8. The rotating Hill frame is defined attached to the chief spacecraft, with constant orbit rate $\dot{\theta} = n$.

A reasonable objective of the on-orbit maneuver is to place a spacecraft in a safe holding orbit. Such applications might include observation black-out windows or abort scenarios, in which the deputy spacecraft must minimize the probability of a future collision. A well-known feature of the linear CW dynamics is the *secular drift* property [194], which describes the along-track drift rate of the center of motion in the x - y plane. The zero secular drift condition can be stated as

$$2nx + \dot{y} = 0 \quad (3.79)$$

which remains compatible with the quadratic drag terms so long as $b < \sqrt{3}/6$ (see Ref. [193]). It is easy to see that the cross-track dynamics and secular drift decouple the in-plane and out-of-plane relative motion states. For simplicity, out-of-plane motion is excluded in this example, although the results still apply to general 3D relative motion case.

Neglecting the cross-track component and casting into state-space form gives

$$\dot{\mathbf{x}} = A\mathbf{x} + B\mathbf{u} \quad (3.80)$$

with linear dynamics

$$A = \begin{bmatrix} 0 & 0 & 1 & 0 \\ 0 & 0 & 0 & 1 \\ 3(1+4b^2)n^2 & 0 & 0 & 2n \\ 0 & 0 & -2n & 0 \end{bmatrix}, \quad B = \begin{bmatrix} 0 & 0 \\ 0 & 0 \\ 1 & 0 \\ 0 & 1 \end{bmatrix} \quad (3.81)$$

$$\mathbf{x} = [x_1, x_2, x_3, x_4]^T, \quad \mathbf{u} = [u_1, u_2]^T \quad (3.82)$$

where $x_1 = x$, $x_2 = y$, $x_3 = \dot{x}$, and $x_4 = \dot{y}$. Consider the objective minimizing secular drift at the end of a maneuver over one nominal chief orbit

$$J = \frac{1}{2}(2nx_1(t_f) + x_4(t_f))^2, \quad t_f = T \quad (3.83)$$

where $T = 2\pi/n$ is the orbital period. The maximum thrust in each dimension is limited to $-u_{\max} \leq u_i \leq u_{\max}$ for $i = 1, 2$. The initial states are fixed as

$$\mathbf{x}(t_0) = \mathbf{x}_0 \quad (3.84)$$

Following the maneuver, suppose the deputy must be placed in a desired holding orbit with geometric properties [194]

$$\sqrt{\left(6x_1(t_f) + \frac{4x_4(t_f)}{n}\right)^2 + \left(\frac{2x_3(t_f)}{n}\right)^2} - A_y = 0 \quad (3.85)$$

$$x_2(t_f) - \frac{2x_3(t_f)}{n} - y_{\text{off}} = 0 \quad (3.86)$$

where A_y is the maximum amplitude of relative motion in the along-track direction, and y_{off} is the desired along-track separation of the relative orbit centroid. The terminal states are otherwise left free in optimization in order to provide additional degrees of freedom in matching the zero secular drift condition.

Comparing Eq. (3.83) to the structure of Problem 2, Proposition 2 indicates that a singular arc with $p \rightarrow \infty$ exists when the zero-drift condition is met Eq. (3.79). Since (A, B) is a controllable pair [195], the feasibility of the solution is dictated by the thrust bound u_{max} , where we assume the terminal constraint is contained in the reachable set. Forming the Hamiltonian for the in-plane CW equations gives

$$H = \lambda_1 x_3 + \lambda_2 x_4 + \lambda_3(3(1 + 4b^2)n^2 x_1 + 2n x_4 + u_1) + \lambda_4(-2n x_3 + u_2) \quad (3.87)$$

with costate dynamics

$$\dot{\lambda}_1 = -\frac{\partial H}{\partial x_1} = -3(1 + 4b^2)n^2 \lambda_3 \quad (3.88a)$$

$$\dot{\lambda}_2 = -\frac{\partial H}{\partial x_2} = 0 \quad (3.88b)$$

$$\dot{\lambda}_3 = -\frac{\partial H}{\partial x_3} = 2n \lambda_4 \quad (3.88c)$$

$$\dot{\lambda}_4 = -\frac{\partial H}{\partial x_4} = -\lambda_2 - 2n \lambda_3 \quad (3.88d)$$

Because control terms u_1 and u_2 appear linearly in the Hamiltonian, Eq. (3.87), the optimal control is bang-bang/singular. The structure of the optimal control policies is

$$u_i^* = \begin{cases} +u_{\text{max}}, & \text{if } \lambda_{i+2} < 0, \\ -u_{\text{max}}, & \text{if } \lambda_{i+2} > 0, \\ \text{indefinite}, & \text{if } \lambda_{i+2} = 0 \end{cases} \quad i = 1, 2 \quad (3.89)$$

We are motivated to consider the existence of singular arcs for the in-plane relative motion system. Considering the switching function for u_1 on a singular arc

$$H_{u_1} = \lambda_3 = 0 \quad (3.90)$$

Successive differentiation gives

$$\frac{d}{dt}(H_{u_1}) = \dot{\lambda}_3 = 2n\lambda_4 = 0 \quad (3.91a)$$

$$\frac{d^2}{dt^2}(H_{u_1}) = 2n\dot{\lambda}_4 = -2n(\lambda_2 + 2n\lambda_3) = 0 \quad (3.91b)$$

$$\frac{d^3}{dt^3}(H_{u_1}) = -2n(\dot{\lambda}_2 + 2n\dot{\lambda}_3) = -2n(2n\lambda_4) = 0 \quad (3.91c)$$

Similarly, for the u_2^* control policy,

$$H_{u_2} = \lambda_4 = 0 \quad (3.92)$$

with successive derivatives

$$\frac{d}{dt}(H_{u_2}) = \dot{\lambda}_4 = -\lambda_2 - 2n\lambda_3 = 0 \quad (3.93a)$$

$$\frac{d^2}{dt^2}(H_{u_2}) = -\dot{\lambda}_2 - 2n\dot{\lambda}_3 = -2n(2n\lambda_4) = 0 \quad (3.93b)$$

Because λ_4 appears cyclicly in derivatives of the switching functions for u_1 and u_2 , the control terms will never reappear in differentiation and the problem has intrinsic order $q \rightarrow \infty$. By Corollary 2.2, existence of an infinite-order singular exists if and only if $\phi_{\mathbf{x}} = 0$, which is precisely the zero secular drift condition in Eq. (3.79). Thus, solution structure exhibits an indeterminate form.

A family of global optimizers is generated for visualization of the infinite-order singular relative motion problem. Parameters for this example are adapted from a prior relative motion study [187]. The reference LEO chief is chosen with a semi-major axis of 6,652 km, giving an orbital period of 90 minutes. The chief orbit is assumed initially circular with an eccentricity of zero. The spacecraft is initialized with fixed 100 m radial and 0 m along-track offsets and zero relative velocities. The final time of the simulation is fixed to $t_f = T$. A maximum thrust limit of 1.5 mm/s² is enforced in the radial and along-track components. A nominal value of the drag parameter b is chosen from Ref. [182] for a chief and deputy spacecraft with mass of 154.4 kg, drag coefficient of 2.5, and drag area of 1.3 m². Boundary conditions and parameters used in the relative motion example are given in Table 3.1. An initial trajectory is propagated forward for one orbit period with rough initial costate guesses. With fixed end-time, the numerical BVP solver is able

Table 3.1: State constraints and problem parameters for CW relative motion example.

	x (m)	y (m)	\dot{x} (m/s)	\dot{y} (m/s)	t (s)
Initial	100	0	0	0	0
Final	Eqs. (3.85–3.86)				T

(a) States

Parameter	n (1/s)	b	A_y (m)	y_{off} (m)	u_{max} (mm/s ²)
Value	0.0011636	0.02105	250	500	1.5

(b) Parameters

to converge to a local minimum without precise initial costates. The cost objective in Eq. (3.83) is minimized to ensure the nominal secular drift at the end of the trajectory trends to zero.

A sample of trajectories along the infinite-order arcs is plotted in Fig. 3.9. In Fig. 3.9a, all trajectories emanate from the fixed initial radial and along-track offsets, terminating on the 250-by-125 m target orbit in Hill frame coordinates. In Fig. 3.9b, the phase portrait indicates that the terminal relative velocity components vary up to 250 mm/s radial and 650 mm/s along-track within the family of solutions. The secular drift along each trajectory is driven identically to zero, and the cost objective of Eq. (3.83) is minimized precisely. This indicates that all solutions produce combinations of radial offset and along-track velocity that (nominally) eliminate along-track drift following the maneuver. The target set in this example can be visualized a 2-dimensional manifold within the state-space that defines a proportional relationship between radial offset and along-track velocity. This illustrates the concepts presented in Sec. 3.3, which argue that a target set coinciding with the reachable set of the system produces infinite local order. In other words, minimizing the drift error alone is not sufficient to resolve the traditional optimality necessary conditions, because the target set is reachable with end-time fixed and bounded control.

The auxiliary covariance relaxation method is a potential candidate for resolving infinite-order singular arcs in the planar CW dynamics. Note from Eq. (3.83) that Eq. (3.50) can be

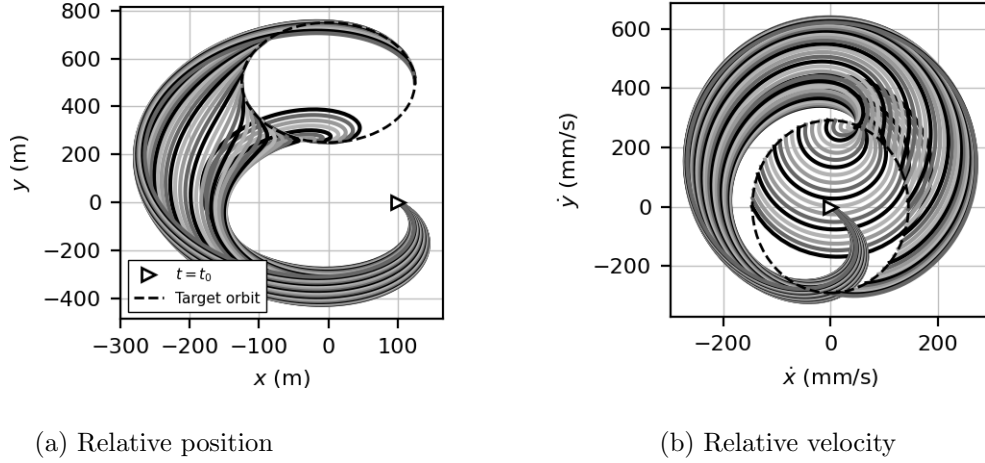


Figure 3.9: Infinite-order singular solution arcs in the CW relation motion example.

expressed as

$$J = \frac{1}{2} \tilde{\phi}(\mathbf{x}(t_f))^2 \quad (3.94)$$

where

$$\tilde{\phi}(\mathbf{x}(t_f)) = 2nx_1(t_f) + x_4(t_f) \quad (3.95)$$

giving the weighting matrix

$$W = \begin{bmatrix} \tilde{\phi}_{\mathbf{x}}^T(t_f) \tilde{\phi}_{\mathbf{x}}(t_f) \end{bmatrix} = \begin{bmatrix} 4n^2 & 0 & 0 & 2n \\ 0 & 0 & 0 & 0 \\ 0 & 0 & 0 & 0 \\ 2n & 0 & 0 & 1 \end{bmatrix} \quad (3.96)$$

Note that the dynamics in Eq. (3.81) are linear, removing path-dependency of the covariance dynamics from the developments of Sec. 3.4.3. However, a parameter uncertainty approach introduces nonlinearity in the system dynamics that can be exploited to resolve the solution structure. Suppose the chief orbit is not precisely circular, but subject to natural variation in the orbit rate due to higher-order gravity harmonics, solar radiation pressure, or other perturbations. The mean orbit rate parameter n is augmented as an uncertain state in the system. This parameter extension approach could also reflect epistemic uncertainty due to assumptions of the system dynamics, which

implicitly rely on the underlying assumptions for the CW relative motion dynamics. The auxiliary problem for the extended state-space is stated as

$$\mathbf{x} = [x_1, x_2, x_3, x_4, n] \quad (3.97)$$

with initial covariance matrix for the extended system

$$P_0 = \text{diag} \{P_{11}(t_0), P_{22}(t_0), P_{33}(t_0), P_{44}(t_0), \sigma_n^2\} \quad (3.98)$$

and sensitivity matrix

$$A = \begin{bmatrix} 0 & 0 & 1 & 0 & 0 \\ 0 & 0 & 0 & 1 & 0 \\ n^2(12b^2 + 3) & 0 & 0 & 2n & 2nx_1(12b^2 + 3) + 2x_4 \\ 0 & 0 & -2n & 0 & -2x_3 \\ 0 & 0 & 0 & 0 & 0 \end{bmatrix} \quad (3.99)$$

Observe that the first-order sensitivities of the system incorporate path-dependent evolution of uncertainty from variation in the mean orbit rate. This behavior is visible in the last column of A , which includes nonlinear effects in the state error covariance propagation. The weighting matrix W is augmented with rows and columns of zeros to retain dimensional consistency with the extended state.

$$W' = \begin{bmatrix} W & 0_{4 \times 1} \\ 0_{1 \times 4} & 0 \end{bmatrix} \quad (3.100)$$

Next, restate the auxiliary objective for the relative motion example as

$$J = \text{tr}\{W'P(t_f)\} = 2P_{14}n + P_{44} + 2n(2P_{11}n + P_{14}) \quad (3.101)$$

with initial constraint $P(t_0) = P_0$ and auxiliary dynamics in Eq. (3.54). Further, we impose the terminal constraint $\tilde{\phi}(\mathbf{x}(t_f)) = 0$ on the nominal trajectory to terminate on the target set. This ensures the zero secular drift condition is exactly satisfied in solution of the auxiliary problem.

Auxiliary states and parameters for the relative motion example are summarized in Table 3.2. These states represent the components of the augmented error covariance dynamics. Process noise

Table 3.2: Auxiliary states and problem parameters for relative motion example. Initial correlated uncertainties are assumed zero.

	P_{11} (m ²)	P_{22} (m ²)	P_{33} (m ² /s ²)	P_{33} (m ² /s ²)	σ_n^2 (1/s ²)
Initial	0.01 ²	0.01 ²	0.001 ²	0.001 ²	(0.0075n) ²
Final	free	free	free	free	free

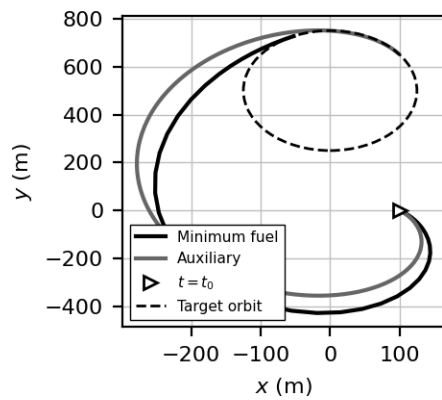
(a) Auxiliary states

Parameter	Q_{11} (m/s)	Q_{22} (m/s)	Q_{33} (m/s ²)	Q_{44} (m/s ²)
Value	0	0	2×10^{-5}	2×10^{-5}

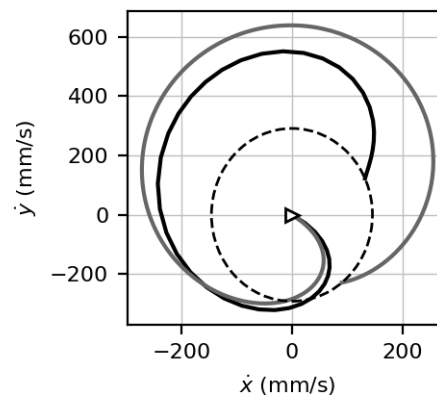
(b) Auxiliary parameters

is omitted from the kinematic equations for x and y . Velocity states are augmented with an artificial noise intensity of 2×10^{-5} m/s² from Ref. [187]. Results are generated through the numerical solution procedure in Sec. 3.5. The augmented states are appended to the BVP solver, where symmetry in the covariance matrix is leveraged to eliminate the lower triangular entries. A numerical continuation procedure is performed on the terminal along-track constraint and secular drift constraint. In order to provide a meaningful basis for comparison, the auxiliary solution is compared to a sample of the infinite-order singular solution set. One such trajectory includes the minimum control (or fuel) solution, which is obtained by minimizing the sum-square integrated control effort. This objective is often pursued in order to minimize propellant usage during the maneuver. This provides a relevant metric for comparison to solution of the auxiliary problem.

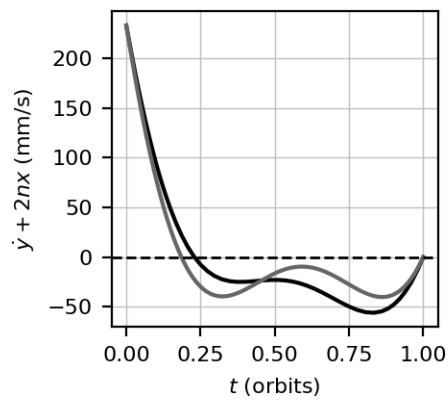
Figure 3.10 illustrates nominal trajectories for the minimum fuel objective and auxiliary covariance minimization objective. The target orbit properties of Eq. (3.85) and Eq. (3.85) are plotted as a dashed line in each plot. The relative position trajectories in Fig. 3.10a show the initial and terminal constraints to be satisfied, as both solutions end on the desired target reference ellipse as in the singular solution case. Both trajectories circumnavigate about the origin with sufficient separation distance, although this constraint is not explicitly enforced. This behavior is desirable for a chief spacecraft placed at the origin in order to reduce collision probability. The



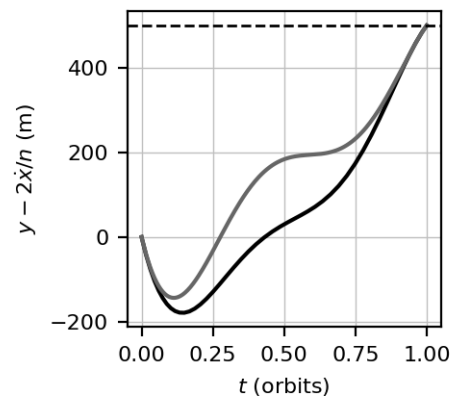
(a) Relative position



(b) Relative velocity



(c) Secular drift



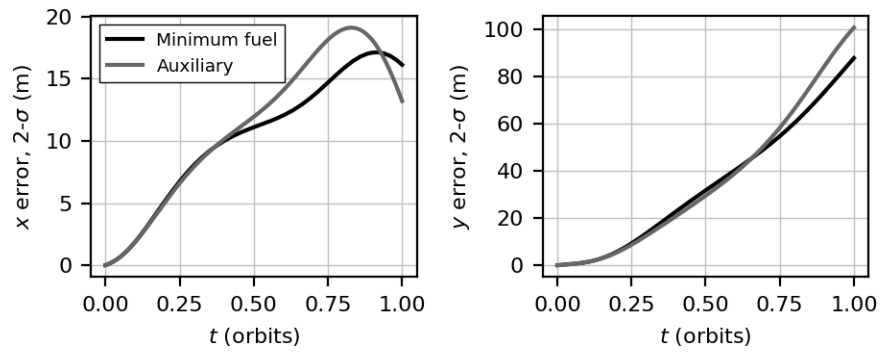
(d) Along-track centroid

Figure 3.10: Infinite-order singular solution arcs in the CW relation motion example.

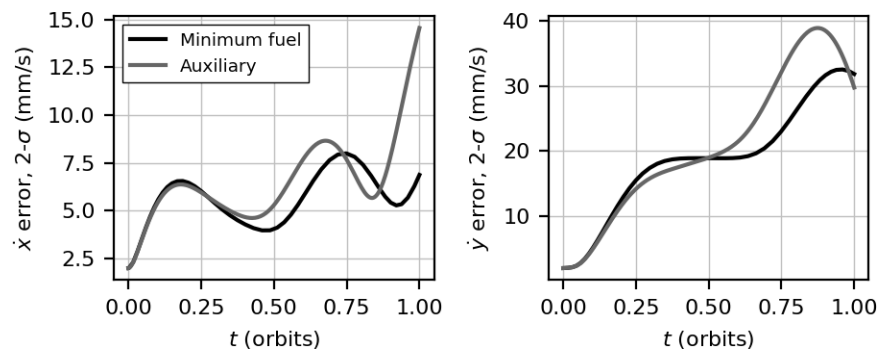
velocity phase portrait for each solution is given in Fig. 3.10b. Constraints on the terminal velocity are also satisfied. However, it is interesting to note that the minimum fuel transfer sees lower excursions in the relative velocity, taking a path interior to the auxiliary minimum solution. The auxiliary solution utilizes 0.501 m/s of integrated ΔV , versus 0.456 m/s in the minimum control effort solution; an increase of about 10%. The nominal secular drift and along-track centroid are illustrated in Figures 3.10c and 3.10d, respectively. Both conditions are matched, indicating a feasible solution is found.

The preceding results for the relative motion example illustrate that, given perfect system state and dynamics knowledge, the relative motion example produces a family of trajectories terminating with zero secular drift. However, these trajectories will not perform identically given imprecise system state knowledge or uncertain parameters. For each solution, a state error covariance is propagated with identical initial conditions and uncertainty. Position and velocity time histories are shown in Fig. 3.11. Referring to Eq. (3.101), the secular drift error is minimized by decreasing terminal errors in radial position x and along-track velocity \dot{y} , as well as the correlation between each. In Fig. 3.11a, the radial position error ends moderately lower for the auxiliary problem solution, whereas the minimum fuel solution has higher errors in the x coordinate. The opposite trend is noted in the along-track position error, which is actually lower for the minimum fuel solution. Similarly, in Fig. 3.11b the terminal radial velocity error is much higher in the auxiliary problem, but the along-track velocity error is decreased. Uncertainty in some state-space dimensions is increased in order to push uncertainty away from the singular manifold, in turn reducing the statistical variation of along-track drift. However, this benefit comes at the cost of increasing uncertainty in other dimensions of the problem.

Figure 3.12a shows errors in the secular drift terms. Both solutions begin with the same drift uncertainty, because the initial covariance is fully constrained. In Fig. 3.12a, the auxiliary solution sees a higher peak at about 0.6 orbits in comparison to the minimum fuel solution. However, the terminal drift error is moderately reduced, indicating that the solution is a local minimum of the cost objective in Eq. (3.101). This concept is further illustrated by Fig. 3.12, which shows the

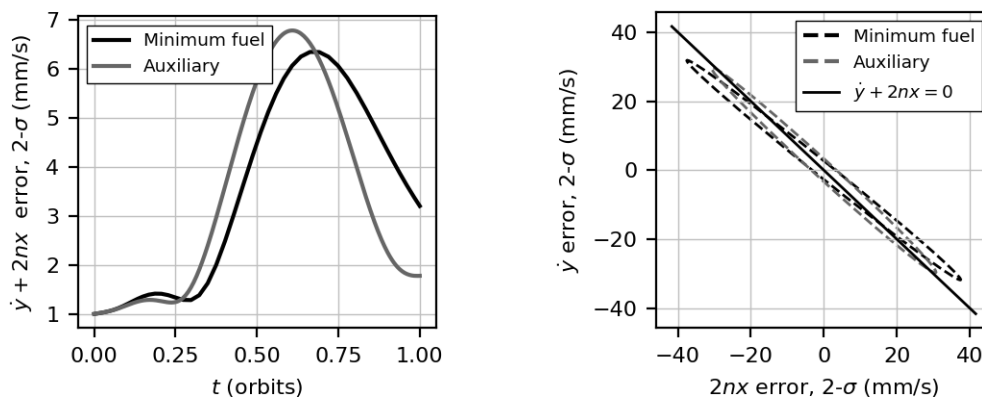


(a) Relative position



(b) Relative velocity

Figure 3.11: Propagated position and velocity errors for relative motion example.



(a) Secular drift error

(b) Secular drift error

Figure 3.12: Terminal state error covariances projected onto zero-drift target manifold.

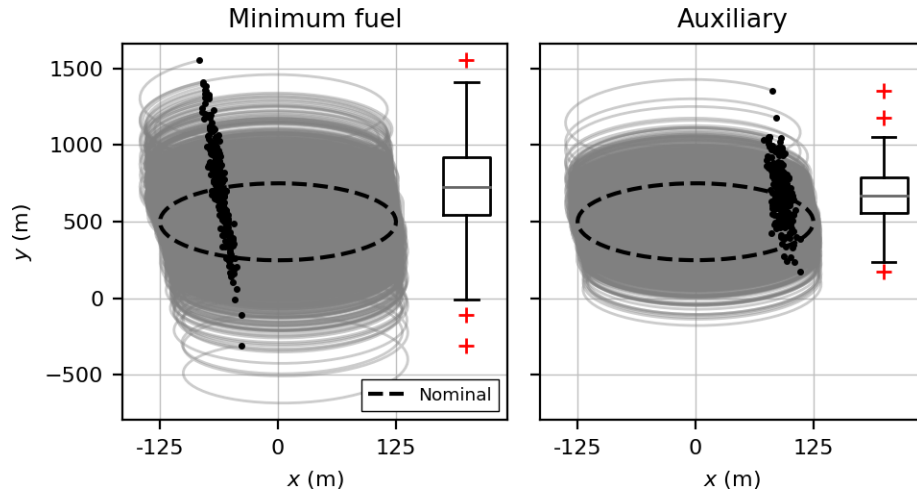


Figure 3.13: Propagated unforced radial and along-track relative motion for 5 chief orbits.

terminal state error covariance ellipses in x and \dot{y} coordinates. In addition, the desired target set for zero secular drift is illustrated as a solid line. In the minimum fuel solution, the semi-major axis of the state error covariance ellipse is rotated partly away from the nominal drift line. The projection of these errors away from the singular manifold produces higher uncertainty in the drift error, even though the nominal state terminates precisely on the manifold. In comparison, the auxiliary solution has the benefit of aligning the axes of the covariance ellipse precisely with the zero-drift condition. This reduces the projection of errors away from the singular manifold, resulting in lower expected drift after the relative orbit maneuver window. These results indicate that, although the CW dynamics are linear in the state variables, parameter uncertainties can introduce nonlinearity that resolves the infinite-order singular arc. Further, these solutions are robust to uncertainty in the orbit rate parameter, which could vary due to a non-circular chief orbit or external perturbations. Although aerodynamic drag will circularize the chief orbit over time, these effects will also affect the mean orbit rate.

Finally, Fig. 3.13 shows an uncontrolled propagation of the deputy terminal state error covariances following each maneuver. These are computed for five nominal chief orbits using a Monte Carlo sampling approach with 250 runs. Both solutions produce the desired orbit in the nominal

case with zero secular drift. However, after five orbits, the minimum fuel solutions start to diverge rapidly, with many cases ending far beyond the initial along-track offset. In comparison, the auxiliary problem moderately desensitizes the maneuver and reduces the secular drift. A conclusion of these results is that, although the auxiliary minimum requires slightly higher ΔV during the maneuver, the resulting uncontrolled trajectories are likely to see lower along-track drift. This will in turn lower station-keeping requirements, meaning overall ΔV usage post-maneuver may actually be lower when considering future chief orbits. This example illustrates concepts regarding error covariance projection onto singular manifolds to produce minimum-drift relative orbits. Through application of the auxiliary covariance relaxation method and control regularization, solutions can be rapidly obtained using indirect methods with little effort required of the designer regarding knowledge of the solution structure.

3.6.2 Planetary Aerocapture

Aerocapture is an aeroassist strategy proposed in the literature [1, 196] consisting of a single pass through the upper atmosphere of a planetary body. The velocity-loss produced by aerodynamic drag forces during entry is designed to dissipate orbital energy and capture the spacecraft from an unbounded approach trajectory. An illustration of such a maneuver is given in Fig. 3.14. Accumulative errors during entry flight will degrade the accuracy of the exit orbit, requiring larger propellant mass margins for ΔV correction burns. As a result, the capability to precisely capture a spacecraft into its desired orbit at atmospheric exit interface directly impacts usable delivered payload. Optimal information regarding these atmospheric flight segments is an enhancing technology for aerocapture.

Reference [91] develops a closed-loop guidance scheme for bank angle modulated aerocapture from application of the Minimum Principle. Their findings indicate that aerocapture permits only bang-bang solution structures, where singular arcs are ruled out. This result serves as the basis for the closed-loop numerical predictor-corrector guidance algorithm in Ref. [91]. In the first phase, the vehicle is initially commanded to fly a lift-up orientation in order to increase the periapsis altitude.

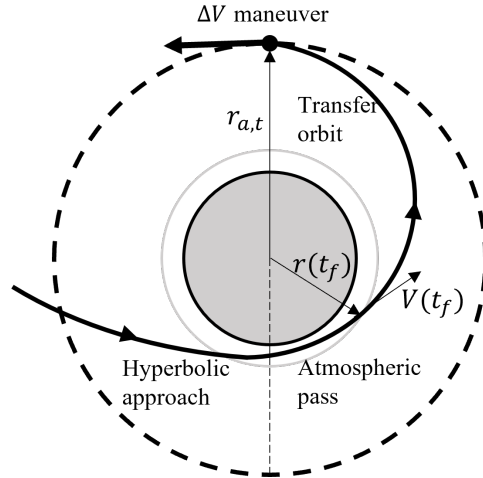


Figure 3.14: Illustration of aerocapture maneuver with single-burn ΔV .

The net effect of this phase is to decrease the nominal ΔV magnitude for an exo-atmospheric periapsis raise burn [53]. Findings for bang-bang aerocapture trajectories have been widely cited as a basis for convex optimization algorithms [197, 198], direct force control (DFC) [123, 199], and drag modulation for aerocapture [200].

While optimal control solutions in aerocapture are well-studied, previous work is largely rooted in certainty equivalent cost objectives. These strategies rely on closed-loop control to mitigate the inherent uncertainty encountered during atmospheric flight. In this example, we demonstrate that the nonlinearity inherent to such problems can be leveraged to produce optimal trajectories minimizing uncertainty, rather than deterministic objectives. Furthermore, we show that a class of aerocapture problems do permit singular arcs; however, the singular arcs appear with infinite local order, leading to an ill-posed problem structure. We consider such cases and apply the auxiliary relaxation method to demonstrate its utility in aerospace mission design.

Mission concepts for aerocapture often employ vehicle concepts leveraging heritage entry systems. Flight-proven technologies such as the successful Mars Science Laboratory (MSL) demonstrated guided entry by modulating its bank angle to target a predicted downrange [18]. Bank angle control essentially amounts to fixed-trim steering of the aerodynamic lift vector in the longitudinal plane. These dynamics are frequently used in first-order analysis of aerocapture performance using

the longitudinal motion of the vehicle. Neglecting planetary rotation effects and assuming a simple radial gravity model, planar motion for unpowered atmospheric flight is described by geocentric radius r , velocity magnitude V , and flight-path angle γ . The system is summarized as

$$\dot{r} = V \sin \gamma \quad (3.102a)$$

$$\dot{V} = -D - \frac{\mu}{r^2} \sin \gamma \quad (3.102b)$$

$$\dot{\gamma} = \frac{1}{V} \left(Lu + \left(V^2 - \frac{\mu}{r} \right) \frac{1}{r} \cos \gamma \right) \quad (3.102c)$$

with initial conditions $r(t_0) = r_0$, $V(t_0) = V_0$, and $\gamma(t_0) = \gamma_0$, as well as a terminal constraint $r(t_f) = r_f$ at the atmospheric exit interface radius. L and D are lift and drag acceleration terms, respectively, from Eq. (2.78). The atmospheric density model is assumed to follow an exponential profile $\rho = \rho_0 \exp(-h/S)$, where S is the atmospheric scale height and ρ_0 is the reference density. Altitude is calculated as $h = r - R_p$ where R_p is the radius of the planet. The control u corresponds to the cosine of the bank angle, which represents the component of lift projected into the vertical plane. Inherent boundedness of u is equivalent to the control constraint $|u| \leq 1$.

Previous studies [91,196,198] develop cost functions for aerocapture with respect to terminal states. Upon reaching the atmospheric exit interface, no external forces other than gravity act on the vehicle. Under the assumption of Keplerian motion, the properties of the final orbit are fully defined by the exit state of the vehicle. Suppose the objective in Fig. 3.14 is to target a semi-major axis a defined as

$$a(t_f) = \frac{\mu}{2\frac{\mu}{r(t_f)} - V(t_f)^2} \quad (3.103)$$

A common objective is to minimize the ΔV cost associated with errors in the final semi-major axis. However, as noted by Bryson [68], states that are fully constrained in optimization can be eliminated from the cost function. Because the exit interface altitude fully defines the terminal radius, Eq. (3.103) reduces to a velocity-matching condition. We are then motivated to consider the following objective for aerocapture

$$J = \frac{1}{2}(V(t_f) - V_f)^2 \quad (3.104)$$

where V_f is the target velocity giving the precise semi-major axis target at the prescribed exit radius.

The Hamiltonian for this system is formulated as

$$H = \lambda_r V \sin \gamma + \lambda_V \left(-D - \frac{\mu}{r^2} \sin \gamma \right) + \lambda_\gamma \frac{1}{V} \left(Lu + \left(V^2 - \frac{\mu}{r} \right) \frac{1}{r} \cos \gamma \right) \quad (3.105)$$

Because the final time is free, the transversality condition Eq. (3.7) defines the stop conditions of the simulation with $H(t_f) = 0$. The control u appears linearly in the Hamiltonian, indicating the solution is bang-bang/singular form. The costate dynamics are summarized as

$$\dot{\lambda}_r = -\frac{\partial H}{\partial r} = -\lambda_V \left(-\frac{\partial D}{\partial r} + 2\frac{\mu}{r^3} \sin \gamma \right) - \lambda_\gamma \frac{1}{V} \left(\frac{\partial L}{\partial r} u + 2\frac{\mu}{r^3} \cos \gamma \right) \quad (3.106a)$$

$$\dot{\lambda}_V = -\frac{\partial H}{\partial V} = -\lambda_r \sin \gamma - \lambda_V \left(-\frac{\partial D}{\partial V} \right) - \lambda_\gamma \frac{\partial \dot{\gamma}}{\partial V} \quad (3.106b)$$

$$\dot{\lambda}_\gamma = -\frac{\partial H}{\partial \gamma} = -\lambda_r V \cos \gamma - \lambda_V \left(-\frac{\mu}{r^2} \cos \gamma \right) - \lambda_\gamma \frac{1}{V} \left(\left(\frac{\mu}{r} - V^2 \right) \frac{1}{r} \sin \gamma \right) \quad (3.106c)$$

where

$$\frac{\partial \dot{\gamma}}{\partial V} = \frac{1}{V} \left(\frac{\partial L}{\partial V} u + 2V \frac{1}{r} \cos \gamma \right) - \frac{1}{V^2} \left(Lu + \left(V^2 - \frac{\mu}{r} \right) \frac{1}{r} \cos \gamma \right) \quad (3.107)$$

The boundary conditions on the costates are $\lambda_r(t_f) = \nu$, $\lambda_V(t_f) = V(t_f) - V_f$, and $\lambda_\gamma(t_f) = 0$, where ν is a Lagrange multiplier appending the terminal radius constraint.

On a candidate singular arc the switching function is

$$H_u = \frac{L}{V} \lambda_\gamma = 0 \quad (3.108)$$

which reduces to $\lambda_\gamma = 0$ since L and V are positive quantities. Consider the velocity-matching condition in Eq. (3.104) for the case when the target velocity V_f is reachable with open end-time. If the solution is a feasible trajectory satisfying all constraints of the problem, by Proposition 2 the solution is a singular arc with local order $p \rightarrow \infty$. In tandem with the boundary condition $\lambda_\gamma(t_f) = 0$, this implies that all solutions must terminate on a singular arc. In fact, this is precisely the degenerate case $\boldsymbol{\lambda}(t) = \mathbf{0} \in \mathbb{R}^n$ for all $t \in [t_0, t_f]$ identified in Ref. [91]. Thus, we conclude that singular arcs in aerocapture are an indeterminate control problem, since the optimal trajectory

Table 3.3: State constraints and problem parameters for Mars aerocapture example.

	h (km)	V (km/s)	γ (deg)	t (s)
Initial	120	7.150	-12	0
Final	120	free	free	free

(a) States

Parameter	μ (km ³ /s ²)	R_p (km)	ρ_0 (kg/m ³)	S (km)	m (kg)	A_{ref} (m ²)	C_L	C_D
Value	4.2830×10^4	3,398.2	0.0172	9.47	7,387.3	16.9823	0.4	1.25

(b) Parameters

belongs to a family of global minimizers. However, Theorem 1 is not violated because the abnormal multiplier $\lambda_0 \neq 0$.

The auxiliary covariance relaxation method is applied to the aerocapture problem to resolve the infinite-order singular arc solutions. The unique elements of the error covariance are augmented to the system state. The sensitivity and error covariance dynamics are omitted here for brevity. These expressions will be further considered in Chapter 4. For the velocity-matching objective in Eq. (3.104), the corresponding expectation cost is

$$J = P_{VV}(t_f) \quad (3.109)$$

with initial conditions $P(t_0) = P_0$ and additional terminal constraint $V(t_f) = V_f$. With this problem structure formulated, we show the following results regarding the utility of the auxiliary covariance relaxation method for the aerocapture mission design problem.

Results for the Mars aerocapture example are generated using the states and problem parameters listed in Table 3.3. These quantities are taken from a previous study [196] or otherwise chosen based on engineering judgement. A continuation methodology is developed to converge to a final solution without prior knowledge of the initial costates. First, a short trajectory of 0.5 seconds is propagated forward in time to provide an initial guess to the BVP solver. The problem is then solved for a final altitude of zero. Once this initial trajectory is obtained, the final altitude is pushed to 120 km over a continuation interval on r_f . This continuation step is illustrated in Fig. 3.15. The

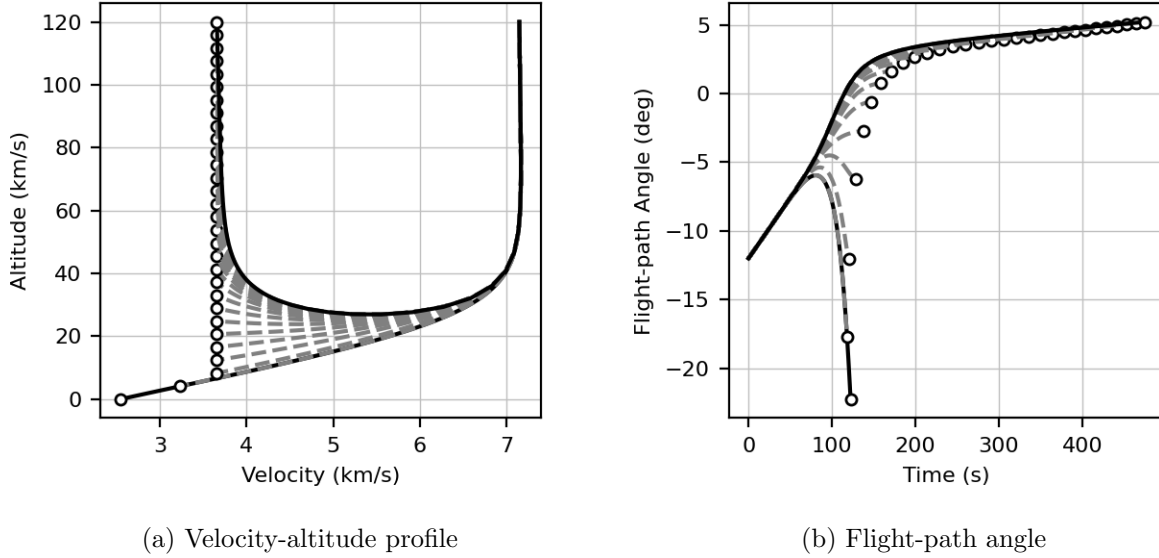


Figure 3.15: Continuation interval over final radius r_f in aerocapture example.

initial trajectory propagated to ground level initially undershoots the target velocity in Fig. 3.15a. These initial solutions are direct entry trajectories, evident in Fig. 3.15b as the final flight-path angle remains below the local horizontal. Over the continuation interval, the higher terminal radius allows for the precise velocity-matching condition to be met, resulting in recognizable aerocapture trajectories exiting the atmosphere.

Figure 3.16 illustrates the family of global minimizers satisfying the semi-major targeting problem. In Fig. 3.16a The solutions are comparable to a theoretical corridor width dictated by the vehicle lift-to-drag ratio. Figure 3.16b shows the control solutions over the singular arc. While the solutions are optimal, they do not remain on the bound of the control set U , which is indicative of singular arcs. Note that a bang-bang solution satisfying the velocity-matching condition is also feasible, but the solution would not be a unique global minimizer. Moreover, since the control bounds are inactive, increasing the control authority cannot further reduce the cost objective. Figure 3.17 shows a 3-dimensional phase portrait of the infinite-order solution family. From this plot, it is clear that the terminal radius constraint and velocity-matching condition are met. However, the trajectories terminate along a range of different flight-path angles because

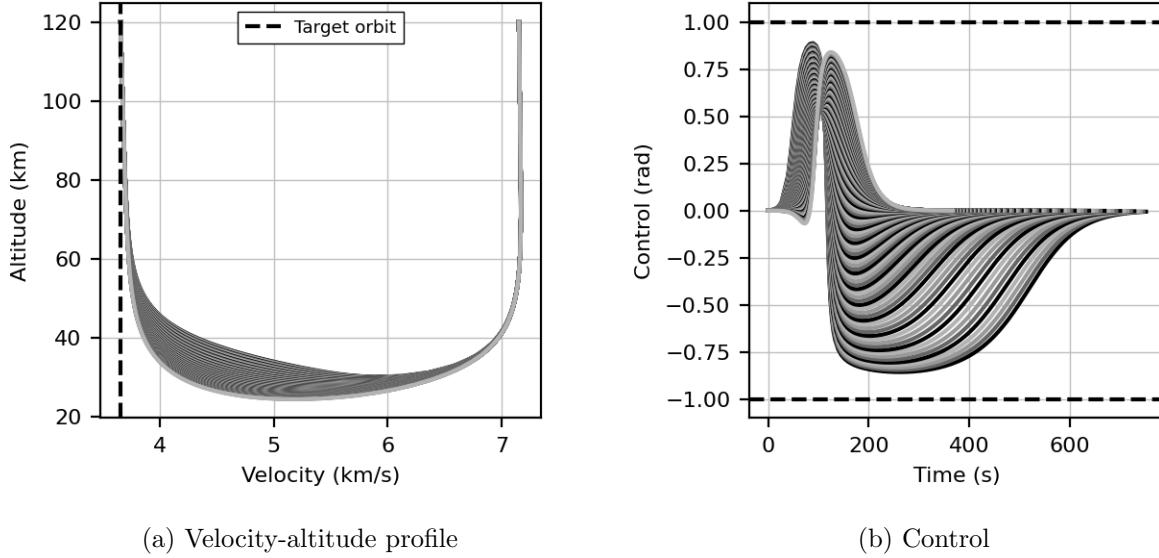


Figure 3.16: Illustrative subset of infinite-order singular arcs in aerocapture example.

$\gamma(t_f)$ is free in optimization. These results support the notion that optimal singular arcs exist in aerocapture problems. Other cost objectives, such as those involving periapsis altitude or out-of-plane orbital elements, may revert to bang-bang form if the solution lies outside the boundary of the reachable set.

The auxiliary covariance relaxation method is applied to the aerocapture to study the behavior of solutions optimizing the weighted trace objective in Eq. (3.109). The additional states and parameters used in the auxiliary problem are summarized in Table 3.4.

As with the preceding example, we compare the solution of the minimum covariance objective to that obtained from the family of infinite-order arcs. Figure 3.18 shows relevant quantities for both cases. The control history Fig. 3.18a for the singular problem remains well within the control upper and lower bound. The corresponding switching function in Fig. 3.18b remain identically zero, indicating a totally singular solution as expected. In comparison, the auxiliary problem generates a well-posed control solution with controls remaining near the bounds of the admissible set U . Finally, Fig. 3.18c illustrates the velocity-altitude corridor of each solution. For clarity, the trajectory is plotted up to an altitude of 80 km. The auxiliary solution tends to dive deeper into the atmosphere,

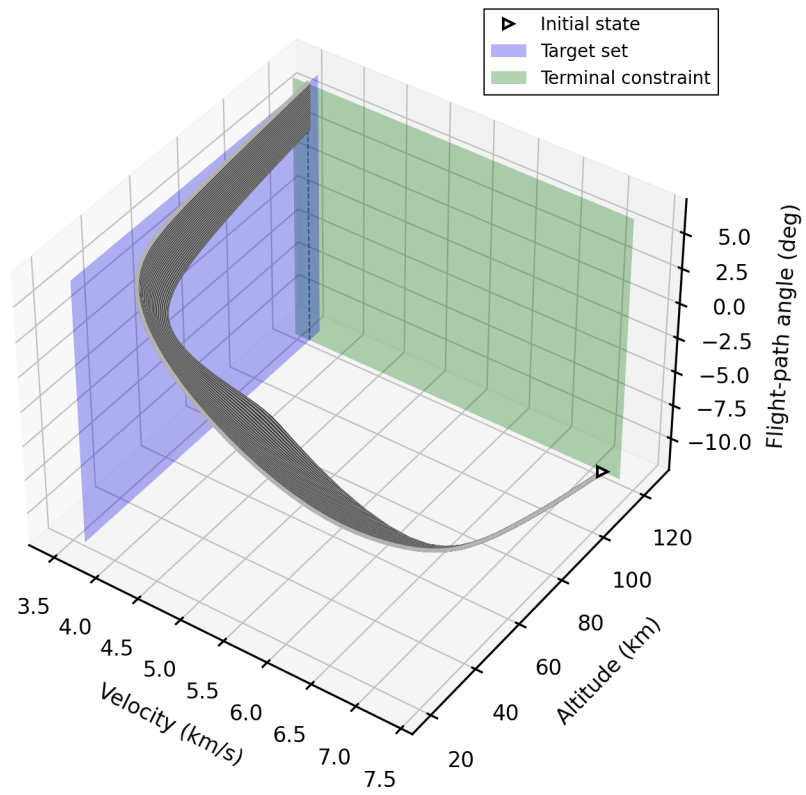


Figure 3.17: Phase-space portrait of infinite-order singular arcs in aerocapture example.

Table 3.4: Auxiliary states and problem parameters for Mars aerocapture example. Initial correlated uncertainties are assumed zero.

	P_{11} (m ²)	P_{22} (m ² /s ²)	P_{33} (deg ²)
Initial	1	0.1 ²	0.01 ²
Final	free	free	free

(a) Auxiliary states

Parameter	Q_{11} (m/s)	Q_{22} (m/s ²)	Q_{33} (deg/s)
Value	0	0.01	0.001

(b) Auxiliary parameters

which is evident from the initial control segment when $u = -1$.

While the auxiliary solutions appear to be bang-bang, we remark on several features of Fig. 3.18. First, the ends of the trajectory show difficulty in convergence of the control. This behavior is likely due to fact that the trajectory begins and ends at high altitudes where the atmospheric density is extremely sparse. In turn, this provides inadequate dynamic pressure to generate aerodynamic forces and therefore impart change on the optimal cost. These segments of the trajectory are nearly singular, since the magnitude of L is near zero. Second, a value for the regularization parameter ϵ of 10^{-3} is the smallest value to converge in the boundary value problem. Further decreasing ϵ would eliminate control smoothing effects noticeable at the corners of the bang arcs. For smaller values of ϵ , these will appear as sharp corners. Fortunately, such smoothing effects are largely superficial, with negligible impact on the solution structure and predicted cost.

The control solutions of the auxiliary problem in Figure 3.18 are in contrast to the typical entry guidance problem. That is, the initial control segment lies on the lower bound where $u = -1$, which corresponds to a lift-down bank angle configuration. These configurations are typically avoided in order to limit the possibility of flying too steep and producing significant inertial or aerothermal impulse. As evident in the solution of the error covariance dynamics, these trajectories may in fact provide more robust solutions given initial state uncertainty. One explanation for

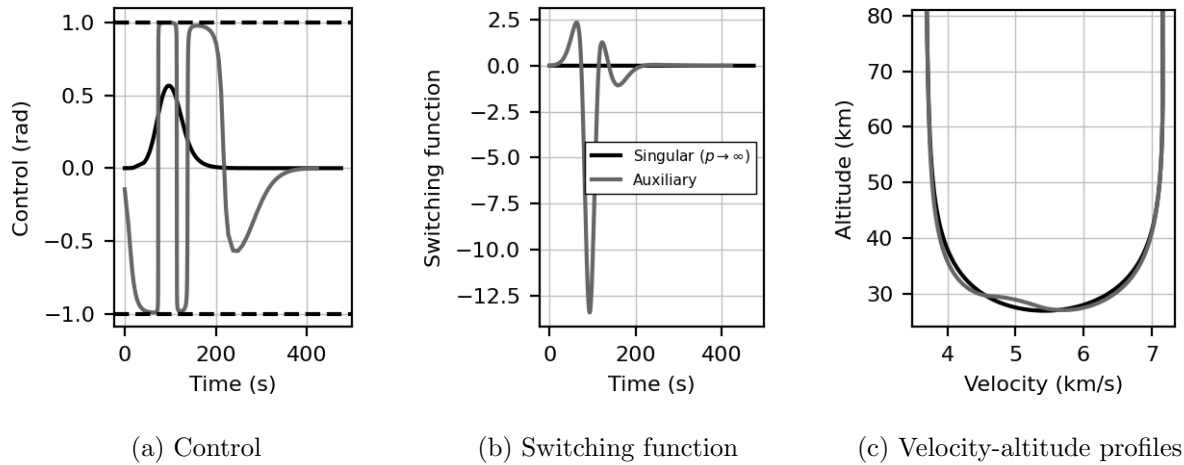


Figure 3.18: Auxiliary minimum solution of aerocapture example.

this behavior is the fact that the initial dive into the atmosphere produces an overall shorter trajectory. This in turn limits the time span over which the error covariance can propagate and grow. This provides only a partial explanation, however, as evidenced in Fig. 3.19. The propagated uncertainties in each state component are plotted for both the singular and auxiliary problem. In the singular case, the trajectory is significantly longer as the vehicle flies higher in the atmosphere. When comparing the two trends, it is apparent that the final time is only partly responsible for the reduction in terminal velocity uncertainty. The main impulse in velocity error occurs around 100 seconds, after which time the velocity uncertainty tapers off leading to atmospheric exit. Thus, although the auxiliary problem produces a larger drag impulse, the indirect formulation finds a solution minimizing the propagated error covariance equations (and not the final time).

The terminal state error covariance ellipses are plotted for each case in Fig. 3.20. It is interesting to note that, while only velocity uncertainty appears in the auxiliary objective 3.109, both velocity and altitude errors are reduced considerably. In addition, a stronger correlation is observed between the two states for the auxiliary problem. This result illustrates the utility of the relaxation method in mitigating uncertainty using optimal control theory. The original aerocapture velocity-matching condition provides insufficient information to resolve the optimal

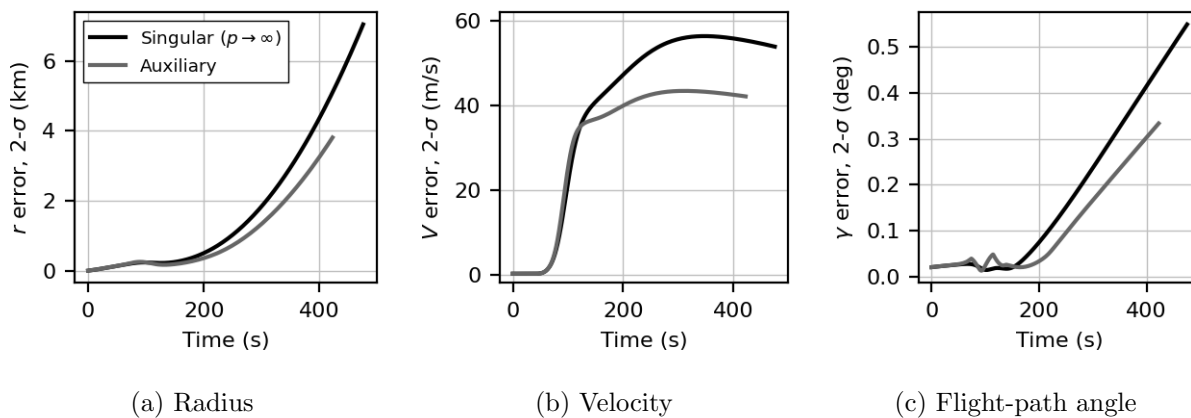


Figure 3.19: Propagated error covariance 2- σ bounds for auxiliary solution to aerocapture example.

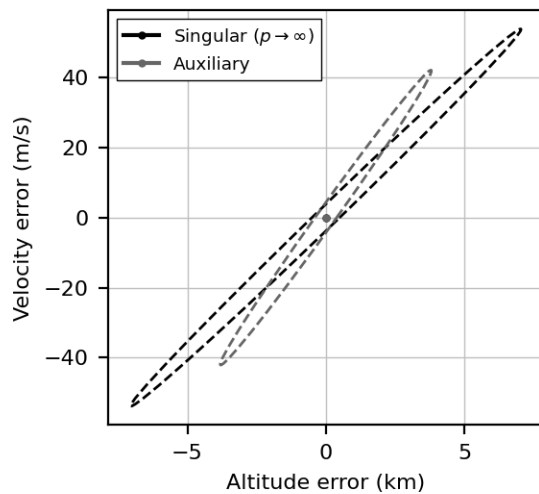


Figure 3.20: Propagated uncertainty 2- σ error ellipses for auxiliary solution to aerocapture example.

control. By extending the system dynamics to include the effects of propagated uncertainty, the indirect approach finds a local minimum that remains consistent with all boundary conditions.

The preceding results illustrate optimal solutions for the aerocapture problem with fixed initial states. Given an initial state error covariance estimate, the strategy could be used to produce a nominal trajectory minimizing the future effects of propagated uncertainty. The cost objective focuses on minimizing velocity uncertainty at the end of the atmospheric pass, but more complicated objectives could be included. Another useful application of the indirect approach is rapid conceptual design through numerical continuation [88]. Once an initial solution is obtained, problem parameters can be rapidly iterated over in neighboring BVPs. This method can be used to produce tradespace plots over a range of vehicle performance parameters. This approach is utilized to demonstrate rapid *risk-adverse* conceptual design for aerocapture. That is, the optimal converged solutions for each design point can include the propagated effects of uncertainty. In addition, these results allow for identification of optimal entry conditions and vehicle shape parameters that minimize uncertainty over the atmospheric pass.

Conceptual design results are generated for a modified case of the preceding aerocapture problem. First, the initial flight-path angle constraint is removed, allowing for freedom in determining its optimal value. Initial altitude and velocity magnitude remain fixed. Second, a parameter extension approach is taken to include effects of propagated uncertainty in the lift and drag coefficients. Errors in the aerodynamic coefficients are assumed normally-distributed with a $3\text{-}\sigma$ range of $\pm 4.5\%$. An initial solution is obtained using the preceding numerical continuation strategy on terminal altitude. Given the initial solution, the problem is then solved successively over a product-space of initial velocity and ballistic coefficient. These quantities represent design parameters that influence entry performance and vehicle shape.

Quantities of interest in the aerocapture conceptual design tradespace are computed for infinite-order singular trajectories in Fig. 3.21 and auxiliary-minimum solutions in Fig. 3.22. The optimal entry flight-path angle is shown for ballistic coefficients ranging from 100 to 500 kg/m^2 and entry velocities ranging 6 to 8 km/s . In the auxiliary problem, the optimal entry flight-path angle

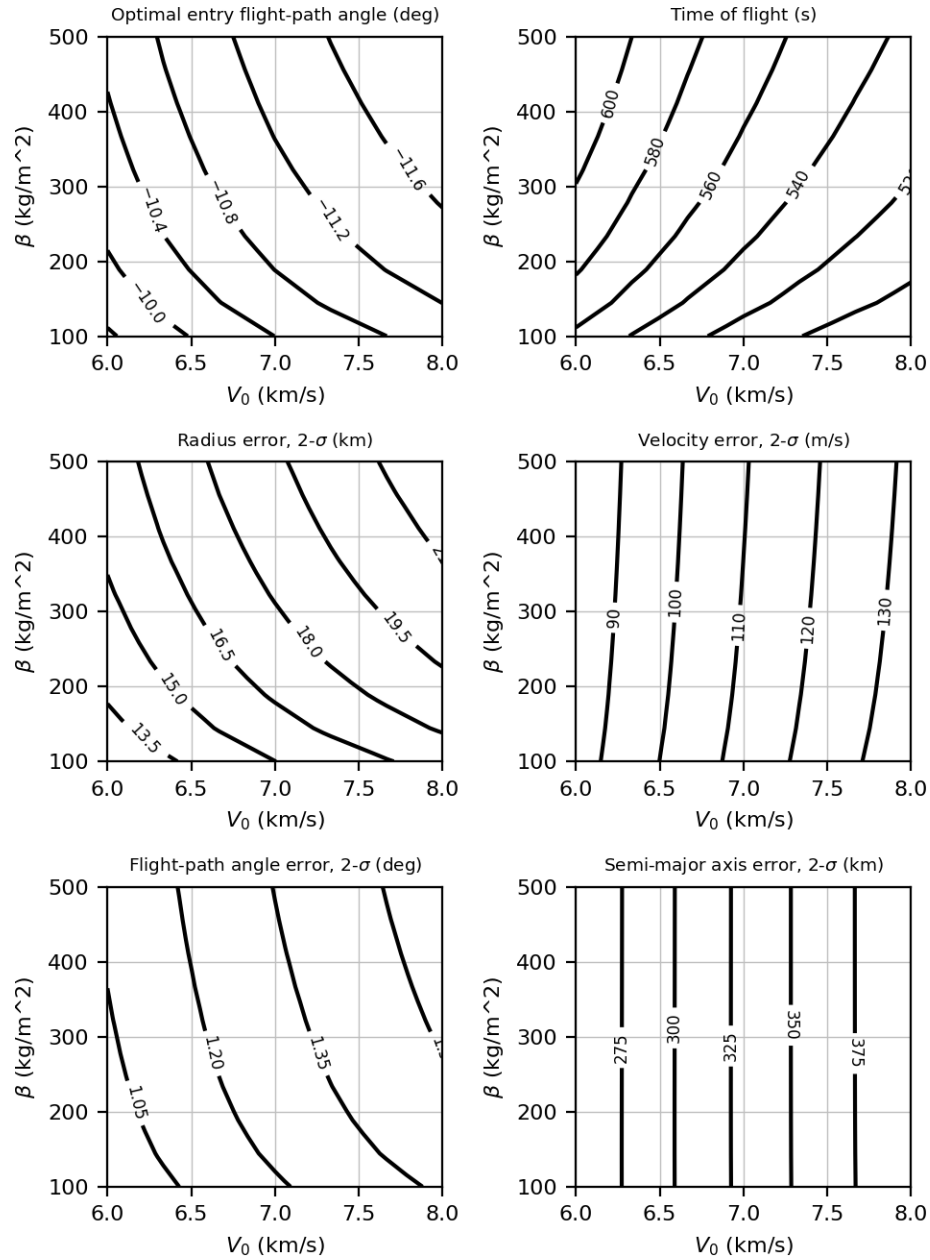


Figure 3.21: Aerocapture conceptual design tradespace for singular solutions.

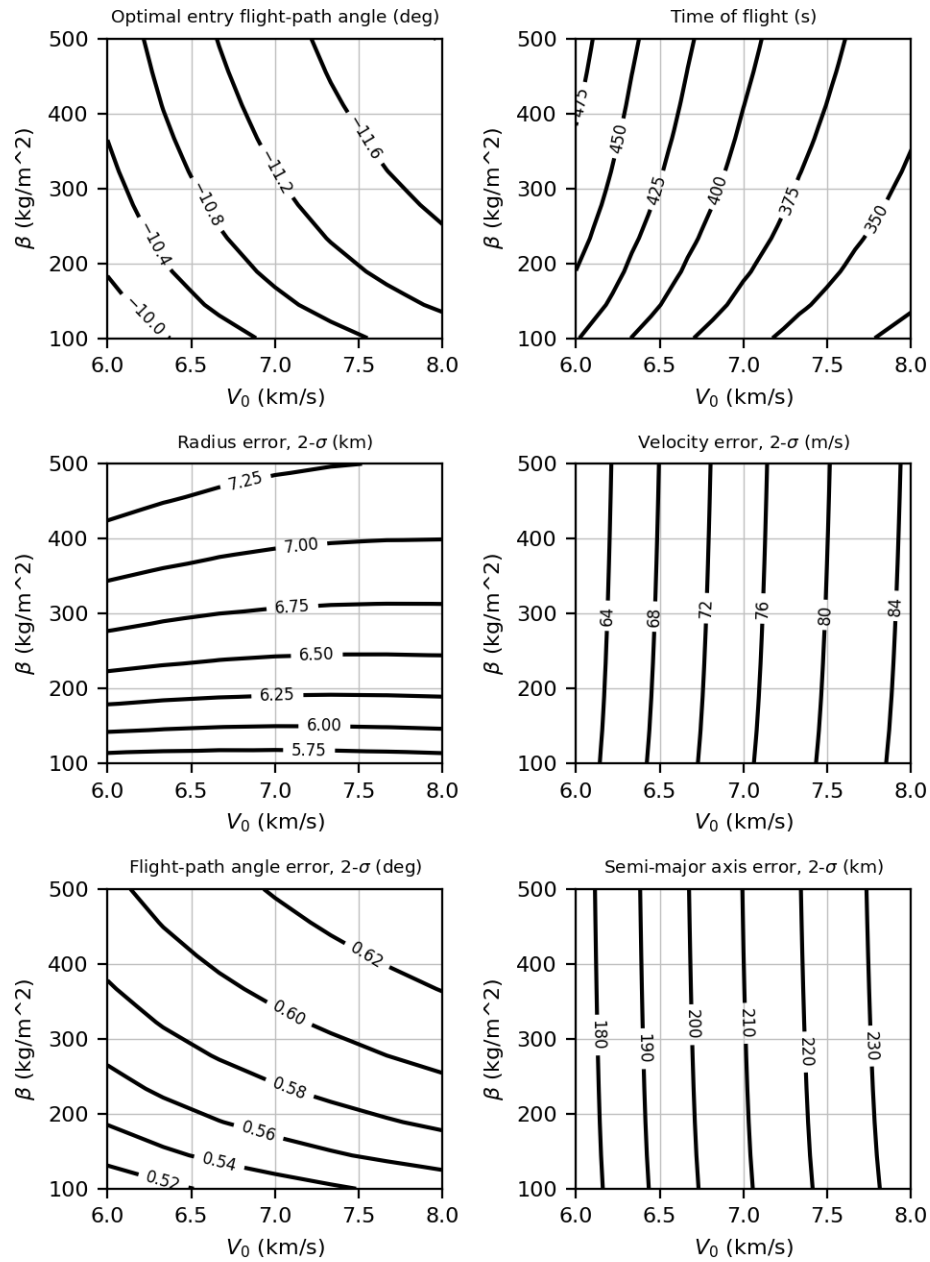


Figure 3.22: Aerocapture conceptual design tradespace for auxiliary minimum solution.

at each design point is determined by minimizing propagated effects of aerodynamic uncertainty. In addition, the time of flight decreases with higher entry velocity and lower ballistic coefficient. Intuitively speaking, a lower ballistic coefficient produces greater drag, in turn providing a greater impulse over the atmospheric pass. Uncertainties in the exit radius, velocity, and flight-path angle show interesting trends. The radius uncertainty increases with both velocity and ballistic coefficient. However, the final velocity error is almost entirely dictated by the entry velocity. Lower velocities tend to reduce the propagated effects the aerodynamic coefficient errors. Similarly, error in the semi-major axis is largely determined by velocity errors, showing a similar trend. The tradespace plot illustrates an extension of rapid conceptual design methodologies applied to minimizing uncertainty in aerocapture.

3.7 Summary

This chapter studies a class of problems containing arcs with infinite local order. These arcs are linked to a reachable subspace minimizing the Mayer objective with admissible controls. Existence conditions are developed for problems with a free terminal state and fixed end-time, as well as a partially-constrained terminal state with free end-time. In the latter case, it is assumed that the terminal constraints do not interfere with the minimum cost in optimization. The resulting problem is shown to produce degenerate control structures for which a family of global minimizers can be found. A novel relaxation method is proposed for optimal control solution structures with this indeterminate form. The linearized error covariance dynamics are appended to the system state with appropriate boundary conditions and cost objectives. The extended problem is shown to permit finite-order arcs by exploiting the effect of nonlinearity in the system on the propagation of uncertainty. The solution can be solved using regularization and numerical homotopy continuation methodologies. Results are shown for classical examples in optimal control, as well as a practical engineering application involving planetary aerocapture. These results aid in the design of optimal entry conditions and vehicle performance parameters for risk-adverse atmospheric entry problems.

Chapter 4

Optimal Information Filtering for Planetary Aerocapture

4.1 Entry Guidance Perspective

Recent advancements in NPC guidance have increased confidence in aerocapture, though there remain avenues for improvement. This chapter in particular concerns the coupling between state estimation and entry guidance. In traditional approaches, entry guidance UQ is performed “outside-the-loop,” where a reference trajectory and guidance algorithm are designed based on nominal values of variable quantities. In some applications, this assumption may hold because of two important principles in control and estimation theory: the *separation principle* and the *certainty equivalence principle* [201]. The separation principle states that control and estimation errors are orthogonal. The certainty equivalence principle is an extension of the separation principle to state that the optimization problem with imperfect state knowledge can be solved in a deterministic manner by substituting an uncertain state with its best estimate. A caveat to these conditions, however, lies in the fact the separation principle can hold while certainty equivalence does not [202]. For example, certainty equivalence may not hold when the optimization objective is a function of a state estimate error covariance. In atmospheric entry flight, control objectives operating solely on deterministic values may not produce optimal behavior in dispersion analysis. A reformulation of aerocapture objectives, embodied by the governing OCP, is needed to better understand optimal atmospheric trajectories in the presence of uncertainty.

Methodologies in robust optimization attempt to incorporate models of uncertainty into an optimal control objective. One approach is to consider the worst case scenario, minimizing the

probability of crossing a threshold of extreme edge cases [175]. Another approach is the sensitivity robustness method [203], where the cost is split into a multi objective problem to minimize a deterministic cost and a weighted sum of sensitivities. Other studies use a weighted sum approach to simultaneously minimize both the expected value of a cost and its variance about the mean [204]. These strategies may require user-defined weighting parameters that rely on subjectivity or intuition, and they may not provide a statistically consistent analysis. In this work, a distributional approach is taken to minimize the mean square deviation (MSD) about a deterministic-optimal terminal state. This provides a statistically consistent analysis to minimize both a mean drift and variance relative to the desired terminal state. The MSD approach does away with any ambiguous weighting parameters, and instead relies on the functional form of the optimal cost measure and underlying probability distribution. These objectives are aligned with the auxiliary covariance problem outlined in Chapter 3, where it is shown that aerocapture problems exhibit infinite-order singular arcs.

Conceptual design in aerocapture has routinely relied on certainty equivalent guidance performance, potentially leading to over-designed vehicles unattractive from a cost and risk perspective. The absence of a cohesive methodology for mitigating uncertainty through atmospheric trajectory design and guidance represents a gap in current research. The primary focus of this work is to bridge this gap through the treatment of uncertainty in hypersonic entry flight problems. This information can provide valuable input on the trajectory planning and entry guidance design process. This work is primarily concerned with the guidance *prediction* step, in which a feasible trajectory must be found to meet downrange conditions. The approach enables optimal tuning and allocation of guidance parameters for entry problems with insufficient state knowledge for precision targeting.

The novel contributions of this chapter are enumerated as follows: 1) reformulation of aeroassist objectives accounting for Gaussian uncertainty, 2) development of an atmospheric density model representative of scientific data and consistent with consider filtering and linear covariance analyses, 3) optimal allocation of guidance parameters based on robust optimization principles, and 4) validation of dispersed atmospheric trajectories using statistical ranking and consistency methods.

A rapid solution method is illustrated for a representative example of aerocapture at Mars. The results inform existing and future entry guidance methods, providing a path of improvement for missions to unexplored and challenging destinations in the solar system.

This chapter is organized as follows. Section 4.2 introduces concepts in robust optimization and estimation of dynamic systems. The methods are stated generally and then simplified for applications in consider filtering. Section 4.3 develops process equations and optimal control objectives as applied to planetary aerocapture guidance. A minor contribution of the section is the development of a MarsGRAM-derived atmospheric data compression model that accurately describes altitude-dependent density perturbations. A parametric control model is developed and a numerical solution strategy is outlined. Section 4.4 applies the new methodology to a baseline aerocapture mission concept with uncertainty in states and environmental parameters. On-line filtering applications are discussed. Finally, Sec. 4.5 summarizes findings for the chapter.

4.2 Observer-based Trajectory Design and Guidance

4.2.1 Robust Optimization of Dynamic Systems

We first provide an outline of relevant theory regarding optimization of uncertain systems as a mathematical basis for the remainder of this chapter. Robust optimization involves modification of a deterministic cost objective to incorporate effects of uncertainty. We develop a distributional cost using expected value measures. To begin, consider a nonlinear system with a general dynamics model

$$\dot{\mathbf{x}} = \mathbf{f}(\mathbf{x}, \mathbf{p}, u, t) + \Gamma \mathbf{w} \quad (4.1)$$

where $\mathbf{x} \in \mathbb{R}^n$ is the system state vector, $\mathbf{p} \in \mathbb{R}^q$ is set of parameters, $u \in \mathbb{R}$ is a scalar control input, $\Gamma \in \mathbb{R}^{n \times r}$ is a process noise mapping, and $\mathbf{w} \in \mathbb{R}^r$ is an additive white Gaussian process. The shorthand notation $\mathbf{w} \sim \mathcal{N}(\mathbf{0}, Q)$ refers to property

$$\mathbb{E}[\mathbf{w}] = \mathbf{0} \quad (4.2)$$

$$\mathbb{E}[\mathbf{w}(t)\mathbf{w}^T(\tau)] = Q(t)\delta(t - \tau) \quad (4.3)$$

The parameters \mathbf{p} do not evolve with time but will influence the motion of system through coupling in dynamics and measurement equations. Assume the system receives sampled-data measurement inputs of the form

$$\mathbf{y}_k = \mathbf{h}(\mathbf{x}_k, \mathbf{p}, t_k) + \mathbf{v}_k \quad (4.4)$$

where $\mathbf{y}_k \in \mathbb{R}^m$ is a measurement vector and $\mathbf{v}_k \in \mathbb{R}^p$ represents measurement noise with $\mathbf{v}_k \sim \mathcal{N}(0, R_k)$. At any epoch, the augmented state is not exactly known, instead belonging to a joint probability density function (PDF) $f_{\mathbf{X}\mathbf{P}}(\mathbf{x}, \mathbf{p}, t)$. As new measurement information is received, the joint PDF is conditioned on the information set $\Lambda[t_0, t]$ which includes a sequence of measurement realizations \mathbf{y}_i , $i = 1, \dots, k$ between t_0 and t .

$$\Lambda[t_0, t] = \{\mathbf{y}_1, \mathbf{y}_2, \dots, \mathbf{y}_k\} \quad (4.5)$$

Problems of interest in this work are Mayer objectives depending only on the terminal state of the system. A distributional cost objective in robust optimization minimizes the expected value of a performance measure J with respect to the uncertainty distribution,

$$J = \mathbb{E}\{\phi[\mathbf{x}(t_f), t_f] \mid f_{\mathbf{X}\mathbf{P}}(\mathbf{x}(t_0), \mathbf{p}, t_0), \Lambda[t_0, t_f]\} \quad (4.6)$$

where $\phi : \mathbb{R}^n \times \mathbb{R} \rightarrow \mathbb{R}$ maps terminal state values to the desired performance metric [78]. The cost index ϕ is assumed to depend only on the distribution of terminal states, not parameters. The joint PDF $f_{\mathbf{X}}(\mathbf{x}, t)$ of the system states can be found at time t by marginalizing out parameters p_i over respective domains \mathcal{D}_i

$$f_{\mathbf{X}}(\mathbf{x}, t) = \int_{\mathcal{D}_1} \dots \int_{\mathcal{D}_q} f_{\mathbf{X}\mathbf{P}}(\mathbf{x}, \mathbf{p}, t) dp_1 \dots dp_q \quad (4.7)$$

The distributional cost objective in Eq. (4.6) can be interpreted as the optimal solution “on-the-average.” Although J depends only on values of system states, the expectation operator accounts for uncertainty in parameters by propagation of the augmented joint-PDF of \mathbf{x} and \mathbf{p} from initial time t_0 to final time t_f . The effect of parameter uncertainty is seen through coupling within the augmented state PDF. At any arbitrary time $t_1 > t_0$, only the realized information

set $\Lambda[t_0, t_1]$ is known. The primary challenge then lies in predicting the conditioning effect over $t \in [t_1, t_f]$. Using standard tools in estimation filtering, this conditioning effect can be predicted well using linear covariance analysis. In the following sections, some minor approximations are taken to reduce Eq. (4.6) to a more tractable form for solution.

4.2.2 Covariance Approximation of the Distributional Cost Measure

The expectation measure in Eq. (4.6) presents a challenge due to the nature of the nonlinear dynamics with augmented state PDF and noise perturbations. It is prudent to develop a modified cost measure utilizing readily-available quantities, such as statistical moments of the state probability distribution, while maintaining the overall structure and behavior of the original objective. This task can be achieved by noting a common feature of the cost measures in aeroassist problems is to minimize the MSD about a desired terminal state. Ref. [166] found most practical aeroassist cost objectives exhibit this form. We define a mapping $\tilde{\phi} : \mathbb{R}^n \times \mathbb{R}^n \times \mathbb{R} \rightarrow \mathbb{R}$, which can be seen as a loss function with respect to \mathbf{x} about a desired state $\mathbf{x}^* \in \mathbb{R}^n$.

$$\phi[\mathbf{x}(t_f), t_f] = \tilde{\phi}^2[\mathbf{x}(t_f), \mathbf{x}^*, t_f] \quad (4.8)$$

Further motivation for this functional form is provided in Sec. 4.3. Defining the shorthand notation of partial derivatives

$$\phi^* := \phi_{\mathbf{x}=\mathbf{x}^*} \quad (4.9a)$$

$$\phi_{\mathbf{x}}^* := \left(\frac{\partial \phi}{\partial \mathbf{x}} \right)_{\mathbf{x}=\mathbf{x}^*} \quad (4.9b)$$

$$\phi_{\mathbf{xx}}^* := \left[\frac{\partial \phi}{\partial x_i \partial x_j} \right]_{\mathbf{x}=\mathbf{x}^*} \quad (4.9c)$$

A Taylor series expansion of Eq. (4.8) up to second order can be written as

$$\phi = \phi^* + \phi_{\mathbf{x}}^* (\mathbf{x} - \mathbf{x}^*) + \frac{1}{2} (\mathbf{x} - \mathbf{x}^*)^T \phi_{\mathbf{xx}}^* (\mathbf{x} - \mathbf{x}^*) + \mathcal{O}(\|\mathbf{x} - \mathbf{x}^*\|^3) \quad (4.10)$$

Using Eq. (4.8), the partial derivatives in Eq. (4.10) can be expressed as $\phi_{\mathbf{x}} = 2\tilde{\phi}\tilde{\phi}_{\mathbf{x}}$ and $\phi_{\mathbf{xx}} = 2\tilde{\phi}_{\mathbf{x}}^T \tilde{\phi}_{\mathbf{x}} + 2\tilde{\phi}\tilde{\phi}_{\mathbf{xx}}$. Ignoring higher order terms and substituting into Eq. (4.10) at $\mathbf{x} = \mathbf{x}^*$ gives

$$\tilde{\phi}^2 \approx \tilde{\phi}^{*2} + 2\tilde{\phi}^* \tilde{\phi}_{\mathbf{x}}^* (\mathbf{x} - \mathbf{x}^*) + \frac{1}{2} (\mathbf{x} - \mathbf{x}^*)^T (2\tilde{\phi}_{\mathbf{x}}^{*T} \tilde{\phi}_{\mathbf{x}}^* + 2\tilde{\phi}^* \tilde{\phi}_{\mathbf{xx}}^*) (\mathbf{x} - \mathbf{x}^*) \quad (4.11)$$

Suppose the desired terminal state \mathbf{x}^* has the property $\tilde{\phi}^* = 0$. The expansion of Eq. (4.11) reduces to

$$\tilde{\phi}^2 = (\mathbf{x} - \mathbf{x}^*)^T W (\mathbf{x} - \mathbf{x}^*) \quad (4.12)$$

where

$$W = \tilde{\phi}_{\mathbf{x}}^{*\top} \tilde{\phi}_{\mathbf{x}}^* \quad (4.13)$$

Thus, the original nonlinear objective can be approximated as a quadratic function of the deviation about a desired reference state \mathbf{x}^* . The weighting matrix W takes into account the functional form of Eq. (4.8) to provide a relative weighting of each state component in the cost objective. This analysis remains valid to second order, as the assumption $\tilde{\phi}^* = 0$ eliminates first-order terms in the expansion. Taking the expectation of Eq. (4.12) gives

$$\begin{aligned} \mathbb{E}[(\mathbf{x} - \mathbf{x}^*)^T W (\mathbf{x} - \mathbf{x}^*)] &= \mathbb{E}[\mathbf{x}^T W \mathbf{x} - 2\mathbf{x}^T W \mathbf{x}^* + \mathbf{x}^{*\top} W \mathbf{x}^*] \\ &= \mathbb{E}[\mathbf{x}^T W \mathbf{x}] - 2\mathbb{E}[\mathbf{x}^T] W \mathbf{x}^* + \mathbf{x}^{*\top} W \mathbf{x}^* \end{aligned} \quad (4.14)$$

The first term in the preceding equation can be expanded by interchanging the expectation operator and noting the invariance property of the trace under cyclic permutations.

$$\begin{aligned} \mathbb{E}[\mathbf{x}^T W \mathbf{x}] &= \mathbb{E}[\text{tr}(\mathbf{x}^T W \mathbf{x})] \\ &= \mathbb{E}[\text{tr}(W \mathbf{x} \mathbf{x}^T)] \\ &= \text{tr}(W \mathbb{E}[\mathbf{x} \mathbf{x}^T]) \end{aligned} \quad (4.15)$$

Next, starting with the definition of the state covariance matrix

$$\begin{aligned} P_{xx} &= \mathbb{E}[(\mathbf{x} - \mathbb{E}[\mathbf{x}])(\mathbf{x} - \mathbb{E}[\mathbf{x}])^T] \\ &= \mathbb{E}[\mathbf{x} \mathbf{x}^T] - \mathbb{E}[\mathbf{x}]\mathbb{E}[\mathbf{x}^T] \end{aligned} \quad (4.16)$$

Solving Eq. (4.16) for $\mathbb{E}[\mathbf{x} \mathbf{x}^T]$ and substituting into Eq. (4.15) gives

$$\begin{aligned} \mathbb{E}[\mathbf{x}^T W \mathbf{x}] &= \text{tr}\{W P_{xx} + W \mathbb{E}[\mathbf{x}]\mathbb{E}[\mathbf{x}^T]\} \\ &= \text{tr}(W P_{xx}) + \mathbb{E}[\mathbf{x}^T] W \mathbb{E}[\mathbf{x}] \end{aligned} \quad (4.17)$$

Finally, including Eq. (4.17) in Eq. (4.14) gives a reduced expression for the expected value of the cost index

$$\begin{aligned}
J &= \mathbb{E}[(\mathbf{x} - \mathbf{x}^*)^T W (\mathbf{x} - \mathbf{x}^*)] \\
&= \text{tr}(W P_{xx}) + \mathbb{E}[\mathbf{x}^T] W \mathbb{E}[\mathbf{x}] - 2\mathbb{E}[\mathbf{x}^T] W \mathbf{x}^* + \mathbf{x}^{*\top} W \mathbf{x}^* \\
&= \text{tr}(W P_{xx}) + (\mathbb{E}[\mathbf{x}] - \mathbf{x}^*)^T W (\mathbb{E}[\mathbf{x}] - \mathbf{x}^*)
\end{aligned} \tag{4.18}$$

The new objective in Eq. (4.18) is a significant reduction compared to the original statement in Eq. (4.6). Instead of tracking the full statistical distribution of the augmented state, the new cost measure requires only the mean and covariance of the joint state PDF. In addition, it becomes necessary to only track statistical moments instead of the full state probability distribution. This property will be leveraged later for rapid solution of the modified objective.

Note that no assumptions on the underlying form of the joint PDF are assumed; because the Mayer cost has a quadratic form (see Eq. (4.12)), the expectation can be evaluated based only on the first and second central statistical moments of \mathbf{x} , even if the uncertainty itself is non-Gaussian. However, we will shortly make the assumption that the uncertainty distribution remains approximately normal and exhibits the Markov property [205]. In this case, the information set Eq. (4.5) reduces to

$$\Lambda[t_0, t] = \{\hat{\mathbf{x}}_k, P_{xx_k}\} \tag{4.19}$$

where $\hat{\mathbf{x}}_k \in \mathbb{R}^n$ is the current state estimate produced by sequential or batch filter and $P_{xx_k} \in \mathbb{R}^{n \times n}$ is its associated post-update estimation error covariance. The approach eliminates the need for user-defined weighting parameters often found in distributional robust optimization approaches such as weighted-sum and ϵ -constraint techniques [204].

Equation (4.18) can be interpreted as a multi-objective statement to simultaneously minimize mean drift from a desired terminal state \mathbf{x}^* along with variation of \mathbf{x} about its mean. In the case where the mean objective $\mathbb{E}[\mathbf{x}] = \mathbf{x}^*$ is exactly satisfied, the problem reduces to minimizing a weighted trace of the final covariance. It is also helpful to note that, because W and P_{xx} are symmetric positive semi-definite matrices, their product will produce a positive semi-definitive

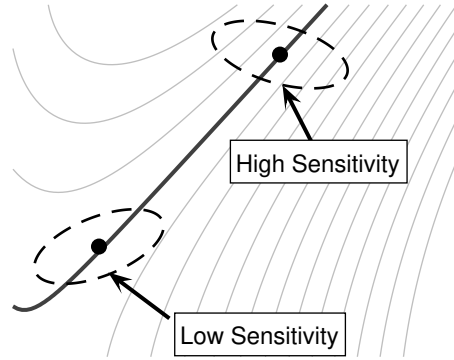


Figure 4.1: Illustrative sensitivity of final covariance with equivalent optimality of mean states.

matrix. Thus, the weighted trace approach accounts for components of the final state estimate covariance relative to sensitive directions in the objective space of Eq. (4.8). This property is illustrated in Fig. 4.1 for two trajectories with equivalent mean optimality. Uncertainty components in sensitive directions of the cost function are penalized more than less-sensitive directions. The weighting matrix W accounts for the relative orientation of the covariance matrix with respect to the Mayer objective function contours. In summary, the modified cost in Eq. (4.18) retains information from the original expectation objective of Eq. (4.6) in terms of the state mean and estimation error covariance, often considered readily-available quantities.

4.2.3 Discrete-time Extended Consider Kalman Filtering

Equation (4.18) transcribes the original optimization objective as a function of the joint PDF of \mathbf{x} . Solving this problem requires propagating statistical moments of the joint PDF of \mathbf{x} from the current time to the final time t_f . The Extended Kalman Filter (EKF) [174, 206] is a well-known tool in nonlinear estimation. The EKF has seen use in hypersonic entry trajectory reconstruction problems [129, 207]. In many scenarios, however, parameters describing the dynamics or measurement models of a system may not be known perfectly. The underlying uncertainty in such quantities can degrade performance or lead to filter divergence if left unaccounted for. Conversely, adding too many states to the filter can lead to burdensome computational requirements that

cannot be met. These parameters can instead be included as *consider* variables in the Kalman filter [208]. Errors in parameters are reflected in the associated covariance update equations of the consider filter, while nominal parameter estimates remain static. We leverage the extended consider Kalman filter (ECKF) in this work to predict propagated uncertainty due to dynamics and measurement updates. While the ECKF may not be desirable for on-board estimation, it is a useful analysis tool for studying uncertainty due to errors in (possibly) unobservable parameters.

Construction of the ECKF equations is briefly summarized as follows. Uncertainty in system parameters \mathbf{p} is encapsulated by a consider covariance matrix $P_{pp} \in \mathbb{R}^{q \times q}$ and correlation $P_{xp_k} \in \mathbb{R}^{n \times q}$, where $P_{xp_k} = P_{px_k}^T$.

$$P_{pp} = E[(\mathbf{p} - \bar{\mathbf{p}})(\mathbf{p} - \bar{\mathbf{p}})^T] \quad (4.20a)$$

$$P_{xp_k} = E[(\mathbf{x}_k - \hat{\mathbf{x}}_k)(\mathbf{p} - \bar{\mathbf{p}})^T] \quad (4.20b)$$

The system dynamic equations are linearized about the current state estimate mean and nominal parameters as

$$\tilde{\mathbf{x}}_{k+1} = \Phi_k \tilde{\mathbf{x}}_k + \Psi_k \tilde{\mathbf{p}} + \mathbf{w}_k \quad (4.21)$$

where $\tilde{\mathbf{x}}_k = \mathbf{x}_k - \hat{\mathbf{x}}_k$ and $\tilde{\mathbf{p}} = \mathbf{p} - \bar{\mathbf{p}}$ are the deviations of each quantity from its respective mean estimate. Discrete-time sensitivity matrices are required in practical estimation problems implemented on a digital computer. These matrices are approximated from the continuous-time Jacobian matrices $A_{\mathbf{x}_k}$ and $A_{\mathbf{p}_k}$ over a sufficiently small sampling period Δt as

$$\Phi_k = [I_{n \times n}] + A_{\mathbf{x}_k} \Delta t + \mathcal{O}(\Delta t^2) \quad (4.22a)$$

$$\Psi_k = A_{\mathbf{p}_k} \Delta t + \mathcal{O}(\Delta t^2) \quad (4.22b)$$

where

$$A_{\mathbf{x}_k} = \left[\frac{\partial \mathbf{f}}{\partial \mathbf{x}} \right]_{\hat{\mathbf{x}}_k, \bar{\mathbf{p}}, u_k} \quad (4.23a)$$

$$A_{\mathbf{p}_k} = \left[\frac{\partial \mathbf{f}}{\partial \mathbf{p}} \right]_{\hat{\mathbf{x}}_k, \bar{\mathbf{p}}, u_k} \quad (4.23b)$$

Similarly, the measurement model in Eq. (4.4) is linearized about the current state estimate mean as

$$\tilde{\mathbf{y}}_k = H_{\mathbf{x}_k} \tilde{\mathbf{x}}_k + H_{\mathbf{p}_k} \tilde{\mathbf{p}} + \mathbf{v}_k \quad (4.24)$$

where

$$H_{\mathbf{x}_k} = \left[\frac{\partial \mathbf{h}}{\partial \mathbf{x}} \right]_{\hat{\mathbf{x}}_k, \bar{\mathbf{p}}} \quad (4.25a)$$

$$H_{\mathbf{p}_k} = \left[\frac{\partial \mathbf{h}}{\partial \mathbf{p}} \right]_{\hat{\mathbf{x}}_k, \bar{\mathbf{p}}} \quad (4.25b)$$

We note that whereas the parameter vector \mathbf{p} is (by definition) constant, its dynamics and measurement sensitivity matrices Ψ_k and $H_{\mathbf{p}_k}$ may change at each epoch due to the influence of system states. The preceding discrete-time sensitivity matrices allow for calculation of both the time propagation and measurement update steps.

The ECKF update equations are briefly summarized as follows, largely following Ref. [174]. First, the filter is initialized with nominal state and parameter estimates, as well as estimation error covariance matrices as

$$\hat{\mathbf{x}}(t_0) = \hat{\mathbf{x}}_0 \quad (4.26a)$$

$$P_{xx}(t_0) = \text{E}[(\mathbf{x}(t_0) - \hat{\mathbf{x}}_0)(\mathbf{x}(t_0) - \hat{\mathbf{x}}_0)^T] \quad (4.26b)$$

$$P_{xp}(t_0) = \text{E}[(\mathbf{x}(t_0) - \hat{\mathbf{x}}_0)(\mathbf{p} - \bar{\mathbf{p}})^T] \quad (4.26c)$$

$$P_{pp} = \text{E}[(\mathbf{p} - \bar{\mathbf{p}})(\mathbf{p} - \bar{\mathbf{p}})^T] \quad (4.26d)$$

Between measurement epochs t_k and t_{k+1} , the mean update equation follows the dynamics of Eq. (4.1) with no process noise.

$$\hat{\mathbf{x}}_{k+1}^- = \int_{t_k}^{t_{k+1}} \mathbf{f}(\hat{\mathbf{x}}(\tau), \bar{\mathbf{p}}, u(\tau), \tau) d\tau + \hat{\mathbf{x}}_k^+ \quad (4.27)$$

Update steps for estimation covariance and cross-covariance are summarized as follows

$$P_{xx_{k+1}}^- = \Phi_k P_{xx_k}^+ \Phi_k^T + \Phi_k P_{xp_k}^+ \Psi_k^T + \Psi_k P_{px_k}^+ \Phi_k^T + \Psi_k P_{pp}^+ \Psi_k^T + \Gamma_k Q_k \Gamma_k^T \quad (4.28a)$$

$$P_{xp_{k+1}}^- = \Phi_k P_{xp_k}^+ + \Psi_k P_{pp}^+ \quad (4.28b)$$

Next, the state estimate measurement update can be found as

$$\hat{\mathbf{x}}_{k+1}^+ = \hat{\mathbf{x}}_{k+1}^- + K_{k+1}(y_{k+1} - h(\hat{\mathbf{x}}_{k+1}^-, \bar{\mathbf{p}}, t_{k+1})) \quad (4.29)$$

The Kalman gain matrix K_{k+1} is calculated as

$$K_{k+1} = (P_{xx_{k+1}}^- H_{x_{k+1}}^\top + P_{xp_{k+1}}^- H_{p_{k+1}}^\top)(H_{x_{k+1}} P_{xx_{k+1}}^- H_{x_{k+1}}^\top + H_{x_{k+1}} P_{xp_{k+1}}^- H_{p_{k+1}}^\top + H_{p_{k+1}} P_{px_{k+1}}^- H_{x_{k+1}}^\top + H_{p_{k+1}} P_{pp_{k+1}}^- H_{p_{k+1}}^\top + R_{k+1})^{-1} \quad (4.30)$$

Finally, the covariance matrix measurement update equations are

$$P_{xx_{k+1}}^+ = (I_{n \times n} - K_{k+1} H_{x_{k+1}}) P_{xx_{k+1}}^- - K_{k+1} H_{p_{k+1}} P_{px_{k+1}}^- \quad (4.31a)$$

$$P_{xp_{k+1}}^+ = (I_{n \times n} - K_{k+1} H_{x_{k+1}}) P_{xp_{k+1}}^- - K_{k+1} H_{p_{k+1}} P_{pp} \quad (4.31b)$$

Following initialization, the dynamics and measurement update steps are repeated until a stop time is reached. A convenient property of the measurement covariance update steps in Eqs. (4.31a) and (4.31b) is that they do not depend on the measurement residual directly. Thus, the update equations can anticipate future measurement conditioning effects relative to a propagated mean state. Coupled with analytical expressions for the sensitivity matrices, this enables solution of the robust optimization objective.

The primary assumption in applying the consider filter is for Gaussian uncertainty in the system state and parameters. This uncertainty may be correlated, but non-Gaussian distributions are not captured by the ECKF. The form of the cost function in Eq. (4.8) represents another assumption, which is required for the expectation in Eq. (4.17) as a function of the state mean and estimate covariance. This form minimizes a sum-square error (SSE) function of terminal states, which is common for set-point tracking or Mayer objectives. However, other practical cost metrics may not conform to this assumption. Finally, by appending the state error covariance of the consider filter to the system, the problems scales quadratically with the number of states. The computational requirements are then increased with the augmented system. In order to reduce the numerical overhead in the augmented system, an assumptions for a fixed solution form is proposed

in the following section. This step is taken to improve feasibility and convergence for on-line guidance applications.

4.2.4 Parametric Control Solution

Determining a feasible solution subject to the ECKF covariance update equations is a non-trivial task. A potential option is to numerically solve the OCP using nonlinear programming (NLP) with direct collocation. NLP methods often require significant computational effort and an initial solution guess, making them particularly difficult for on-line guidance applications. In this work, however, we take a less arduous approach by utilizing a parametric control solution [78]. A parametric control fixes the functional form of a solution and reduces the problem to a set of *decision variables*, denoted $\mathbf{k} \in \mathbb{R}^{n_k}$, that define its magnitude and phase.

$$\mathbf{u} = \mathbf{u}(t, \mathbf{k}) \tag{4.32}$$

Optimization over the decision variables can be performed in a similar manner to direct methods, which discretize the control solution in time over a large number of collocation points. However, the computational effort of the parametric control solution is significantly lower as fewer optimization variables are present. We note that the functional form of a control may not permit globally optimal minima. For this work, a solution form is chosen inspired by bang-bang optimal control arguments [209] in aerocapture problems. These solution structures provide sufficient degrees of freedom in this problem, and they also give insight on optimal parameter tuning of existing entry guidance methods.

Given a parametric control solution in Eq. (4.32), we summarize the robust optimization

problem to be solved as follows.

$$\min_{\mathbf{k}} \quad \text{tr}(W P_{xx}(t_f)) + (\hat{\mathbf{x}}(t_f) - \mathbf{x}^*)^T W (\hat{\mathbf{x}}(t_f) - \mathbf{x}^*) \quad (4.33a)$$

$$\text{Subject to: } \psi[\hat{\mathbf{x}}(t_f), t_f] = 0 \quad (4.33b)$$

$$\mathbf{u}^T \mathbf{u} - 1 \leq 0 \quad (4.33c)$$

$$t_f \text{ free} \quad (4.33d)$$

The problem is subject to system dynamics, terminal state constraint $\psi : \mathbb{R}^n \times \mathbb{R} \rightarrow \mathbb{R}$, control magnitude bounds, and end-time free conditions. The terminal state constraint is assumed not to interfere with the optimal cost. It should be noted that uncertainty in the system states prevents satisfying the constraint exactly; however, it can be enforced by requiring the mean state to lie on the terminal constraint manifold. With an end-time free condition, the terminal state constraint implicitly defines the *stop conditions* of the problem, usually based on a predefined threshold of system states.

4.3 Application to Aerocapture

4.3.1 Process and Measurement Models

A planar model of the planetary entry vehicle dynamics [91] is given in Eqs. (4.34a–4.34c). These equations neglect planetary rotation effects and assume a simple radially-varying gravity model. The system states include geocentric position r , planet-relative velocity magnitude V , planet-relative velocity flight-path angle γ . Convention for flight-path angle is positive above the local horizontal.

$$\dot{r} = V \sin \gamma \quad (4.34a)$$

$$\dot{V} = -D - \frac{\mu}{r^2} \sin \gamma \quad (4.34b)$$

$$\dot{\gamma} = \frac{1}{V} \left(L \cos \sigma - \frac{\mu}{r^2} \cos \gamma + \frac{V^2}{r} \cos \gamma \right) \quad (4.34c)$$

The lift L and drag D acceleration terms are

$$L = \frac{1}{2}\rho V^2 \left(\frac{C_L A}{m} \right) \quad (4.35)$$

$$D = \frac{1}{2}\rho V^2 \left(\frac{C_D A}{m} \right) \quad (4.36)$$

where ρ is the atmospheric density, C_L and C_D are the aerodynamic lift and drag coefficients, respectively, and m is the vehicle mass. The control input is bank angle σ representing a rotation of the lift force about its velocity vector. Bank angle is defined as zero for a full lift-up orientation in the vertical plane, and positive for a right-wing-down rotation. In the absence of planetary rotation effects, the inertial and relative velocity magnitude and flight-path angle coincide.

An observer is assumed to provide new state information from sensor data during atmospheric flight. A reasonable model is the sensed acceleration magnitude [207], which is dictated by the net aerodynamic force on the vehicle. This information would be readily available from accelerometers mounted to the body axes of a vehicle. We assume a simple measurement model to be the magnitude of the lift and drag acceleration as

$$\mathbf{h}(\mathbf{x}_k, \mathbf{p}, t_k) = \sqrt{L^2 + D^2} \quad (4.37)$$

The partial derivatives with respect to the entry vehicle dynamics are generated using the symbolic toolbox in MATLAB. These are given in Appendix D.

The measurement model is assumed a function of several consider parameters, most importantly aerodynamic and atmospheric quantities. Though certain approaches exist for atmospheric estimation, these methods operate in a deterministic manner and are unable to decouple aerodynamic and atmospheric uncertainty. More intricate sensor data based on pressure sensors on the vehicle forebody may provide additional state information [130], but for the purpose of this work the sensed acceleration model in Eq. (4.37) is sufficient to represent anticipated measurement effects during entry. Further information on traditional atmospheric estimation methods is provided in Appendix E.

4.3.2 Optimal Control Objectives

Optimization objectives should reflect the overall goal of an aerocapture maneuver, which typically involve properties of the post-capture orbit. The accuracy of this orbit is important as it dictates the overall ΔV budget needed to correct for targeting errors during the atmospheric pass. Under Keplerian motion, the orbital properties following the atmospheric pass are well-defined at the exit interface. An objective can be formulated to minimize the apoapsis error [122], with the goal of matching a desired apoapsis radius r_a^* as

$$\tilde{\phi}[\mathbf{x}(t_f), t_f] = r_a(t_f) - r_a^* \quad (4.38)$$

The apoapsis radius can be calculated from

$$r_a(t_f) = a(t_f)(1 + e(t_f)) \quad (4.39)$$

Semi-major axis a can be computed from the radial position r and velocity magnitude V at the final time as

$$a(t_f) = \frac{\mu}{2\mu/r(t_f) - V(t_f)^2} \quad (4.40)$$

In addition, e is the orbital eccentricity related to r , V , and γ as

$$e(t_f) = \sqrt{1 - \frac{r^2(t_f)V^2(t_f)\cos^2\gamma(t_f)}{\mu a(t_f)}} \quad (4.41)$$

Another practical approach consists of the combined ΔV cost of a two-burn correction [91]. The burns include a periapsis raise ΔV_1 performed at the first apoapsis crossing, followed by an apoapsis correction ΔV_2 at the next periapsis. Since vehicle mass dedicated to ΔV margins reduces useful delivered mass to orbit, these propulsive burns dictate the overall efficiency of the maneuver. The corresponding cost function involves the total in-plane ΔV budget with respect to a desired apoapsis radius r_a^* and periapsis radius r_p^* . Since the goal is to minimize the magnitude of each burn, the cost can be posed as the sum-squared of the series of correction burns. The objective is summarized as follows

$$\Delta V_{\text{total}} = |\Delta V_1| + |\Delta V_2| \quad (4.42)$$

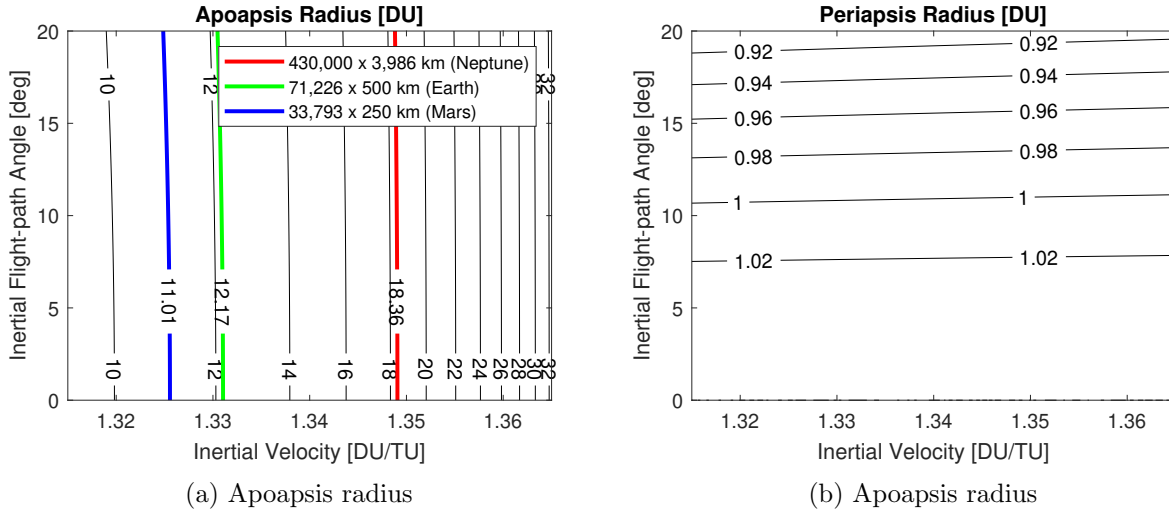


Figure 4.2: Exit interface orbital parameters for select aerocapture mission concepts (Heidrich *et al.* [166]).

where

$$\Delta V_1 = \sqrt{2\mu} \left(\sqrt{\frac{1}{r_a} - \frac{1}{r_a + r_p^*}} - \sqrt{\frac{1}{r_a} - \frac{1}{2a}} \right) \quad (4.43a)$$

$$\Delta V_2 = \sqrt{2\mu} \left(\sqrt{\frac{1}{r_p^*} - \frac{1}{r_a^* + r_p^*}} - \sqrt{\frac{1}{r_p^*} - \frac{1}{r_a + r_p^*}} \right) \quad (4.43b)$$

For this study, only the apoapsis radius targeting cost index is considered, though other cost metrics may be important depending on mission criteria. The weighting matrix is needed in order to evaluate the robust cost measure of Eq. (4.33a). Referring to the definition in Eq. (4.13), the partial derivatives of Eq. (4.39) are evaluated with respect to each state to give the weighting matrix W . These derivatives are obtained using the symbolic toolbox in MATLAB.

Figure 4.2 illustrates relationships between terminal flight-path angle and velocity for several aerocapture concept missions. At atmospheric exit, inertial velocity strongly influences apoapsis radius, whereas inertial flight-path angle largely influences periapsis radius. It is apparent that apoapsis radius errors of zero are generally feasible in aerocapture. On the other hand, a periapsis radius above the atmospheric interface altitude is not reachable. During the aerocapture pass, flight-path angle passes through zero (from negative to positive), leaving the vehicle close to periapsis at

atmospheric exit. Practically speaking, it is not possible to raise the periapsis out of the atmosphere and still exit with a positive flight-path angle. Therefore, cost functions involving periapsis radius error (or ΔV) fall into the category of bang-bang control, since the target set S is not reachable. A broad class of problems, however, fall into the degenerate singular control form, such as the apoapsis or semi-major axis targeting problem.

4.3.3 Consider Parameter Uncertainty Models

Constructing the ECKF process and model equations for aerocapture requires information on the underlying sources of uncertainty. Moreover, the UQ models must also be consistent with underlying assumptions in the ECKF, namely that the estimates of each parameter remain constant and normally distributed. Two major sources of uncertainty in atmospheric entry problems are atmospheric variability and aerodynamic coefficients [130,210]. Traditional density estimation methodologies cannot estimate both quantities simultaneously. Thus, treatment of these quantities as consider parameters in an ECKF is a reasonable model of unobservable coupling between atmospheric and aerodynamic uncertainty.

Atmospheric properties play an important role in quantifying performance margins and robustness in entry flight problems. Lift and drag forces are determined by aerodynamic pressure and therefore the local altitude-density relationship of a planet's atmosphere. Any entry guidance approach can expect improved performance with better understanding of the atmosphere. However, inherent variability, as well as short-term and seasonal variations of the atmospheric structure preclude exact knowledge of the environment prior to entry. MarsGRAM [211] is currently considered a state-of-the-art model for quantifying atmospheric variations. The program provides a nominal mean density profile and dispersed atmospheric profiles with respect to latitudinal and temporal behavior. Secondary effects can also be modeled in the MarsGRAM software; these include winds, horizontal variation along a flight-path at fixed altitudes, and high-frequency variations. However, such effects are often minor compared to the primary altitude-density variations dictating the bulk structure of the atmospheric uncertainty.

Previous studies have approached the atmospheric UQ problem using Monte Carlo methods [5]. In these studies, a large number of runs are performed in which the guidance operates on a nominal GRAM density profile, while the outer loop of the simulation operates on a dispersed “truth” model. More recent efforts have approached atmospheric uncertainty using Gaussian processes [115], machine learning algorithms [212], or other advanced methods such as the Ensemble Correlation Filter [213]. However, these strategies are not immediately applicable to linear covariance analysis as required by the ECKF.

We propose a new approach to atmospheric uncertainty modeling to overcome limitations of GRAM data to estimation filtering. Under some mild assumptions, the atmospheric variability as a function of altitude is represented as a set of independent normally-distributed constants. These constants are included as consider parameters in the ECKF update equations. This allows for rapid propagation of uncertainty due to density variations without the need for computationally intensive simulation of GRAM data. First, consider a variation of the true density profile ρ relative to a nominal value $\bar{\rho}$. The difference between these quantities is a small perturbation $\delta\rho$ defined as a percent difference from mean density [211, 214]. The true density profile at each altitude is described by

$$\rho = \bar{\rho}(1 + \delta\rho) \quad (4.44)$$

The dependence of both ρ and $\delta\rho$ on altitude h is implied, where we ignore longitudinal and latitudinal variations. A common expression for the nominal density profile is an exponential model

$$\bar{\rho} = \rho_0 \exp\left(-\frac{h}{H}\right) \quad (4.45)$$

where ρ_0 is the reference surface density and H is the density scale height. Suppose the true density variations can be accounted for with $\delta\eta_i$, $i = 1, \dots, l$ polynomial expansion terms about the nominal profile. The density perturbation is expressed as

$$\delta\rho = \delta\eta_1 + \delta\eta_2 \left(\frac{h}{h_e}\right) + \dots + \delta\eta_l \left(\frac{h}{h_e}\right)^{l-1} \quad (4.46)$$

where h_e is a scaling parameter to provide numerical stability. For this work, an h_e of 125 km

(the atmospheric entry interface altitude) works well. We assume $\delta\eta_i \sim \mathcal{N}(0, \sigma_{\delta\eta_i}^2)$ are a set of independent random variables reflecting inherent randomness in the density process. The total density is expressed as

$$\rho = \rho_0 \exp\left(-\frac{h}{H}\right) \left(1 + \delta\eta_1 + \delta\eta_2 \left(\frac{h}{h_e}\right) + \dots + \delta\eta_l \left(\frac{h}{h_e}\right)^{l-1}\right) \quad (4.47)$$

We note that $\delta\eta_i = 0$ in Eq. (4.47) returns the nominal profile Eq. (4.45). The consider parameter matrix for atmospheric uncertainty is

$$P_{pp} = \mathbb{E}[\delta\boldsymbol{\eta}\delta\boldsymbol{\eta}^T] = \text{diag}(\delta\eta_1, \dots, \delta\eta_l) \quad (4.48)$$

A least-squares fitting of dispersed atmospheric density data is performed to estimate the $\delta\eta_i$ perturbation parameters with respect to data generated by the built-in Monte Carlo functionality of the MarsGRAM software. Values are based on 1,000 GRAM profiles with 100 m altitude steps. See Fig. 4.4. Three density perturbation terms prove sufficient to represent the MarsGRAM altitude-dependent density variations to within a high degree of accuracy. See Sec. 4.4 for these values.

An individual dispersion profile is illustrated in Fig. 4.3 along with the upper and lower $2\text{-}\sigma$ bounds of the GRAM data. The polynomial series perturbation model is compared to an exponential density perturbation model [215], which models reference density and scale height as variable parameters. The predicted bounds for each model are indicated with dashed lines. The polynomial model in Eq. (4.47) is a close representation of true variations in atmospheric density, whereas the exponential model lacks the structural form to accurately predict density variations, particularly at higher altitudes. This model is not valid above altitudes of about 125 km, at which point perturbations may grow large enough to generate negative density values. Across the range of applicable altitudes in this problem, the polynomial model allows for density uncertainty to be carried forward via the ECKF update equations.

The approach assumes adequate knowledge of the density uncertainty is available to the designer. Performance is expected to decrease if the atmospheric density uncertainty deviates significantly from predicted values. The nominal profile is also assumed fixed, whereas the encountered

density is likely to change with day-of flight conditions and spatial variations. The true density is unlikely to be a zero-mean process, as required in this analysis. However, atmospheric estimation techniques may improve these limitations by providing an estimate of the mean profile. In addition, there may exist an opportunity to append atmospheric model parameters in Eq. (4.47) as states in the estimation filter. For the purposes of this study, these quantities are assumed unobservable, though future work may consider density estimation in tandem with optimal trajectory design.

In addition to atmospheric uncertainty, inherent volatility in aerodynamic performance during hypersonic entry flight plays a major role in dispersion analysis. The aerodynamic forces on the vehicle are dictated by lift and drag coefficients C_L and C_D , and possibly pitching moment C_m . While aerodynamic UQ is an important aspect of entry guidance performance, a full analysis of this uncertainty is beyond the scope of this paper. Instead, we assume the aerodynamic coefficients as normally distributed static parameters. Previous work regarding guided entry at Mars [216] take a similar approach to aerodynamic uncertainty. This approach allows for aerodynamic model uncertainty to be incorporated into an ECKF through consider parameter analysis.

4.3.4 Bang-bang Parametric Control

A solution strategy for Eq. (4.33a) is outlined in Sec. 3.2 utilizing a parametric control. The functional form for u must be chosen carefully to permit admissible solutions adhering to problem constraints. For example, FNPAG [91] uses a bang-bang control in its algorithmic structure, which consists of two phases. In the first phase, σ_d is held constant while the vehicle commands an initial bank angle σ_0 . This value is typically chosen as a shallow bank angle in order to provide a raise in periapsis radius while avoiding steeper reentry trajectories. At each guidance call, the optimal switch time t_s is recalculated from the current state with σ_d and σ_0 fixed such that the apoapsis targeting condition in Eq. (4.39) or ΔV cost in Eq. (4.42) is met. Once t_s is predicted to take place within the next guidance cycle, the algorithm switches to Phase 2. The second phase is a bank-to-steer strategy that continuously updates the bank angle σ_d based on the previous targeting conditions. This is repeated until the vehicle reaches atmospheric exit or other stop conditions.

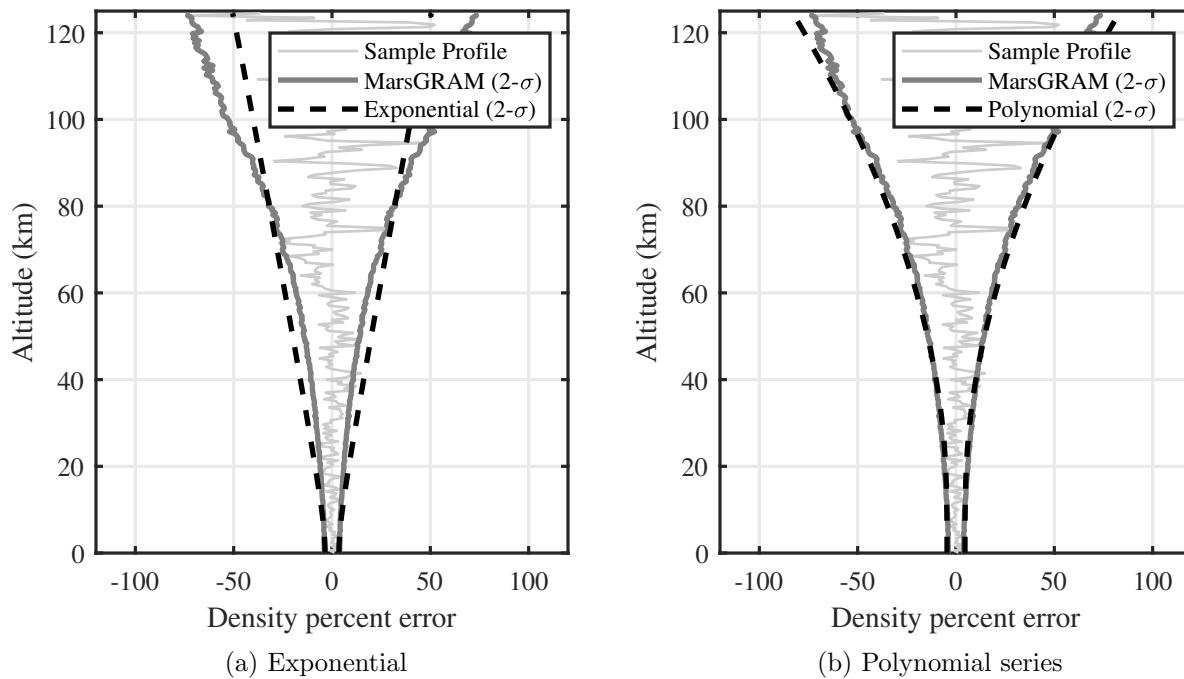


Figure 4.3: Density perturbation models from MarsGRAM dispersion data.

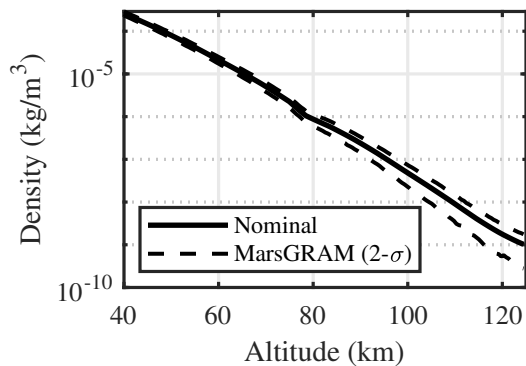


Figure 4.4: GRAM atmospheric density variations as a function of altitude.

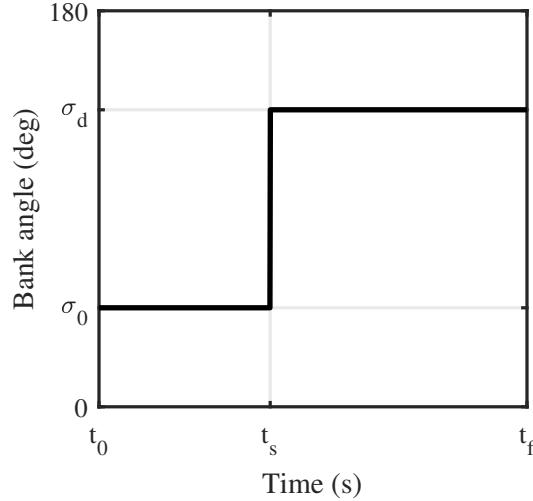


Figure 4.5: Representative bang-bang bank angle control profile with single switch time.

The bang-bang bank angle control profile [91] is a viable candidate for a parametric control solution of the robust optimization objective. This open-loop control structure is illustrated in Fig. 4.5. The control form is described by a set of shape parameters σ_0 , σ_d , and t_s such that

$$u^*(t, \mathbf{k}) = \begin{cases} \cos \sigma_0 & \text{if } t \leq t_s \\ \cos \sigma_d & \text{if } t > t_s \end{cases} \quad (4.49)$$

$$\mathbf{k} = [\sigma_0, \sigma_d, t_s]^T \quad (4.50)$$

Note that Eq. (4.49) is not a true bang-bang control since $0 < \sigma_0 < \sigma_d < 180^\circ$ are interior points of the control bounds. However, as shown in Sec. 4.4, this functional form permits sufficient degrees of freedom to find local minima.

Although the dimension of the optimization search space is drastically reduced, determining the decision variables \mathbf{k} in real-time (such on a flight computer as a synchronous guidance routine) may still pose challenges. To alleviate this issue, σ_0 is set to 15 degrees, corresponding to a fixed initial bank angle. This value is sufficient to provide a near lift-up lofting trajectory, while leaving margin for cross range control if required. The bank angle switch σ_d is then treated as a trade parameter. This leaves switch time t_s as the remaining unknown in the control solution. With

a fixed functional form, direct solution is achieved through numerical integration of the equations of motion in a 4th-order Runge-Kutta integrator. A bisection root-finding method is employed to solve for t_s given σ_d and σ_0 , thus fully defining the decision variables \mathbf{k} . This method is applied to solve Eq. (4.33a). We note that this solution is open-loop; a closed-loop implementation could continue to update guidance parameters at predetermined time increments. In this study, only the open-loop solution is studied in order to allocate guidance parameters \mathbf{k} for optimal prediction of future states.

4.4 Results

4.4.1 Mars Aerocapture Mission

Solution of the robust optimization procedure is illustrated for a Mars aerocapture study in order to demonstrate its utility in mission design. Low arrival velocities for small spacecraft at Mars typically enable propulsive orbit insertion with modest mass requirements. However, larger vehicles may see improved scaling and mass-savings using aerocapture. These entry systems are expected to support Earth return missions such as the Mars Sample Return (MSR) program using flight-proven heritage entry technologies. A multi-center NASA study [196] identified potential vehicle concepts for delivering spacecraft into Mars orbit using aerocapture. Problem parameters are assumed for a 4.65 m diameter 70 degree sphere-cone forebody aeroshell. The vehicle has a ballistic coefficient of 300 kg/m², entry mass of 7,387 kg, and reference area of 16.98 m². The vehicle is trimmed at an angle-of-attack of 16 degrees producing a hypersonic lift-to-drag ratio (L/D) of 0.24. The aerocapture target is a 500 km altitude circular orbit.

The nominal entry state is given in Table 4.1 along with corresponding uncertainties in each state component at the entry interface epoch. Uncertainty in the initial position and velocity represents interplanetary entry interface delivery errors at Mars. Consider parameters are given in Table 4.1 for the corresponding atmosphere and aerodynamic models discussed in Sec. 4.3. These models are a reasonable approximation of entry environment uncertainty at Mars. However,

Table 4.1: Initial state and parameter uncertainties for Mars aerocapture mission.

Quantity	Nominal	Uncertainty, 1- σ
<i>Initial States</i>		
Geocentric radius, r	3521 km	1700 m
Velocity, V	7.150 km/s	70 m/s
Flight-path angle, γ	-12.731 deg	0.1 deg
<i>Consider Parameters</i>		
Drag coefficient, C_D	1.45	$\pm 7.5\%$
Lift coefficient, C_L	0.348	$\pm 7.5\%$
Density perturbation, η_i	0	{0.0237, 0.0453, 0.4094}
<i>Process Noise</i>		
Geocentric radius, Q_{11}	0	0
Velocity, Q_{22}	0	0.001 m/s
Flight-path angle, Q_{33}	0	0.0275 deg

the number of parameters could be greatly increased to incorporate numerous other sources of uncertainty if needed. Measurement noise is based on an accelerometer root mean square (RMS) intensity value of 1,500 $\mu\text{g-rms}$ [207]. Measurements are processed at a rate of 20 Hz, with a main simulation integration rate of 100 Hz. An additive process noise covariance matrix Q is constructed based on a previous study [129] of reentry trajectory estimation at Mars. Process noise is excluded from the kinematic equation for radius, as these relationships are generally well-understood. Bank angle lower and upper bounds of 15 and 165 degrees, respectively, are enforced to conserve bank angle margin for out-of-plane motion. A full discussion of cross-range control is outside the scope of this work, but these margins are typically sufficient to ensure lateral targeting needs.

4.4.2 Numerical Results and Discussion

A nominal trajectory for the Mars aerocapture mission is shown in Fig. 4.6. The trajectory corresponds to a chosen bank angle switch σ_d of 90 degrees with a calculated switch time t_s of 120.01 seconds. At this value of σ_d , the component of lift in the vertical flight plane is forced to zero. Thus, this trajectory could be interpreted as a midpoint value of the bank angle switch parameter. These values for σ_d and t_s result in an exit trajectory with the precise 500 km altitude apoapsis radius axis. In Fig. 4.6, the velocity-altitude profile starts at an initial velocity of 7.15 km/s and is

dissipated through aerodynamic forces to the required velocity of about 3.53 km/s. The minimum capture altitude remains above 25 km, on par with similar Mars studies [53]. The peak dynamic pressure occurs at about 100 seconds. The vehicle reaches periapsis crossing at approximately the same time. Finally, Fig. 4.6 illustrates the orbit energy during the atmospheric pass. The target orbit corresponding to the desired apoapsis radius is also shown, indicating that the vehicle reaches precise exit conditions on the nominal trajectory. While these parameters satisfy the certainty equivalent objective of the aerocapture pass, further analysis will reveal the robust optimal bank angle switch subject to uncertainty in system states and parameters.

A time history of the ECKF estimation performance along the nominal trajectory is shown in Fig. 4.7. Each subplot illustrates filter performance with various contributing sources of uncertainty. Figure 4.7a shows estimation error with state uncertainty alone. This behavior is identical to the baseline EKF with no parameter uncertainty models. The plots show a $2\text{-}\sigma$ bound of the state estimate error, as well a particle sampling using 500 simulation runs to validate filter consistency. The radius uncertainty starts just above 2 km but rapidly declines prior to peak dynamic pressure. This indicates the radius state is largely observable throughout the atmospheric pass, even with larger initial uncertainty. The velocity magnitude takes longer to converge to a lower bound. The flight-path angle uncertainty has an opposite trend, and appears to grow initially. Poor observability characteristics of the flight-path angle are evident when process and measurement noise terms dominate higher in the atmosphere, which is visible in the initial and final legs of the trajectory as the error bounds increase. Uncertainty in all states will factor into the dispersed performance due to dynamic coupling in Eqs. (4.34a–4.34c). Figure 4.7b shows the ECKF performance with parameter uncertainty and no initial state uncertainty. The effect of parameter uncertainty is seen later in the trajectory as opposed to Fig. 4.7a. This behavior is explained by the fact the parameter uncertainties in Table 4.1 appear in the measurement and dynamics equations proportional to dynamic pressure. Thus, at higher altitudes parameter uncertainty has less influence. Finally, Fig. 4.7c shows the combined state and parameter uncertainty as coalesced by the ECKF. The filter achieves considerably lower estimation accuracy, particularly with the radius and velocity states

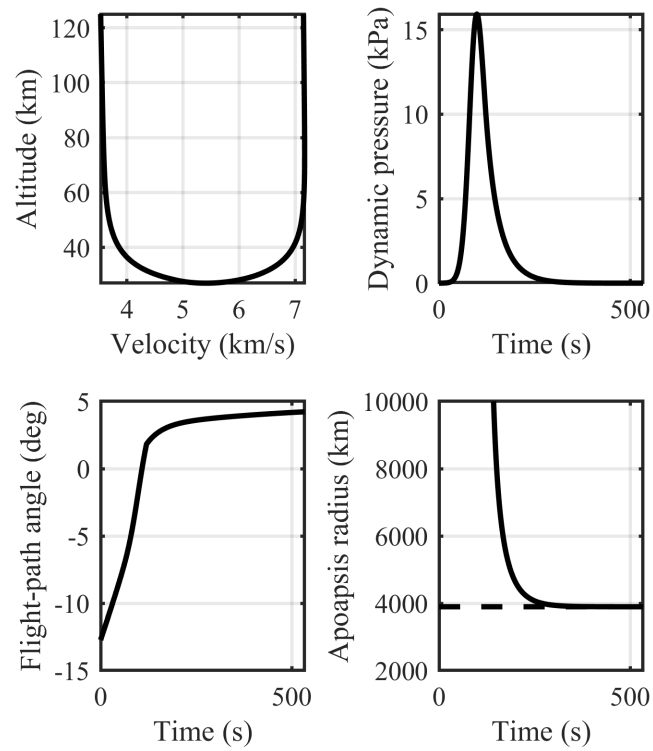
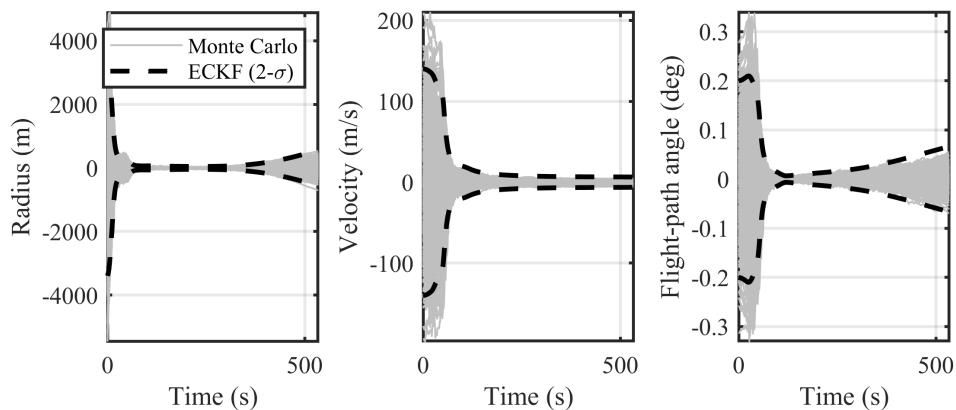
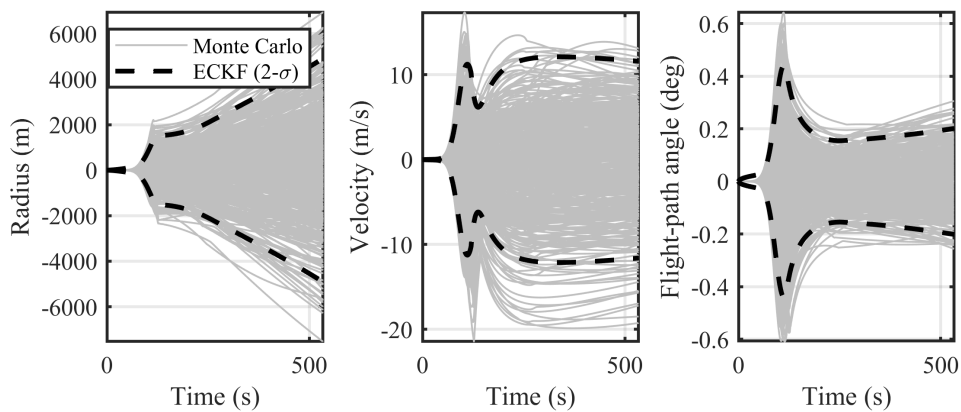


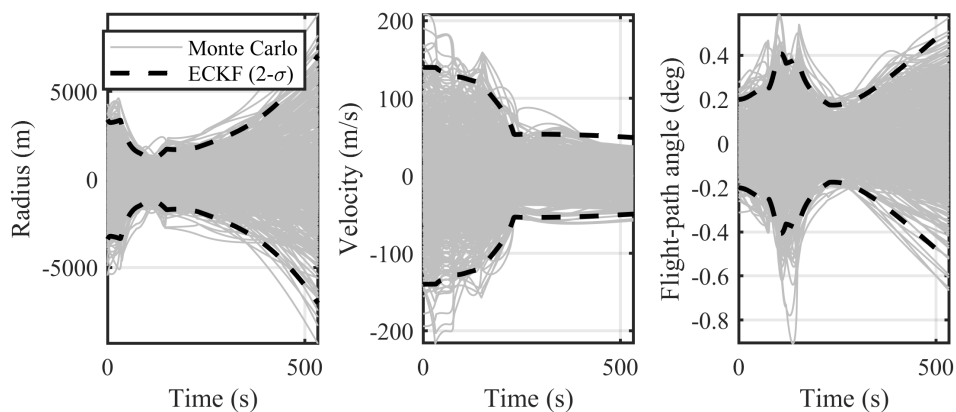
Figure 4.6: Nominal Mars aerocapture trajectory ($\sigma_d = 90$ deg). Target orbit energy shown as dashed line.



(a) State uncertainty



(b) Parameter uncertainty



(c) Combined uncertainty

Figure 4.7: ECKF estimation error residuals ($\sigma_d = 90$ deg).

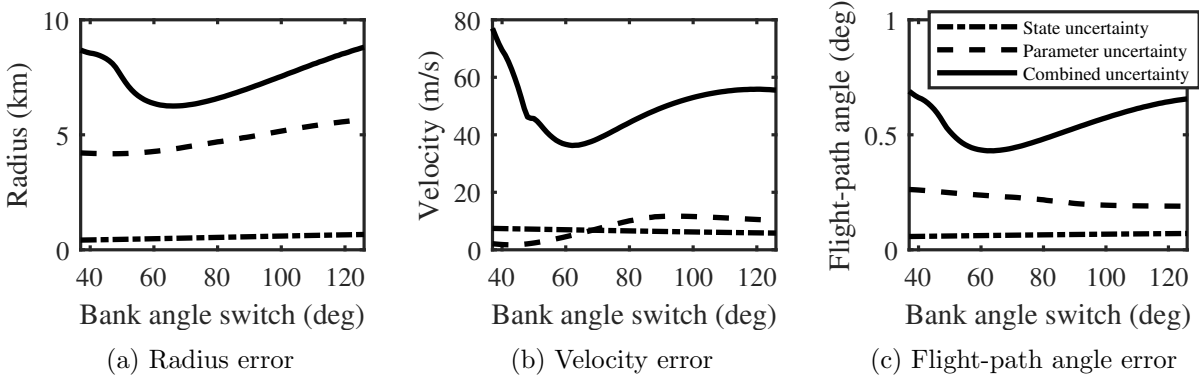


Figure 4.8: ECKF $2\text{-}\sigma$ exit state estimate uncertainty as a function of bank angle switch.

which are critical to precision of the exit orbit. These results illustrate the expected performance of the ECKF with uncertainty in the underlying dynamics and measurement models. The coupling of these uncertainties in the system dynamics may preclude perfect state knowledge as a viable assumption on entry problems with limited measurement information.

Imprecise state information during entry will inevitably degrade dispersed capture performance and hinder the ability of on-board guidance to predict future states. The robust optimization cost in Eq. (4.18) provides an alternative objective for aerocapture, with the goal of reducing the statistical deviation from a target state. A trade is performed across the bank angle switch parameter σ_d for the robust cost problem, where the initial bank command σ_0 remains fixed at 15 degrees for each solution. Figure 4.8 shows the ECKF terminal state error $2\text{-}\sigma$ bounds versus bank angle switch. The state errors are influenced by the bank angle switch, as a switch timed too early or too late may result in more rapid growth of uncertainty. The radius and flight-path angle states appear to suggest a steeper bank angle switch to minimize error bounds, whereas the velocity uncertainty is minimized at a bank angle switch of about 60 degrees.

Figure 4.9 shows the combined effect of this uncertainty on the overall apoapsis radius cost objective. An optimal bank angle switch is found at 60 degrees to provide a robust solution. The switch time corresponding to this σ_d occurs at about 105 seconds in Fig. 4.10. Time of maximum dynamic pressure (max-Q) shown as dashed line for Nominal entry flight-path angle of -12.731 deg.

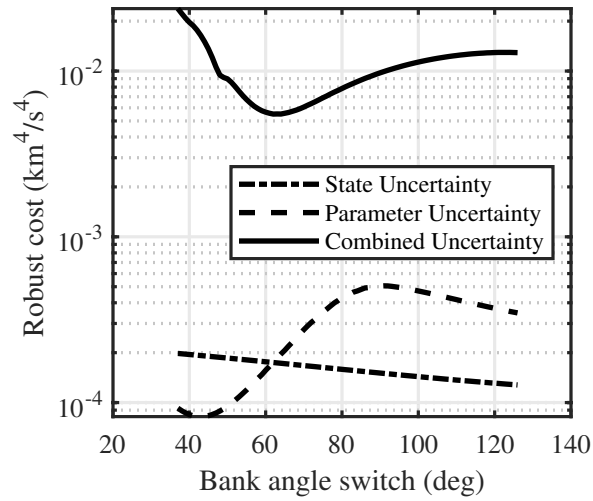


Figure 4.9: Robust cost trade as a function of bank angle switch parameter.

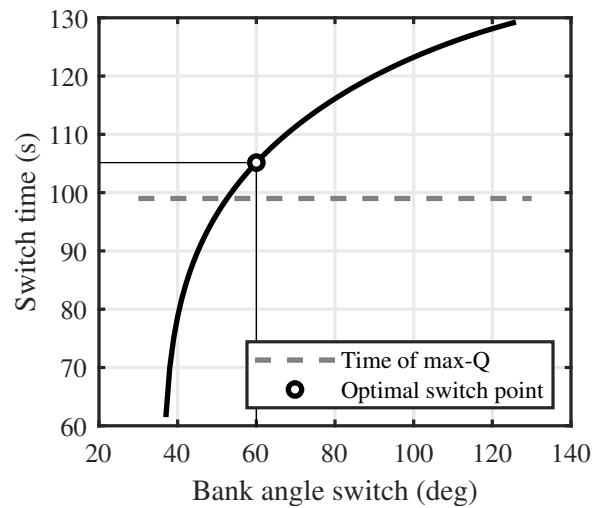


Figure 4.10: Optimal switch time for robust cost minimum. Time of maximum dynamic pressure shown as dashed line.

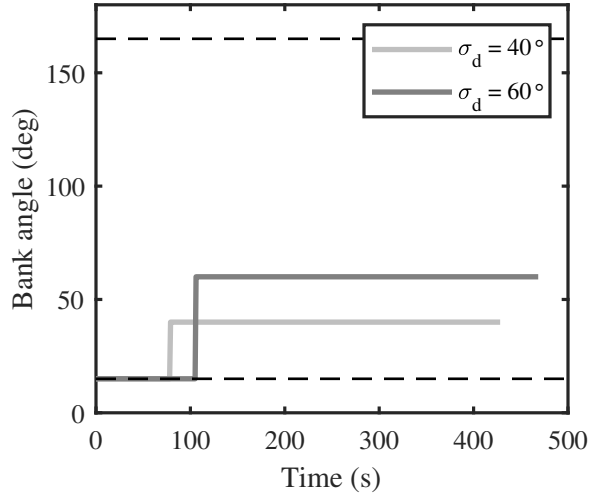


Figure 4.11: Time history of bank angle input for chosen σ_d cases.

Note that Fig. 4.10 illustrates optimal switch times for the nominal entry state. A perturbation in the initial flight-path angle or velocity will give a different switch time relationship. An interesting feature of Fig. 4.9 is that, in the case of parameter uncertainty alone, the robust cost points to a shallower bank angle switch of 40 degrees. Previous studies on NPC guidance [91] suggest shallower σ_d values will provide robust performance by conserving bank angle margin for later in the trajectory. However, as evident from Fig. 4.9, the robust solution may require a steeper bank angle switch to produce better measurements for estimation filtering. The robust optimal solution can therefore be interpreted as providing the most information over a full aerocapture pass. This mindset is in contrast to certainty equivalent NPC strategies, which treat σ_d as a tuning parameter with an inversely proportional tradeoff between performance and robustness.

The tradeoff of σ_d versus the robust cost objective provides a metric for evaluating dispersed aerocapture trajectories. To further illustrate this point, a 2,500 run Monte Carlo simulation of the dispersed ECKF performance is shown for two selected σ_d values of 40 and 60 degrees. These values correspond to the worst and best-case solutions in Fig. 4.9 for the combined uncertainty. Statistical distributions at the exit interface are plotted for both bank angle switch values in Fig. 4.12. Both cases remain approximately normally-distributed, satisfying the underlying assumptions for nor-

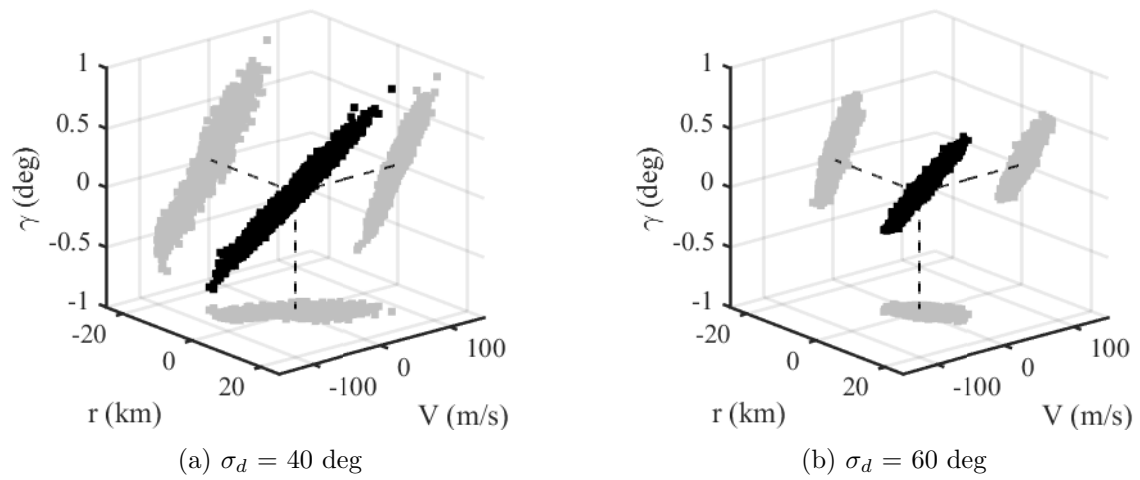


Figure 4.12: Terminal state error distribution at atmospheric exit interface.

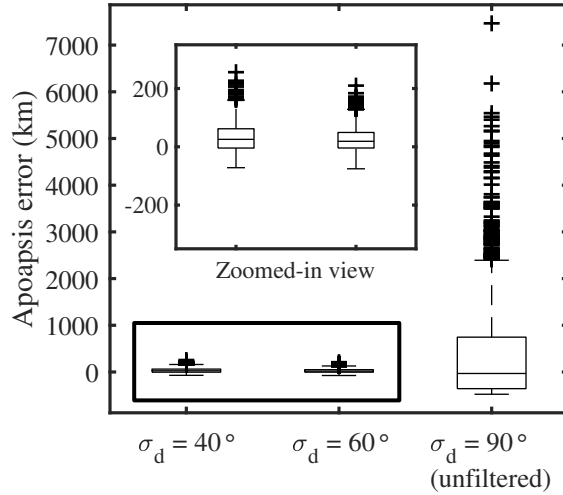


Figure 4.13: Apoapsis targeting for selected bank angle switch values.

mality in the ECKF update equations. The final states appear strongly correlated even though the initial uncertainty is uncorrelated. The output state distribution is much wider for the non-optimal σ_d solution in Fig. 4.12a, whereas in Fig. 4.12b the distribution bounds are moderately reduced.

Existing strategies predict future states of the vehicle by propagated the nominal state and parameter values within a numerical optimizer [15, 20]. Thus, results for an unfiltered case facilitate comparison to the current state of the art in guidance prediction. In the unfiltered case, measurement and consider parameter conditioning effects are omitted. The initial state uncertainty probability distribution is then propagated as a pure prediction problem with σ_d of 90 degrees. Figure 4.13 shows quartiles of apoapsis radius errors for the filtered and unfiltered cases. In the filtered case, both are approximately zero mean, but the optimal σ_d of 60 degrees indicates a much tighter distribution of apoapsis error. Moreover, fewer outliers are found for the optimal bank angle switch.

Figure 4.13 shows that the non-optimal σ_d of 40 degrees produces outliers in the overshoot direction. These cases represent nonlinear effects that are not adequately modeled by the linear covariance update equations. However, the optimal σ_d of 60 degrees results in fewer outliers, remaining close to the nominal estimate consistent with these assumptions. Thus, an additional benefit of the robust optimization approach is to reduce filter divergence in outlier cases. This

σ_d (deg)	Failed Cases	95% - ΔV (m/s)	99.5% - ΔV (m/s)
40	61	213.3	238.0
60	0	167.3	173.2
90 (unfiltered)	850	479.9	672.7

Table 4.2: Monte Carlo simulation statistics for ECKF and unfiltered cases.

comparison illustrates the contrast with existing approaches relying on certainty equivalence.

Table 4.2 gives capture rate and predicted ΔV performance for each bank angle switch case. A significantly higher rate of failed runs is evident in the unfiltered case, resulting from direct entry trajectories that fail to reach orbit. The direct entry cases are removed from simulation results before computing ΔV statistics, as these runs are not feasible solutions of the aerocapture problem. Figure 4.14 shows the cumulative ΔV performance for both the filtered and unfiltered cases. The unfiltered cases see rapid uncertainty growth, with a comparatively high number of overshoot trajectories. These runs provide insufficient velocity-loss to capture into the target orbit apoapsis radius. The optimal bank angle switch of 60 degrees gives an overall lower expected total ΔV , with the cumulative distribution showing strong stochastic dominance over the 40 degree bank angle switch case. These results indicate that the robust optimization procedure can moderately improve prediction accuracy in aerocapture.

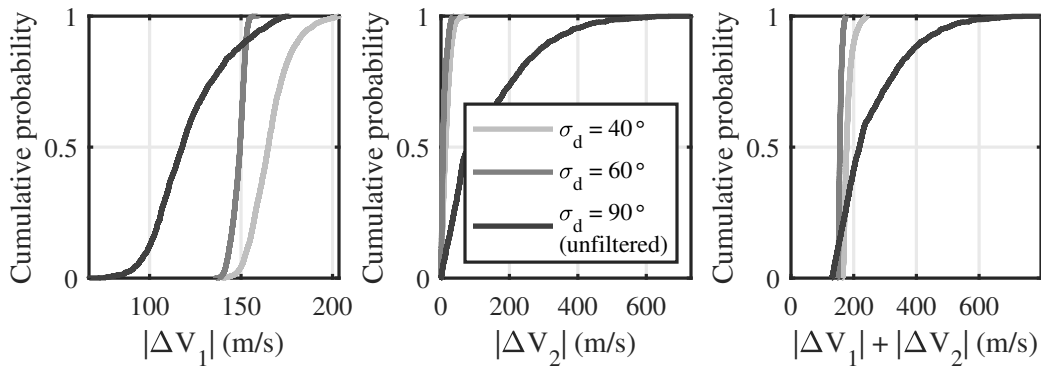


Figure 4.14: Comparison of ΔV performance for selected bank angle switch values.

4.5 Summary

Successful guided entry requires precise knowledge of system states, environmental conditions, and vehicle performance parameters. Errors in these quantities directly impact the capability of any guidance algorithm to precisely target desired exit conditions. Existing strategies are strongly rooted in certainty equivalence, with the assumption that running closed-loop is sufficient to mitigate the influence of imperfect system knowledge. This work introduces a novel framework for incorporating uncertainty in entry flight problems into an overall optimization objective. A robust cost index is proposed for general problems in aeroassist. The ECKF equations are used for propagating state and parameter uncertainties, as well as for predicting the conditioning effect of future measurements on the estimation error covariance. Models of uncertainty in entry flight problems are developed, including a novel density perturbation model derived from MarsGRAM data. Results are generated for a representative Mars mission concept subject to uncertainty in initial states, atmospheric density structure, and vehicle aerodynamic coefficients. Utilizing the robust optimization procedure moderately desensitizes the guidance prediction error, therefore decreasing the necessary ΔV budget by about 50%. These findings have application to robust tuning of existing NPC guidance strategies. This work is expected to better inform mission design for a wide class of aeroassist problems, including aerocapture, and may enable improved performance of entry guidance under uncertainty.

Chapter 5

Conclusions and Future Work

Optimal control represents a challenging, yet informative field within aerospace engineering. Indirect methods provide high solution precision and reveal deeper mathematical insights not available with direct methods. Further, these methods enable solution of complex, high-dimensional systems that represent real problems faced by aerospace designers today. In practice, numerical solution of the resulting Hamiltonian BVP from indirect methods presents numerous challenges, particularly in constrained problems when the solution structure cannot be known a priori. Tractable solution methodologies for indirect methods are key to improving their reliability and range of application. Improvements to numerical homotopy and regularization methods will continue to positively impact the state-of-the-art for the foreseeable future.

Uncertainty in atmospheric entry flight has dampened aeroassist mission outlook, particularly for highly-enabling maneuvers such as aerocapture. Risk assessment of these missions has historically relied on certainty-equivalent guidance and TCW for conceptual design. As a result, the parameter design space is often restricted to high L/D vehicles with low TRL, particularly for missions to the outer planets where the navigated delivery accuracy and environmental models are not known with high confidence. Large strides in entry technology advancements are needed to visit these challenging destinations. Scientific exploration in the solar system can provide critical information regarding planetary formation and origins. Thus, enhancing technologies to improve reliability of entry systems with lower risk posture provides greater benefits to society, beyond academic and engineering interest alone.

Chapter 2 develops a novel regularization method for constrained optimal control problems. The main feature of the new approach is to produce a fully-analytical control law following substitution of control smoothing and error-control terms. This useful property is not typical to existing approaches. The control variables are restated in terms of states and costates alone, enabling elimination from the Hamiltonian BVP by direct substitution. Functional orthogonality is ensured, in turn minimizing projected errors due to smoothing. The method is non-intrusive and easy to implement. In addition, the method forgoes point-wise application of the Minimum Principle along the trajectory, reducing numerical overhead and programmatic complexity. Desirable numerical convergence behavior is observed for simple examples with known solutions, as well as more complex aerospace systems. A differential extension approach enables application of the new method to a broad class of problems. Novel path constraint barrier functions are also studied. These contributions greatly improve the applicability of indirect methods in complex problems by removing any burden on the designer to derive complicated control laws or constraint multipliers.

Chapter 3 examines a special case of OCP structure in which the necessary conditions fail to reveal an optimal control policy. This behavior is linked to singular arcs appearing with infinite local order. Existence conditions are developed based on the concept of reachable singular manifolds. The terminal objective must be stated such that a global minimum resides in the reachable set of the system using admissible controls. This in turns causes the standard necessary conditions to break down. Because of the exact nature of indirect methods, no solution is produced even though a family of global optimizers can be found. We develop a novel relaxation method based a first-order local error covariance propagated about the nominal state. Although the dimension of the optimization problem is increased, the regularization approach lends well to solving these problems. The relaxation method resolves infinite-order singularities and produces a well-posed OCP structure. Further, the work has relevance to engineering problems, as real-world systems are usually subject to some level of uncertainty. Results show moderately reduced uncertainty due to propagated initial state and parameter errors for several relevant applications.

Chapter 4 explores connections between state estimation and entry guidance for planetary

aerocapture. Optimal allocation of guidance parameters is posed as a robust optimization problem. Measurement conditioning effects can be predicted well by propagating the discrete-time consider-EKF equations. The approach effectively enhances state estimation through trajectory design. Solutions are obtained using a parameterized control structure and explicit integration methods, reflecting the current state-of-the-art in NPC guidance. The bank angle switch parameter can strongly influence terminal state uncertainty. An optimal bank angle switch value can be found minimizing the propagated errors due to atmospheric structure, parameter uncertainty, and state estimation error. This is in contrast to current approaches, which posit the bank angle switch as a monotonic tradeoff between performance and robustness. Results for a Mars aerocapture mission illustrate coupling between atmospheric trajectory design and estimation accuracy in entry guidance.

Innovations in the construction and solution of complex optimization problems benefit the aerospace sciences from many perspectives. Regularization applies to a broad class of OCP structures and greatly reduces the complexity required of the designer. By removing the need for prior knowledge of the constraint structure and junction points, the resulting Hamiltonian BVP has a much simpler construction and solution process. The generalized regularization method enables application with optimization software libraries and numerical BVP solvers that require fully-analytical process equations and boundary condition Jacobians. Advancements that reduce complexity and improve ease of implementation make the field more approachable, increasing the likelihood of wider adaptation in the research and engineering community. Similarly, the auxiliary relaxation method provides a set of necessary conditions for resolving ill-posed problem structures that may appear in practical problems. By minimizing projections of the propagated uncertainty covariance about singular manifolds, characteristics of the original problem are retained. The relaxation approach enables the generation of precise and robust trajectories that can improve system performance for uncertain operating conditions. Finally, advancements to state-of-the-art in atmospheric flight mechanics and entry guidance will benefit mission design for challenging destinations in the solar system. Estimation-enhanced guidance can improve entry guidance prediction accuracy

and increase confidence in aeroassist mission capability.

Future work could consider further generalization of the regularization methods developed in this thesis. For example, error-control terms could apply to nonlinear controls directly, without utilizing differential system extension. This process should retain the fully-analytic character of the optimal control policy, without relying on point-wise application of the Minimum Principle. Certain boundary conditions can also introduce irregularities in the control solution on the boundary following regularization, warranting further study. Regarding the infinite-order singular arc relaxation method, nonlinear or non-Gaussian uncertainty could be used in the auxiliary problem, or advanced propagation techniques such as particle filtering or unscented transforms. Another area for improvement includes solution of the NPC guidance strategy in on-line applications. The robust prediction framework should be studied for improving prediction accuracy in closed-loop. Finally, there exists current literature regarding optimal costate estimation through deep learning neural networks. These principles could be applied to the auxiliary relaxation problem for rapid estimation of optimal costates of the covariance dynamics along singular manifolds. Deep learning for online trajectory generation using indirect methods could greatly benefit robust trajectory design under uncertainty.

Bibliography

- [1] Jeffery L Hall, Muriel A Noca, and Robert W Bailey. Cost-Benefit Analysis of the Aerocapture Mission Set. Journal of Spacecraft and Rockets, 42(2):309–320, 2005.
- [2] JA Page and RO Rogers. Guidance and Control of Maneuvering Reentry Vehicles. In IEEE Conference on Decision and Control, pages 659–664, 1977.
- [3] Christopher Gracey, EM Cliff, FH Lutze, and HJ Kelley. Fixed-Trim Re-Entry Guidance Analysis. Journal of Guidance, Control, and Dynamics, 5(6):558–563, 1982.
- [4] Oliver Hill. An Adaptive Guidance Logic for an Aeroassisted Orbital Transfer Vehicles. Advances in the Astronautical Sciences, 54:495–518, 1984.
- [5] Robert D Braun and Richard W Powell. Predictor-corrector guidance algorithm for use in high-energy aerobraking system studies. Journal of Guidance, Control, and Dynamics, 15(3):672–678, 1992.
- [6] JG Gurley. Guidance for an aerocapture maneuver. Journal of Guidance, Control, and Dynamics, 16(3):505–510, 1993.
- [7] Axel J Roenneke and Albert Markl. Re-Entry Control to a Drag-vs-Energy Profile. Journal of Guidance, Control, and Dynamics, 17(5):916–920, 1994.
- [8] Steven W Evans and Greg A Dukeman. Examination of a Practical Aerobraking Guidance Algorithm. Journal of Guidance, Control, and Dynamics, 18(3):471–477, 1995.
- [9] Ping Lu. Regulation About Time-Varying Trajectories: Precision Entry Guidance Illustrated. Journal of Guidance, Control, and Dynamics, 22(6):784–790, 1999.
- [10] Kuang-Yang Tu, Mohammad S Munir, Kenneth D Mease, and David S Bayard. Drag-Based Predictive Tracking Guidance for Mars Precision Landing. Journal of Guidance, Control, and Dynamics, 23(4):620–628, 2000.
- [11] K Mease, D Chen, S Tandon, D Young, and S Kim. A Three-Dimensional Predictive Entry Guidance Approach. In AIAA Guidance, Navigation, and Control Conference and Exhibit, page 3959, 2000.
- [12] Gavin Mendek and Gilbert Carman. Guidance Design for Mars Smart Landers Using the Entry Terminal Point Controller. In AIAA Atmospheric Flight Mechanics Conference and Exhibit, page 4502, 2002.

- [13] Erwin Mooij. Model Reference Adaptive Guidance for Re-Entry Trajectory Tracking. In AIAA Guidance, Navigation, and Control Conference and Exhibit, page 4775, 2004.
- [14] Ashok Joshi, K Sivan, and S Savithri Amma. Predictor-Corrector Reentry Guidance Algorithm with Path Constraints for Atmospheric Entry Vehicles. Journal of Guidance, Control, and Dynamics, 30(5):1307–1318, 2007.
- [15] Ping Lu. Predictor-Corrector Entry Guidance for Low-Lifting Vehicles. Journal of Guidance, Control, and Dynamics, 31(4):1067–1075, 2008.
- [16] Zachary R Putnam, SH Bairstow, RD Braun, and GH Barton. Improving Lunar Return Entry Range Capability Using Enhanced Skip Trajectory Guidance. Journal of Spacecraft and Rockets, 45(2):309–315, 2008.
- [17] Songbai Xue and Ping Lu. Constrained Predictor-Corrector Entry Guidance. Journal of Guidance, Control, and Dynamics, 33(4):1273–1281, 2010.
- [18] Gavin Mendeck and Lynn Craig. Entry Guidance for the 2011 Mars Science Laboratory Mission. In AIAA Atmospheric Flight Mechanics Conference, page 6639, 2011.
- [19] Xinfu Liu, Zuojun Shen, and Ping Lu. Entry Trajectory Optimization by Second-Order Cone Programming. Journal of Guidance, Control, and Dynamics, 39(2):227–241, 2015.
- [20] Ping Lu, Christopher Brunner, Susan Stachowiak, Gavin F Mendeck, Michael Tigges, and Christopher Cerimele. Verification of a Fully Numerical Entry Guidance Algorithm. In AIAA Guidance, Navigation, and Control Conference, page 0377, 2016.
- [21] Wyatt R Johnson, Ping Lu, and Susan Stachowiak. Automated Re-Entry System Using FNPEG. In AIAA Guidance, Navigation, and Control Conference, page 1899, 2017.
- [22] Qing Lu and Jun Zhou. LQR Tracking Guidance Law for Hypersonic Vehicle. In 2017 29th Chinese Control and Decision Conference (CCDC), pages 7090–7094. IEEE, 2017.
- [23] Sarah N D’Souza and Nesrin Sarigul-Klijn. Survey of Planetary Entry Guidance Algorithms. Progress in Aerospace Sciences, 68:64–74, 2014.
- [24] David W Way. Preliminary Assessment of the Mars Science Laboratory Entry, Descent, and Landing Simulation. In 2013 IEEE Aerospace Conference, pages 1–16. IEEE, 2013.
- [25] Matthew Golombek, D Kipp, N Warner, Ingrid J Daubar, R Ferguson, Randolph L Kirk, R Beyer, A Huertas, Sylvain Piqueux, NE Putzig, et al. Selection of the InSight landing site. Space Science Reviews, 211(1):5–95, 2017.
- [26] Naruhisa Takashima, Brian Hollis, Joe Oleniczak, Mike Wright, and Kenneth Sutton. Preliminary Aerothermodynamics of Titan Aerocapture Aeroshell. In 39th AIAA/ASME/SAE/ASEE Joint Propulsion Conference and Exhibit, page 4952, 2003.
- [27] Mary Kae Lockwood. Titan Aerocapture Systems Analysis. In 39th AIAA/ASME/SAE/ASEE Joint Propulsion Conference and Exhibit, page 4799, 2003.
- [28] Brett Starr, Carlos Westhelle, and James Masciarelli. Aerocapture Performance Analysis for a Neptune-Triton Exploration Mission. In AIAA Atmospheric Flight Mechanics Conference and Exhibit, page 4955, 2004.

- [29] Ronald R Sostaric, Christopher J Cerimele, Edward A Robertson, and Joseph A Garcia. A Rigid Mid Lift-to-Drag Ratio Approach to Human Mars Entry, Descent, and Landing. In AIAA Guidance, Navigation, and Control Conference, page 1898, 2017.
- [30] Robert D Braun, Richard W Powell, and JEvans Lyne. Earth Aerobraking Strategies for Manned Return from Mars. Journal of Spacecraft and Rockets, 29(3):297–304, 1992.
- [31] Prasun N Desai, Robert A Mitcheltree, and F McNeil Cheatwood. Entry Dispersion Analysis for the Stardust Comet Sample Return Capsule. Journal of Spacecraft and Rockets, 36(3):463–469, 1999.
- [32] Prasun N Desai and F McNeil Cheatwood. Entry Dispersion Analysis for the Genesis Sample Return Capsule. Journal of Spacecraft and Rockets, 38(3):345–350, 2001.
- [33] Zachary R Putnam, Robert D Braun, Reuben R Rohrschneider, and John A Dec. Entry System Options for Human Return from the Moon and Mars. Journal of Spacecraft and Rockets, 44(1):194–202, 2007.
- [34] Richard W Powell and Robert D Braun. Six-Degree-of-Freedom Guidance and Control Analysis of Mars Aerocapture. Journal of Guidance, Control, and Dynamics, 16(6):1038–1044, 1993.
- [35] Mary Kae Lockwood, Brett R Starr, John W Paulson Jr, Dean A Kontinos, YK Chen, Bernard Laub, Joseph Olejniczak, Michael J Wright, Naruhisa Takashima, and Carl G Justus. Systems Analysis for a Venus Aerocapture Mission. Technical Report NASA/TM-2006-214291, NASA Langley Research Center, Hampton, VA, 2006.
- [36] Robert D Braun and Robert M Manning. Mars Exploration Entry, Descent and Landing Challenges. In 2006 IEEE Aerospace Conference, pages 18–pp. IEEE, 2006.
- [37] CR Heidrich, S Dutta, and RD Braun. Modern Aerocapture Guidance to Enable Reduced-Lift Vehicles at Neptune. AAS 19, 221, 2019.
- [38] Muriel Noca and Robert Bailey. Mission Trades for Aerocapture at Neptune. In 40th AIAA/ASME/SAE/ASEE Joint Propulsion Conference and Exhibit, page 3843, 2004.
- [39] Mark Hofstdater, Amy Simon, Kim Reh, and John Elliot. Ice Giants Pre-Decadal Survey Mission Study Report. Technical Report JPL D100520, NASA Jet Propulsion Laboratory, 2017.
- [40] Eric M Queen. Angle-of-Attack-Modulated Terminal Point Control for Neptune Aerocapture. In 14th AAS/AIAA Space Flight Mechanics Conference, 2004.
- [41] Mary Kae Lockwood. Neptune Aerocapture Systems Analysis. In AIAA Atmospheric Flight Mechanics Conference and Exhibit, page 4951, 2004.
- [42] Sarag J. Saikia. Aerocapture Assessment at Uranus and Neptune for NASA’s Ice Giant Studies. In NASA Technical Report, pages PU–AAC–201–MC–0002, 2016.
- [43] PE Moseley. The Apollo Entry Guidance: A Review of the Mathematical Development and its Operational Characteristics. Task MSC/TRW A-220, 1969.

- [44] James Masciarelli, Stephane Rousseau, Hubert Fraysse, and Etienne Perot. An analytic aerocapture guidance algorithm for the Mars Sample Return Orbiter. In Atmospheric Flight Mechanics Conference, page 4116, 2000.
- [45] Yu-ming Peng, Bo Xu, Bao-dong Fang, and Han-lun Lei. Analytical Predictor-Corrector Guidance Algorithm Based on Drag Modulation Flight Control System for Mars Aerocapture. International Journal of Aerospace Engineering, 2018, 2018.
- [46] Jean-Francois Hamel and Jean De Lafontaine. Improvement to the Analytical Predictor-Corrector Guidance Algorithm Applied to Mars Aerocapture. Journal of Guidance, Control, and Dynamics, 29(4):1019–1022, 2006.
- [47] Zeal-Sain Kuo and Kuo-Chung Liu. Explicit Guidance of Aeroassisted Orbital Transfer Using Matched Asymptotic Expansions. Journal of Guidance, Control, and Dynamics, 25(1):80–87, 2002.
- [48] Theodore Ro and Eric Queen. Study of Martian aerocapture terminal point guidance. In 23rd Atmospheric Flight Mechanics Conference, page 4571, 1998.
- [49] David Way, Richard Powell, James Masciarelli, Brett Starr, and Karl Edquist. Aerocapture Simulation and Performance for the Titan Explorer Mission. In 39th AIAA/ASME/SAE/ASEE Joint Propulsion Conference and Exhibit, page 4951, 2003.
- [50] Brett Starr and Carlos Westhelle. Aerocapture Performance Analysis of a Venus Explorer Mission. In AIAA Atmospheric Flight Mechanics Conference and Exhibit, page 5913, 2005.
- [51] James Masciarelli, Carlos Westhelle, and Claude Graves. Aerocapture Guidance Performance for the Neptune Orbiter. In AIAA Atmospheric Flight Mechanics Conference and Exhibit, page 4954, 2004.
- [52] Stephane Rousseau, Etienne Perot, Claude Graves, James Masciarelli, and Eric Queen. Aerocapture Guidance Algorithm Comparison Campaign. In AIAA/AAS Astrodynamics Specialist Conference and Exhibit, page 4822, 2002.
- [53] Daniel A Matz, Ping Lu, Gavin F Mendeck, and Ronald R Sostaric. Application of a Fully Numerical Guidance to Mars Aerocapture. In AIAA Guidance, Navigation, and Control Conference, page 1901, 2017.
- [54] J Berges, S Rousseau, and E Perot. A Numerical Predictor-Corrector Guidance Algorithm for the Mars Sample Return Aerocapture. Association A’eronautique et Astronautique de France, pages 14–66, 2001.
- [55] Abhishek Halder and Raktim Bhattacharya. Dispersion Analysis in Hypersonic Flight During Planetary Entry Using Stochastic Liouville Equation. Journal of Guidance, Control, and Dynamics, 34(2):459–474, 2011.
- [56] Armen Der Kiureghian and Ove Ditlevsen. Aleatory or Epistemic? Does it Matter? Structural Safety, 31(2):105–112, 2009.
- [57] Michael S Eldred, Laura Painton Swiler, and Gary Tang. Mixed Aleatory-Epistemic Uncertainty Quantification with Stochastic Expansions and Optimization-Based Interval Estimation. Reliability Engineering & System Safety, 96(9):1092–1113, 2011.

- [58] Massimiliano Vasile. Robustness Optimisation of Aerocapture Trajectory Design Using a Hybrid Co-evolutionary Approach. In 18th International Symposium on Space Flight Dynamics, volume 548, page 601. ESA Special Publication, 2004.
- [59] Philip Knocke, Geoffrey Wawrzyniak, Brian Kennedy, Prasun Desai, Timothy Parker, Matthew Golombek, Thomas Duxbury, and David Kass. Mars Exploration Rovers Landing Dispersion Analysis. In AIAA/AAS Astrodynamics Specialist Conference and Exhibit, page 5093, 2004.
- [60] Shuang Li and Yuming Peng. Mars entry trajectory optimization using DOC and DCNLP. Advances in Space Research, 47(3):440–452, 2011.
- [61] Harald Niederreiter. Random Number Generation and Quasi-Monte Carlo Methods, volume 63. Siam, 1992.
- [62] Brent Sohngen and Robert Mendelsohn. An Optimal Control Model of Forest Carbon Sequestration. American Journal of Agricultural Economics, 85(2):448–457, 2003.
- [63] Nils C Framstad, Bernt Øksendal, and Agnes Sulem. Sufficient Stochastic Maximum Principle for the Optimal Control of Jump Diffusions and Applications to Finance. Journal of Optimization Theory and Applications, 121(1):77–98, 2004.
- [64] Suzanne Lenhart and John T Workman. Optimal Control Applied to Biological Models. Chapman and Hall/CRC, New York, 2007.
- [65] Oluwaseun Sharomi and Tufail Malik. Optimal control in epidemiology. Annals of Operations Research, 251(1-2):55–71, 2017.
- [66] Folashade B Agosto, Nizar Marcus, and Kaseem O Okosun. Application of optimal control to the epidemiology of malaria. Electronic Journal of Differential Equations, 81:1–22, 2012.
- [67] Divya Garg, Michael A Patterson, Camila Francolin, Christopher L Darby, Geoffrey T Huntington, William W Hager, and Anil V Rao. Direct trajectory optimization and costate estimation of finite-horizon and infinite-horizon optimal control problems using a Radau pseudospectral method. Computational Optimization and Applications, 49(2):335–358, 2011.
- [68] Arthur E Bryson and Yu-Chi Ho. Applied Optimal Control: Optimization, Estimation, and Control. Routledge, 2018.
- [69] Michael A Patterson and Anil V Rao. GPOPS-II: A MATLAB Software for Solving Multiple-Phase Optimal Control Problems Using hp-Adaptive Gaussian Quadrature Collocation Methods and Sparse Nonlinear Programming. ACM Transactions on Mathematical Software, 41(1):1–37, 2014.
- [70] Philip E Gill, Walter Murray, and Michael A Saunders. SNOPT: An SQP Algorithm for Large-Scale Constrained Optimization. SIAM Review, 47(1):99–131, 2005.
- [71] David A Benson, Geoffrey T Huntington, Tom P Thorvaldsen, and Anil V Rao. Direct Trajectory Optimization and Costate Estimation via an Orthogonal Collocation Method. Journal of Guidance, Control, and Dynamics, 29(6):1435–1440, 2006.

- [72] Emmanuel Trélat. Optimal Control and Applications to Aerospace: Some Results and Challenges. Journal of Optimization Theory and Applications, 154(3):713–758, 2012.
- [73] I Michael Ross and Fariba Fahroo. Legendre Pseudospectral Approximations of Optimal Control Problems. In New Trends in Nonlinear Dynamics and Control and their Applications, pages 327–342. Springer, 2003.
- [74] MI Zelikin and VF Borosov. Optimal Synthesis Containing Chattering Arcs and Singular Arcs of the Second Order. In Nonlinear synthesis, pages 283–296. Springer, 1991.
- [75] John T Betts. Practical Methods for Optimal Control Using Nonlinear Programming. Applied Mechanics Reviews, 55(4):B68, 2002.
- [76] Michael J Sparapany and Michael J Grant. Trajectory Reduced-Order Modeling Using Indirect Methods. In 2020 IEEE Aerospace Conference, pages 1–10. IEEE, 2020.
- [77] Yang Shi and Zhenbo Wang. A Deep Learning-Based Approach to Real-Time Trajectory Optimization for Hypersonic Vehicles. In AIAA Scitech 2020 Forum, page 0023, 2020.
- [78] Robert F Stengel. Optimal Control and Estimation. Dover, New York, 1994.
- [79] Stephan Uebel, Nikolce Murgovski, Conny Tempelhahn, and Bernard Bäker. Computationally Efficient Velocity and Power Split Control of Hybrid Electric Vehicles. In 2017 IEEE Conference on Control Technology and Applications (CCTA), pages 1619–1624. IEEE, 2017.
- [80] Thomas Antony and Michael J Grant. Rapid Indirect Trajectory Optimization on Highly Parallel Computing Architectures. Journal of Spacecraft and Rockets, 54(5):1081–1091, 2017.
- [81] Divya Garg, Michael Patterson, Christopher Darby, Camila Francolin, Geoffrey Huntington, William Hager, and Anil Rao. Direct Trajectory Optimization and Costate Estimation of General Optimal Control Problems Using a Radau Pseudospectral Method. In AIAA Guidance, Navigation, and Control Conference, page 5989, 2009.
- [82] Thomas Antony, Michael J Grant, Michael Sparapany, Sean M Nolan, Justin Mansell, Kshitij Mall, David A Hannasch, and Casey Ryan Heidrich. Beluga: General Purpose Indirect Trajectory Optimization. <https://github.com/Rapid-Design-of-Systems-Laboratory/beluga>, 2021.
- [83] Toshiyuki Ohtsuka and Hironori Fujii. Stabilized Continuation Method for Solving Optimal Control Problems. Journal of Guidance, Control, and Dynamics, 17(5):950–957, 1994.
- [84] Hongwei Yang, Shuang Li, and Xiaoli Bai. Fast Homotopy Method for Asteroid Landing Trajectory Optimization Using Approximate Initial Costates. Journal of Guidance, Control, and Dynamics, 42(3):585–597, 2019.
- [85] Mihir Vedantam, Maruthi R Akella, and Michael J Grant. Multi-Stage Stabilized Continuation for Indirect Optimal Control of Hypersonic Trajectories. In AIAA Scitech 2020 Forum, page 0472, 2020.
- [86] Michael J Sparapany, Sean M Nolan, and Michael J Grant. Reduction of Hamiltonian Systems with Involutory Functions. In 2020 IEEE Aerospace Conference, pages 1–10. IEEE, 2020.

- [87] Michael Grant, Ian Clark, and Robert Braun. Rapid Design Space Exploration for Conceptual Design of Hypersonic Missions. In AIAA Atmospheric Flight Mechanics Conference, page 6576, 2011.
- [88] Michael J Grant and Robert D Braun. Rapid Indirect Trajectory Optimization for Conceptual Design of Hypersonic Missions. Journal of Spacecraft and Rockets, 52(1):177–182, 2015.
- [89] Yiyu Zheng, Hutao Cui, and Yuanhang Ai. Indirect Trajectory Optimization for Mars Entry with Maximum Terminal Altitude. Journal of Spacecraft and Rockets, 54(5):1068–1080, 2017.
- [90] Harish Saranathan and Michael J Grant. Relaxed Autonomously Switched Hybrid System Approach to Indirect Multiphase Aerospace Trajectory Optimization. Journal of Spacecraft and Rockets, 55(3):611–621, 2018.
- [91] Ping Lu, Christopher J Cerimele, Michael A Tigges, and Daniel A Matz. Optimal Aerocapture Guidance. Journal of Guidance, Control, and Dynamics, 38(4):553–565, 2015.
- [92] Marco Sagliano and Erwin Mooij. Optimal drag-energy entry guidance via pseudospectral convex optimization. Aerospace Science and Technology, 117:106946, 2021.
- [93] Qi Gong, I Michael Ross, and Friba Fahroo. Costate Computation by a Chebyshev Pseudospectral Method. Journal of Guidance, Control, and Dynamics, 33(2):623–628, 2010.
- [94] Régis Bertrand and Richard Epenoy. New smoothing techniques for solving bang-bang optimal control problems—numerical results and statistical interpretation. Optimal Control Applications and Methods, 23(4):171–197, 2002.
- [95] Cristiana Silva and Emmanuel Trélat. Smooth Regularization of Bang-Bang Optimal Control Problems. IEEE Transactions on Automatic Control, 55(11):2488–2499, 2010.
- [96] Gerd Wachsmuth and Daniel Wachsmuth. Convergence and regularization results for optimal control problems with sparsity functional. ESAIM: Control, Optimisation and Calculus of Variations, 17(3):858–886, 2011.
- [97] Kshitij Mall and Michael James Grant. Epsilon-Trig Regularization Method for Bang-Bang Optimal Control Problems. Journal of Optimization Theory and Applications, 174(2):500–517, 2017.
- [98] Thomas Antony and Michael J Grant. Path Constraint Regularization in Optimal Control Problems Using Saturation Functions. In 2018 AIAA Atmospheric Flight Mechanics Conference, page 0018, 2018.
- [99] Kshitij Mall, Michael J Grant, and Ehsan Taheri. Uniform Trigonometrization Method for Optimal Control Problems with Control and State Constraints. Journal of Spacecraft and Rockets, pages 995–1007, 2020.
- [100] Lev Semenovich Pontryagin. Mathematical Theory of Optimal Processes. Routledge, 2018.
- [101] BS Goh. Necessary conditions for singular extremals involving multiple control variables. SIAM Journal on Control, 4(4):716–731, 1966.
- [102] HM Robbins. A Generalized Legendre-Clebsch Condition for the Singular Cases of Optimal Control. IBM Journal of Research and Development, 11(4):361–372, 1967.

- [103] WF Powers. On the Order of Singular Optimal Control Problems. Journal of optimization theory and applications, 32(4):479–489, 1980.
- [104] RM Lewis. Definitions of order and junction conditions in singular optimal control problems. SIAM Journal on Control and Optimization, 18(1):21–32, 1980.
- [105] R Bortins, NM Boustany, and WF Powers. The infinite-order singular problem. Optimal Control Applications and Methods, 1(3):279–302, 1980.
- [106] Hans Seywald and Renjith R Kumar. Singular Control in Minimum Time Spacecraft Reorientation. Journal of Guidance, Control, and Dynamics, 16(4):686–694, 1993.
- [107] Matthew W Harris. Abnormal and Singular Solutions in the Target Guarding Problem with Dynamics. Journal of Optimization Theory and Applications, 184(2):627–643, 2020.
- [108] Z Foroozandeh, M Shamsi, and Maria Do Rosário De Pinho. A Hybrid Direct–Indirect Approach for Solving the Singular Optimal Control Problems of Finite and Infinite Order. Iranian Journal of Science and Technology, Transactions A: Science, 42(3):1545–1554, 2018.
- [109] Oswaldo Andrés-Martínez, Antonio Flores-Tlacuahuac, Shivakumar Kameswaran, and Lorenz T Biegler. An efficient direct/indirect transcription approach for singular optimal control. AIChE Journal, 65(3):937–946, 2019.
- [110] Roman Y Jits and Gerald D Walberg. Blended control, predictor–corrector guidance algorithm: an enabling technology for Mars aerocapture. Acta Astronautica, 54(6):385–398, 2004.
- [111] Jack Ridderhof and Panagiotis Tsiotras. Uncertainty Quantification and Control During Mars Powered Descent and Landing Using Covariance Steering. In 2018 AIAA Guidance, Navigation, and Control Conference, page 0611, 2018.
- [112] Sean M Nolan, Michael J Grant, and Adam Rutkowski. Navigation Based Path Planning by Optimal Control Theory. In AIAA Scitech 2020 Forum, page 1346, 2020.
- [113] Venkata Ramana Makkapati, Jack Ridderhof, Panagiotis Tsiotras, Joseph Hart, and Bart van Bloemen Waanders. Desensitized Trajectory Optimization for Hypersonic Vehicles. In 2021 IEEE Aerospace Conference (50100), pages 1–10. IEEE, 2021.
- [114] Kai Jin, David Geller, and Jianjun Luo. Development and Validation of Linear Covariance Analysis Tool for Atmospheric Entry. Journal of Spacecraft and Rockets, 56(3):854–864, 2019.
- [115] Jack Ridderhof and Panagiotis Tsiotras. Stochastic Atmosphere Modeling for Risk Adverse Aerocapture Guidance. In 2020 IEEE Aerospace Conference, pages 1–7. IEEE, 2020.
- [116] Jack Ridderhof, Panagiotis Tsiotras, and Breanna J Johnson. Stochastic Entry Guidance. arXiv preprint arXiv:2103.05168, 2021.
- [117] Ehsan Taheri and John L Junkins. Generic Smoothing for Optimal Bang-Off-Bang Spacecraft Maneuvers. Journal of Guidance, Control, and Dynamics, 41(11):2470–2475, 2018.
- [118] G Fraser-Andrews. Finding Candidate Singular Optimal Controls: A State of the Art Survey. Journal of Optimization Theory and Applications, 60(2):173–190, 1989.

- [119] Scott Zimmer, Cesar Ocampo, and Robert Bishop. Reducing Orbit Covariance for Continuous Thrust Spacecraft Transfers. IEEE Transactions on aerospace and electronic systems, 46(2):771–791, 2010.
- [120] Kenshiro Oguri and Jay W McMahon. Risk-aware Trajectory Design with Continuous Thrust: Primer Vector Theory Approach. In AAS/AIAA Astrodynamics Specialist Conference, Portland, Maine, 2019.
- [121] Erica L Jenson and Daniel J Scheeres. Multi-Objective Optimization of Covariance and Energy for Asteroid Transfers. Journal of Guidance, Control, and Dynamics, 44(7):1253–1265, 2021.
- [122] Kyle D Webb, Ping Lu, and Alicia M Dwyer Cianciolo. Aerocapture Guidance for a Human Mars Mission. In AIAA Guidance, Navigation, and Control Conference, page 1900, 2017.
- [123] Rohan G Deshmukh, David A Spencer, and Soumyo Dutta. Investigation of direct force control for aerocapture at Neptune. Acta Astronautica, 175:375–386, 2020.
- [124] Hongying Xu and Hutao Cui. Robust trajectory design scheme under uncertainties and perturbations for Mars entry vehicle. In 2015 IEEE International Conference on Computational Intelligence & Communication Technology, pages 762–766. IEEE, 2015.
- [125] Pingyuan Cui, Zeduan Zhao, Zhengshi Yu, and Juan Dai. Terminal altitude maximization for Mars entry considering uncertainties. Acta Astronautica, 145:446–455, 2018.
- [126] Ilan Shaviv and Yaakov Oshman. Estimation-Guided Guidance. In AIAA Guidance, Navigation, and Control Conference and Exhibit, page 6217, 2006.
- [127] Ilan G Shaviv and Yaakov Oshman. Estimation-Guided Guidance and Its Implementation via Sequential Monte Carlo Computation. Journal of Guidance, Control, and Dynamics, 40(2):402–417, 2016.
- [128] Xu Jianwei, Qiao Jianzhong, Guo Lei, and Chen Wenhua. Enhanced predictor–corrector Mars entry guidance approach with atmospheric uncertainties. IET Control Theory & Applications, 13(11):1612–1618, 2019.
- [129] Soumyo Dutta, Robert D Braun, Ryan P Russell, Scott A Striepe, and Ian G Clark. Comparison of Statistical Estimation Techniques for Mars Entry, Descent, and Landing Reconstruction. Journal of Spacecraft and Rockets, 50(6):1207–1221, 2013.
- [130] Soumyo Dutta, Robert D Braun, and Christopher D Karlgaard. Uncertainty Quantification for Mars Entry, Descent, and Landing Reconstruction Using Adaptive Filtering. Journal of Spacecraft and Rockets, 51(3):967–977, 2014.
- [131] James M Longuski, José J Guzmán, and John E Prussing. Optimal Control with Aerospace Applications. Springer, 2014.
- [132] Namwook Kim, Sukwon Cha, and Huei Peng. Optimal Control of Hybrid Electric Vehicles Based on Pontryagin’s Minimum Principle. IEEE Transactions on control systems technology, 19(5):1279–1287, 2010.

- [133] James Phillip McDanell and WF Powers. Necessary Conditions Joining Optimal Singular and Nonsingular Subarcs. SIAM Journal on Control, 9(2):161–173, 1971.
- [134] D Jacobson, S Gershwin, and M Lele. Computation of Optimal Singular Controls. IEEE Transactions on Automatic Control, 15(1):67–73, 1970.
- [135] David J Bell and David H Jacobson. Singular Optimal Control Problems. Academic Press, New York, 1975.
- [136] Knut Graichen, Andreas Kugi, Nicolas Petit, and Francois Chaplais. Handling constraints in optimal control with saturation functions and system extension. Systems & Control Letters, 59(11):671–679, 2010.
- [137] Paul Malisani, François Chaplais, and Nicolas Petit. An interior penalty method for optimal control problems with state and input constraints of nonlinear systems. Optimal Control Applications and Methods, 37(1):3–33, 2016.
- [138] Kshitij Mall and Ehsan Taheri. Optimal Control of Wave Energy Converters Using Epsilon-Trig Regularization Method. In 2020 American Control Conference (ACC), pages 1773–1778. IEEE, 2020.
- [139] Kshitij Mall, Sean M Nolan, and Daniel A DeLaurentis. Solving Mixed State-Control Constraint Problems Using Uniform Trigonometrization Method. In AIAA Scitech 2021 Forum, page 1067, 2021.
- [140] Eleanor M James. Time Optimal Control and the Van Der Pol Oscillator. IMA Journal of Applied Mathematics, 13(1):67–81, 1974.
- [141] Helmut Maurer and Nikolai P Osmolovskii. Second Order Sufficient Conditions for Time-Optimal Bang-Bang Control. SIAM journal on control and optimization, 42(6):2239–2263, 2004.
- [142] Gottfried Vossen. Switching Time Optimization for Bang-Bang and Singular Controls. Journal of optimization theory and applications, 144(2):409–429, 2010.
- [143] Helmut Maurer and NP Osmolovskii. Second order optimality conditions for bang-bang control problems. Control and Cybernetics, 32:555–584, 2003.
- [144] C D Johnson. Singular Solutions in Problems of Optimal Control. Advances in Control Systems, 2:209–267, 1965.
- [145] Linda R Petzold. Numerical solution of differential-algebraic equations in mechanical systems simulation. Physica D: Nonlinear Phenomena, 60(1-4):269–279, 1992.
- [146] Kathryn E Brenan and Linda R Petzold. The Numerical Solution of Higher Index Differential/Algebraic Equations by Implicit Methods. SIAM Journal on Numerical Analysis, 26(4):976–996, 1989.
- [147] Kshitij Mall, Michael J Grant, and Ehsan Taheri. Solving Complex Optimal Control Problems with Nonlinear Controls Using Trigonometric Functions. Optimal Control Applications and Methods, 42(3):616–628, 2021.

- [148] Zhong Wang and Yan Li. An Indirect Method for Inequality Constrained Optimal Control Problems. IFAC-PapersOnLine, 50(1):4070–4075, 2017.
- [149] Lijun Zong and M Reza Emami. Concurrent base-arm control of space manipulators with optimal rendezvous trajectory. Aerospace Science and Technology, 100:105822, 2020.
- [150] Donald E Kirk. Optimal Control Theory: An Introduction. Courier Corporation, 2012.
- [151] Nguyen X Vinh, Adolf Busemann, and Robert D Culp. Hypersonic and planetary entry flight mechanics. NASA STI/Recon Technical Report A, 81:16245, 1980.
- [152] Sanjay Bharadwaj, Anil V Rao, and Kenneth D Mease. Entry Trajectory Tracking Law via Feedback Linearization. Journal of Guidance, Control, and Dynamics, 21(5):726–732, 1998.
- [153] Andrei Venediktovich Dmitruk and NV Kuz’kina. Existence Theorem in the Optimal Control Problem on an Infinite Time Interval. Mathematical Notes, 78(3):466–480, 2005.
- [154] Richard B Holmes. A Course on Optimization and Best Approximation, volume 257. Springer, 2006.
- [155] SJ Li and WY Zhang. Hadamard well-posed vector optimization problems. Journal of Global Optimization, 46(3):383–393, 2010.
- [156] Raman Mehra and R Davis. A Generalized Gradient Method for Optimal Control Problems with Inequality Constraints and Singular Arcs. IEEE Transactions on Automatic Control, 17(1):69–79, 1972.
- [157] Joseph P La Salle. The Time Optimal Control Problem. Princeton University Press, 2016.
- [158] Joseph Z Ben-Asher. Optimal Control Theory with Aerospace Applications. American institute of aeronautics and astronautics, 2010.
- [159] I Michael Ross. A historical introduction to the convector mapping principle. In Proceedings of Astrodynamics Specialists Conference. Citeseer, 2005.
- [160] Semen Ya Serovaiskii. Counterexamples in Optimal Control Theory. De Gruyter, 2011.
- [161] Boris S Mordukhovich. Variational Analysis and Generalized Differentiation I: Basic theory, volume 330. Springer Science & Business Media, 2006.
- [162] Jeffery S Logsdon and Lorenz T Biegler. Accurate Solution of Differential-Algebraic Optimization Problems. Industrial & engineering chemistry research, 28(11):1628–1639, 1989.
- [163] DJ Gunn and WJ Thomas. Mass transport and chemical reaction in multifunctional catalyst systems. Chemical Engineering Science, 20(2):89–100, 1965.
- [164] Jack Ridderhof and Panagiotis Tsiotras. Minimum-Fuel Powered Descent in the Presence of Random Disturbances. In AIAA Scitech 2019 Forum, page 0646, 2019.
- [165] Lars Blackmore, Behçet Açikmeşe, and Daniel P Scharf. Minimum-Landing-Error Powered-Descent Guidance for Mars Landing Using Convex Optimization. Journal of guidance, control, and dynamics, 33(4):1161–1171, 2010.

- [166] Casey R Heidrich and Robert D Braun. Aerocapture Trajectory Design in Uncertain Entry Environments. In AIAA Scitech 2020 Forum, page 1741, 2020.
- [167] Donald T Greenwood. Principles of Dynamics. Prentice-Hall Englewood Cliffs, NJ, 1988.
- [168] Marcus J Holzinger, Daniel J Scheeres, and John Hauser. Reachability Using Arbitrary Performance Indices. IEEE Transactions on Automatic Control, 60(4):1099–1103, 2015.
- [169] Joseph K Scott and Paul I Barton. Bounds on the reachable sets of nonlinear control systems. Automatica, 49(1):93–100, 2013.
- [170] Mo Chen, Sylvia L Herbert, Mahesh S Vashishtha, Somil Bansal, and Claire J Tomlin. Decomposition of Reachable Sets and Tubes for A Class of Nonlinear Systems. IEEE Transactions on Automatic Control, 63(11):3675–3688, 2018.
- [171] DJ Bell. Lie Brackets and Singular Optimal Control. IMA Journal of Mathematical Control and Information, 1(1):83–94, 1984.
- [172] DV Stoep. Trajectory Shaping for the Minimization of State-Variable Estimation Errors. IEEE Transactions on Automatic Control, 13(3):284–286, 1968.
- [173] Nikolai M Filatov and Heinz Unbehauen. Survey of adaptive dual control methods. IEE Proceedings-Control Theory and Applications, 147(1):118–128, 2000.
- [174] John L Crassidis and John L Junkins. Optimal Estimation of Dynamic Systems. CRC press, 2011.
- [175] Hans-Georg Beyer and Bernhard Sendhoff. Robust optimization – A comprehensive survey. Computer Methods in Applied Mechanics and Engineering, 196(33-34):3190–3218, 2007.
- [176] Casey R Heidrich, Michael J Sparapany, and Michael J Grant. Investigation of Control Regularization Functions in Bang-Bang/Singular Optimal Control Problems. In AIAA Scitech 2021 Forum, page 2037, 2021.
- [177] Donghun Lee, Hyochoong Bang, and Hae-Dong Kim. Optimal Earth-Moon Trajectory Design Using New Initial Costate Estimation Method. Journal of guidance, control, and dynamics, 35(5):1671–1676, 2012.
- [178] Max Cerf. Fast solution of minimum-time low-thrust transfer with eclipses. Proceedings of the Institution of Mechanical Engineers, Part G: Journal of Aerospace Engineering, 233(7):2699–2714, 2019.
- [179] J-B Caillau, Olivier Cots, and Joseph Gergaud. Differential continuation for regular optimal control problems. Optimization Methods and Software, 27(2):177–196, 2012.
- [180] MA Mehrpouya, M Shamsi, and M Razzaghi. A combined adaptive control parametrization and homotopy continuation technique for the numerical solution of bang–bang optimal control problems. The ANZIAM Journal, 56(1):48–65, 2014.
- [181] Hanspeter Schaub. Relative Orbit Geometry Through Classical Orbit Element Differences. Journal of Guidance, Control, and Dynamics, 27(5):839–848, 2004.

- [182] Joshua Sullivan, Sebastian Grimberg, and Simone D’Amico. Comprehensive Survey and Assessment of Spacecraft Relative Motion Dynamics Models. Journal of Guidance, Control, and Dynamics, 40(8):1837–1859, 2017.
- [183] Yoshihiro Ichimura and Akira Ichikawa. Optimal Impulsive Relative Orbit Transfer Along a Circular Orbit. Journal of guidance, control, and dynamics, 31(4):1014–1027, 2008.
- [184] Mauro Pontani and Bruce A Conway. Minimum-Fuel Finite-Thrust Relative Orbit Maneuvers via Indirect Heuristic Method. Journal of Guidance, Control, and Dynamics, 38(5):913–924, 2015.
- [185] T Alan Lovell and S Tragesser. Guidance for relative motion of low earth orbit spacecraft based on relative orbit elements. In AIAA/AAS Astrodynamics Specialist Conference and Exhibit, page 4988, 2004.
- [186] Lukas M Steindorf, Simone D’Amico, Julian Scharnagl, Florian Kempf, and Klaus Schilling. Constrained low-thrust satellite formation-flying using relative orbit elements. In 27th AAS/AIAA Space Flight Mechanics Meeting, pages 5–9, 2017.
- [187] Marcus Holzinger, Jeremiah DiMatteo, Jeremy Schwartz, and Mark Milam. Passively Safe Receding Horizon Control for Satellite Proximity Operations. In 2008 47th IEEE Conference on Decision and Control, pages 3433–3440. IEEE, 2008.
- [188] Kyle J DeMars, Yang Cheng, and Moriba K Jah. Collision Probability with Gaussian Mixture Orbit Uncertainty. Journal of Guidance, Control, and Dynamics, 37(3):979–985, 2014.
- [189] Sangjin Lee, Hao Lyu, and Inseok Hwang. Analytical Uncertainty Propagation for Satellite Relative Motion Along Elliptic Orbits. Journal of Guidance, Control, and Dynamics, 39(7):1593–1601, 2016.
- [190] Ethan R Burnett and Hanspeter Schaub. Study of highly perturbed spacecraft formation dynamics via approximation. Advances in Space Research, 67(11):3381–3395, 2021.
- [191] Mohamed Okasha and Brett Newman. Guidance, Navigation and Control for Satellite Proximity Operations using Tschauner-Hempel Equations. The Journal of the Astronautical Sciences, 60(1):109–136, 2013.
- [192] WH Clohessy and RS Wiltshire. Terminal Guidance System for Satellite Rendezvous. Journal of the Aerospace Sciences, 27(9):653–658, 1960.
- [193] Thomas Carter and Mayer Humi. Clohessy-Wiltshire Equations Modified to Include Quadratic Drag. Journal of Guidance, Control, and Dynamics, 25(6):1058–1063, 2002.
- [194] Thomas A Lovell and David A Spencer. Relative Orbital Elements Formulation Based upon the Clohessy-Wiltshire Equations. The Journal of the Astronautical Sciences, 61(4):341–366, 2014.
- [195] Mai Bando and Akira Ichikawa. In-Plane Motion Control of Hill–Clohessy–Wiltshire Equations by Single Input. Journal of Guidance, Control, and Dynamics, 36(5):1512–1522, 2013.
- [196] Henry S Wright, David Y Oh, Carlos H Westhelle, Jody L Fisher, R Eric Dyke, Karl T Edquist, James L Brown, Hilary L Justh, and Michelle M Munk. Mars Aerocapture Systems Study. NASA Technical Memorandum TM-2006-214522, 2006.

- [197] Xinfu Liu, Zuojun Shen, and Ping Lu. Entry Trajectory Optimization by Second-Order Cone Programming. Journal of Guidance, Control, and Dynamics, 39(2):227–241, 2016.
- [198] Hongwei Han, Dong Qiao, Hongbo Chen, and Xiangyu Li. Rapid planning for aerocapture trajectory via convex optimization. Aerospace Science and Technology, 84:763–775, 2019.
- [199] Daniel A Matz and Christopher Cerimele. Development of a Numeric Predictor-Corrector Aerocapture Guidance for Direct Force Control. In AIAA Scitech 2020 Forum, page 0847, 2020.
- [200] Hongwei Han, Dong Qiao, and Hongbo Chen. Optimal Ballistic Coefficient Control for Mars Aerocapture. In 2016 IEEE Chinese Guidance, Navigation and Control Conference (CGNCC), pages 2175–2180. IEEE, 2016.
- [201] Charalambos D Charalambous. Stochastic nonlinear minimax dynamic games with noisy measurements. IEEE transactions on automatic control, 48(2):261–266, 2003.
- [202] Yaakov Bar-Shalom and Edison Tse. Dual effect, certainty equivalence, and separation in stochastic control. IEEE Transactions on Automatic Control, 19(5):494–500, 1974.
- [203] Kalyanmoy Deb and Himanshu Gupta. Introducing Robustness in Multi-Objective Optimization. Evolutionary Computation, 14(4):463–494, 2006.
- [204] Zoltan K Nagy and Richard D Braatz. Open-loop and closed-loop robust optimal control of batch processes using distributional and worst-case analysis. Journal of Process Control, 14(4):411–422, 2004.
- [205] Allen L Barker, Donald E Brown, and Worthy N Martin. Bayesian Estimation and the Kalman Filter. Computers & Mathematics with Applications, 30(10):55–77, 1995.
- [206] Dan Simon. Optimal State Estimation. John Wiley & Sons, 2006.
- [207] John Christian, Amanda Verges, and Robert Braun. Statistical Reconstruction of Mars Entry, Descent, and Landing Trajectories and Atmospheric Profiles. In AIAA SPACE 2007 Conference & Exposition, page 6192, 2007.
- [208] Tai-Shan Lou, Nan-Hua Chen, Zhi-Wu Chen, and Xiao-Lei Wang. Robust Partially Strong Tracking Extended Consider Kalman Filtering for INS/GNSS Integrated Navigation. IEEE Access, 7:151230–151238, 2019.
- [209] Ye Lu and Sarag J Saikia. Feasibility Assessment of Aerocapture for Future Titan Orbiter Missions. Journal of Spacecraft and Rockets, 55(5):1125–1135, 2018.
- [210] SA Striepe, DW Way, AM Dwyer, and J Balaram. Mars Science Laboratory Simulations for Entry, Descent, and Landing. Journal of Spacecraft and Rockets, 43(2):311–323, 2006.
- [211] CG Justus, BF James, SW Bougher, AFC Bridger, RM Haberle, JR Murphy, and S Engel. Mars-GRAM 2000: A Mars atmospheric model for engineering applications. Advances in Space Research, 29(2):193–202, 2002.
- [212] Davide Amato and Jay W McMahon. Deep Learning Method for Martian Atmosphere Reconstruction. Journal of Aerospace Information Systems, 18(10):728–738, 2021.

- [213] Evan Roelke, Jay W McMahon, Robert D Braun, and Phillip D Hattis. Universal Atmospheric Density Estimation Techniques for Aerocapture. In Journal of Spacecraft and Rockets, 2021. Manuscript ID 2021-06-A35197 (not yet published).
- [214] Shuang Li, Xiuqiang Jiang, and Yufei Liu. High-precision Mars Entry Integrated Navigation Under Large Uncertainties. The Journal of Navigation, 67(2):327–342, 2014.
- [215] Taishan Lou and Liangyu Zhao. Robust Mars atmospheric entry integrated navigation based on parameter sensitivity. Acta Astronautica, 119:60–70, 2016.
- [216] Ian M Meginnis, Zachary R Putnam, Ian G Clark, Robert D Braun, and Gregg H Barton. Guided Entry Performance of Low Ballistic Coefficient Vehicles at Mars. Journal of Spacecraft and Rockets, 50(5):1047–1059, 2013.
- [217] Hans P Geering. Optimal Control with Engineering Applications. Springer, 2007.
- [218] Zachary R Putnam, Matthew D Neave, and Gregg H Barton. Predguid Entry Guidance for Orion Return from Low Earth Orbit. In 2010 IEEE Aerospace Conference, pages 1–13. IEEE, 2010.

Appendix A

Relating UTM and GCRM Control Laws

The uniform trigonometrization method (UTM) [99] is a strategy representing the current state-of-the-art in OCP constraint regularization. The method leverages trigonometric functions, notably for control terms appearing in linear and in nonlinear form, as well as state path constraints. A drawback of current approaches lies in the fact that the UTM optimal control law is not uniquely determined. The piecewise control structure can be resolved using PMP to select the control input minimizing the Hamiltonian at each time step. However, PMP must be applied at each instant along the trajectory. This introduces numerical and implementation overhead. Moreover, it eliminates the analytical form of the control, requiring programmatic logic to calculate the Hamiltonian for each possible control permutation. The proposed GCRM regularization functions have the major benefit of resolving the ambiguity in the control structure through sigmoid functions. This is in contrast to the trigonometric terms utilized by UTM, which are bounded to unity but not monotonic in their arguments.

In this section, we summarize issues regarding quadrant ambiguity of the optimal control solution. We also draw a parallel between the GCRM and UTM control laws, and show that the two methods can be related. The major distinction is that the GCRM control law is uniquely determined, without application of PMP. Upon application of the necessary condition $\partial H/\partial u = 0$, it is typical to solve for the control in terms of states and costates and substitute the expression back into the problem. This step eliminates u and results in a well-defined two-point Hamiltonian BVP. An interesting observation is that, upon substituting the UTM optimal control solution back

into the Hamiltonian, the control takes a similar form to the algebraic regularization function in Table 2.1. This is shown by substituting the UTM error-control and penalty terms into Eq. (2.16). We limit our case to a single scalar control input, but the results apply to an arbitrary number of control terms.

The UTM performs regularization by replacing control terms with a sine-smoothing function and augmenting the integral cost with a cosine penalty factor. The regularized Hamiltonian for UTM can be written as

$$\tilde{H}_{UTM} = H_0 + H_1 \sin u + \epsilon \cos u \quad (\text{A.1})$$

The optimal control law is then derived as

$$\frac{\partial \tilde{H}_{UTM}}{\partial u} = 0 = H_1 \cos u - \epsilon \sin u \quad (\text{A.2})$$

resulting in the possible control branches

$$u_{UTM}^* = \begin{cases} \arctan\left(\frac{H_1}{\epsilon}\right) \\ \arctan\left(\frac{H_1}{\epsilon}\right) + \pi \end{cases} \quad (\text{A.3})$$

For a single-input system, two control laws are possible, leaving to the user the task of checking which option is optimal or converges. For l controls, the possible combinations will grow by a factor of 2^l , introducing further complexity in constructing and solving the Hamiltonian BVP.

We are interested in relating the UTM and GCRM control laws. Noting the following relationships for an arbitrary variable X

$$\sin(\arctan(X)) = \frac{X}{\sqrt{X^2 + 1}} \quad (\text{A.4a})$$

$$\cos(\arctan(X)) = \frac{1}{\sqrt{X^2 + 1}} \quad (\text{A.4b})$$

The possible form of the Hamiltonian for the UTM sine and cosine terms is then

$$\tilde{H}_{UTM} = \begin{cases} H_0 + H_1 \frac{\left(\frac{H_1}{\epsilon}\right)}{\sqrt{\left(\frac{H_1}{\epsilon}\right)^2 + 1}} + \epsilon \frac{1}{\sqrt{\left(\frac{H_1}{\epsilon}\right)^2 + 1}} \\ H_0 - H_1 \frac{\left(\frac{H_1}{\epsilon}\right)}{\sqrt{\left(\frac{H_1}{\epsilon}\right)^2 + 1}} - \epsilon \frac{1}{\sqrt{\left(\frac{H_1}{\epsilon}\right)^2 + 1}} \end{cases} \quad (\text{A.5})$$

The negative signs in the second expression in Eq. (A.5) are a result of the additive π term. Comparing to the expressions in Table 2.1, it is apparent that, after substituting the UTM optimal control back into the Hamiltonian, it is functionally similar to the algebraic regularization function. In addition, for $H_1 \neq 0$, the second control option is always optimal since it will minimize \tilde{H}_{UTM} regardless of the sign of H_1 . However, the ambiguity is not fully resolved on singular arcs. In addition, the associated penalty term in Eq. (A.5) is a non-positive-definite term, resulting in an artificial time-minimization objective appended to the running cost. By selection of the GCRM error-control and associated penalty terms, the ambiguity can be fully resolved while greatly simplifying the optimal control expression.

Appendix B

Singular Controls and Differential Extension

The system extension differential control (SEDC) problem involves augmenting control variables as additional states in the Hamiltonian BVP. The optimal control policy for the extended system is considered in this section. We show that a solution of $\text{OCP}(v)$ corresponding to a minimum of $\text{OCP}(u)$ must be totally singular. To begin, we establish an equivalency between the two problem structures. The extended problem has Hamiltonian

$$H^{(v)} = h(\mathbf{x}, \boldsymbol{\lambda}, u, t) + \lambda_u v \quad (\text{B.1})$$

where λ_u is a costate corresponding to the auxiliary state u with dynamics

$$\dot{\lambda}_u = -\frac{\partial h}{\partial u} \quad (\text{B.2})$$

Let $\{\mathbf{x}^*, \boldsymbol{\lambda}, u^*\}$ be an optimal trajectory of $\text{OCP}(u)$ such that

$$\frac{\partial^2}{\partial u^2} [h(\mathbf{x}^*, \boldsymbol{\lambda}^*, u^*, t)] \geq 0 \quad (\text{B.3})$$

At the final time, the Hamiltonian for $\text{OCP}(v)$ is

$$H^{(v)}(t_f) = h(\mathbf{x}(t_f), \boldsymbol{\lambda}(t_f), u(t_f), t_f) + \lambda_u(t_f)v(t_f) \quad (\text{B.4})$$

From Eq. (2.62d), the costate boundary conditions are $\lambda_u(t_f) = 0$, which implies $H^{(v)}(t_f) = h(\mathbf{x}(t_f), \boldsymbol{\lambda}(t_f), u(t_f), t_f)$. Next, taking a time derivative of Eq. (B.1) and noting Eq. (B.2) gives

$$\begin{aligned} \dot{H}^{(v)} &= \dot{h} + \dot{\lambda}_u v + \lambda_u \dot{v} \\ &= \underbrace{\frac{\partial h}{\partial \mathbf{x}} \dot{\mathbf{x}} + \frac{\partial h}{\partial \boldsymbol{\lambda}} \dot{\boldsymbol{\lambda}}}_{=0} + \underbrace{\frac{\partial h}{\partial u} \dot{u} - \frac{\partial h}{\partial u} v}_{=0} + \lambda_u \dot{v} = 0 \end{aligned} \quad (\text{B.5})$$

where the last equality results from minimization of the Hamiltonian function. This is true even if v is on the boundary of the admissible control set, since λ_u and \dot{v} are transversal (see Geering [217, pp. 36]). Equations (B.4) and (B.5) imply on the optimal trajectory,

$$\lambda_u v = 0 \tag{B.6}$$

The Hamiltonian functions are therefore equal for all time. On a singular arc,

$$H_v^{(v)} = \lambda_u = 0 \tag{B.7}$$

and time derivatives of the switching function give

$$\frac{d}{dt} H_v^{(v)} = \dot{\lambda}_u = -\frac{\partial h}{\partial u} = 0 \tag{B.8a}$$

$$\frac{d^2}{dt^2} H_v^{(v)} = -\frac{\partial}{\partial \mathbf{x}} \left(\frac{\partial h}{\partial u} \right) \dot{\mathbf{x}} - \frac{\partial}{\partial \boldsymbol{\lambda}} \left(\frac{\partial h}{\partial u} \right) \dot{\boldsymbol{\lambda}} - \left(\frac{\partial^2 h}{\partial u^2} \right) v = 0 \tag{B.8b}$$

Application of the Legendre-Clebsch convexity condition, Eq. (2.13), requires

$$(-1) \frac{\partial}{\partial v} \left[\frac{d^2}{dt^2} \left(H_v^{(v)} \right) \right] = \frac{\partial^2 h}{\partial u^2} \geq 0 \tag{B.9}$$

which is precisely the condition stated in Eq. (B.3), since u^* is a minimum of $\text{OCP}(u)$. Because $\lambda_u(t_f) = 0$, Eqs. (B.6) and (B.8a) imply that $\lambda_u = 0$. Therefore, the optimal solution of $\text{OCP}(v)$ utilizing the SEDC approach is totally singular.

Appendix C

Proof of Proposition 2

The proof proceeds in a similar manner as Proposition 1. The transversality conditions Eq. (3.5d) dictate the boundary conditions

$$\boldsymbol{\lambda}(t_f) = \boldsymbol{\nu}^T \boldsymbol{\psi}_{\mathbf{x}}(t_f) \quad (\text{C.1})$$

with terminal multipliers $\boldsymbol{\nu} \in \mathbb{R}^m$. Let us assume $\text{rank}(\boldsymbol{\psi}_{\mathbf{x}}(t_f)) = m$ with $m \leq n$ such that $\boldsymbol{\psi}_{\mathbf{x},i}$, $i = 1, \dots, m$ are linearly independent.

The terminal multipliers $\boldsymbol{\nu}$ remain to be found. We do so following the so-called *influence function* approach from Bryson [68, pp. 55–59] and Stengel [78, pp. 224–226]. Let $\boldsymbol{\lambda}^{(J)} \in \mathbb{R}^n$ be an optimal costate solution of Problem 2 neglecting the terminal state constraint. The Hamiltonian $H^{(J)}$ for the unconstrained problem is

$$H^{(J)} = (\boldsymbol{\lambda}^{(J)})^T (f + gu) + \lambda_0 \phi_{\mathbf{x}}(f + gu) \quad (\text{C.2})$$

with $\boldsymbol{\lambda}^{(J)}(t_f) = \mathbf{0} \in \mathbb{R}^n$. A first variation in the cost can be expressed as

$$\begin{aligned} \delta J &= (\boldsymbol{\lambda}^{(J)}(t_0))^T \delta \mathbf{x}(t_0) + \int_{t_0}^{t_f} \frac{\partial H^{(J)}}{\partial u} \delta u \, dt \\ &= \int_{t_0}^{t_f} \left((\boldsymbol{\lambda}^{(J)})^T + \lambda_0 \phi_{\mathbf{x}} \right) g \delta u \, dt \end{aligned} \quad (\text{C.3})$$

where $\delta \mathbf{x}(t_0) = \mathbf{0} \in \mathbb{R}^n$ for a fixed initial state. Using the influence function approach, a suitable variation is constructed to satisfy the terminal constraints while minimizing the objective such that $\delta J \leq 0$.

Next, let $\boldsymbol{\lambda}^{(i)} \in \mathbb{R}^n$ represent a costate solution zeroing the terminal constraint $\psi_i(t_f) = 0$, $i = 1, \dots, m$ without regard to the optimal cost objective. The Hamiltonian $H^{(i)}$ for the constraint alone is

$$H^{(i)} = (\boldsymbol{\lambda}^{(i)})^T (f + gu) \quad (\text{C.4})$$

A first variation in the terminal state is expressed as

$$\delta\psi_i(t_f) = \int_{t_0}^{t_f} \frac{\partial H^{(i)}}{\partial u} \delta u(t) dt = \int_{t_0}^{t_f} (\boldsymbol{\lambda}^{(i)})^T g \delta u dt \quad (\text{C.5})$$

For the i -th terminal multiplier ν_i , define the augmented cost

$$J' = J + \nu_i \psi_i(t_f) \quad (\text{C.6})$$

Substituting Eqs. (C.3) and (C.5) gives the first variation in J' as

$$\delta J' = \delta J + \nu_i \delta\psi_i(t_f) = \int_{t_0}^{t_f} \left((\nu_i \boldsymbol{\lambda}^{(i)} + \boldsymbol{\lambda}^{(J)})^T + \lambda_0 \phi_{\mathbf{x}} \right) g \delta u dt \quad (\text{C.7})$$

By choice, let the variation in the control be

$$\delta u = -\epsilon g^T (\nu_i \boldsymbol{\lambda}^{(i)} + \boldsymbol{\lambda}^{(J)} + \lambda_0 \phi_{\mathbf{x}}^T) \quad (\text{C.8})$$

for some arbitrary $\epsilon \in \mathbb{R}_{>0}$. Equation (C.7) can then be restated compactly as

$$\delta J + \nu_i \delta\psi_i(t_f) = - \int_{t_0}^{t_f} \epsilon \|\delta u\|^2 dt \quad (\text{C.9})$$

which clearly gives a decreasing (or stationary) value in the augmented cost. Using Eq. (C.8) in Eq. (C.5) gives an expression for the terminal multipliers minimizing each of the terminal constraints ψ_j for $j = 1, \dots, m$.

$$\delta\psi_j(t_f) = -\epsilon \int_{t_0}^{t_f} (\boldsymbol{\lambda}^{(i)})^T g g^T (\nu_j \boldsymbol{\lambda}^{(j)} + \boldsymbol{\lambda}^{(J)} + \lambda_0 \phi_{\mathbf{x}}^T) dt = 0 \quad (\text{C.10})$$

or

$$\underbrace{\nu_j \int_{t_0}^{t_f} (\boldsymbol{\lambda}^{(i)})^T g g^T \boldsymbol{\lambda}^{(j)} dt}_{Q_{i,j}} + \underbrace{\int_{t_0}^{t_f} (\boldsymbol{\lambda}^{(i)})^T g g^T (\boldsymbol{\lambda}^{(J)} + \lambda_0 \phi_{\mathbf{x}}^T) dt}_{b_i} = 0 \quad (\text{C.11})$$

resulting in the system of equations

$$Q_{i,j}\nu_j + b_i = 0, \quad i, j = 1, \dots, m \quad (\text{C.12})$$

Concatenating Eq. (C.12) into a linear matrix equation gives an expression for the terminal multipliers

$$\boldsymbol{\nu} = Q^{-1}\mathbf{b} \quad (\text{C.13})$$

where

$$Q = \begin{bmatrix} Q_{1,1} & \cdots & Q_{1,m} \\ \vdots & \ddots & \vdots \\ Q_{m,1} & \cdots & Q_{m,m} \end{bmatrix}, \quad \mathbf{b} = \begin{bmatrix} b_1 \\ \vdots \\ b_m \end{bmatrix} \quad (\text{C.14})$$

Invertibility of the Q matrix can be interpreted as a controllability condition [68], wherein terminal constraints must be satisfied with admissible controls. This property is ensured by the assumption $\mathbf{x}(t_f) \in \Theta$, such that the target set Θ is in the reachable set of the system.

Finally, we are motivated to examine the b_i expressions in Eq. (C.11). In a similar fashion to Proposition 1, define $\boldsymbol{\sigma}^{(J)} = \boldsymbol{\lambda}^{(J)} + \lambda_0 \phi_{\mathbf{x}}^T$. We express b_i as

$$b_i = \int_{t_0}^{t_f} (\boldsymbol{\lambda}^{(i)})^T g g^T \boldsymbol{\sigma}^{(J)} dt \quad (\text{C.15})$$

As in Eq. (3.21), the dynamics can be expressed as $\dot{\boldsymbol{\sigma}}^{(J)} = (f_{\mathbf{x}} + g_{\mathbf{x}}u)^T \boldsymbol{\sigma}^{(J)}$ with boundary conditions $\boldsymbol{\sigma}^{(J)}(t_f) = \boldsymbol{\lambda}^{(J)}(t_f) + \lambda_0 \phi_{\mathbf{x}}^T(t_f) = \mathbf{0} \in \mathbb{R}^n$. Thus, $\boldsymbol{\sigma}^{(J)}(t) = \mathbf{0} \in \mathbb{R}^n$ for all $t \in [t_0, t_f]$ and therefore $b_i = 0$ for $i = 1, \dots, m$. Observing Eq. (C.13), this gives the trivial solution for the terminal multipliers $\boldsymbol{\nu} = Q^{-1}\mathbf{b} = \mathbf{0} \in \mathbb{R}^m$. This in turn requires $\boldsymbol{\lambda}(t_f) = \boldsymbol{\nu}^T \psi_{\mathbf{x}}(t_f) = \mathbf{0} \in \mathbb{R}^n$ and $\boldsymbol{\lambda}(t) = \mathbf{0} \in \mathbb{R}^n$ for all $t \in [t_0, t_f]$ with $\lambda_0 \neq 0$. As developed in Proposition 1 this requires $p \rightarrow \infty$, completing the proof.

Appendix D

Linearized Dynamics and Measurement Models

The ECKF update equations require computation of discrete-time dynamics and measurement sensitivities in Eqs. (4.22a) and (4.22b). These are computed from the continuous-time jacobian matrices. The atmospheric density is assumed to be a function of altitude and perturbation parameters such that $\rho = \rho(h, \delta\eta_1, \dots, \delta\eta_l)$. Given the state vector $\mathbf{x}_k = [r, V, \gamma]^T$ and consider parameters $\mathbf{p} = [C_L, C_D, \delta\eta_1, \dots, \delta\eta_l]$, the state sensitivity matrices are computed as follows.

$$A_{\mathbf{x}_k} = \begin{bmatrix} 0 & \sin \gamma & V \cos \gamma \\ \frac{2\mu \sin \gamma}{r^3} - \frac{A C_D V^2 \frac{\partial \rho}{\partial r}}{2m} & -\frac{A C_D V \rho}{m} & -\frac{\mu \cos \gamma}{r^2} \\ \frac{A C_L u V^2 r^3 \frac{\partial \rho}{\partial r} - 2m \cos \gamma V^2 r + 4m \mu \cos \gamma}{2V m r^3} & \frac{2m \mu \cos \gamma + 2V^2 m r \cos \gamma + A C_L V^2 r^2 u \rho}{2V^2 m r^2} & \frac{\sin \gamma (\mu - V^2 r)}{V r^2} \end{bmatrix} \quad (\text{D.1})$$

$$A_{\mathbf{p}_k} = \begin{bmatrix} 0 & 0 & 0 & \dots & 0 \\ 0 & -\frac{A V^2 \rho}{2m} & -\frac{A C_D V^2 \frac{\partial \rho}{\partial \delta\eta_1}}{2m} & \dots & -\frac{A C_D V^2 \frac{\partial \rho}{\partial \delta\eta_l}}{2m} \\ \frac{A V u \rho}{2m} & 0 & \frac{A C_L V u \frac{\partial \rho}{\partial \delta\eta_1}}{2m} & \dots & \frac{A C_L V u \frac{\partial \rho}{\partial \delta\eta_l}}{2m} \end{bmatrix} \quad (\text{D.2})$$

Similarly, the measurement model sensitivity matrices are

$$H_{\mathbf{x}_k} = \begin{bmatrix} \frac{A V^2 \frac{\partial \rho}{\partial r} \sqrt{C_D^2 + C_L^2}}{2m} & \frac{A V \rho \sqrt{C_D^2 + C_L^2}}{m} & 0 \end{bmatrix} \quad (\text{D.3})$$

$$H_{\mathbf{p}_k} = \begin{bmatrix} \frac{A C_L V^2 \rho}{2m \sqrt{C_D^2 + C_L^2}} & \frac{A C_D V^2 \rho}{2m \sqrt{C_D^2 + C_L^2}} & \frac{A V^2 \frac{\partial \rho}{\partial \delta\eta_1} \sqrt{C_D^2 + C_L^2}}{2m} & \dots & \frac{A V^2 \frac{\partial \rho}{\partial \delta\eta_l} \sqrt{C_D^2 + C_L^2}}{2m} \end{bmatrix} \quad (\text{D.4})$$

Sensitivities of the density profile are also required. Noting the definition of the density perturbation in Eq. (4.44), the sensitivity with respect to radius can be computed as

$$\frac{\partial \rho}{\partial r} \approx \frac{\partial \rho}{\partial h} = \frac{\partial \bar{\rho}}{\partial h} (1 + \delta \rho) + \bar{\rho} \frac{\partial \delta \rho}{\partial h} \quad (\text{D.5})$$

with

$$\frac{\partial \bar{\rho}}{\partial h} = -\frac{\rho_0}{H} \exp\left(-\frac{h}{H}\right) \frac{\partial \delta \rho}{\partial h} = \frac{1}{h_e} \left(\delta \eta_2 + \dots + \delta \eta_l \left(\frac{h}{h_e}\right)^{l-2} \right) \quad (\text{D.6a})$$

Since the nominal profile does not depend on the density perturbation terms, the sensitivities with respect to $\delta \eta_i$ are

$$\frac{\partial \rho}{\partial \delta \eta_i} = \bar{\rho} \frac{\partial \delta \rho}{\partial \delta \eta_i} \quad (\text{D.7})$$

with

$$\frac{\partial \delta \rho}{\partial \delta \eta_i} = \left(\frac{h}{h_e}\right)^{i-1} \quad (\text{D.8})$$

These expressions complete the necessary components of all sensitivities for the studied state and consider parameters. In general, computation of these matrices analytically will improve numerical stability in comparison to finite difference equations. These expressions can be easily extended to additional states, parameters, or measurement models using the same approach.

Appendix E

Traditional Atmospheric Estimation

The sensed acceleration model in Eq. (4.37) is functionally similar to traditional approaches for density estimation during reentry. These calculate a density estimate ρ_{est} in a deterministic manner by equating the expected and measured aerodynamic drag acceleration [218].

$$\rho_{est} = \frac{2ma_{sens}}{V_r^2 C_D A} \quad (\text{E.1})$$

These strategies may update the density ratio on-board using a first-order fading memory filter to average out noisy behavior of the density estimate. While often practical for closed-loop guidance applications, traditional atmospheric estimation methods do not account for uncertainty in the atmospheric model, mass, or aerodynamic coefficients. In contrast, the ECKF update equations use current knowledge of the state uncertainty and noise intensity to minimize the sum square residual of the estimate errors. This represents the best-available knowledge at any given measurement epoch, even though the density is not measured directly.

Appendix F

Acknowledgements for Chapter 2

This report was prepared as an account of work sponsored by an agency of the United States Government. Neither the United States Government, nor any agency thereof, nor any of their employees, nor any of their contractors, subcontractors, or their employees, make any warranty, express or implied, or assume any legal liability or responsibility for the accuracy, completeness, or usefulness of any information, apparatus, product, or process disclosed, or represent that its use would not infringe privately owned rights. Reference herein to any specific commercial product, process, or service by trade name, trademark, manufacturer, or otherwise, does not necessarily constitute or imply its endorsement, recommendation, or favoring by the United States Government, any agency thereof, or any of their contractors or subcontractors. The views and opinions expressed herein do not necessarily state or reflect those of the United States Government, any agency thereof, or any of their contractors.

Supported by the Laboratory Directed Research and Development program at Sandia National Laboratories, a multimission laboratory managed and operated by National Technology and Engineering Solutions of Sandia LLC, a wholly owned subsidiary of Honeywell International Inc. for the U.S. Department of Energy's National Nuclear Security Administration under contract DE-NA0003525.